

ISSN 1916-9698 (Print)  
ISSN 1916-9701 (Online)

# INTERNATIONAL JOURNAL OF CHEMISTRY

Vol. 10, No. 1, February 2018



CANADIAN CENTER OF SCIENCE AND EDUCATION

# International Journal of Chemistry

*An International Peer-reviewed and Open Access Journal for Chemistry*

International Journal of Chemistry (IJC) is an international, peer-reviewed, open-access journal, published by Canadian Center of Science and Education. The journal is published Quarterly (February, May, August and November) in both print and online versions. IJC aims to promote excellence through dissemination of high-quality research findings, specialist knowledge, and discussion of professional issues that reflect the diversity of this field.

## The scopes of the journal include:

Analytical  
Biochemistry  
Inorganic  
Materials  
Neurochemistry  
Nuclear Chemistry  
Organic  
Physical Chemistry

## The journal is included in:

Academic Journals Database  
Bibliography and Index of Geology  
CABI  
CAS (Chemical Abstracts Service, ACS)  
EBSCOhost  
Elektronische Zeitschriftenbibliothek EZB  
Google Scholar  
Ulrich's

## Open-Access Policy

We follow the Gold Open Access way in journal publishing. This means that our journals provide immediate open access for readers to all articles on the publisher's website. The readers, therefore, are allowed to read, download, copy, distribute, print, search, link to the full texts or use them for any other lawful purpose. The operations of the journals are alternatively financed by publication fees paid by authors or by their institutions or funding agencies.

## Copyright Policy

Copyrights for articles are retained by the authors, with first publication rights granted to the journal/publisher. Authors have rights to reuse, republish, archive, and distribute their own articles after publication. The journal/publisher is not responsible for subsequent uses of the work.

## Submission Policy

Submission of an article implies that the work described has not been published previously (except in the form of an abstract or as part of a published lecture or academic thesis), that it is not under consideration for publication elsewhere, that its publication is approved by all authors and tacitly or explicitly by the authorities responsible where the work was carried out. However, we accept submissions that have previously appeared on preprint servers (for example: arXiv, bioRxiv, Nature Precedings, Philica, Social Science Research Network, and Vixra); have previously been presented at conferences; or have previously appeared in other "non-journal" venues (for example: blogs or posters). Authors are responsible for updating the archived preprint with the journal reference (including DOI) and a link to the published articles on the appropriate journal website upon publication.



The publisher and journals have a zero-tolerance plagiarism policy. We check the issue using the plagiarism prevention tool and a reviewer check. All submissions will be checked by iThenticate before being sent to reviewers.



This is an 'Open Access' journal published under a creative commons license. You are free to copy, distribute, display, and perform the work as long as you clearly attribute the work to the authors.

IJC accepts both Online and Email submission. The online system makes readers to submit and track the status of their manuscripts conveniently. For any questions, please contact [ijc@ccsenet.org](mailto:ijc@ccsenet.org).



Online Available: <http://ijc.ccsenet.org>

## EDITORIAL TEAM

### EDITOR-IN-CHIEF

Thirupathi Barla, Harvard University, United States

### ASSOCIATE EDITORS

Maria Rambla-Alegre, Ghent University, Belgium

Mohamedi Mohamed, Institut National de la Recherche Scientifique, Canada

Nanda Gunawardhana, Saga University, Japan

Ong Siew-Teng, Universiti Tunku Abdul Rahman, Malaysia

Patrick Marcel Schaeffer, James Cook University, Australia

Priya Mohan, University of Tennessee, United States

### EDITORIAL ASSISTANT

Albert John, Canadian Center of Science and Education, Canada

### REVIEWERS

Abdul Rouf Dar, United States

Adel Fahmy Shoukry, Kuwait

Ahmad Galadima, Nigeria

Ahmad Sazali Hamzah, Malaysia

Ahmet Ozan Gezerman, Turkey

Amer A. Taqa, Iraq

Amirsalar Khandan, Turkey

Ana Silva, Portugal

Anshuman Mangalum, United States

Asghari Gul, Pakistan

Ayodele Temidayo Odularu, Nigeria

Bhargava Karumudi, United States

Binod P Pandey, United States

Chanchal Kumar Malik, United States

Damião Pergentino de Sousa, Brazil

Debashis Mandal, United States

Desheng Zheng, United States

Duncan Leonard Smith, United Kingdom

Farkhondeh Fathi, Canada

Fatima Tuz Johra, Korea

Greg Peters, United States

Harsha D. Magurudeniya, United States

Hesham G. Ibrahim, Libya

Ho Soon Min, Malaysia

Jalal Isaad, France

Jiajue Chai, United States

Jian Zhang, United States

Jignasu Purnendu Mehta, India

Juan Jose Giner-Casares, Spain

Juan Rafael Garcia, Argentina

Kallen Mulilo Nalyanya, Kenya

Khaldun Mohammad Al Azzam, Saudi Arabia

K. Ishara Silva, United States

Konstantinos Kasiotis, Greece

Laila A. Abouzeid, Egypt

Lalith P. Samankumara, United States

Lei Shen, United States

Leiming Wang, United States

Madduri Srinivasarao, United States

Marcos Taveira, Portugal

Maolin Lu, United States

Marianna Torok, United States

Meriem Belhachemi, Algeria

Michael Rajesh Stephen, United States

Mohamed Abass, Egypt

Monira Nessem Michael, Egypt

Mustafa Oguzhan Kaya, Turkey

Nejib Hussein Mekni, Tunisia

Nisha Saxena, India

Prathapan Sreedharan, India

Praveen Kumar, United States

Priyanka Singh, United States

Qin Hu, United States

Qun Ye, Singapore

R. K. Dey, India

Rabia Rehman, Pakistan

Rajasekhar Reddy Naredla, United States  
Rodrigo Vieira Rodrigues, Brazil  
Saroj Kumar Panda, Saudi Arabia  
Sayandev Chatterjee, United States  
Severine Queyroy, France  
Shu-Ching Ou, United States  
Sirshendu De, India  
Sitaram Acharya, United States  
Sitaram Bhavaraju, United States  
Sudheer Chava, United States  
Sujan Kumar Sarkar, Germany  
Sunday Fes Fabiyi, Nigeria  
Shyamal Kumar Chattopadhyay, India  
Syed A. A. Rizvi, United States

Sie-Tiong Ha, Malaysia  
Takeshi Imai, Japan  
Teodora Emilia Coldea, Romania  
Thirupathi Barla, United States  
Valter Aragao Nascimento, Brazil  
Vijayakumar Ramalingam, United States  
Waseem Hassan, Brazil  
Yu Chen, United States  
Yu Hou, United States  
Yuetao Zhang, United States  
Zihuan Weng, United States  
Zhixia Liu, United States  
Zhixin Tian, China

---

## Content

Theoretical Study of the Coordination of Semicarbazone and Its Methylated Derivatives <i>Urbain A. Kuevi, Gaston A. Kpotin, Guy S. Y. Atohou, Jean-Baptiste Mensah</i>	1
Analysis of Butyl Butyrate Mass Spectrum <i>Abdalla Mustafa Walwil</i>	11
Graph Theory of Chemical Series and Broad Categorization of Clusters <i>Enos Masheija Rwantale Kiremire</i>	17
Green Preparation of Sulfonated Polystyrene/Polyaniline/Silver Composites with Enhanced Anticorrosive Properties <i>Guangfu Liao</i>	81
Graph Theory of Capping Golden Clusters <i>Enos Masheija Rwantale Kiremire</i>	87
Using Solar-TiO <sub>2</sub> and Biocarbon to Decompose and Adsorb Amoxicillin from Polluted Waters <i>Nilce Ortiz, Andre Silva, Giselle Natalia Silva Lima, Fernanda Pagano Hyppolito</i>	131
Modeling the Transition State Structures of the Reductive-Half Reaction Active Site of Xanthine Oxidase Bound to Guanine Analogues: A Density Functional Theory Approach <i>Mamaru Bitew Alem, Yilkal Bezie Ayele</i>	137
Derivatives of 2-Aminopyridines as Inhibitors of Multidrug Resistant Staphylococcus Aureus Strains <i>Inibong E. Ante, Sherifat A Aboaba, Hina Siddiqui, Muhammad A Bashir, Muhammad I Choudhary</i>	153
Reviewer Acknowledgements for International Journal of Chemistry, Vol. 10, No. 1 <i>Albert John</i>	162

# Theoretical Study of the Coordination of Semicarbazone and Its Methylated Derivatives

Urbain A. Kuevi<sup>1</sup>, Gaston A. Kpotin<sup>1</sup>, Guy S. Y. Atohoun<sup>1</sup>, Jean-Baptiste Mensah<sup>1</sup>

<sup>1</sup>Laboratoire de Chimie Théorique et de Spectroscopie Moléculaire (LACTHESMO), Université d'Abomey-Calavi, Bénin

Correspondence: Urbain A. Kuevi, Laboratoire de Chimie Théorique et de Spectroscopie Moléculaire (LACTHESMO), Université d'Abomey-Calavi, Bénin. E-mail: urviana@gmail.com

Received: November 2, 2017 Accepted: December 7, 2017 Online Published: January 3, 2018

doi:10.5539/ijc.v10n1p1

URL: <https://doi.org/10.5539/ijc.v10n1p1>

## Abstract

Semicarbazone is a molecule with a group  $R^1R^2C=N-NR^3-C(=O)-NR^4R^5$ .

The oxygen atom has two free electron pairs; each nitrogen atom has one free electron pair. These free electron pairs are potential sites of coordination. The simplest molecule in this series is the semicarbazone which the formula is  $H_2C=N-NH-C(=O)NH_2$ . By replacing the oxygen atom by a sulfur atom is obtained a thiosemicarbazone. Some semicarbazones, such as nitrofurazone, and some thiosemicarbazones are known to have many properties: antiviral, antibacterial, antitrypanosomal, anticonvulsant, antitumor, anticancer. They are usually mediated by an association with copper or iron.

Indeed transition metal complexes with given chemical structures are useful alternatives in the treatment of certain diseases since coordination of active ingredients deeply modifies both the physiological properties of metals and ligands in the meaning of overall improvement of these properties.

The present work focuses on quantum study of the complexation of semicarbazone and its methylated derivatives. The purpose of this study is to determine the most favorable coordination site of each of these ligands. It was found that the oxygen atom appears more favorable to the coordination of semicarbazones.

Complexes of these ligands with the Zn (II) were modeled. The calculations were made by the method DFT / B3LYP with the orbital basis 6-31G (d, p).

**Keywords:** coordination compounds, semicarbazones, DFT/ B3LYP, 6-31G (d,p) basis set

## 1. Introduction

The study at the molecular level of the interaction between metals and bioligands (proteins, nucleic acids, their fragments, and other substances contained in the organism) is topical (Knouniats, 1990) (Williams, 1975) (Yatsimirskii, 1976) (Kembal, 1975). The bioinorganic chemistry which is currently in full swing is concerned, inter alia, with the coordination of trace elements with organic ligands. The results of these studies find their applications in various fields of science and technology such as medicine, agriculture, environmental protection, catalysis.

In fact, the coordination of bioligands profoundly modifies both the physiological properties of metals and those of ligands with an overall improvement in the activity of the pure ligand or of the complexing metal salt (Azizov, 1969) (Büchel, Moretto et al. 2000) (Bäuerlein, Arias et al. 2007) (Bäuerlein, Kawasaki et al., 2007) (Bäuerlein, Frankel et al. 2007) (Andersen, 1999) (Wong & Giandomenico, 1999) (Shaw 1999), (Caravan & Ellison, 1999).

Semicarbazones (SCZ) are molecules having a group  $R^1R^2C=N-NR^3-C(=O)-NR^4R^5$ , thus having donor atoms (N and O) capable of forming bonds with complexing metals. They are of particular interest as ligands. Semicarbazones are derivatives of aldehydes or ketones. They are formed by condensation of these compounds with a semicarbazide as shown by the reaction:  $H_2NNHC(=O)NH_2 + RC(=O)R^2 \rightarrow RR^2C=NNHC(=O)NH_2 + H_2O$

where  $R^2$  is a hydrogen atom (if it is an aldehyde) or an alkyl group (if it is a ketone). The simplest molecule of this series is the semicarbazone of formula  $H_2C=N-NH-C(=O)NH_2$ . Certain semicarbazones, such as nitrofurazone, and certain thiosemicarbazones are known for their antiviral, antibacterial, antitrypanosomal (antiparasitic), anticonvulsive, anti-tumor, anti-cancer, etc. activities, generally mediated by a binding with copper or iron (Picot, 2008) (Sakirigui et al., 2011) (Kenneth, 1999).

The present work deals with a quantum study of the complexation of semicarbazone and its methylated derivatives. The aim of this study is to determine the most favorable coordination site for each of these ligands and to provide some insights into the complex geometry without which metabolic issues cannot be addressed. The coordination indicators (ICs) used in the studies are: interatomic bond lengths, atomic charges, boundary orbital structures and indexes of electrophilic superdelocalisability.

## 2. Materials and Methods

The present work, which is a theoretical study of the complexation of semicarbazone and its methylated derivatives, was carried out by quantum chemical calculations. These calculations were carried out using the density functional theory (DFT) method with the functional B3LYP. The calculation basis set was 6-31g (d, p). The software used to perform the calculations is the Gaussian 03 and 09 (Frisch et al. 1998). The used computer was a Samsung intel® core i32.4 GHz; the indexes of electrophilic superdelocalisability of the atoms were determined by the D-Cent-QSAR program (Gómez-Jeria, 2014). The different figures were made by the software Gauss view and by Chem Draw ultra 8. After studying the possibility of complexation of the different ligands with respect to criteria such as geometric parameters, atomic charges, HOMO components and the indexes of electrophilic superdelocalisability (IESD) of the atoms, we have modeled the formation of their respective complexes with zinc chloride (II).

We have tried to elucidate the type of hybridization of Zn (II) and consequently the shape of the complex. The ligands which have been the subject of the present study are semicarbazone and its methylated derivatives. Studies were performed at 25°C and 1 atm.

## 3. Results and Discussion

### 3.1 Study about the Ligands

This study allowed predicts the coordinatating sites of ligands by analysis of some system parameters known as coordinating indexes (CI). These IC was the geometric data, the atomic charges, the frontier orbitals, the energetic data, the atomic indexes of superdelolalisability. These data allow to explain the bond formation between donor and acceptor atoms. Figure 1 shows the molecules of the studied in this work semicarbazones (SCZs).

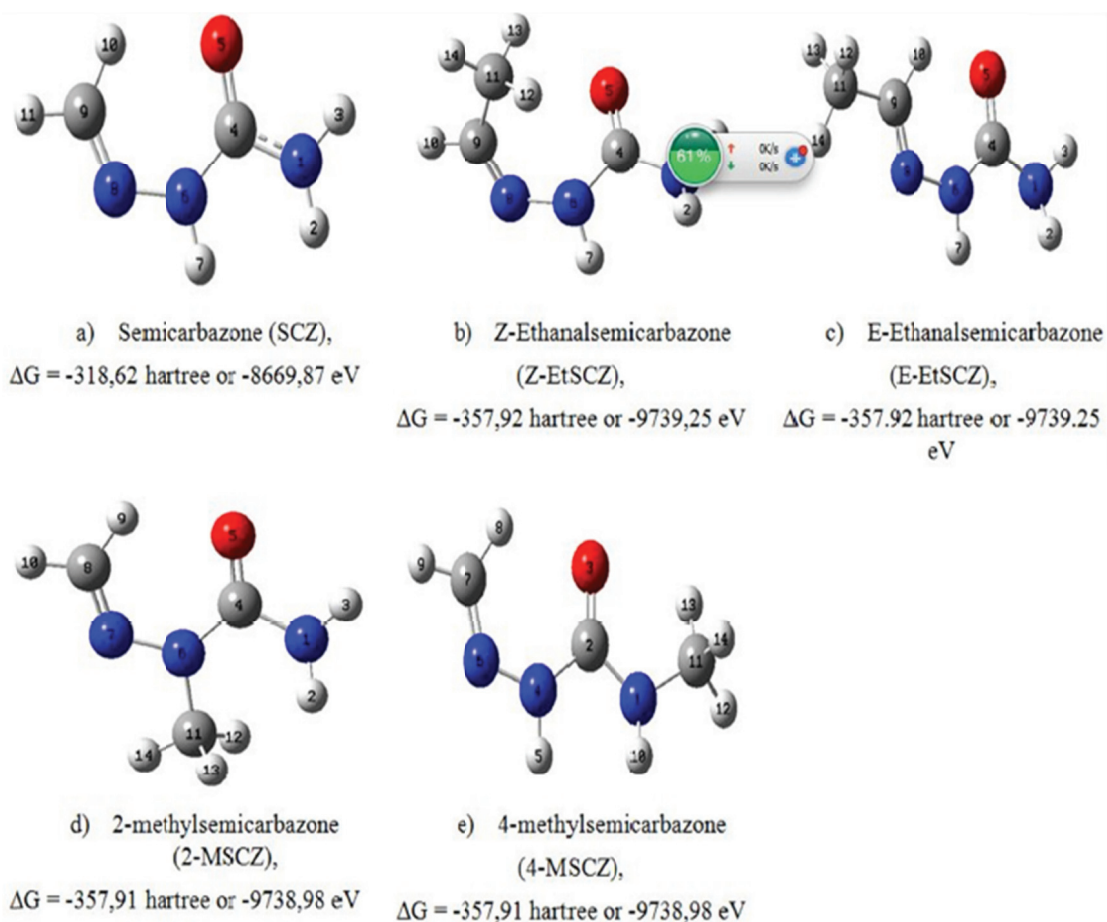


Figure 1. Calculated, on DFT/B3LYP level, geometries of the studied semicarbazones at 25°C and their energies

It is important to note that the more complete values of  $\Delta G$  are -357.919752 hartree for the Z-Ethanalsemicarbazone and -357.924990 hartree for E-Ethanalsemicarbazone. The value -357.92 hartree which appears under these two isomers is written in the authors' concern to stop at two digits after the decimal point. So there is no question of thinking that the two isomers have the same stability.

### 3.1.1 Geometric Analysis

The table 1 contains some geometric data of the studied ligands. Analysing SCZs molecules we notice that bond lengths  $N^1C^4$  and  $N^6C^4$  are equal to about 1.39Å. This value is intermediate between 1.47 Å (C-N length) and 1.27 Å (C=N length) (Mason, 1961) (Potapov & Tatarintchik, 2008) (Sakurai, Yoshikawa, Yasui, 2008). In other hand we found that  $C^4O^5$  bonds are about 1.22 Å long, it correspond to a double C=O bond. These observations suggest that the double C=O bond interacts with the free  $\pi$  electronic pairs of  $N^1$  and  $N^6$  nitrogen atoms while a part of electronic pairs clouds off O atom compenses the electronic defect, which issued from this conjugation, at the level of C=O double bond. That's why its length has not varied.

Table 1. Geometric parameters of investigated SCZs, \*Exp.= experimental values

Parameters	SCZ	Z-EtSCZ	E-EtSCZ	2-MSCZ	4-MSCZ	xp (Mason, 1961) (Potapov & Tatarintchik, 008) (Sakurai, Yoshikawa & Yasui, 2008)*
<b>Lengths (Å)</b>						
$N^1C^4$	1.39	1.39	1.39	1.39	1.38	C-N→1.47 ; C=N→1.27
$C^4N^6$	1.39	1.40	1.39	1.39	1.40	C-N→1.47 ; C=N→1.27
$N^6N^8$	1.37	1.41	1.38	1.38	1.37	N-N→1.40; N=N→1.23
$N^8C^9$	1.28	1.28	1.28	1.28	1.28	C-N→1.47 ; C=N→1.27
$C^4O^5$	1.22	1.22	1.22	1.22	1.22	C-O→1.43 ; C=O→1.21
$C^9C^{11}$	-	1.50	1.50	-	1.45	$C^1C^{11}$
$N^6C^{11}$	-	-	-	1.46	-	
<b>Angles (°)</b>						
$N^1C^4O^5$	122.78	123.21	122.52	121.35	123.3	
$N^1C^4N^6$	112.49	112.03	112.47	114.41	112.53	
$O^5C^4N^6$	124.72	124.75	125.00	124.18	124.17	
$C^4N^6N^8$	129.23	120.89	128.91	125.88	129.13	
$N^6N^8C^9$	121.15	117.04	120.77	122.97	121.33	
$N^8C^9C^{11}$	-	129.92	118.30	-	-	
$N^4C^6C^{11}$	-	-	-	121.54	119.51	$N^4C^1C^{11}$
<b>Dihedrals(°)</b>						
$N^1C^4O^5N^6$	178.14	178.69	178.51	177.13	178.93	
$N^1C^4N^6N^8$	-174.70	-162.11	-170.99	175.19	-173.96	
$O^5C^4N^6N^8$	3.60	16.71	7.64	-7.52	5.07	
$C^4N^6N^8C^9$	-10.77	-64.71	-17.11	2.99	-12.00	
$N^6N^8C^9C^{11}$	-	-3.25	-179.17	1.02	-171.92	$N^6C^4N^1C^{11}$

The  $N^6N^8$ , bond length of which about 1.37, is a single bond while the  $N^8C^9$  bond (1.28 Å) is a double one (Mason, 1961) (Potapov & Tatarintchik, 2008) (Sakurai, Yoshikawa & Yasui, 2008).

The sum of the bond angles around  $C^4$  atom equals  $360^\circ$  and the dihedral  $N^1C^4O^5N^6$  is about  $180^\circ$ ; this means that the three bonds (and the three atoms) which are around  $C^4$  are in the same plane. Consequently the clouds of the  $\pi$  free electronic pairs of  $N^1$  et  $N^6$  and that of  $\pi$  C=O have a same orientation, so it is a confirmation that they forms conjugation bonds  $N^1C^4$ ,  $N^6C^4$  and  $C^4O$ . This electronic pairs delocalization is not favorable to a coordination trough the  $N^1$  and  $N^6$  nitrogen atoms. Thus we can tell that the bond lengths as CI are not favorable to coordination with a metal ion trough the  $N^1$  and  $N^6$ ; contrarily that indice is favorable to coordination trough O and  $N^8$  because their free electronic pairs are quasi no delocalized (Douglas & Anthony, 1993).

### 3.1.2 Atomic Charges Analysis

The table 2 corresponds to the atomic charges of the investigated ligands. In these ligands one notice that the atomic charges of  $N^1$ ,  $N^6$  et  $O^5$  are about -0,7 a.u.; the  $N^8$  atoms carry rather positive charges (0.086 ; 0.035 ; 0.077 et 0.105 a.u. respectively for SCZ, Z-EtSCZ, E-EtSCZ, 2-MSCZ and 4-MSCZ). Thus the charge as CI is not favorable to a coordination trough  $N^8$ . Although the  $N^1$  and  $N^6$  atoms are negatively charged, the coordination through them is disadvantaged by their rather positive environment; in fact  $H^2$ ,  $H^3$ ,  $H^7$  et  $C^{11}$  carry high positive charges (about 0.2 a.u. for hydrogen atoms and 0.3 a.u. for  $C^{11}$ ) capable of repelling the coordination cation. These reasons assume that the charge is favorable for the coordination of the semicarbazones via the oxygen atom.



Table 2. Atomic charges (a.u.)

	SCZ	Z-EtSCZ	E-EtSCZ	2MSCZ	4MSCZ
N <sup>1</sup>	-0.734	-0.723	-0.75	-0.705	-0.773
N <sup>6</sup>	-0.659	-0.591	-0.689	-0.699	-0.658
N <sup>8</sup>	0.086	-0.138	0.035	0.077	0.105
O <sup>5</sup>	-0.724	-0.717	-0.732	-0.752	-0.778
C <sup>4</sup>	1.279	1.261	1.298	1.243	1.3
C <sup>9</sup>	0.045	0.285	0.188	0.025	0.035
H <sup>2</sup> ou	0.205	0.205	0.203	0.202	0.373
C <sup>11</sup>					
H <sup>3</sup>	0.217	0.215	0.214	0.217	0.181
H <sup>7</sup> ou	0.21	0.185	0.182	0.328	0.19
C <sup>N</sup>					

## 3.1.3 Frontier Orbitals Analysis

The table 3 shows some energetic values of studied SCZs. One notice that the HOMO et HOMO-1 are respectively of -6,5 eV et -7 eV; these molecular orbitals are dominated respectively by the p<sub>z</sub> atomic orbital of N<sup>6</sup> and the p<sub>x</sub> atomic orbital of O. According to this analysis, the frontier orbitals indicate that the coordinating favorable sites of studied SCZs in this investigation work are N<sup>6</sup> nitrogen atom and O.

Table 3. Energetic values of the investigated SCZs

Orbitals	SCZ		Z-EtSCZ		E-EtSCZ	
	Energies (eV)	dominant atomic orbitals	Energies (eV)	dominant atomic orbitals	Energies (eV)	dominant atomic orbitals
HOMO-1	-6,85	O	-7,08	O px(0,74)	-6,73	O
HOMO	-6,66	px (0.72) N <sup>6</sup> pz (0.78)	-6,29	N <sup>6</sup> pz(0,74)	-6,35	px(0,72) N <sup>6</sup> pz(0.76)
Sites favorables	O and N <sup>6</sup>		O and N <sup>6</sup>		O and N <sup>6</sup>	
Orbitals	2MSCZ,		4MSCZ		ZnCl <sub>2</sub> ,	
	Energies (eV)	dominant atomic orbitals	Energies (eV)	dominant atomic orbitals	Energies (eV)	dominant atomic orbitals
HOMO-1	-6,72	O p (0,71)	-6,69	O px (0,67)	-	-
HOMO	-6,35	N <sup>6</sup> pz (0.82)	-6,52	N <sup>6</sup> pz (0.77)	-	-
LUMO	-	-	-	-	-2,18	Zn s(2,01)
LUMO+1	-	-	-	-	-0,82	Zn py(1,5)
Sites favorables	O and N <sup>6</sup>		O and N <sup>6</sup>		-	

## 3.1.4 Atomic Indexes of Electrophilic Superdelocalisability (IESD) Analysis

The main IESDs are shown in the table 4. We can notice that all these indexes are negatives.

Table 4. IESD values of studied SCZs atoms

Atoms	IESD, eV				
	SCZ	Z-EtSCZ	E-EtSCZ	2MSCZ	4MSCZ
N <sup>1</sup>	-0.449	-0.453	-0.454	-0.452	-0.450
N <sup>6</sup>	-0.418	-0.436	-0.426	-0.418	-0.424
N <sup>8</sup>	-0.459	-0.479	-0.476	-0.464	-0.463
O <sup>5</sup>	-0.603	-0.611	-0.611	-0.616	-0.612
C <sup>4</sup>	-0.234	-0.241	-0.237	-0.237	-0.234
C <sup>9</sup>	-0.354	-0.326	-0.338	-0.359	-0.358
H <sup>2</sup>	0.049	-0.050	-0.050	-0.049	-
H <sup>3</sup>	-0.048	-0.049	-0.049	-0.049	-0.234
H <sup>7</sup>	-0.048	-0.050	-0.049	-	-0.049

The atomic index of electrophilic superdelocalizability is a magnitude which shows the capacity of given specie to attract a electrophile system. The coordination is thought to be more likely at the level of the atom with the most negative IESD (Gómez-Jeria, 2014). Thus the table 5 reveals that oxygen atom. (-0,6eV) is the more favorable coordination site for all studied ligands. It is followed by the trigonal nitrogen atom N<sup>8</sup> (about 0,46eV).

### 3.1.5 Recapitulative Analysis

In the table 5 you can read, at the intersection of each ligand with each CI, the atom through which coordination can occur during a complexation process.

Table 5. Recapitulative analysis, \* BL= Bond lengths, \*\* AC= Atomic charges

molecules	SCZ	E-EtSCZ	E-EtSCZ	2MSCZ	4MSCZ
CI					
BL*	O, N <sup>8</sup>	O, N <sup>8</sup>	O, N <sup>8</sup>	O, N <sup>8</sup>	O, N <sup>8</sup>
AC**	O	O	O	O	O
HOMO	O, N <sup>6</sup>	O, N <sup>6</sup>	O, N <sup>6</sup>	O, N <sup>6</sup>	O, N <sup>6</sup>
ISDE	O	O	O	O	O

It can be seen that all the CIs considered are favorable for the coordination of the studied semicarbazones via the oxygen atom. Coordination through N<sup>8</sup> or N<sup>6</sup> is less likely. No CI is favorable for coordination of semicarbazones, object of the present study, by N<sup>1</sup>.

These results should be confirmed by modeling the complexes of these molecules.

The choice in the present study is focused on zinc (II), a trace element that is very present in the treatment of various pathologies. Its electronic structure is 1s<sup>2</sup>2s<sup>2</sup>2p<sup>6</sup>3s<sup>2</sup>3p<sup>6</sup> 4s<sup>0</sup>3d<sup>10</sup>4p<sup>0</sup>. Zinc (II) generally gives tetrahedral complexes close to the Td point group. This is understandable when one observes its electronic structure: the orbital s, p<sub>x</sub>, p<sub>y</sub> and p<sub>z</sub> are vacant and are capable of sp<sup>3</sup> hybridization. The sp<sup>3</sup> hybrid orbitals point to the tops of a tetrahedron. The orbital p of atoms recognized as favorable for the coordination of the ligands studied are capable to overlap with these sp<sup>3</sup> orbitals.

## 3.2 Modeling of Coordination Compounds

### 3.2.1 Modeling

Semicarbazone complexes ZnCl<sub>2</sub>.Ligand were modeled. They are ZnCl<sub>2</sub>.SCZ, ZnCl<sub>2</sub>.Z-EtSCZ, ZnCl<sub>2</sub>.E-EtSCZ, ZnCl<sub>2</sub>.2MSCZ and ZnCl<sub>2</sub>.4MSCZ. Their structures and geometric parameters are shown respectively in the figure 2a and the table 7a. They are some chelates having tetrahedral structure. The coordination with the complexing atom took place via the oxygen atom (the length of Zn-O equals about 2 Å) and the trigonal nitrogen atom of the ligand (length of Zn-N<sup>8</sup> equals about 2 Å) forming a pentagonal ring, which is known to be more stable than if the coordination was established by N<sup>6</sup> instead of N<sup>8</sup> since the cycle tension would be, in this case, higher. These results are consistent with the literature data (Douglas, West & Anthony, 1993) (Alomar., 2012).

Semicarbazone complexes ZnCl<sub>2</sub>.2Ligand (ZnCl<sub>2</sub>.2SCZ, ZnCl<sub>2</sub>.2 (Z-EtSCZ), ZnCl<sub>2</sub>.2(E-EtSCZ), ZnCl<sub>2</sub>.2(2MSCZ) et ZnCl<sub>2</sub>.2(4MSCZ)) were modeled too. These complexes have tetrahedral structure too. Their structures are shown in figure 2b and, in the table 6b, are recorded some of their geometric data. It is found that the interatomic distances ZnO are of the order 2 Å, length of the Zn-O bond according to the data of the literature (Kuevi, 1992); there is no ZnN link. It can be deduced that the molecules of the semicarbazones that are the subject of the present works, in the proportion Zn / ligand = 1/2, have entered into coordination via the oxygen atom.

From all the foregoing it emerges that the combination of the analysis of interatomic distances, atomic charges, electrostatic potentials, atomic indices of superdelocalizability and the frontier orbitals of the ligands constitute a fairly effective means of studying the coordination of semicarbazones. An energetic study of the complexation processes made it possible to assess the stability of the coordination compounds of these ligands with Zn (II).

Table 6a. Some geometric data of the modelised complexes ZnCl<sub>2</sub>.Ligand

	ZnCl <sub>2</sub> .SCZ	ZnCl <sub>2</sub> .E-EtSCZ	ZnCl <sub>2</sub> .Z-EtSCZ	ZnCl <sub>2</sub> .2MSCZ	ZnCl <sub>2</sub> .4MSCZ
Distances (Å)					
Zn-O <sup>5</sup>	2,09	2,09	2,09	2,07	2,08
Zn-N <sup>1</sup>	4,17	4,17	4,17	4,15	4,16
Zn-N <sup>6</sup>	2,94	2,93	2,94	2,97	2,94
Zn-N <sup>8</sup>	2,19	2,17	2,17	2,17	2,19
Zn-Cl <sup>13</sup>	2,19	2,19	2,19	2,19	2,19
Zn-Cl <sup>14</sup>	2,19	2,19	2,19	2,19	2,19
Dihedrals (°)					
O <sup>5</sup> C <sup>4</sup> N <sup>6</sup> N <sup>8</sup>	-0,57	-2,77	-2,74	8,34	-2,79
N <sup>1</sup> C <sup>4</sup> N <sup>6</sup> N <sup>8</sup>	178,23	176,42	176,44	-177,65	176,79
C <sup>4</sup> N <sup>6</sup> N <sup>8</sup> C <sup>9</sup>	-175,08	-174,72	-174,75	-179,33	-176,23
N <sup>6</sup> N <sup>8</sup> C <sup>9</sup> C <sup>11</sup>	-	0,12	0,12	3,07	-
ZnOC <sup>4</sup> N <sup>1</sup>	177,54	-179,35	-179,37	169,91	-176,99
ZnOC <sup>4</sup> N <sup>6</sup>	-3,73	-0,22	-0,24	-12,17	2,55

Table 6b. Some geometric data of the modelised complexes ZnCl<sub>2</sub>.2Ligand

	ZnCl <sub>2</sub> .2SCZ	ZnCl <sub>2</sub> .2E-EtSCZ	ZnCl <sub>2</sub> .2Z-EtSCZ	ZnCl <sub>2</sub> .2(2MSCZ)	ZnCl <sub>2</sub> .2(4MSCZ)
Distances (Å)					
Zn-O <sup>5</sup>	2.00	1.99	1.99	2.00	2.00
Zn-O <sup>19</sup>	2.00	1.99	1.99	2.00	2.00
Zn-N <sup>1</sup>	3.40	3.40	3.42	3.40	3.36
Zn-N <sup>15</sup>	3.40	3.40	3.42	3.40	3.36
Zn-N <sup>6</sup>	4.21	4.14	4.22	4.21	4.22
Zn-N <sup>20</sup>	4.21	4.14	4.22	4.21	4.22
Zn-N <sup>8</sup>	4.84	4.71	4.72	4.84	4.86
Zn-N <sup>22</sup>	4.84	4.71	4.72	4.84	4.86
Zn-Cl <sup>13</sup>	2.20	2.22	2.21	2.20	2.20
Zn-Cl <sup>14</sup>	2.31	2.30	2.31	2.31	2.33
Diedrals (°)					
O <sup>5</sup> C <sup>4</sup> N <sup>6</sup> N <sup>8</sup>	0.51	9.24	16.5	0.51	-0.13
N <sup>1</sup> C <sup>4</sup> N <sup>6</sup> N <sup>8</sup>	-177.32	-169.08	-162.74	-177.32	-179.31
C <sup>4</sup> N <sup>6</sup> N <sup>8</sup> C <sup>9</sup>	-19.61	-45.39	-70.01	-19.61	-14.82
N <sup>6</sup> N <sup>8</sup> C <sup>9</sup> C <sup>11</sup>	-	179.82	-2.8	-5.76	-4.27
ZnOC <sup>4</sup> N <sup>1</sup>	-25.36	-38.20	-20.57	-25.36	-19.56
ZnOC <sup>4</sup> N <sup>6</sup>	156.97	143.59	160.24	156.97	161.31

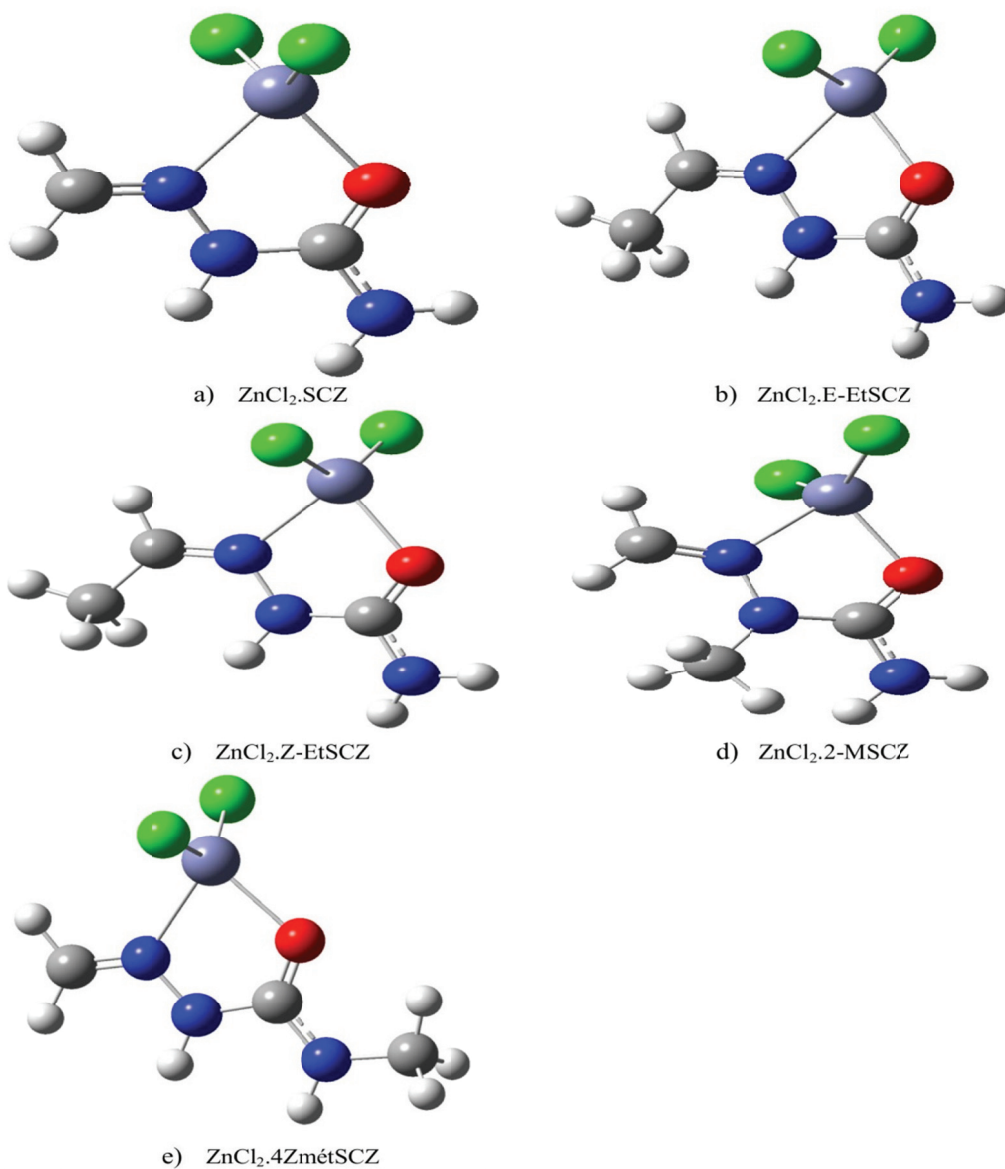
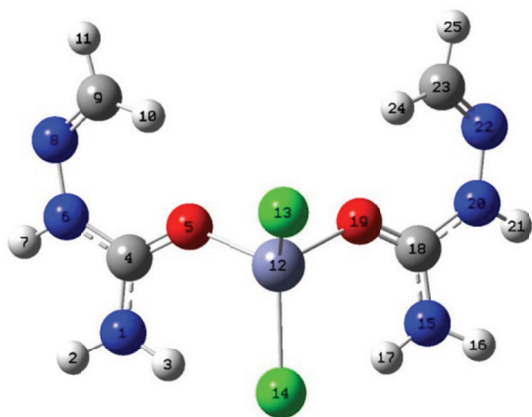
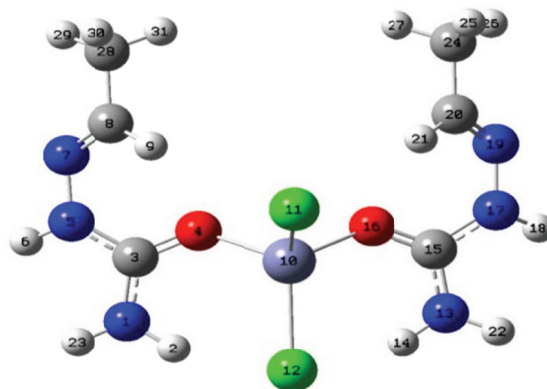


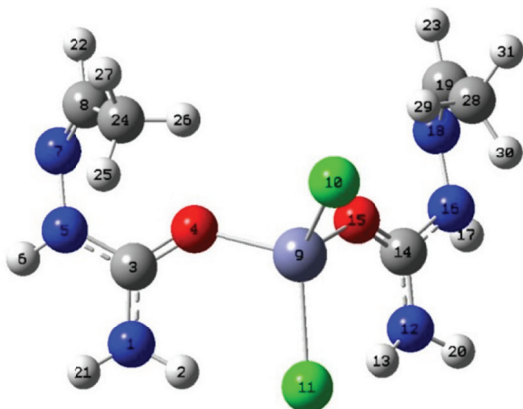
Figure 2a. Structures of the modelised complexes  $ZnCl_2.Ligand$



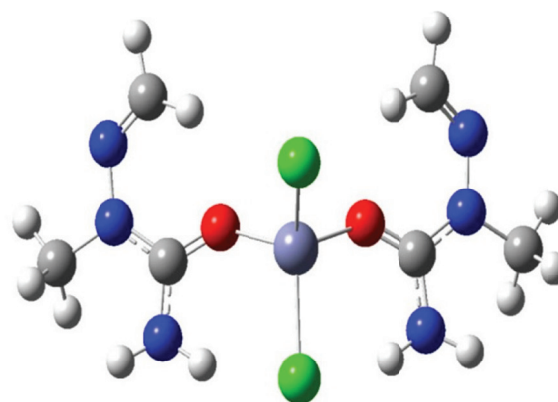
$ZnCl_2(SCZ)_2$   
Dichlorodisemicarbazonezinc(II)



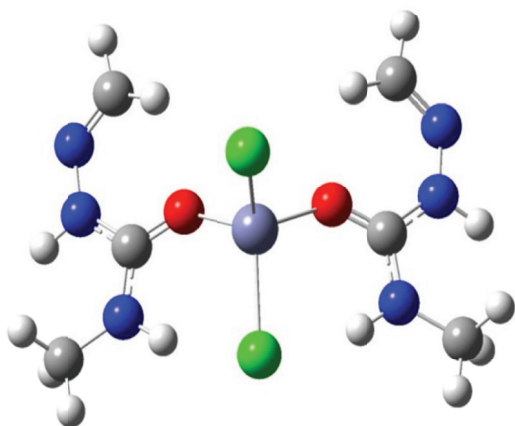
$ZnCl_2(E-EtSCZ)_2$   
DichlorodiE-ethanalsemicarbazonezinc(II)



$ZnCl_2(Z-EtSCZ)_2$   
DichlorodiZ-ethanalsemicarbazonezinc(II)



$ZnCl_2(2MSCZ)_2$   
Dichlorodi2-methylsemicarbazonezinc(II)



$ZnCl_2(4MSCZ)_2$   
Dichlorodi4-methylsemicarbazonezinc(II)

Figure 2b. Structures of the modelised complexes  $ZnCl_2 \cdot 2Ligand$

### 3.2.2 Energy Study

The study of the energy of coordination between ligands and zinc (II) chloride was used to assess the stability of the coordination bond. Le table 8 present shows energy values.

$\Delta G$ = Free enthalpy of the species

$\Delta G_{\text{coord}}$ = Free enthalpy of coordination

$\Delta G_{\text{coord}} = \Delta G_{\text{complex}} - (\Delta G_{\text{ligand}} + \Delta G_{\text{ZnCl}_2})$  ou  $\Delta G_{\text{coord}} = \Delta G_{\text{complex}} - (2\Delta G_{\text{ligand}} + \Delta G_{\text{ZnCl}_2})$

$\Delta H$ = Enthalpy of the species

$\Delta H_{\text{coord}}$ = Enthalpy of coordination

$\Delta H_{\text{coord}} = \Delta H_{\text{complex}} - (\Delta H_{\text{ligand}} + \Delta H_{\text{ZnCl}_2})$  ou  $\Delta H_{\text{coord}} = \Delta H_{\text{complex}} - (2\Delta H_{\text{ligand}} + \Delta H_{\text{ZnCl}_2})$

Table 7. Some energies of the studied systems

	$\Delta H$ , eV	$\Delta H_{\text{coord}}$ , eV	$\Delta G$ , eV	$\Delta G_{\text{coord}}$ , eV	Type de processus
ZnCl <sub>2</sub>	-73458,28	-	-73459,09	-	-
SCZ	-8669,06	-	-8669,87	-	-
E-EtSCZ	-9738,17	-	-9739,25	-	-
Z-EtSCZ	-9738,17	-	-9739,25	-	-
2MSCZ	-9737,89	-	-9738,98	-	-
4MSCZ	-9737,89	-	-9738,98	-	-
Complexes ZnCl <sub>2</sub> .Ligand					
ZnCl <sub>2</sub> .SCZ	-82128,70	-1,35	-82130,33	-1,37	Exothermic and Spontaneous
ZnCl <sub>2</sub> .E-EtSCZ	-83197,80	-1,35	-83199,71	-1,37	Exothermic and Spontaneous
ZnCl <sub>2</sub> .Z-EtSCZ	-83198,07	-1,62	-83199,71	-1,37	Exothermic and Spontaneous
ZnCl <sub>2</sub> .2MSCZ	-83197,53	-1,36	-83199,16	-1,09	Exothermic and Spontaneous
ZnCl <sub>2</sub> .4MSCZ	-83197,53	-1,36	83199,16	-1,09	Exothermic and Spontaneous
Complexes ZnCl <sub>2</sub> .2Ligand					
ZnCl <sub>2</sub> .2SCZ	-90798,57	-2,17	-90800,47	-1,64	Exothermic and Spontaneous
ZnCl <sub>2</sub> .2(E-EtSCZ)	-92937,06	-2,44	-92939,23	-1,64	Exothermic and Spontaneous
ZnCl <sub>2</sub> .2(Z-EtSCZ)	-92937,33	-2,71	-92939,23	-1,64	Exothermic and Spontaneous
ZnCl <sub>2</sub> .2(2MSCZ)	-92936,24	-2,18	-92938,42	-1,37	Exothermic and Spontaneous
ZnCl <sub>2</sub> .2(4MSCZ)	-92936,24	-2,18	-92938,42	-1,37	Exothermic and Spontaneous

The negative values of the free enthalpies of coordination show that the coordination of the studied semicarbazones is spontaneous process. The enthalpies are negative, so the process concerning the ligands is exothermic.

From the both conformers of ethanalsemicarbazone one obtains the same chelate; instead the Z-ETSCZ was transformed, during the complexation, into the E- form to avoid congstion with the ZnCl<sub>2</sub> system. The value -1.62 eV obtained in the column of the enthalpies of coordination for the complex Z-ETSCZ would be the sum of the coordination enthalpy of this complex and the reorganization energy of the Z-ETSCZ molecule to E-ETSCZ one.

It should be noted that the introduction of the methyl group in semicarbazone did not involve any significant modification of the properties.

## 4. Conclusion

The present works constitute a theoretical study of the coordination of the molecules of some semicarbazones. These were semicarbazone, E-ethanalsemicarbazone, Z-ethanalsemicarbazone, 2-methylsemicarbazone, 4-methylsemicarbazone. This has been possible through the analysis of coordination indicators such as bond lengths, atomic charges, electrostatic atom potentials, boundary orbitals, and atomic electrophilic superdelocalizability indexes.

The results from our calculations showed that these molecules are able to form complexes with metal ions. Zn<sup>2+</sup> is one of those ions. It has been found that the most favorable coordination site is the oxygen atom for these semicarbazones followed by the trigonal nitrogen atom. The methyl group in semicarbazone did not involve any significant modification of the properties.

The complexes obtained with Zinc (II) provided by the zinc (II) chloride are of the proportion Zn / ligand equal to 1/1 and 1/2. The central element, Zn (II), has a tetrahedral structure in all the complexes obtained. The vertices of the tetrahedra are occupied by two chlorine atoms and two oxygen atoms for the 1/2 structures; in the 1/1 structures, the vertices of the tetrahedron are occupied by the two Cl atoms, the O atom and the trigonal N atom of the ligand. The complexes of the proportion Zn / ligand equal to 1/1 are chelates resulting from the coordination of the ligands via the O and Ntrigonal atoms thus forming a five-membered ring.

All complexation processes were spontaneous and exothermic under the study conditions of 25 ° C and one atmosphere.

## References

- Alomar, K. (2012). *Synthese, caracterisation st ructurale de complexes de thiosemicarbazones, semicarbazones et oximes mono et bifonctionnelles d'ald\_ehydes thiopheniques avec des metaux de transition. Etude de propriétés biologiques.* (Doctoral dissertation) <https://tel.archives-ouvertes.fr/tel-01277204>
- Andersen, O. (1999). Principles and recent developments in chelation treatment of metal intoxication, *Chem. Rev.*, *99*, 2683–2710. <https://doi.org/10.1021/cr980453a>
- Azizov, M. A. (1969). *O Komplekxnih soédineniah nekotarih microélémentov s bioaktivnimi vechstvami*, (ed. Médétsina), Tachkent
- Bäuerlein, E., Arias, J. L. et al. (2007). *Handbook of biomineralization: biological aspects and structure formation, 1, Biological aspects and structure formation*, 309-327. <https://doi.org/10.1002/9783527619443>
- Bäuerlein, E., Kawasaki, K. et al. (2007). *Handbook of biomineralization: biological aspects and structure formation, 1, Biological aspects and structure formation.*
- Bäuerlein, E.; Frankel, R. B. et al., (2007). *Handbook of biomineralization: biological aspects and structure formation, 1, Biological aspects and structure formation.* <https://doi.org/10.1002/9783527619443>
- Büchel, K. H., Moretto, H. H. et al., (2000). *Industrial inorganic chemistry.* <https://doi.org/10.1002/9783527613328>
- Caravan, P., Ellison, J. J. et al. (1999). Gadolinium(III) chelates as MRI contrast agents: structure, dynamics, and applications, *Chem. Rev.*, *99*, 2293–2352. <https://doi.org/10.1021/cr980440x>
- Douglas, X., & West, A. (1993). *Coordination Chemistry Reviews*, *123*(s1–2), 49–71.
- Frisch, M. J. et al. (2009). *Gaussian 09W*, Gaussian Inc., Pittsburgh PA,
- Gómez-Jeria, J. S. (2014). D-Cent-QSAR, *1*. Santiago, Chile.
- Kemal, J. ((1975). *Sovrémiénaya obchaya himia*, (ed. Mir), Moscou
- Kenneth, L. (1999). *Macroscale and Microscale Organic Experiments*, (3rd ed.), ISBN 978-0-395-90220-2, LCCN 98072094
- Knouniats, I. L. (1990). *Himitcheskaya Entsiklopédiya*, Ed. Sovietskaya entsiklopédiya, Moscou .
- Kuevi, U. A. (1992). *Etude quanto-chimique de la coordination du benzamide, du N,N-diméthylbenzamide et du succinimide*, (Unpublished master's thesis), Université Russe de l'Amitié des Peuples, Moscou, Russia
- Mason, R. (1961). *Acta crystallogr.*, *14*, 720. <https://doi.org/10.1107/S0365110X61002199>
- Picot, D. (2008). *Modelisation de la reaction d'alkylation du motif zinc-thiolate*, (Doctoral dissertation). <https://pastel.archives-ouvertes.fr/pastel-00004269>
- Potapov, V., & Tatarintchik, S. (1988). *Chimie organique*, (Ed. Mir), Moscou
- Sakirigui, A. et al, (2011). *J. Soc. Ouest-Afr: Chim.*, *31*, 11-20.
- Sakurai, H., Yoshikawa, Y., & Yasui, H. (2008). *Chem Soc Rev.*, *37*(11), 2383-2392. <https://doi.org/10.1039/b710347f>
- Shaw, C. F. (1999). Gold-based therapeutic agents, *Chem. Rev.*, *99*, 2589–2600. <https://doi.org/10.1021/cr980431o>
- Williams, D. (1975). *Mettalli Jizni*, (ed. Mir) Moscou .
- Wong, E., & Giandomenico, C. M. (1992). Current status of platinum-based antitumor drugs, *Chem. Rev.*, *99*, 2451-2466. <https://doi.org/10.1021/cr980420v>
- Yatsimirskii, K. V. (1976). *Vvedenie v bioniorganitsheskouyou himiou*, (ed. NaoukovaDoumka).

## Copyrights

Copyright for this article is retained by the author(s), with first publication rights granted to the journal.

This is an open-access article distributed under the terms and conditions of the Creative Commons Attribution license (<http://creativecommons.org/licenses/by/4.0/>).

## Analysis of Butyl Butyrate Mass Spectrum

Abdalla Mustafa Walwil

Correspondence: Abdalla Mustafa Walwil, Department of Chemistry, Arab American University, Palestine.

Received: October 29, 2017 Accepted: November 26, 2017 Online Published: January 3, 2018

doi:10.5539/ijc.v10n1p11

URL: <https://doi.org/10.5539/ijc.v10n1p11>

### Abstract

The aim of this educational work is targeting chemistry students and interested instructors. The presented work will analyze the mass spectrum of butyl butyrate (butyl butanoate). The analysis will concentrate on the mechanisms showing how the characteristic fragments are formed. The mechanisms discussed in this paper include  $\alpha$ -cleavage,  $\beta$ -cleavage, McLafferty Rearrangements, first and second proton transfer, a double proton transfer.

**Keywords:**  $\alpha$ -cleavage,  $\beta$ -cleavage, McLafferty Rearrangement, base peak, butyl butanoate, proton transfer, double proton transfer, MS spectrophotometer

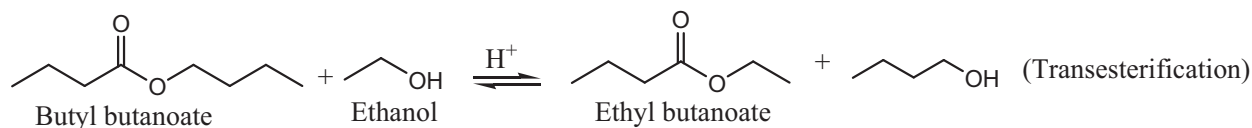
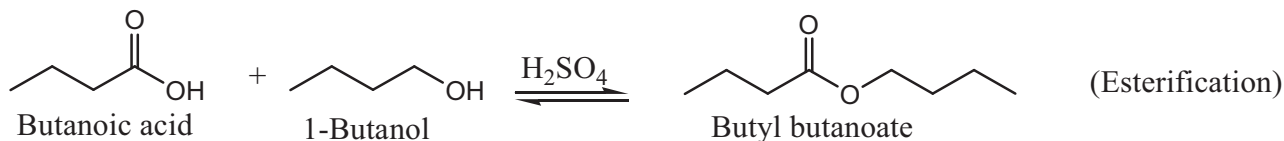
### 1. Introduction

Butyl butyrate is the second compound to be discussed in a series of MS spectral analysis of organic compounds. The MS spectra for  $\alpha$ -Ionone and  $\beta$ -Ionone were analyzed earlier (Walwil, 2017). The intended analysis of MS spectra will cover, besides the current analysis, ester, and the earlier one, ketone, ionones, all other classes includes carboxylic acids, aldehydes, amides, amines, alcohols, ethers, etc. Butyl butyrate was chosen for analysis since its mass spectrum shows many characteristic signals and their analysis is straightforward and easy to follow.

The current work will provide a thorough analysis of the EI-MS spectrum of one flavor aroma compound butyl butyrate. The fragmentation mechanisms of all major peaks will comprehensively be analyzed (Yang, Minkler, Hoppel, & Tserng, 2006).

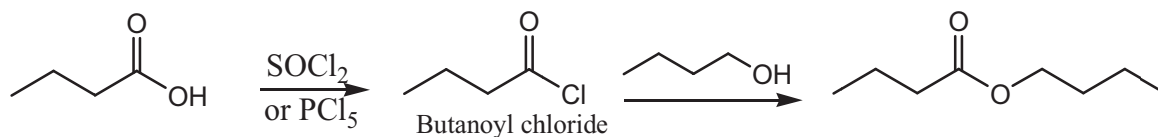
Butyl butanoate is the IUPAC name for butyl butyrate. It is an aroma ester found in various kinds of fruits such as berries, strawberry, apple and banana. Butyl butyrate is used industrially as sweet flavors for pineapple which is important for food and beverages industries.

The most common methods for preparing esters are esterification and transesterification (Varma & Madros, 2008). Butyl butyrate can be synthesized by reacting butanoic acid with n-butanol in the presence of an acid catalyst.



Since alkanoyl chlorides are readily made from the corresponding acids by using either thionyl chloride or phosphorous tri or pentachloride, then, the sequence  $R_1CO_2H \rightarrow R_1COCl \rightarrow R_1CO_2R$  is found to be a better method for esterification. This method is faster and avoids the troubles associated with the equilibrium of acid-catalyzed formation (Loudon, 2002) (Clark, 2015).





In contrast to all spectroscopic machines, mass spectrometry involves no absorption of electromagnetic radiation. Mass spectrometry is one of the most important techniques for determining molecular masses. The objective here is the study of the mechanisms of how the characteristic fragments of butyl butanoate are formed and how it can be applied to structure elucidation. In a mass spectrometer, a sample of butyl butyrate will be vaporized in a vacuum and bombarded with an electron beam of high energy (around 70 electron volts); the results will knock an electron off of the molecules and break them into smaller fragments, charged and neutral ones (Solomons, & Fryhle, Organic Chemistry).

## 2. Spectral Analysis

According to Figure 1, the main characteristic peaks of butyl butanoate observed are at  $m/z = 116, 101, 89, 88, 73, 71, 61, 60, 57, 56, 43,$  and  $29$ ; the numbers indicated on the signals represent the mass of ions of the corresponding charged fragments. The peaks at  $m/z = 15, 29, 43, 57,$  and  $71$  are known as cluster peaks (fragments). Note that the main peak, the molecular ion peak, is missing; this is expected for some esters, especially those esters of alcohols larger than four carbon atoms (the carbonyl oxygen R group). The absence of the molecular ion,  $M^+$ , peak indicates that it is somewhat unstable and fragments too quickly to be observed. The ion fragment requires around  $5 \times 10^{-5}$  seconds to reach the detector and for a signal to be observed (Pavia, Lampman, Kriz, & Vyvyan, Introduction to Spectroscopy).

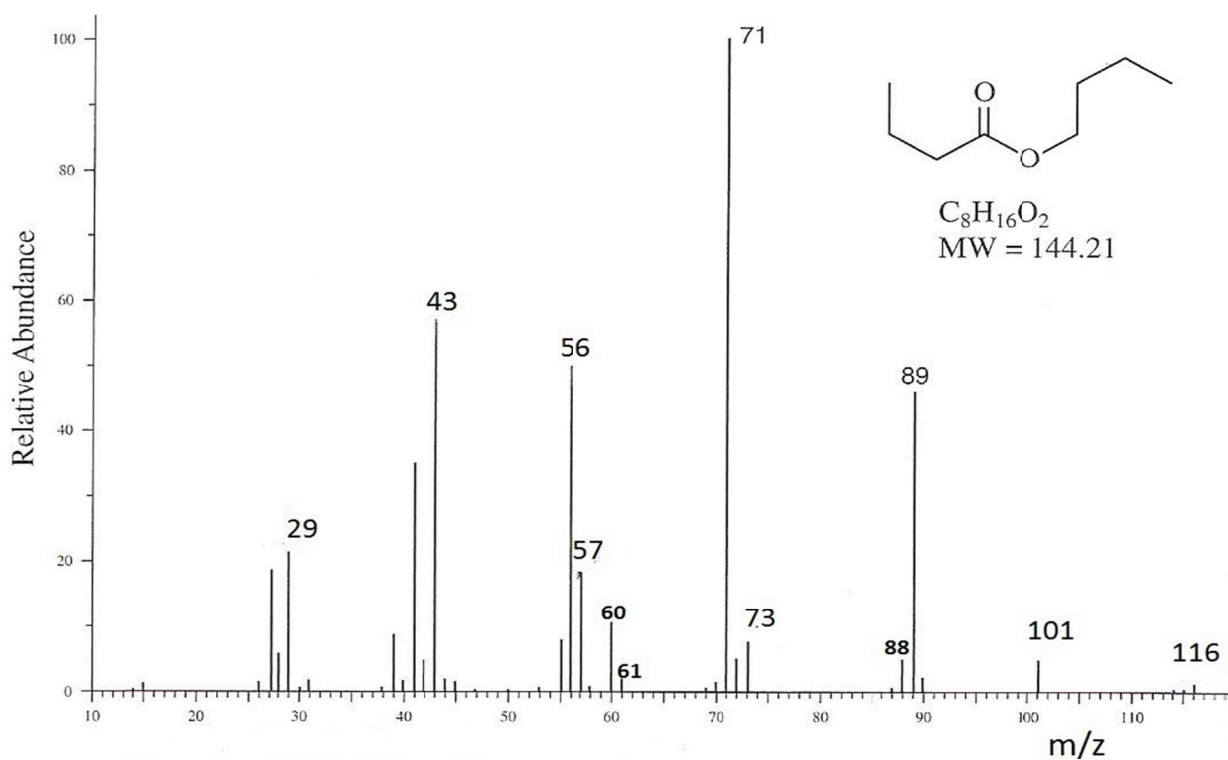


Figure 1. EI-MS of Butyl butanoate

## 3. The Structures of the Major Fragment Ions

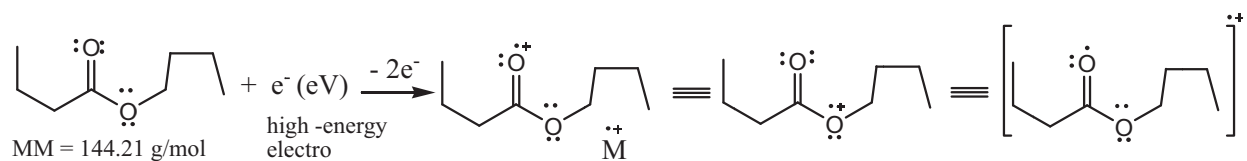
Once the gaseous molecules of the studied compound are bombarded with a beam of high-energetic electron, a valence electron from the gas-phase molecules will be dislodged leaving them with positive charges and unshared electrons ( $M^+$ ); the charged ones will further break into smaller fragments. Table 1 represents the major characteristic ion fragments (Vollhardt, & Schore, Organic Chemistry/Structure and Function):

Table 1. The structure and the weight of the main fragment ions for butyl butanoate

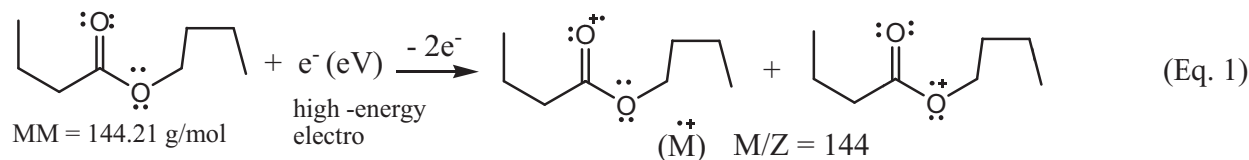
Fragment	m/z	Fragment	m/z
	144		71
	144		61
	116		60
	101		60
	89		57
	88		43
	73		43
		$\text{CH}_3 = \text{CH}_2^+$	29

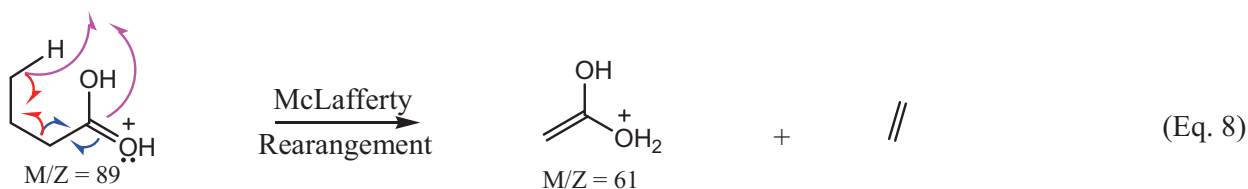
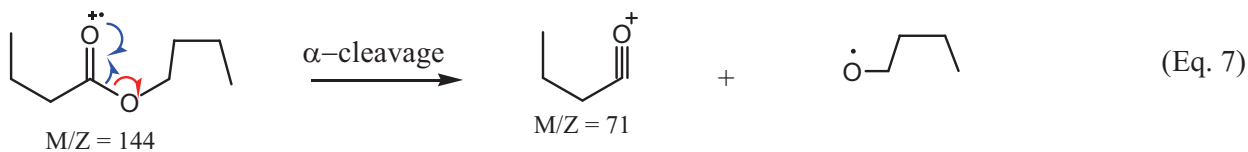
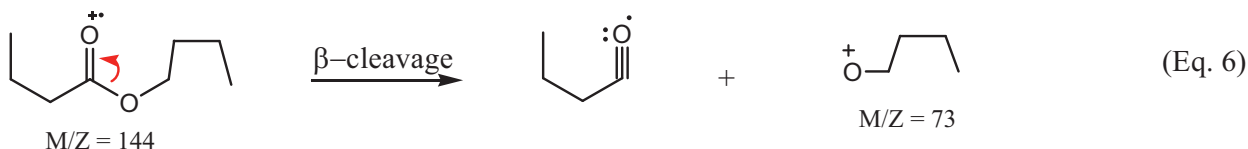
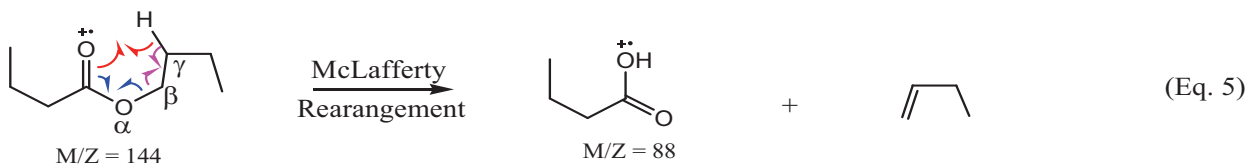
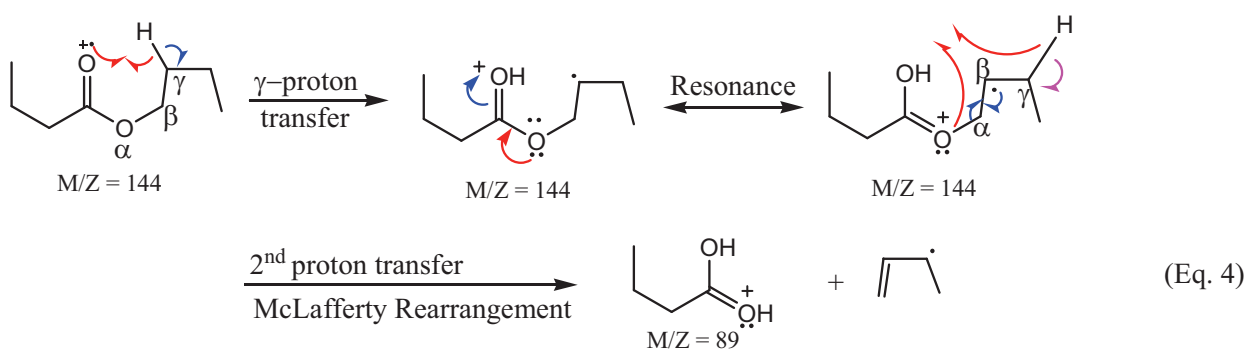
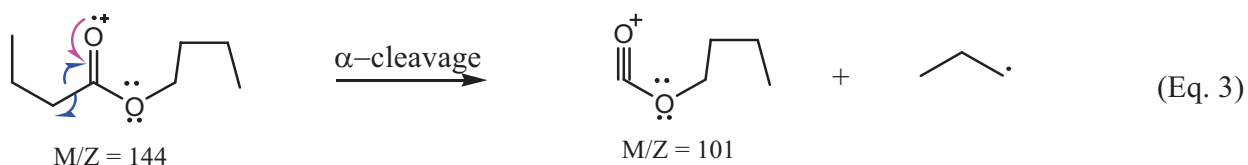
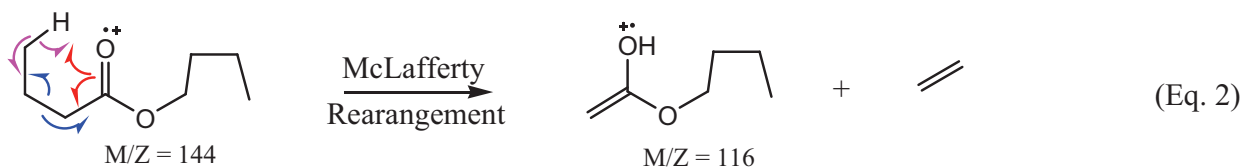
#### 4. Spectral Mechanism

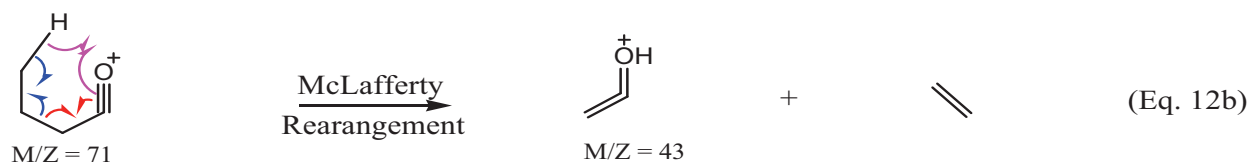
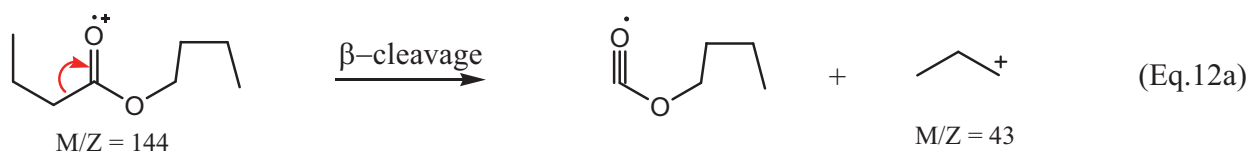
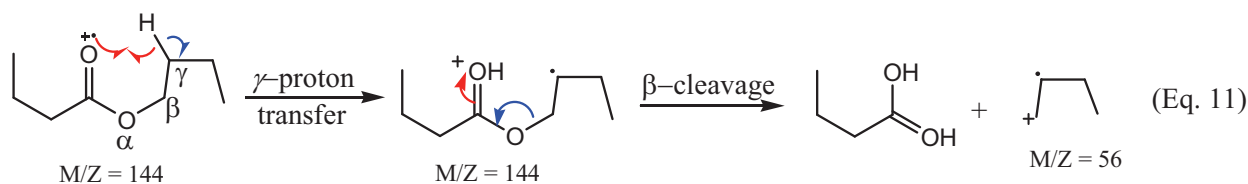
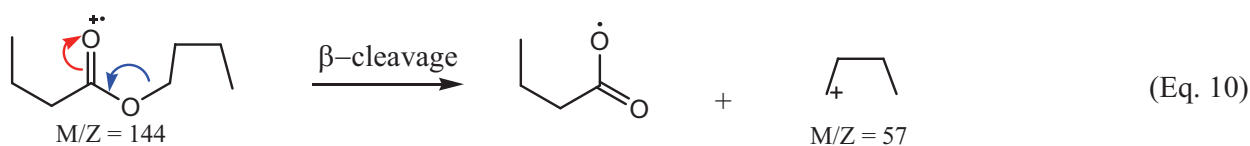
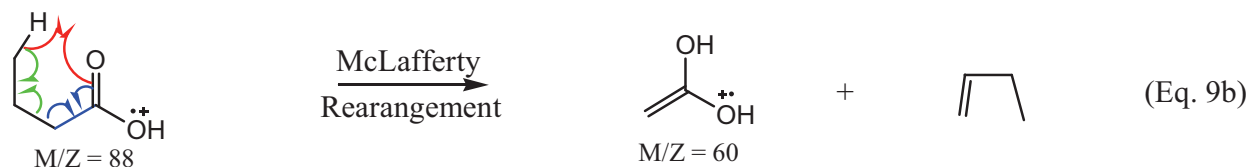
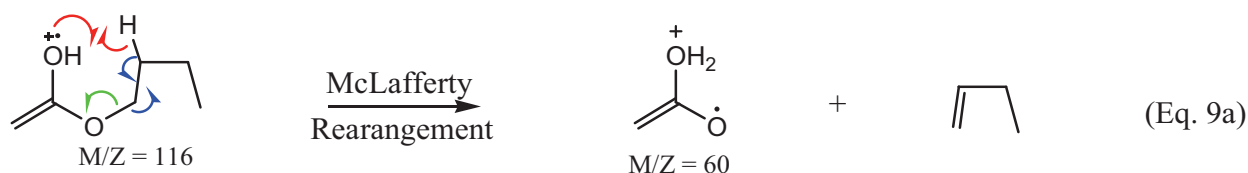
The EI, electron ionization, is the ion source used in the study. An electron will be knocked off of the vaporized sample of butyl butanoate when bombarded with a beam of high-energetic electrons (usually 70 eV, or about 1600 Kcal/mol) leading to the formation of a radical-positively charged ion called the molecular ion,  $\text{M}^+$ , as shown below.



Usually and for most organic compounds, the molecular ions break down into fragments due to the high energy imparted on them in the ionization chamber. The butyl butanoate molecular ions or the corresponding fragments may fractionate in different characteristic ways, a neutral and a charged fragments. The MS spectrum for butyl butanoate showed many characteristic peaks due to one or more of these mechanisms: McLafferty Rearrangement,  $\alpha$ -cleavage, or  $\beta$ -cleavage, or  $\gamma$ -Proton Transfer Processes (Solomons, & Fryhle, Organic Chemistry).







## 5. Discussion

Regarding the butyl butyrate's mass spectrum, the molecular ion peak is not observed which indicates that it was fragmented before it got to the detector, meaning that it could not live the  $5 \times 10^{-5}$  of a second fraction required to get processed.

Bond Cleavages of molecules in the EI-Mass Spectrophotometer will lead to charged and neutral fractions. Those cleavages which considered characteristic cleavages inflicted on butyl butyrate are:  $\alpha$ -cleavage,  $\beta$ -cleavage (known as inductive cleavage), McLafferty Rearrangement, a proton transfer and a double proton transfer.

Only the ionized fragments can be detected and leads to singlet peaks as a function of their abundance to m/z ratio. The height of a peak, its intensity, depends on the number of ions formed; the most abundant ions will give rise to the tallest peak called the base peak. Usually the highest m/z ratio signal of the spectrum is the molecular ion,  $M^+$ , if appears, not to confuse with the isotopic peaks,  $M + 1$  and  $M + 2$ . Usually the isotopic peaks are in much smaller intensity relative to the  $M^+$  peak (Walwil, 2017).

For the analysis of the target molecule spectrum, I chose the sequential analyses of the mechanisms in correspondence to the formation of the heaviest fragment ions, Eq1, to the lightest, Eq12. The butyl butanoate molecular ions undergo

McLafferty rearrangements and  $\alpha$ -cleavage, the most common fragmentation usually occurs, to form the positively-charged radical moiety at  $m/z = 116$  along with ethylene and the acylium ion at  $m/z = 101$  along with propyl radical respectively. (Eq. 2 & Eq. 3)

A double proton transfer of the molecular ion leads to a butenyl radical and the corresponding diol-like fragment ion of weight  $m/z = 89$ . As indicated in equation 4, the first  $\gamma$ -proton transfer leads to the oxonium intermediate which is resonance stabilized, followed by a second  $\gamma$ -proton transfer (McLafferty-like rearrangement). (Eq. 4)

A second McLafferty rearrangement takes place on the side of the carbonyl oxygen R group of the molecular ion, the butyl attached to the carbonyl oxygen, to form butenyl radical and the fragment ion at  $m/z = 88$ . (Eq. 5)

Through  $\beta$ -cleavage (inductive cleavage), the carbonyl carbon-oxygen bonds break leading to the loss of acylium radical and the formation of the oxonium cation at  $m/z = 73$ . (Eq. 6)

Through  $\alpha$ -cleavage of the molecular ion, the carbonyl carbon-oxygen bonds break readily because the resulting acylium carbocation at  $m/z = 71$  is resonance stabilized which leads to the most abundant fragment ions. (Eq. 7)

The fragmented ions of  $m/z = 89$  undergo another fragmentation through McLafferty rearrangements to form the positively-charged ions at  $m/z = 61$ . (Eq. 8)

Usually, the fragment ions themselves might break into a second or a third mode of fragmentations. Both of the followings represent the second mode of fragmentation and they are in the type of McLafferty Rearrangements. Although their contributions to the corresponding peak intensity is weak, but it's worth presenting since it is considered characteristics. Both fragment ions at  $m/z = 116$  and  $88$  undergo McLafferty rearrangements to form the corresponding fragment ions at  $m/z = 60$  and  $60$  respectively. (Eq. 9a and 9b)

Furthermore, the carbon-oxygen bonds of the molecular ions break inductively (through  $\beta$ -cleavage) to form the butyl cation at  $m/z = 57$ . (Eq. 10)

A  $\gamma$ -proton-transfer of the ester's alkyl moiety of the molecular ions followed by  $\beta$ -cleavages results in the loss of the diol-like moiety and the formation of butyl radical cation at  $m/z = 56$ . (Eq. 11)

Both  $\beta$ -cleavages of the molecular ions,  $M^+$ , of the carbonyl carbon-carbon and McLafferty rearrangements of the fragment ions at  $m/z = 71$  lead to the formation of the positively-charged ions at  $m/z = 43$  and  $43$  respectively. (Eq. 12a & 12b)

## 6. Conclusion

The novelty of this work, as an educational work, is that the EI-MS spectrum of butyl butanoate is analyzed thoroughly. No other source found where all characteristic fragment ions mechanistically discussed thoroughly.

As known, the mode of fragmentation is characteristic and hence predictable. For butyl butyrate the mechanisms involved in the analysis were  $\alpha$ -cleavage,  $\beta$ -cleavage, McLafferty Rearrangements, first and second proton transfer. There are more modes that will be discussed in further studies such as Two-Proton Cleavage and Retro Diels-Alder Cleavage. The next study will cover the MS spectra of butanamide and methyl 2-methylbutanoate.

## References

- Clark, J. (2015). [https://chemguide.co.uk/organic\\_props/alcohols/esterification](https://chemguide.co.uk/organic_props/alcohols/esterification)
- Loudon, G. M. (2002). *Organic Chemistry*, Oxford: Oxford University Press.
- Pavia, D. L., Lampman, G. M., Kriz, G. S., & Vyvyan J. R. *Introduction to Spectroscopy*, 4<sup>th</sup> Ed. Brooks/Cole, 418-450.
- Solomons, T. W., & Fryhle, C. B. *Organic Chemistry*. 9<sup>th</sup> Ed. Wiley, 401-413.
- Varma, M. N., & Madros, G. (2008). *J. chem. Technol. Biotechnol.*, 83(8), 1135-1144. <https://doi.org/10.1002/jctb.1897>
- Vollhardt, K. P., & Schore, N. E. *Organic Chemistry/Structure and Function*, 3<sup>rd</sup> Ed. W. H. Freeman and Company, 907-918.
- Walwil, A. M. (2017). *International Journal of Chemistry*, 9(3), 61-66. <https://doi.org/10.5539/ijc.v9n3p61>
- Yang, S., Minkler, P., Hoppel, C., & Tserng, K. Y. (2006). *Journal of the American Society for Mass Spectrometry*, 17(11), 1620-1628. <https://doi.org/10.1016/j.jasms.2006.07.004>

## Copyrights

Copyright for this article is retained by the author(s), with first publication rights granted to the journal.

This is an open-access article distributed under the terms and conditions of the Creative Commons Attribution license (<http://creativecommons.org/licenses/by/4.0/>).

# Graph Theory of Chemical Series and Broad Categorization of Clusters

Enos Masheija Rwantale Kiremire

Correspondence: Enos Masheija Rwantale Kiremire, Retired Professor of Chemistry, University of Namibia, Tauben Glen, Hochland Park, P. O. Box 98013 Pelican Square, Windhoek, Namibia. E-mail: kiremire15@yahoo.com

Received: November 15, 2017 Accepted: December 29, 2017 Online Published: January 25, 2018

doi:10.5539/ijc.v10n1p17

URL: <https://doi.org/10.5539/ijc.v10n1p17>

## Abstract

The recent introduction of skeletal numbers has made it much easier to analyze and categorize a wide range of many chemical clusters. In the process, it has been found that a large number of transition metal clusters with and without ligands are capped and do possess closo nuclear clusters. On the basis of the nuclear index, the clusters have been categorized into groups. The categorization of the clusters will greatly assist in promoting deeper understanding and the synthesis of novel clusters and their applications. A simple concept of graph theory of capping clusters has been introduced.

**Keywords:** graphs, categorization, capping, index, clusters, numbers, series, ligands, distribution, valence, numerical, groups, period

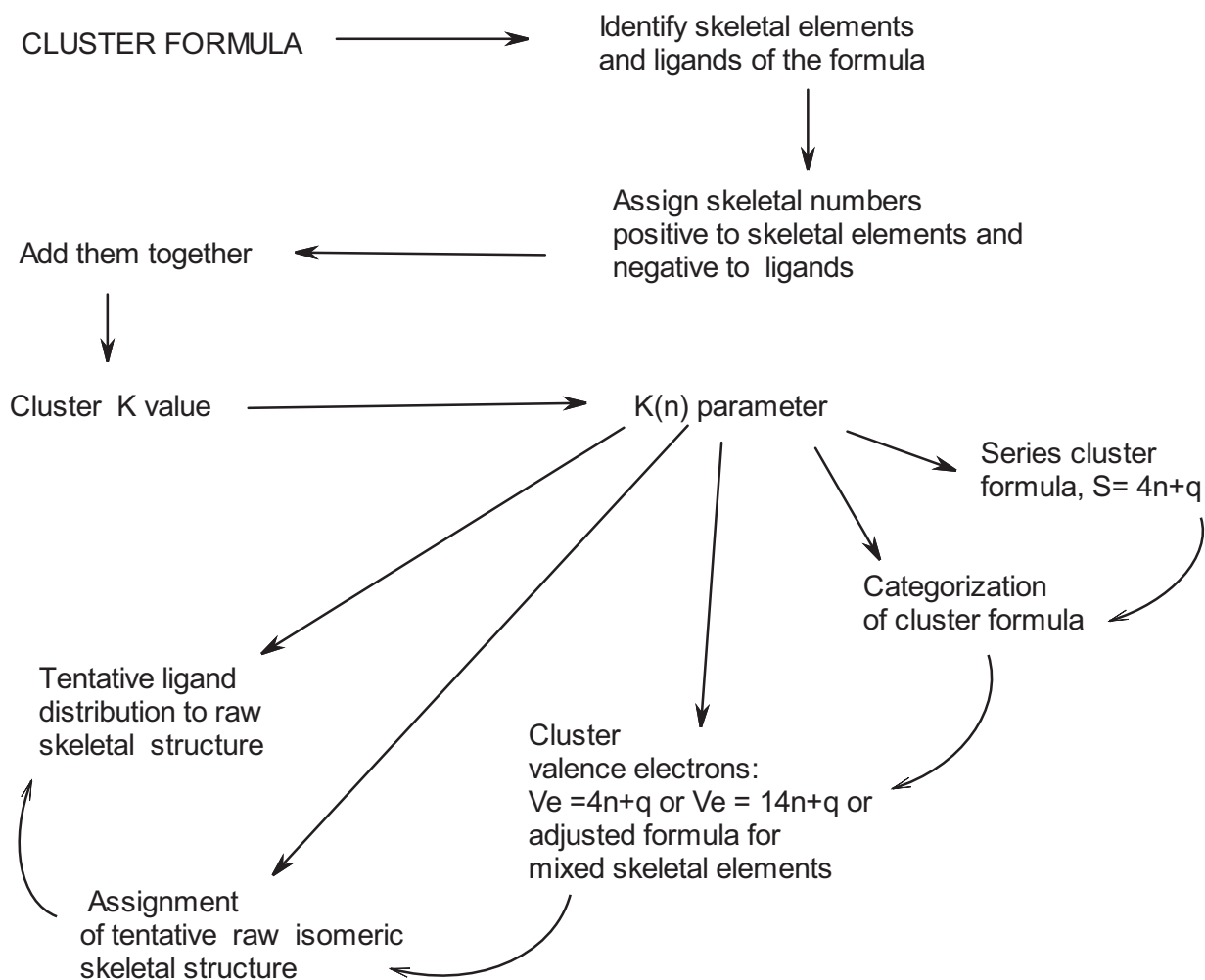
## 1. Introduction

The recently published excellent article by Alan Welch outlines the historical development of chemical clusters (Welch, 2013). The major highlights include STYX numbers (Lipscomb, 1963), Wade's rules (Wade, 1971, 1976), Mingos's rules (Mingos, 1972, 1984, 1987), Rudolph's symmetry correlation system (Rudolph, 1976) and Jemmis research group work (Jemmis, 2005, 2006, 2008) among others. The current  $4n$  series method being utilized to analyze clusters was developed by the identification of a simple pattern within clusters (Kiremire, 2014, 2015, 2016). The method regards all clusters comprising of skeletal elements from the main group and transition metals as interrelated and can be categorized by the  $4n$  series method. The method uses skeletal numbers to analyze and categorize clusters (Kiremire, 2016a, 2016b, 2017a, 2017b, 2017c).

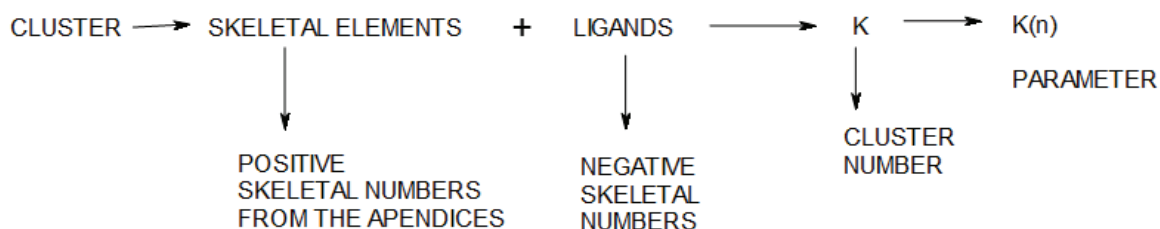
## 2. Results and Discussions

### 2.1 Brief Background

The early research on clusters pointed to the possibility of explaining boranes using numbers (Lipscomb, 1963), Jemmis' MNO numbers (Jemmis, 2008), topological numbers (Teo et al, 1984), and cluster shapes numbers (Fehlner and Halet, 2007) (18-monomer, 34-dimer, 48-trimer, 60-tetrahedron, and so on). The existence of cluster series was also detected and implied through the work of Wade (Wade, 1976), Mingos (Mingos, 1987) and the correlation of cluster symmetries by Rudolph (Rudolph, 1976). This is confirmed by the current work of applying skeletal numbers derived from the  $4n$  series method (Kiremire, 2015b) which clearly indicate the existence of a whole vast universe of clusters linking up naked metallic elements to metal carbonyls (Kiremire, 2016b), metalloboranes (Kiremire, 2016c), Zintl ions (Kiremire, 2016d), carboranes and other heteroboranes, boranes, and main group element clusters (Kiremire, 2017c). Using the skeletal numbers, a cluster comprising of a mono-skeletal element to a giant one of several hundred skeletal elements can readily be decomposed and represented by a single number now referred to as a cluster number  $Kor [K(n)parameter]$  (Kiremire, 2017b). The method can be broken into the following simple steps of analysis summarized in Scheme 1(SC-1). Further simplification is shown in Scheme 2(SC-2).



SC-1. Simple step for categorizing a cluster using skeletal numbers



$n$  = number of skeletal elements in a cluster

FP = FUNDAMENTAL PRINCIPLE

SC-2. Simplified principle for calculating the cluster number K

### 3. Outline of Cluster Analysis

#### 3.1 Construction of a Cluster

- The FORMULA of a cluster is categorized first using skeletal numbers. For capped clusters the series  $S = 4n+q$  ( $q \leq 0$ ).
- If the cluster is a capped one, the type of CLOSO nucleus is deduced from the series formula,  $S = 4n+q$ .
- The CLOSO nucleus is then sketched according to its K value determined from the CLOSO SERIES,  $S = 4n+2$ , and  $K = 2n-1$ .

- The number of capping elements are deduced from the overall cluster formula (capped cluster).
- The capping elements are added to the nuclear geometry each with 3 linkages as the capping mono-skeletal fragment has  $S = 4n-2$  and  $K = 2n-1 = 2(1)-(-1) = 3$ .
- Verify to ensure the K value of the constructed structure is the same as that originally calculated from the parent formula [to ensure goodness of fit of the cluster].
- Using the skeletal number of each element and considering each linkage behaving as a hydrogen ligand (since 1e is involved as a donation), the K value of the skeletal element in the skeletal structure is calculated for each element.
- The K value for an individual skeletal element obtained for the raw skeletal structure, represents the number of ligands to be attached to that skeletal element.
- Once the ligands have been distributed according to the skeletal numbers obtained for each skeletal element, the framework is referred to as a raw skeletal structure. Ideally, the individual skeletal element obeys the noble gas configuration. The cluster formula derived from the raw skeletal structure will then correspond to the original cluster formula. The sum of the ligands added to the skeletal structure will be equal to the number of ligands including the charges (if present), in the parent cluster formula (the goodness of fit).

These concepts will be demonstrated in the examples of the chemical clusters Ex-1 to Ex-6. The series method is a good guide to construct isomeric skeletal shapes in agreement with 18 or 8 electron rules. The fine details of the structures can be established by X-ray structural analysis. For ease of structural drawing and ligand distribution, it is better and easier to leave them in the RAW SKELETAL FORMS. The concept of 'raw skeletal form' has recently been introduced (Kiremire, 2017c).

The principle for calculating the cluster parameter,  $K(n)$  as derived from the series method (Kiremire, 2016b), can be summarized as shown in the fundamental principle in SC-2.

EVERY 1 ELECTRON (1e) DONATED BY LIGAND,  $K = -0.5$ .

Examples:  $H(K = -0.5)$ ,  $CO[K = 2(-0.5) = -1]$ ,  $Cp[K = -5(0.5) = -2.5]$ ,  $PR_3(K = 2(-0.5) = -1)$  and  $C_2H_4[K = 2(-0.5) = -1]$ , negative charge [ $1^-$ ,  $K = -0.5$ ] and positive charge [ $1^+$ ,  $K = 0.5$ ].

### 3.2 Graph Theory of Clusters Based upon Series

The concept of graph theory of chemical clusters is based upon the  $K(n)$  parameter of the cluster. It simply means the distribution of K skeletal linkages and their corresponding valences to n skeletal elements according to the law of 4n series in a precise manner. Let us take a few examples as illustrations.

Ex-1  $Os_5(CO)_{16}$

(a) Using 14n fragments:  $F = Os_5(CO)_{16} = 5[Os(CO)_3] + CO$

Each of the 5 fragments  $[Os(CO)_3]$  has  $8+3(2) = 14$  valence electron content. The additional CO ligand simply provides an additional 2 electrons. Clearly, the overall valence electron content of the cluster can be expressed as  $Ve = S = 14n+2(n=5)$ ;  $Ve =$  cluster valence electron content and  $S =$  cluster series. The S symbol is introduced as many other clusters obey the same law of series. If we substitute  $n = 5$  in  $Ve = 14n+2$ , we get  $Ve = 14(5) + 2 = 72$ . This can be verified by substituting the valence electrons of the cluster elements and ligands  $VF = 5[8] + 16(2) = 72$ . By analyzing many clusters, it was discovered that the skeletal linkages of the skeletal elements is given by another simple formula  $K = 2n-1$  when  $S = 14n+2$ . Therefore the skeletal linkages  $K = 2n-1 = 2(5)-1 = 9$ . This means that the 5 skeletal osmium elements in  $Os_5(CO)_{16}$  are bound by 9 skeletal linkages. A cluster parameter for this was introduced as  $K(n) = 9(5)$ . We know that this cluster has a trigonal bipyramid ( $D_{3h}$ ) skeletal shape, hence, a sketch of 5 elements joined by 9 linkages to mimic a trigonal bipyramid shape can be drawn as shown in Figure 1. It was also discovered that the main group clusters follow the series,  $S = 4n+q$ . However there is an isolobal relationship  $14n+q$  between  $4n+q$  and hence  $S = 4n+q$  formula works very well for all types of clusters and has been adopted for application to all the clusters (Kiremire, 2016b) except when the number of cluster valence electrons are being calculated when  $S = 14n+q$  is retained for transition metals clusters.



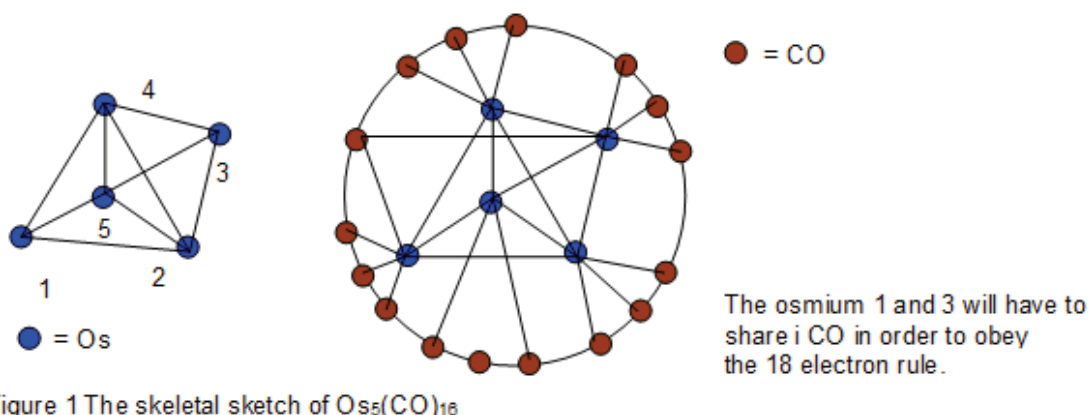


Figure 1 The skeletal sketch of  $\text{Os}_5(\text{CO})_{16}$

#### LIGAND DISTRIBUTION $\text{Os}(K = 5, V = 10), \text{CO}(K = -1)$

The skeletal elements have been numbered. Each of the lines to a skeletal element can be regarded as donating 1 electron to the skeletal element under consideration. Let us focus on the skeletal element number one. We can use the skeletal number of osmium  $K = 5$  as obtained from appendix 2.

$K1 = 5 - 3(0.5) = 3.5$ . That there are 3.5 electron pairs needed by osmium 1 after obtaining 3 electrons from skeletal linkages. Since a CO ligand is a 2 electron donor, then it means that osmium 1 will need 3.5 CO ligands in order for it to obey the 18 electron rule. Other  $K$  values of the skeletal elements can similarly be calculated.

$K2 = 5 - 4(0.5) = 3$ . This means osmium 2 which has 4 linkages supplying (4) electrons to it, will need 3 CO ligands in order to obey the 18 electron rule.

$K3 = K1 = 3.5$ ;  $K4 = K2 = 3$ ; and  $K5 = K2 = 3$ . It is now easy to distribute the 16 CO ligands to the skeletal framework in Figure 1. A circle has been added as a guide to draw a nice sketch of CO ligands.

Figure 1. The skeletal sketch of  $\text{Os}_5(\text{CO})_{16}$

(b) Calculating  $K$  using skeletal numbers:  $\text{Os}(K = 5), \text{CO}(K = -1)$

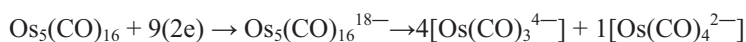
For  $\text{Os}_5(\text{CO})_{16}$ ,  $K = 5[5] - 16(1) = 9$ . This calculation is based on the observation from series that the skeletal elements act as providers of skeletal number values some of which are utilized by the ligands in a cluster. It is based on the observation that for every ONE electron donated the skeletal number value decreases by 0.5. Thus,  $1\text{H}(K = -0.5)$  when acting as a ligand while a  $\text{CO}(K = -1)$  since it is a 2 electron donor. The  $K$  value can be utilized to calculate the  $q$  value in the series  $S = 4n + q$ . Thus,  $K = 2n - \frac{1}{2}q = 2(5) - \frac{1}{2}q = 9$ ,  $\frac{1}{2}q = 1$  and  $q = 2$ . The cluster belongs to the series  $S = 4n + 2$  as derived earlier. The use of skeletal numbers to derive the cluster number,  $K$  is much faster than using the cluster fragments. The method used in Ex-1(b) has been applied in most of the cluster categorizations in this paper.

#### 3.3 The Double Meaning of $K(n)$ Parameter

This concept will be discussed further in this paper. We have seen that  $K(n) = 9(5)$  in  $\text{Os}_5(\text{CO})_{16}$  cluster represents 9 linkages to bind 5 skeletal osmium skeletal elements and in so doing figure is obtained. However, after scrutinizing the series deeper,  $K$  also represents the SHORTAGE of the number of the electron pairs needed to ensure that every skeletal element attains the Nobel gas configuration. Let us use this same cluster to demonstrate this concept.



As we know  $[\text{Os}(\text{CO})_5]$  fragment obeys the 18 electron rule. Alternatively, the 9 electron pairs could be added directly to the cluster.



In this alternative option, both  $[\text{Os}(\text{CO})_3^{4-}]$  and  $[\text{Os}(\text{CO})_4^{2-}]$  fragments obey the 18 electron rule.

#### 3.4 Capping Clusters

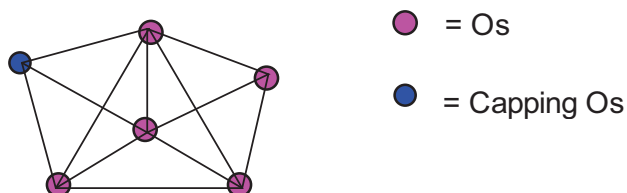
Let us use the VERTICAL series as a reference. The scheme for linking up series are given in Table 1. The capping series begin when the cluster series becomes  $S = 4n + 0$  and  $K_p = C^1C[\text{Mx}]$ . The  $C^1$  symbol means the cluster is mono-capped. The inner symbol  $[\text{Mx}]$  in the capping cluster represents a cluster nucleus which belongs to the CLOSO series  $S = 4n + 2$ .

Table 1. Capping series scheme

SERIES, $S=4n+q$		CAPPING, $K_p = C^nC[M-x]$	NAME
$4n-40$	$2n+20$	$C^{21}C$	
$4n-38$	$2n+19$	$C^{20}C$	
$4n-36$	$2n+18$	$C^{19}C$	
$4n-34$	$2n+17$	$C^{18}C$	
$4n-32$	$2n+16$	$C^{17}C$	
$4n-30$	$2n+15$	$C^{16}C$	
$4n-28$	$2n+14$	$C^{15}C$	
$4n-26$	$2n+13$	$C^{14}C$	
$4n-24$	$2n+12$	$C^{13}C$	
$4n-22$	$2n+11$	$C^{12}C$	
$4n-20$	$2n+10$	$C^{11}C$	
$4n-18$	$2n+9$	$C^{10}C$	
$4n-16$	$2n+8$	$C^9C$	
$4n-14$	$2n+7$	$C^8C$	OCTACAP
$4n-12$	$2n+6$	$C^7C$	HEPTACAP
$4n-10$	$2n+5$	$C^6C$	HEXACAP
$4n-8$	$2n+4$	$C^5C$	PENTACAP
$4n-6$	$2n+3$	$C^4C$	TETACAP
$4n-4$	$2n+2$	$C^3C$	TRICAP
$4n-2$	$2n+1$	$C^2C$	BICAP
$4n+0$	$2n+0$	$C^1C$	MONOCAP
$4n+2$	$2n-1$	$C^0C$	CLOSO
$4n+4$	$2n-2$	$C^{-1}C$	NIDO
$4n+6$	$2n-3$	$C^{-2}C$	ARACHNO
$4n+8$	$2n-4$	$C^{-3}C$	HYPHO
$4n+10$	$2n-5$	$C^{-4}C$	KLADO

Ex-2  $Os_5(CO)_{18}$ : Skeletal numbers: Os( $K = 5, V = 10$ ), CO( $K = -1$ );  $Os_6(CO)_{18}$ :  $K = 6[5]-18 = 12$ ;  $n = 6, K(n) = 12(6), S = 4n+0, K_p = C^1C[M5]$ ;  $Ve = 14n+0 = 14(6)+0 = 84, VF = 6[8]+18(2) = 84$ . Since the skeletal number of osmium  $K = 5$ , its valence  $V = 10$ . The  $K = 5$  means that the osmium element has a shortage of 5 electron pairs in order for it to obey the 18 electron rule. That is why osmium can form the complex  $Os(CO)_5$  or  $OsH_{10}[OsH_6^{4-}]$  (Yvon, 2004).

The symbol  $K_p = C^1C[M5]$  means that the cluster is a mono-capped trigonal bipyramid. This is sketched in Figure 2.

Figure 2 Sketch of skeletal shape of  $Os_6(CO)_{18}$ 

Ex-3  $Ru_9(CO)_{23}^{2-}$ : Using skeletal numbers, Ru( $K = 5, V = 10$ ), CO( $K = -1$ ),  $(-1e)(K = -0.5)$ ;  $K = 9[5]-23-1 = 21, n = 9, K(n) = 21(9), S = 4n-6, K_p = C^4C[M5]$ ;  $Ve = 14n-6 = 14(9)-6 = 120$ ,

$VF = 9[8] + 23(2) + 2 = 120$ . The capping symbol  $K_p = C^4C[M5]$  means it is a tetra-capped trigonal bipyramid. This shape is sketched in Figure 3.



$K = 9[5]-23-1 = 21$ ,  $n = 9$ ,  $K(n) = 21(9)$ ,  $S = 4n-6$

Skeletal numbers:  $Ru(K = 5, V = 10)$ ,  $CO(K = -1)$ ,  $(-1)(K = -0.5)$

$K(n) = 21(9)$

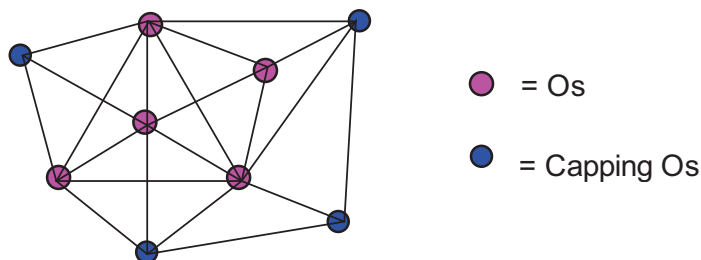
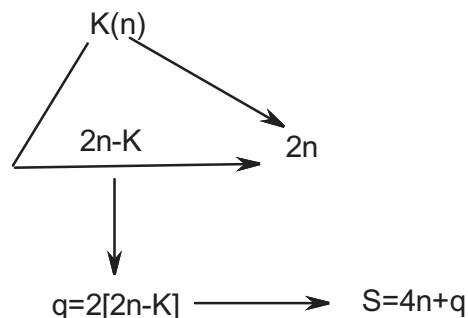


Figure 3 Sketch of skeletal shape of tetra-capped trigonalbipyramid.

A short-cut for extracting the K value from a cluster formula is given in SC-3.

$K=2n-(1/2)q$ ;  $(1/2)q = 2n-K$ ,  $q = 2[2n-K]$  and  $S = 4n+q$



SHORT-CUT DERIVATION OF SERIES FROM  $K(n)$  PARAMETER

SC-3

Ex-4  $Pd_{30}(CO)_{30}L_{10}$ : Skeletal numbers,  $Pd(K = 4, V = 8)$ ,  $CO(K = -1)$ ,  $L(K = -1)$ ; for the cluster,  $K = 30[4]-30-10 = 80$ ;  $K(n) = 80(30)$ ,  $S = 4n-40$ ;  $K_p = C^{21}C[M9]$ . This capping symbol can be verified numerically. Thus,  $K = 21(3)+2(9)-1 = 80$ ; or the flow of  $K(n)$  numbers: 80(30), 77(29), 74(28), 71(27), 68(26), 65(25), 62(24), 59(23), 56(22), 53(21), 50(20), 47(19), 44(18), 41(17), 38(16), 35(15), 32(14), 29(13), 26(12), 23(11), 20(10) and 17(9). The  $K(n) = 17(9)$  is for the nucleus  $[M9]$  which belongs to the CLOSO SERIES,  $S = 4n+2$  and  $K = 2n-1 = 2(9)-1 = 17$ . The capping involves an electron valence content fragment of 12. In this case of the palladium cluster, the  $[Pd(CO)]$  is the right fragment [ $Ve = 10+2 = 12$ ] while in osmium clusters it is  $[Os(CO)_2]$  fragment [ $Ve = 8+2(2) = 12$ ]. The series formula for such a fragment is  $S = 14n-2$  or  $S = 4n-2$  and  $K = 2n+1$  which is numerically equal to  $K = 2(1) + 1 = 3$ . Thus, the K value changes by  $\Delta K = \pm 3$ . We can also verify the cluster valence electrons, for the cluster  $Pd_{30}(CO)_{30}L_{10}$ ,  $Ve = 14n-40 = 14(30)-40 = 380$  using the series formula;  $VF = 30[10]+30(2)+10(2) = 380$  using the cluster formula. A sketch of the skeletal graph is shown in Figure 4. The number of skeletal linkages =  $3[7 \times 3] + 17$  {from  $[M9]$  nucleus} = 80. A seven sided ring (figure) was arbitrarily used since it is a multiple of 21 – the number of capping elements. Hence, we will get 3 rings comprising 21 skeletal elements around the nucleus of 9 skeletal elements. The final sketch of the cluster  $Pd_{30}(CO)_{30}L_{10}$  is shown in Figure 4.

Ex-4  $\text{Pd}_{30}(\text{CO})_{30}\text{L}_{10}$ :  $K(n) = 80(30)$ ;  $S = 4n-40$ ,  $K_p = \text{C}^{21}\text{C}[\text{M9}]$

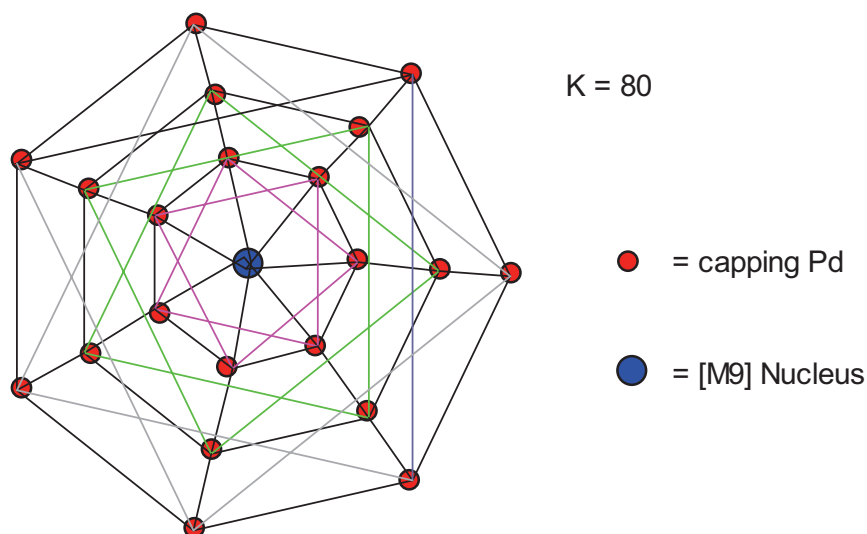


Figure 4 The skeletal graph of  $\text{Pd}_{30}(\text{CO})_{30}\text{L}_{10}$  cluster

If we focus on the inner ring (circle) of Figure 4, there are 7 lines linked to the nucleus. This is followed by another 7 linkages to the 7 skeletal elements themselves. Then the internal periphery linkages of one to the next jumping the middle one, gives another 7 linkages. Thus, in total, we have 21 linkages from the inner "circle". The next circle also contributes to another set of 21 linkages. The last circle gives the last 21 linkages. Thus, the gross total of capping linkages is  $21(3) = 63$ . Then the CLOSO NUCLEUS is nine skeletal elements [M9], which gives us  $K = 2n-1 = 2(9)-1 = 17$ . This means that the total linkages of the cluster as sketched in the isomeric Figure 4 will be  $63+17 = 80$ . This is an example of one form of representation of the graph of the cluster  $\text{Pd}_{30}(\text{CO})_{30}\text{L}_{10}$ . The cluster  $\text{Pd}_{30}(\text{CO})_{26}\text{L}_{10}$  can be treated in the same manner as  $\text{Pd}_{30}(\text{CO})_{30}\text{L}_{10}$ . Its graph is shown in Figure 5.

Ex-5  $\text{Pd}_{30}(\text{CO})_{26}\text{L}_{10}$ :  $K = 30[4] - 26 - 10 = 84$ ,  $n = 30$ ,  $K(n) = 84(30)$ ,  $S = 4n - 48$ ,  $K_p = \text{C}^{25}\text{C}[\text{M}5]$   
 Skeletal numbers: Pd( $K = 4$ ), CO( $K = -1$ ), L( $K = -1$ )

This is a cluster with a trigonal bipyramid nucleus surrounded by 25 skeletal elements.  
 $V_e = 14n - 48 = 14(30) - 48 = 372$ ,  $V_f = 30[10] + 26(2) + 10(2) = 372$

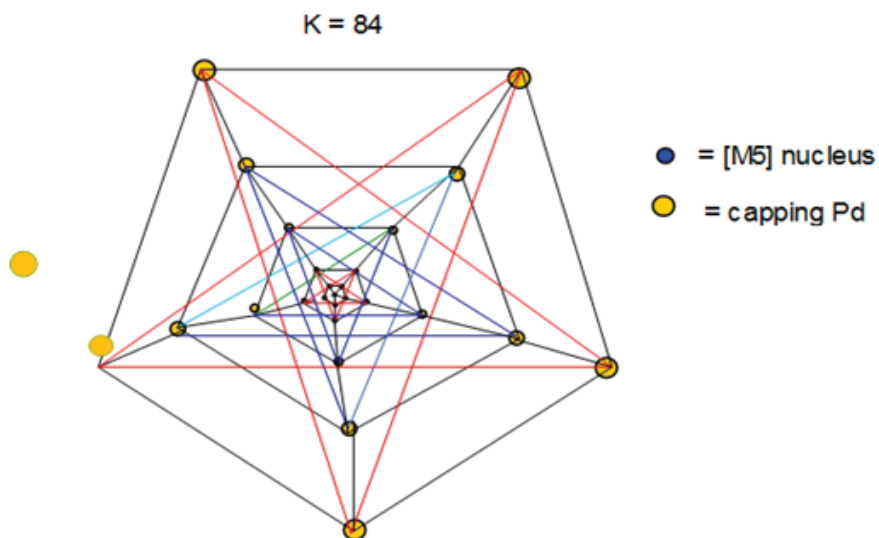


Figure 5 The sketch of the skeletal graph of  $\text{Pd}_{30}(\text{CO})_{26}\text{L}_{10}$

The number of skeletal linkages =  $5[5 \times 3]$  from 'rings' + 9 from the trigonal bipyramid = 84. For every ring around the nucleus, there are 15 linkages. Since there are 5 rings, then there will be a total of  $15 \times 5 = 75$ . Since the inner nucleus obeys the closo series  $S = 4n + 2$ , then  $K = 2n - 1 = 2(5) - 1 = 9$ . The grand total is  $75 + 9 = 84$ . In order to test the concept of ligand distribution in Figure 5, we can make a simple calculation on the outer Pd skeletal element and they are all similar. The palladium skeletal number is 4 (appendix 2). Since there are 5 skeletal linkages to it, that means it is already receiving 2.5 electron pairs internally from the skeletal linkages. The deficit of the electron pairs will be provided by the ligands. Hence,  $K = 4 - 5(0.5) = 1.5$ . This means that each of the Pd skeletal elements in the outermost ring will need 1.5 CO ligands. A similar calculation can be done for each of the inner rings. The cluster  $\text{Pd}_{30}(\text{CO})_{26}\text{L}_{10}$  was obtained from literature (Mednikov and Dahl, 2010).

Ex-6  $\text{Pt}(\text{AuL})_8^{2+}$ :  $K = 1[4] + 8[3.5] - 8 + 1 = 25$ ,  $K(n) = 25(9)$ ,  $S = 4n - 14$ ,  $K_p = C^8C[M-1]$   
 Skeletal numbers:  $\text{Pt}(K = 4, V = 8)$ ,  $\text{Au}(K = 3.5, V = 7)$ ,  $L(K = -1)$ ,  $(+1)(K = 0.5)$

$[M-1]$ ,  $K = 2n - 1 = 2(1) - 1 = 1$   $\text{Pt}(K = 4, V = 8)$ ,  $\text{Au}(K = 3.5, V = 7)$

FROM SHAPE, LINKAGES =  $8 + 8 + K[M1]$   
 $= 24 + 1 = 25$

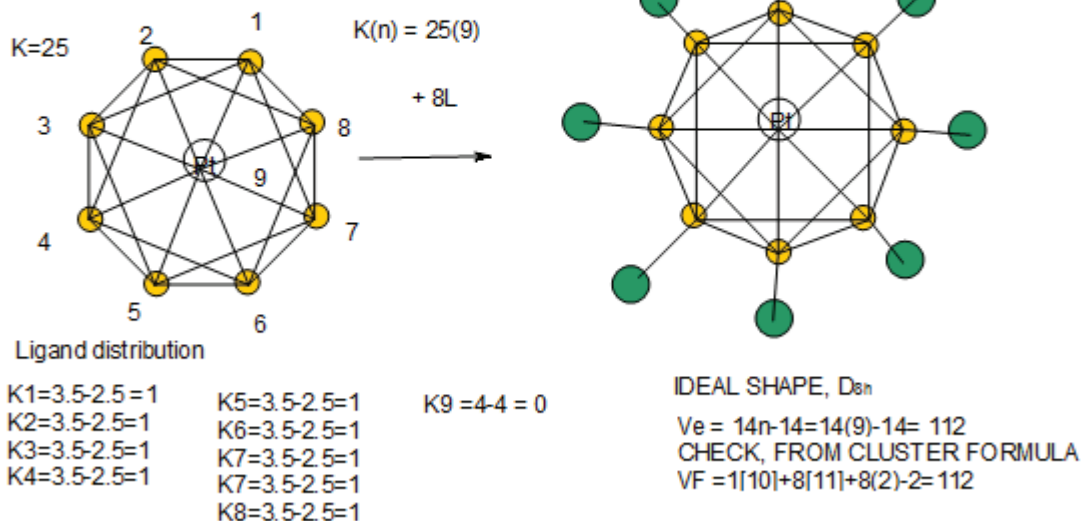


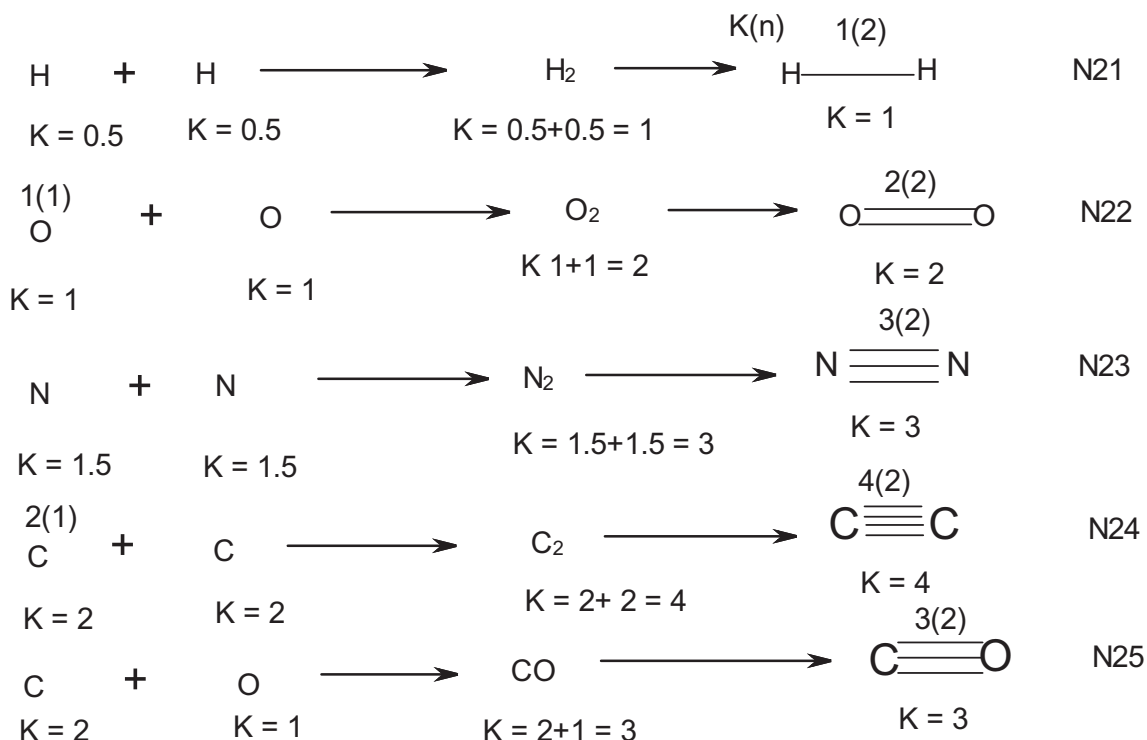
Figure 6 The skeletal structure of  $\text{Pt}(\text{AuL})_8^{2+}$

In Ex-6, the series method predicts that the platinum golden cluster will have a single nuclear skeletal atom [M1] surrounded by 8 other skeletal elements,  $K_p = C^8C[M1]$ . This has been found to be the case and the Pt is in the nucleus while 8 Au skeletal elements occupy the periphery. This is sketched in Figure 6. Since the cluster is small, one ring of  $C^8$  can readily be utilized to sketch its graph. The number of skeletal linkages =  $8 \times 3 + [M1]$  linkages. Surprisingly, even the one skeletal nuclear element obeys the CLOSO series formula,  $S = 4n + 2$  and  $K = 2n - 1 = 2(1) - 1 = 1$ . This means the single skeletal nuclear element is entitled to 1 skeletal linkage. Hence, the TOTAL number of skeletal linkages =  $24 + 1 = 25$ . What is also interesting is that there are 5 linkages to each periphery Au skeletal element. Since the Au element has a K value of 3.5, then the shortfall on the periphery element is  $K = 3.5 - 2.5 = 1$ . This means each of the 8 periphery Au elements is allowed to accommodate ONE ligand in order for it to obey the 18 electron rule, hence the predominance of [AuL] fragments (Mingos, 1984) in the golden clusters. In summary the graph theory of series involves the construction of skeletal structures in such a way that the skeletal elements (n) are linked in a mathematical precision with the corresponding k skeletal linkages as derived from the cluster formula. In other words, the  $K(n)$  parameter of a cluster must obey the 'goodness of fit' principle. The concepts that have been revealed in examples Ex-1 to Ex-6 have been applied as closely as possible in the rest of the clusters in this paper.

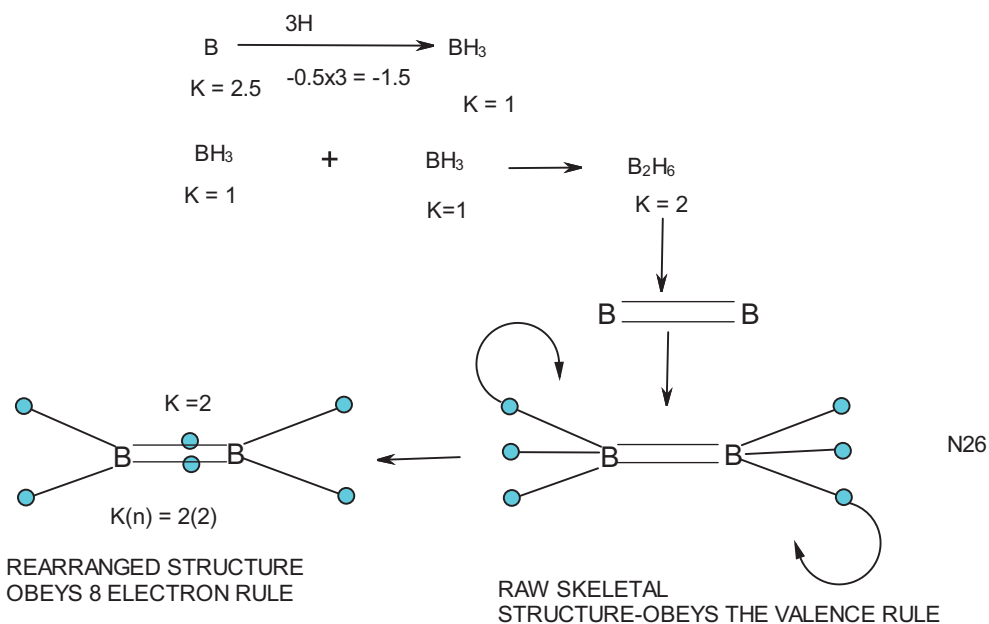
### 3.5 More Examples to Illustrate the Categorization of Clusters Using 4n Series Method

The examples have been arranged according to nuclearity index.

DIATOMIC (N2) MOLECULES AND SKELETAL NUMBERS

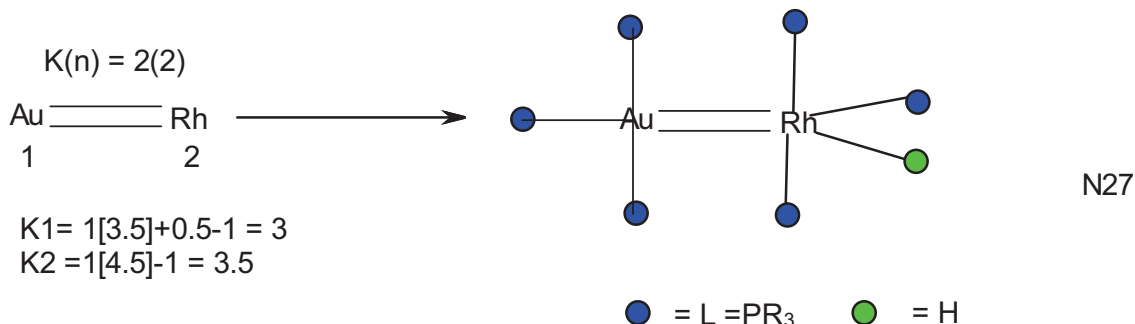


B, [K = 2.5, V= 2(2.5)] = 5 = skeletal linkages



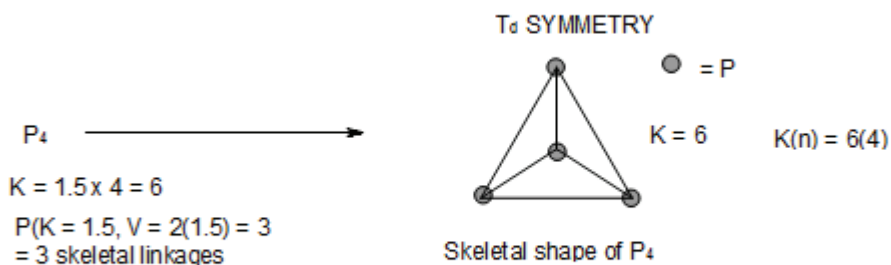
N27 AuRh(H)L<sub>6</sub><sup>+</sup>:  $K = 1[3.5] + 1[4.5] - 0.5 - 6 + 0.5 = 2$   
 $n = 1 + 1 = 2$ ,  $K(n) = 2(2)$ ,  $K = 2n - (1/2)q = 2 = 2(2) - (1/2)q$ ,  $q = 4$ ;  $S = 4n + q = 4n + 4$   
 $Ve = 14n + 4 = 14(2) + 4 = 32$ ;  $VF = 1[11] + 1[9] + 1 + 6(2) - 1 = 32$   
 $Ve =$  CLUSTER VALENCE ELECTRONS FROM SERIES FORMULA  
 $VF =$  CLUSTER VALENCE ELECTRONS FROM CLUSTER FORMULA

Skeletal numbers: Au(K = 3.5), Rh(K = 4.5), H(K = -0.5), L(K = -1), +1(K = 0.5)

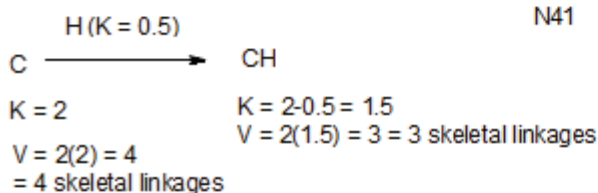


N27

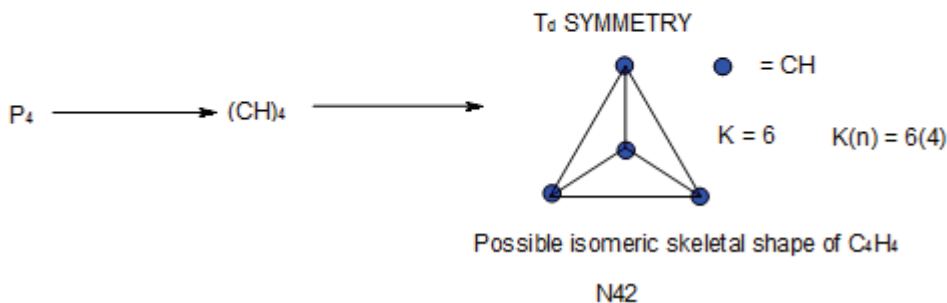
N4 CLUSTERS



N41

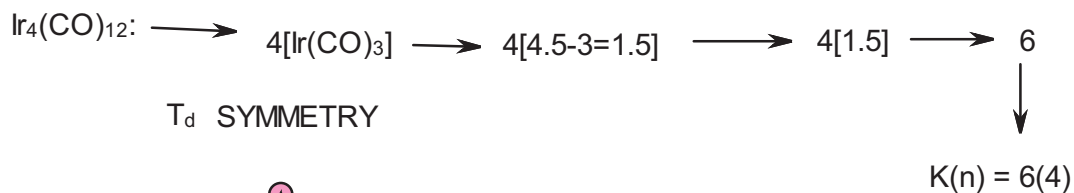


Hence, CH = P in terms of K value and skeletal linkages or valences. Hence,  $P \xleftrightarrow{\quad} CH$

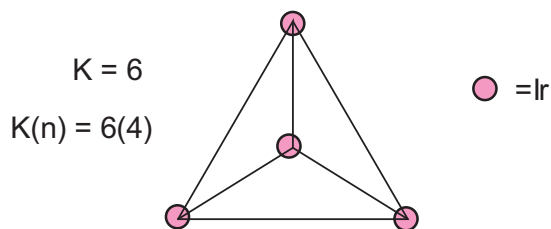




Skeletal numbers: Ir(K = 4.5, V=9), CO(K = -1)



T<sub>d</sub> SYMMETRY



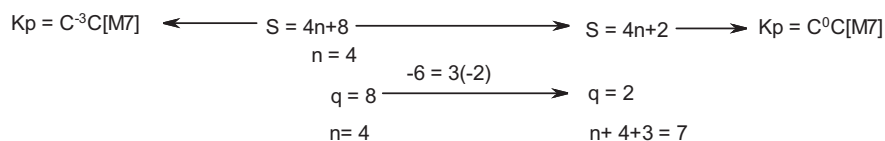
Ideal skeletal shape of Ir<sub>4</sub>(CO)<sub>12</sub>

N43

I

N44 Pt<sub>4</sub>(ac)<sub>8</sub>; ac = CH<sub>3</sub>COO, K= 4[4]-8(1.5) = 4; K(n) = 4(4), S = 4n+8,

Ve = 14n+8 = 14(4)+8 = 64; VF = 4[10]+8[3] = 64 Skeletal numbers: Pt(K = 4, V=8), ac(K = -1.5)



CHECK: [M7]; S = 4n+2, K = 2n-1 = 2(7)-1 = 13, K(n) = 13(7)

K(n) SERIES: 13(7), 10(6), 7(5), 4(4); thus, the cluster 4(4) is 3 steps below the CLOSO REFERENCE.[M7].

The ideal shape is a square.

K(n) = 4(4)



← Ideal shape of N44

N44

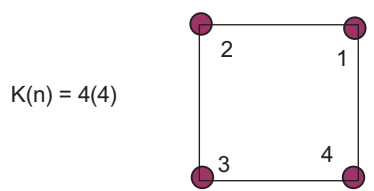
N45  $\text{Re}_4\text{H}_4(\text{CO})_{16}$ :  $K = 4[5.5] - 2 - 16 = 4$ ;  $K(n) = 4(4)$ ,  $K = 2n - (1/2)q = 4$ ,  $n=4$ ,  $q=8$ ,  
 $S = 4n + q = 4n + 8$  (ARACHNO FAMILY)

Skeletal numbers:  $\text{Re}(K = 5.5, V = 11)$ ,  $\text{H}(K = -0.5)$ ,  $\text{CO}(K = -1)$

$$F_B = 4n + 8 = [\text{BH}](4) + 8\text{H} = \text{B}_4\text{H}_{12}$$

$$F_C = 4n + 8 = [\text{C}](4) + 8\text{H} = \text{C}_4\text{H}_8$$

$$F_{\text{Os}} = 14n + 8 = [\text{Os}(\text{CO})_3](4) + 4\text{CO} = \text{Os}_4(\text{CO})_{12} + 4\text{CO} = \text{Os}_4(\text{CO})_{16}$$



$$K(n) = 4(4)$$

Ligand distribution

$$K_1 = 5.5 - 1 = 4.5$$

$$K_2 = K_1 = 4.5$$

$$K_3 = K_1 = 4.5$$

$$K_4 = K_1 = 4.5$$

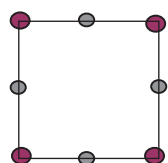
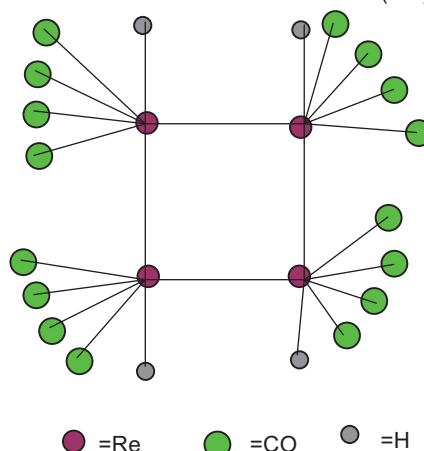
Cluster interconversions using series

$$V_e = 14n + 8 = 14(4) + 8 = 64$$

$V_e$  = cluster valence electrons

$$F_{\text{Rh}} = 14n + 8 = [\text{Rh}(\text{H})(\text{CO})_2](4) + 4\text{CO} = \text{Rh}_4\text{H}_4(\text{CO})_8 + 4\text{CO} = \text{Rh}_4(\text{CO})_2(\text{CO})_8 + 4\text{CO} = \text{Rh}_4(\text{CO})_{14}$$

RAW ISOMERIC SKELETAL SHAPE OF  $\text{Re}_4\text{H}_4(\text{CO})_{16}$



N45

Observed skeletal structure of  $\text{Re}_4\text{H}_4(\text{CO})_{16}$

In example 1 (N45),  $\text{Re}(K = 5.5)$ , see Appendix 2), the hydrogen atom ( $\text{H}^\bullet$ ) when regarded as a single electron donor is assigned a K value of  $-0.5$ . Similarly, the ( $:\text{CO}$ ) ligand when is regarded as a two electron donor ligand is assigned a value [ $K = 2(-0.5) = -1$ ]. In case of ligands, the assigned negative K value is directly proportional to the number of electrons donated. For instance a 3 electron donor has a K value of  $3[-0.5] = -1.5$  while for a cyclopentadienyl ligand, Cp which donates 5 electrons,  $K = 5[-0.5] = -2.5$ . The cluster K value is calculated as indicated in N45. This means the 4 rhenium skeletal elements are connected by 4 linkages (bonds) and a reasonable possible ISOMERIC shape is a square. In constructing skeletal shapes, there may be more than one structure. In order to assign tentative ligand distribution to a skeletal element, its k value is utilized. Just as in the  $\text{CH}_4$  molecule each H atom is considered to donate an electron to the carbon atom for it to attain an octet rule (noble gas configuration), in the  $\text{Re}_4$  skeletal shape (N45), each linkage to Re skeletal element behaves as a hydrogen atom donor and hence it is assigned a K value of  $-0.5$ . In the skeletal cluster shape, each skeletal element receives electron donations from the ligands as well as SKELETAL linkages to it. Using this knowledge, we can determine the skeletal linkages AVAILABLE to the external ligands after the linkages to the elements have been taken into account. For instance, in N45 there are 2 linkages to each Re skeletal atom and therefore skeletal linkages available to each skeletal element  $K_1 = K_2 = K_3 = K_4 = 5.5 - 2(0.5) = 4.5$  as indicated in N45. Clearly, a K value of 4.5 implies, in principle, there will be  $4\text{CO} + 1\text{H}$  distributed to each Re skeletal element since a CO ligand is a 2 electron donor and H ligand a 1 electron donor. Essentially, a K value of 1 represents or corresponds to 1 electron pair. The actual structure can be determined from X-ray structural analysis. In this case, one of the skeletal isomers of  $\text{Re}_4\text{H}_4(\text{CO})_{16}$  is found to have bridged H ligands as sketched in CC-1. The skeletal shape without taking into account ligand rearrangements, has been referred to as a "raw skeletal structure". Once the raw skeletal structure has been constructed and ligands distributed according to skeletal numbers and valences, then it is expected that each skeletal element obeys the noble gas configuration. This can be illustrated by the N45 sketch:  $\text{Re}$  1, valence electrons,  $V_e = 1[\text{Re}] + 4\text{CO} + 2[\text{Re-Re}] + 1[\text{H}] = 7 + 4(2) + 2 + 1 = 18$ . We can also use skeletal numbers to verify if the rhenium elements in the cluster obey the 18 electron rule:  $K = 1[5.5] - 4 - 1 - 0.5 = 0$ . The concepts applied in N45 have been used in the rest of the clusters summarized in the following sections of this paper. A wide range of examples have been analyzed using the skeletal numbers so as to expose the readers to a wide scope of applications of the skeletal numbers to cluster analysis. Note: for every single 1 electron donated by a ligand to a skeletal element,  $k = -0.5$ . Also all the skeletal numbers used in the calculations are given in the appendices 1 and 2.

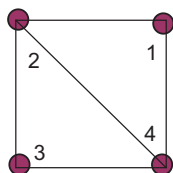
N46  $\text{Re}_4(\text{CO})_{16}^{2-}$ :  $K = 4[5.5] - 16 - 1 = 5$ ;  $K(n) = 5(4)$ ,  $K = 2(4) - (1/2)q = 5$ ,  $n=4$ ,  $q=6$ ,  
 $S = 4n+q = 4n+6$ (ARACHNO FAMILY)

Skeletal numbers:  $\text{Re}(K = 5.5)$ ,  $\text{CO}(K = -1)$ ,  $(-1)(K = -0.5)$

RAW ISOMERIC SKELETAL SHAPE OF  $\text{Re}_4(\text{CO})_{16}^{2-}$

$F_B = 4n+6 = [\text{BH}](4)+6\text{H} = \text{B}_4\text{H}_{10}$

$F_C = 4n+6 = [\text{C}](4)+6\text{H} = \text{C}_4\text{H}_6$



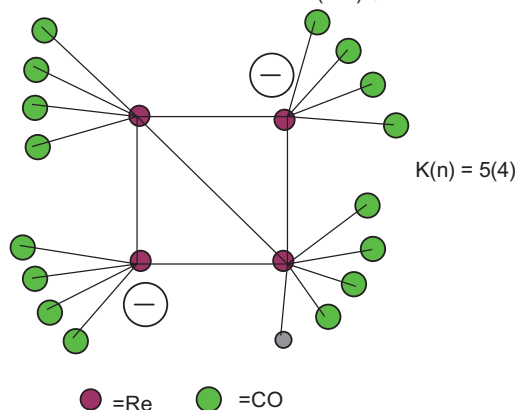
Ligand distribution

$K1 = 5.5 - 1 = 4.5$

$K2 = 5.5 - 1.5 = 4$

$K3 = K1 = 4.5$

$K4 = K2 = 4$



Cluster interconversions using series

$V_e = 14n+6 = 14(4)+6 = 62$

$F_{Os} = 14n+6 = [\text{Os}(\text{CO})_3](4)+3\text{CO} = \text{Os}_4(\text{CO})_{15}$

$F_{Rh} = 14n+6 = [\text{Rh}(\text{H})(\text{CO})_2](4)+3\text{CO} = \text{Rh}_4\text{H}_4(\text{CO})_{11} = \text{Rh}_4(\text{CO})_{13}$

N46

N47  $\text{Re}_4\text{H}_4(\text{CO})_{12}$ :  $K = 4[5.5] - 2 - 12 = 8$ ;  $K(n) = 8(4)$ ;  $K = 2(4) - (1/2)q = 8$ ,  $q = 0$ ,  $S = 4n+0$ ,  $K_p = \text{C}^1\text{C}[\text{M}3]$

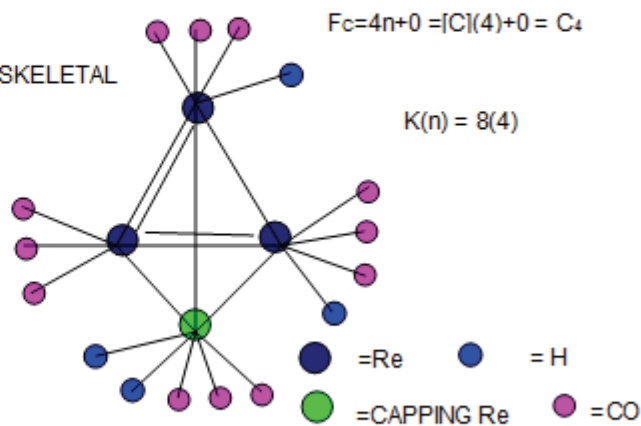
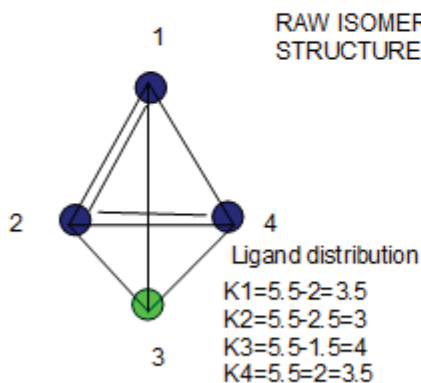
Skeletal numbers:  $\text{Re}(K = 5.5, V = 11)$ ,  $\text{H}(K = -0.5)$ ,  $\text{CO}(K = -1)$

$[\text{M}3], S = 4n+2, K = 2n-1 = 2(3)-1 = 5$

$F_B = 4n+0 = [\text{BH}](4)+0 = \text{B}_4\text{H}_4$

$V_e = 14n+0 = 14(4)+0 = 56$

$F_C = 4n+0 = [\text{C}](4)+0 = \text{C}_4$



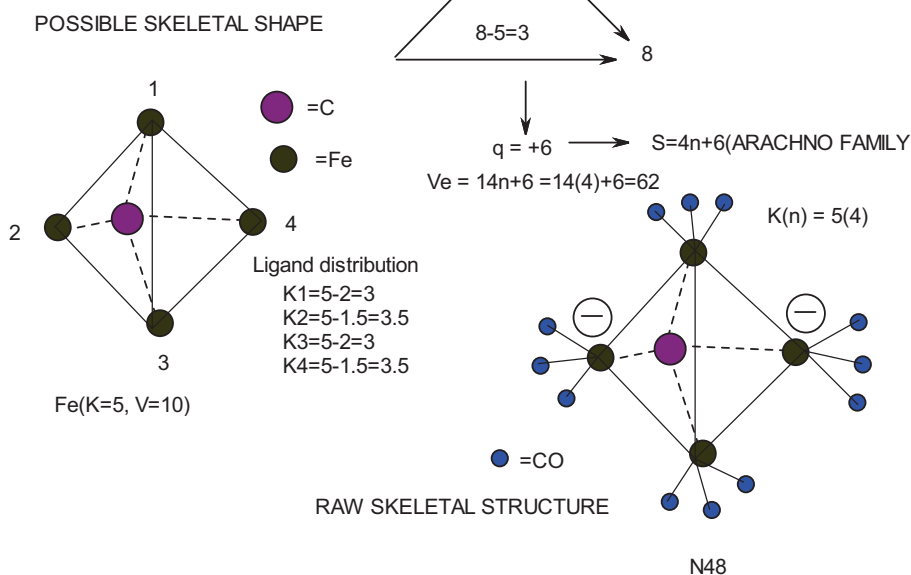
$F_{Os} = 14n+0 = [\text{Os}(\text{CO})_3](4)+0 = \text{Os}_4(\text{CO})_{12}$

$F_{Rh} = 14n+0 = [\text{Rh}(\text{H})(\text{CO})_2](4) = \text{Rh}_4\text{H}_4(\text{CO})_8 = \text{Rh}_4(\text{CO})_{10}$

N47

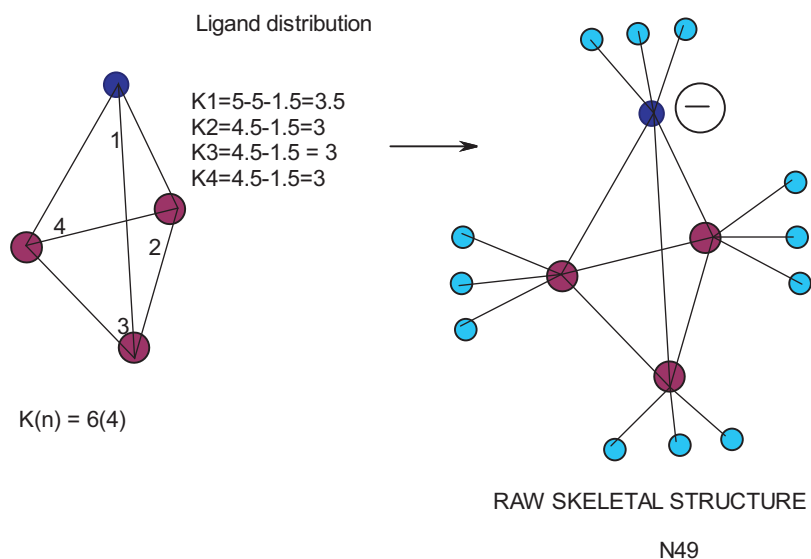
N48 Skeletal numbers: Fe(K = 5, V = 10), C(K = -2), CO(K = -1), (-1)(K = -0.5)

$$\text{Fe}_4(\text{C})(\text{CO})_{12}^{2-}: K = 4[5] - 2 - 12 - 1 = 5; K(n) = 5(4)$$



N49  $\text{FeIr}_3(\text{CO})_{12}$ :  $K = 1[5] + 3[4.5] - 12 - 0.5 = 6; K(n) = 6(4), S = 4n + 4$  (NIDO)

Skeletal numbers: Fe(K = 5), Ir(K = 4.5), CO(K = -1), (-1)(K = -0.5)



### 3.6 N5 Clusters

#### $\text{B}_5\text{H}_9$ Cluster

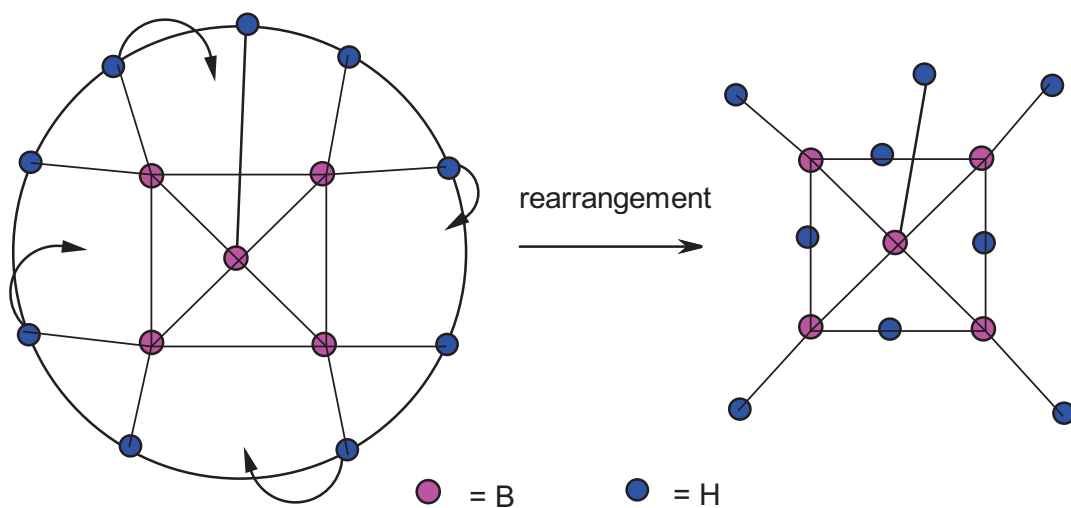
Skeletal numbers: B(K = 2.5, V = 5), H(K = -0.5);  $K = 5[2.5] - 9(0.5) = 8$ . This means there are 5 skeletal elements linked by 8 lines. In 3 dimensions, such a shape will be a square pyramid. When presented in a 2 dimensional form and the hydrogen ligand atoms are added, the figure N51 (N51 means a cluster with 5 defined skeletal elements, and the last digit refers to the position of such a skeletal sketch - in this case it is the first sketch involving 5 skeletal elements) can be constructed. Deducing from N51, we have 5 skeletal elements [5B] and 9 hydrogen atoms to give a geometrical shape whose skeletal elements hypothetically obey the 8 electron rule by just referring to each of the linkages as a provider of 1 electron to the skeletal element, rather than the normal concept of 2 valence electrons provided by each bond. In order to get the semblance of the normal 2 electron type of bond, we can assume that the structure N51

undergoes some re-arrangement to give us the structure N52 where some 4 H hydrogen atoms form bridges. Since all the boron skeletal elements in  $B_5H_9$  are observed to have a H ligand each, then the apex B skeletal element in N52 can be viewed as retaining its linkage of 5 while the 4 basal B skeletal elements have 4 'usual' 2-electron bonds. Figure N51 was referred to as a raw isomeric skeletal structure and N52 as the rearranged isomeric skeletal structure. The raw skeletal structure when done correctly according to series fulfilling the rule of skeletal valences, generally gives a derivation of the cluster formula as is illustrated in N51. The last figure N53 just gives us insight on the general shape of the cluster.

N51-N53  $B_5H_9$

$B(K=2.5, V=5)$

K = Skeletal linkage value, V = skeletal valence or linkages



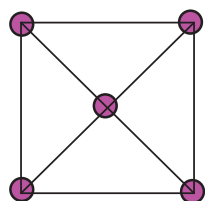
Raw skeletal structure of  $B_5H_9$

Rearranged structure of  $B_5H_9$

N51

N52

K = 8

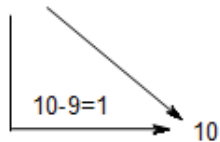


N53

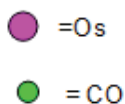
N54  $\text{Os}_5(\text{CO})_{16}$ :  $K = 5[5] - 16 = 9$ ;

Skeletal numbers:  $\text{Os}(K = 5, V = 10), \text{CO}(K = -1)$

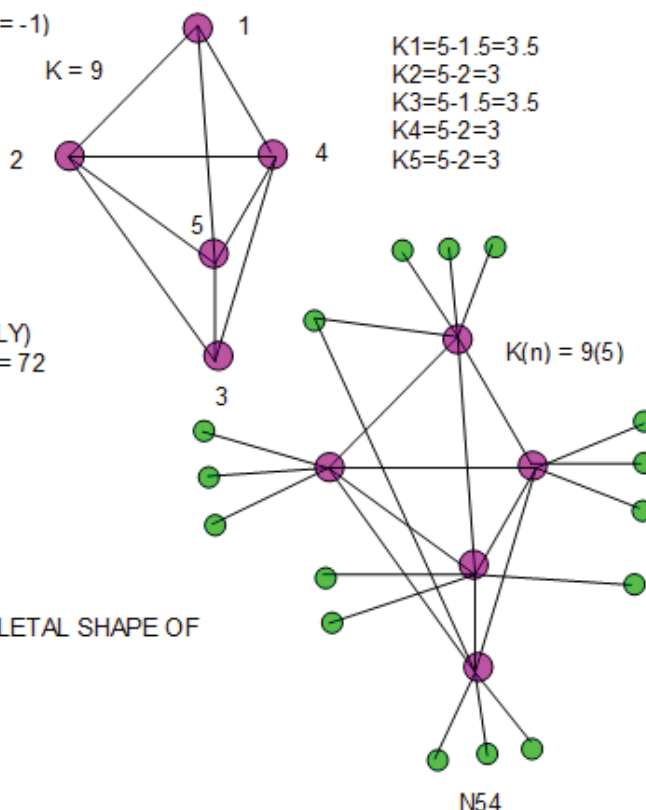
$K(n) = 9(5)$



+2 →  $S = 4n + 2(\text{CLOSO FAMILY})$   
 $V_e = 14n + 2 = 14(5) + 2 = 72$



RAW SKELETAL SHAPE OF  
 $\text{Os}_5(\text{CO})_{16}$



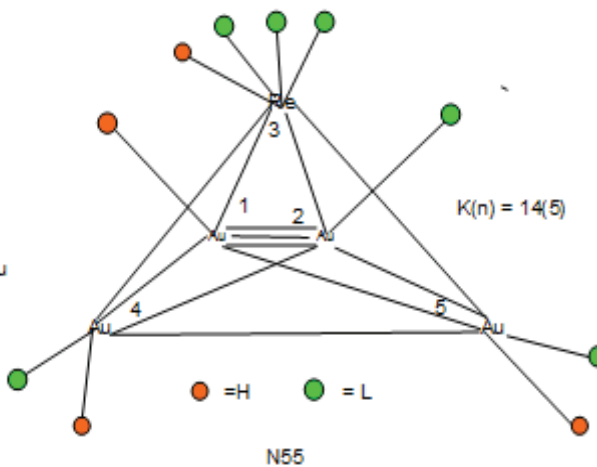
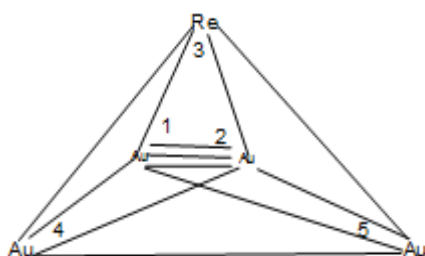
N55  $\text{Au}_4\text{Re}(\text{H})_4\text{L}_6^+$ :  $K = 4[3.5] + 1[5.5] - 4(0.5) - 6(1) + 1(0.5) = 12$ ;  $n = 4 + 1 = 5$ ,  $K(n) = 12(5)$ ,  $S = 4n - 4$ ,  
 $K_p = \text{C}^3\text{C}[\text{M}_2]$

Skeletal numbers:  $\text{Au}(K = 3.5), \text{Re}(K = 5.5), \text{H}(K = -0.5), \text{L}(K = -1), (+1)(K = 0.5)$

$V_e = 14n - 4 = 14(5) - 4 = 66$ ;  $V_f = 4[11] + 1[7] + 4 + 6(2) - 1 = 66$

$V_e = \text{CLUSTER VALENCE ELECTRONS FROM SERIES FORMULA}$ ,  $V_f = \text{VALENCE ELECTRONS FROM CLUSTER FORMULA}$

$K_1 = 1[3.5] - 6(0.5) = 0.5$ ,  $K_2 = 1[3.5] + 0.5 - 3 = 1$   
 $K_3 = 5.5 - 2 = 3.5$ ,  $K_4 = 3.5 - 2 = 1.5$ ,  $K_5 = 3.5 - 2 = 1.5$



N6 CLUSTERS

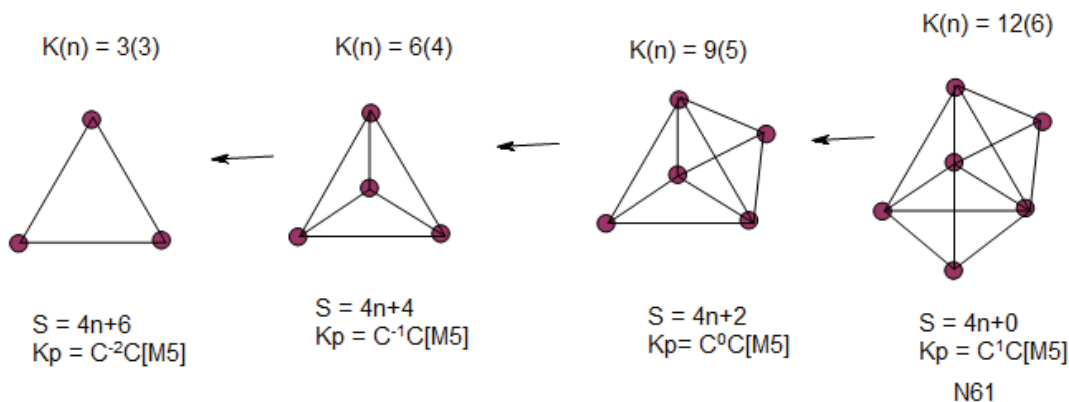
N61  $Os_6(CO)_{18}$ :  $K = 6[5] - 18 = 12$ ,  $n = 6$ ,  $K(n) = 12(6)$ ;  $S = 4n + 0$ ,  $K_p = C^1C[M5]$

The capping symbol tells us the cluster is a mono-capped trigonal bipyramid.

Let us also have a look at the flow of  $K(n)$  numbers:

[12(6), monocapped]; [9(5), trigonal bipyramid]; [6(4), tetrahedral], [3(3), triangle]

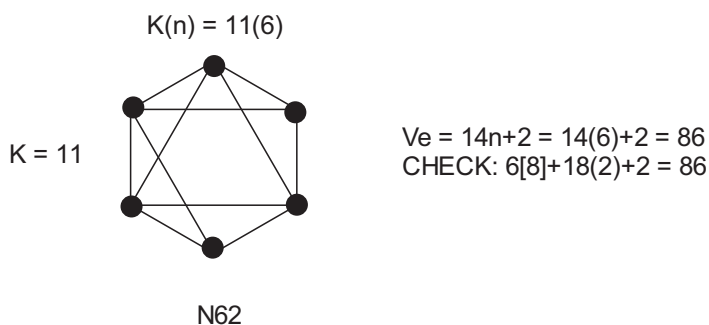
Hence,  $K(n) = 12(6)$  is not an  $O_h$  symmetry.



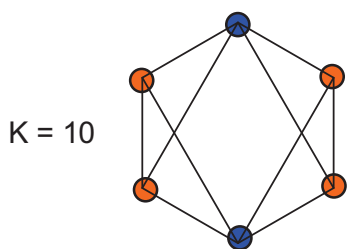
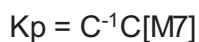
$K(n) = 12(6)$  cluster is described as a mono-capped trigonal bipyramid or a bi-capped tetrahedral. Despite the expectation for it to be an octahedral since  $K = 12$ , it is not, as the cluster is obeying the series rules rather than geometrical rules.

AN EXAMPLE ILLUSTRATING THE CORRELATION OF VERTICAL(RUDOLPH TYPE) CLUSTERS.

N62  $Os_6(CO)_{18}^{2-}$ :  $K = 6[5] - 18 - 1 = 11$ ;  $K(n) = 11(6)$ ,  $S = 4n + 2$  OR  $K = 2n - 1 = 2(6) - 1 = 11$   
 According to the series, this cluster has an ideal  $O_h$  symmetry, despite its having a  $K$  value of 11.



N63  $\text{Fe}_4(\text{CO})_{12}(\text{PR})_2$ :  $K = 4[5] + 2[1.5 - 0.5] - 12 = 10$ ;  $K(n) = 10(6)$ ,  $S = 4n + 4$



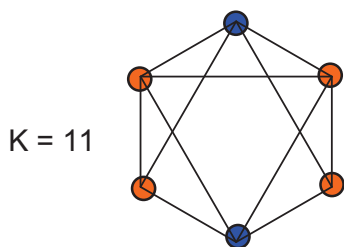
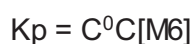
$K = 10$

N63

$K(n) = 10(6)$

NIDO CLUSTER

N64  $\text{Fe}_4(\text{CO})_{12}(\text{PR})_2$ :  $K = 4[5] + 2[1.5 - 0.5] - 11 = 11$   $K(n) = 11(6)$ ,  $S = 4n + 2$



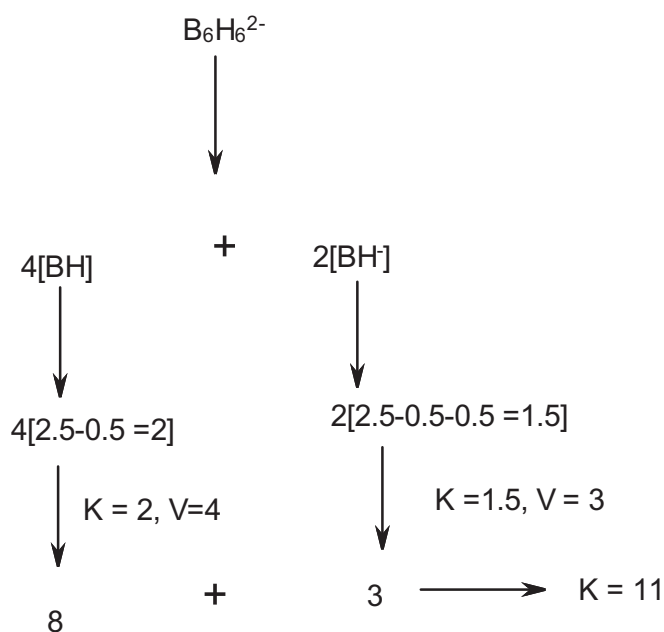
$K = 11$

N64

$K(n) = 11(6)$

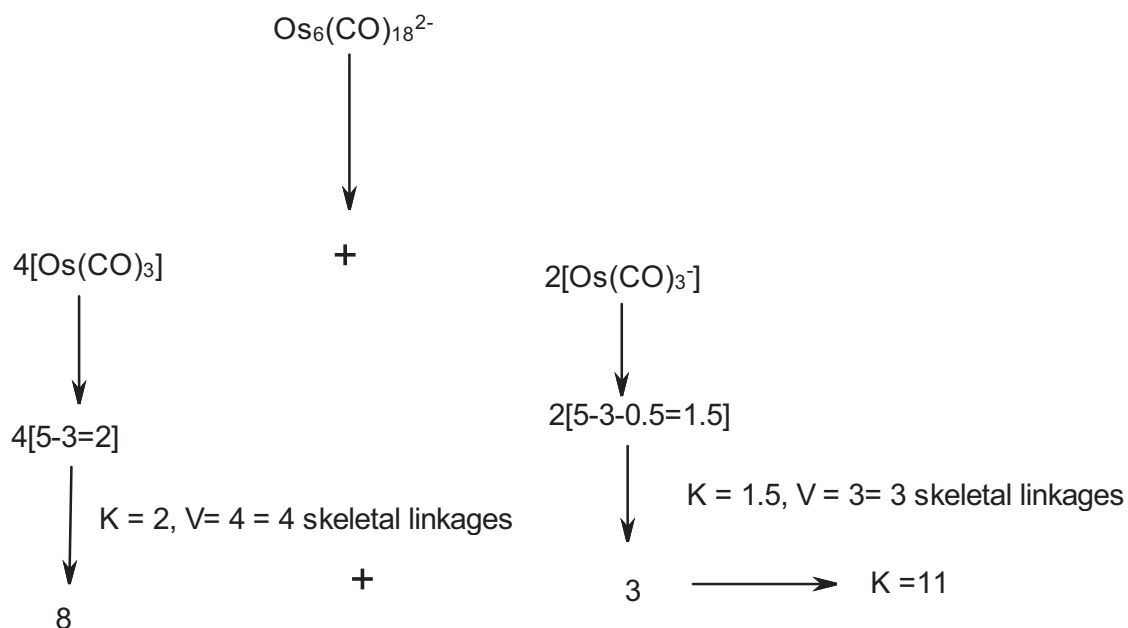
CLOSO CLUSTER

DERIVATION OF K FROM CLUSTER FRAGMENTS AND SKELETAL NUMBERS

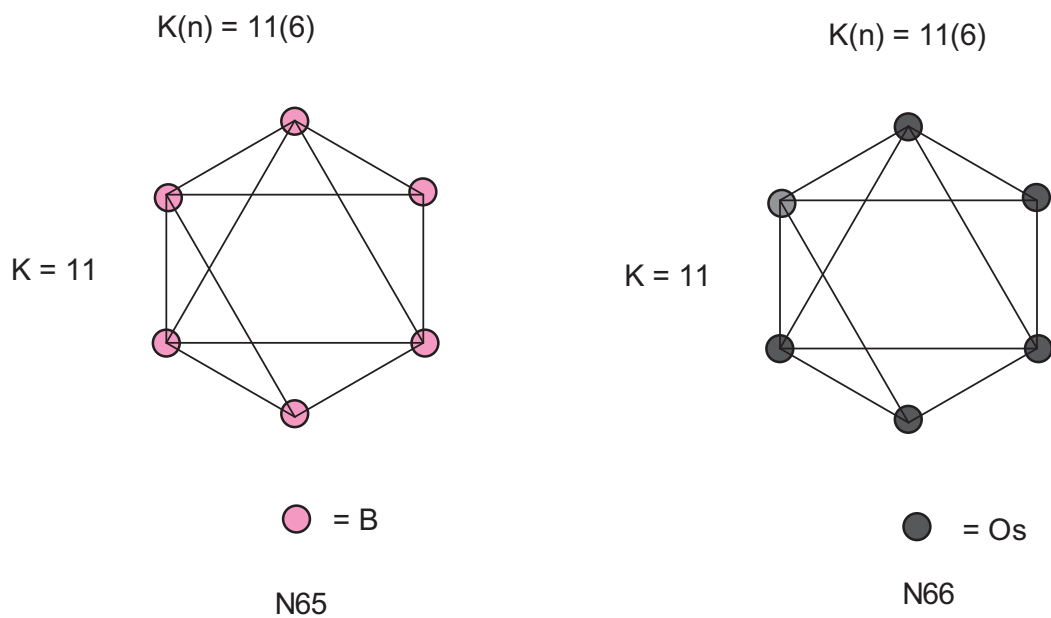




### DERIVATION OF K FROM CLUSTER FRAGMENTS AND SKELETAL NUMBERS

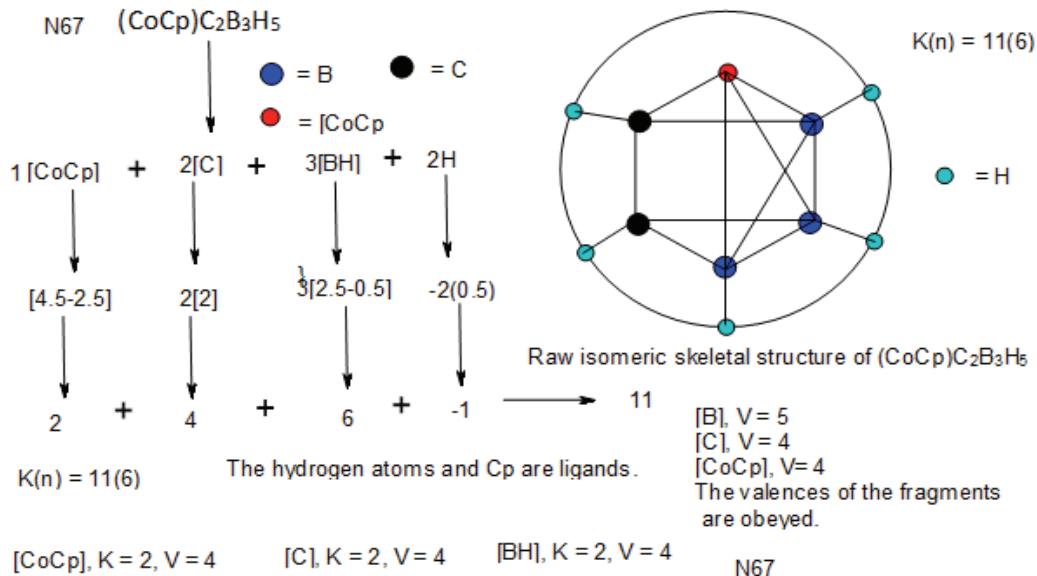


### THE SIMILARITY OF SKELETAL STRUCTURES OF $\text{B}_6\text{H}_6^{2-}$ AND $\text{Os}_6(\text{CO})_{18}^{2-}$



DIFFERENT FORM OF  $K(n) = 11(6)$  SKELETAL ISOMER THAT OBEYS THE SKELETAL VALENCE RULE

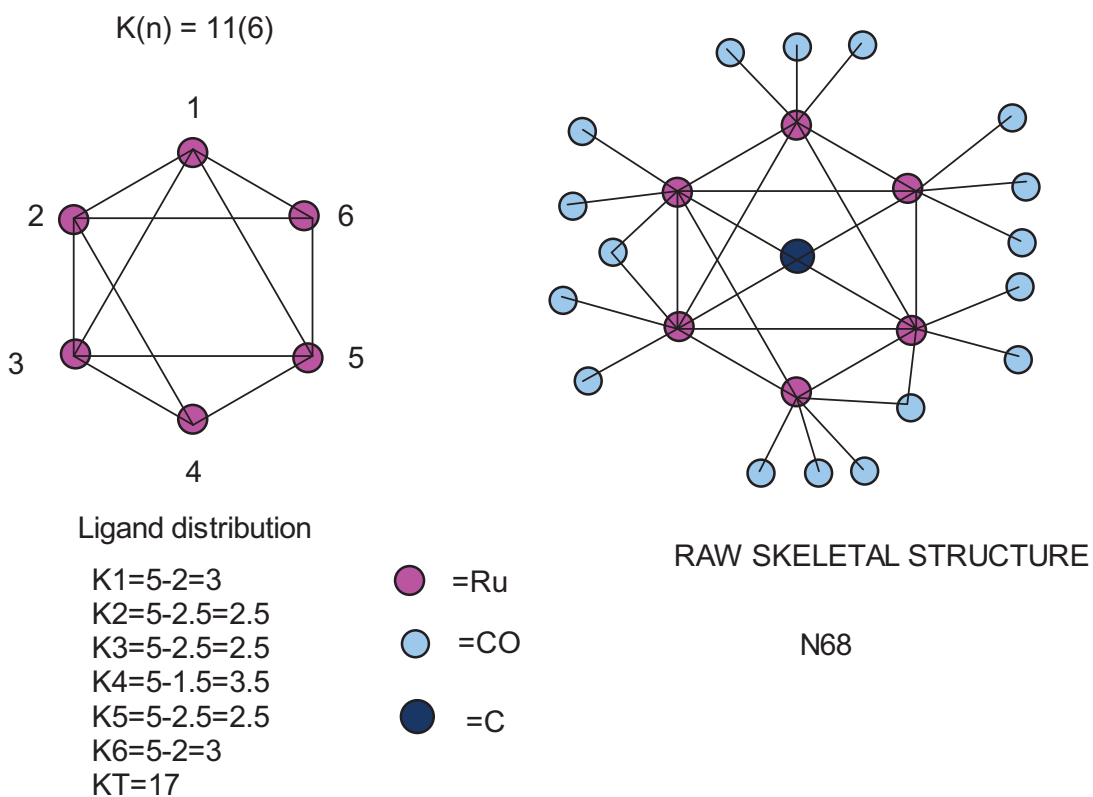
DERIVATION OF  $K(n)$  FROM FRAGMENTS



As can be seen from the skeletal figures of both  $\text{B}_6\text{H}_6^{2-}$  and  $\text{Os}_6(\text{CO})_{18}^{2-}$ , each figure has 4 corners of 4 linkages each and 2 corners of 3 linkages each.

N68  $\text{Ru}_6(\text{C})(\text{CO})_{17}$ :  $K = 6[5] - 2 - 17 = 11$ ,  $K(n) = 11(6)$ ,  $S = 4n + 2$  (CLOSO FAMILY)

Skeletal numbers:  $\text{Ru}(K = 5, V = 10)$ ,  $\text{C}(K = -2)$ ,  $\text{CO}(K = -1)$



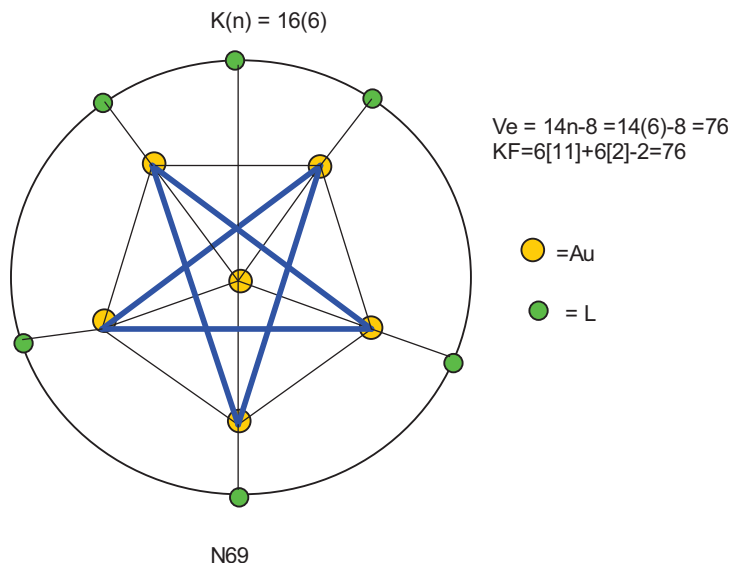
N69  $Au_6L_6^{2+}$ :  $K = 6[3.5] + 1 - 6 = 16$ ;  $K(n) = 16(6)$ ,  $S = 4n - 8$ ,  $Kp = C^5C[M1]$

Skeletal numbers:  $Au(K = 3.5)$ ,  $L(K = -1)$ ,  $(+1)(K = 0.5)$

$[M1]$ ,  $S = 4n + 2$ ,  $K = 2n - 1 = 2(1) - 1 = 1$

$KL = 6[3.5] + 2[0.5] - 5[2.5] - 5[0.5] - 1 = 6$

THERE ARE 6 LINKAGES AVAILABLE FOR THE 6 LIGANDS.



According to the series method, there is one atom in the nucleus which is capped by 5 others.

According to the series symbol  $Kp = C^5C[M1]$ , it implies that the cluster has ONE skeletal element in the nucleus with 5 other capping elements. Each of the 5 capping elements has 3 linkages giving a total of 15 linkages. Since the cluster has a K value 16 the nuclear element  $[M1]$  has an intrinsic K value of 1, and this is in agreement with the series prediction. According to the series, the nuclear cluster fragment,  $[M1]$  obeys the CLOSO series formula  $S = 4n + 2$  and  $K = 2n - 1 = 2(1) - 1 = 1$  in agreement with the above prediction. It has been found easier for clusters with nuclearity index 1-13 (N1-N13) (Kiremire, 2017d) to use the capping symbol as a guide to construct the RAW SKELETAL STRUCTURE of clusters. In this regard, the symbol  $C^5$  acts as a guide to enable us construct a 2-dimensional shape of the cluster. Thus, we can use a 5-membered structure for the capping cluster with a mono-skeletal nucleus; thus the  $Au_6L_6^{2+}$  structural frame-work shown in figure N69. There are 5 capping elements and each is connected to the nuclear skeletal element. This utilizes 5 linkages. The 5 periphery skeletal elements are connected to one another giving us another 5 skeletal linkages. Then there are internal alternating linkages which are also 5. This gives us a total of  $5 + 5 + 5 = 15$ . This agrees with the capping symbol  $C^5$  which indicates there are 5 capping elements each of which consumes 3 linkages. The calculation of K value from  $Au_6L_6^{2+}$ , gives us  $K = 16$  for the entire cluster. On the surface, it appears as if there is ONE missing linkage. In order to find it, we must look at the whole capping symbol,  $Kp = C^5C[M1]$ . If  $C^5$  represents 15 linkages, then the missing link must be hidden within the  $[M1]$  CLOSO fragment. Since the capping nuclei belong to the CLOSO FAMILY, the mono-skeletal nucleus obeys the series formula  $S = 4n + 2$  and  $K = 2n - 1$ . Since  $n = 1$  for a mono-skeletal fragment, then its K value is given by  $K = 2n - 1 = 2(1) - 1 = 1$ . Therefore the grand total of cluster linkages =  $5 + 5 + 5 + 1 = 16$  which takes into account the one linkage associated with the nucleus.

### 3.7 Distribution of Ligands in Golden Clusters

The number of ligands associated with golden clusters is usually relatively small. Therefore a simple calculation can act as a guide on how the ligands are distributed among all the skeletal elements.

N610  $Au_6L_6^{2+}$ 

Skeletal numbers: Au(K=3.5, V=7), L(K=-1), (+1)(K=0.5)

$$K = 6[3.5] - 6(1) + 2(0.5) = 16, n = 6, K(n) = 16(6), S = 4n - 8, Kp = C^5C[M1]$$

This means, there is one skeletal element in the cluster nucleus surrounded by other 5 capping skeletal elements

skeletal elements are numbered as shown in N610.

## LIGAND DISTRIBUTION SUMMARIZED

## PERIPHERY Au ELEMENTS

$$K1 = 3.5 - 5(0.5) = 1$$

$$K2 = 3.3 - 2.5 = 1$$

$$K3 = 3.5 - 2.5 = 1$$

$$K4 = 3.5 - 2.5 = 1$$

$$K5 = 3.5 - 2.5 = 1$$

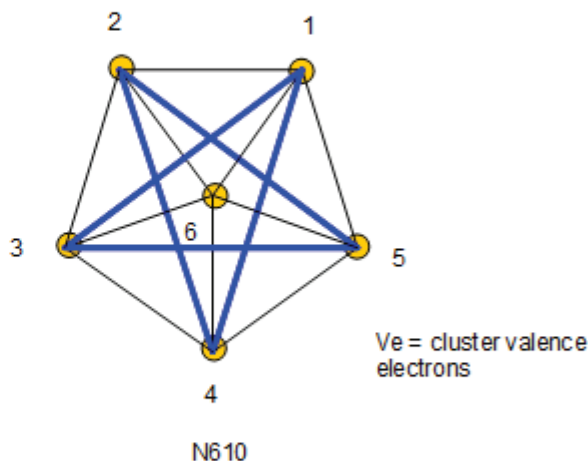
NUCLEAR ELEMENT [Au<sup>2+</sup>]

The closo element [M1] obeys  $S = 4n + 2$ ,

$$K = 2n - 1 = 2(1) - 1 = 1$$

$$\text{Hence } K6 = 3.5 + 2(0.5) - 5(0.5) - 1 = 1$$

THIS MEANS EACH OF THE NUMBERED Au SKELETAL ELEMENTS, 1-6 WILL BIND 1 LIGAND. THIS IS REFLECTED IN N69.



Ve = cluster valence electrons

$$S = 4n - 8$$

$$Ve = 14n - 8, n = 6; Ve = 14(6) - 8 = 76$$

$$VF = 6[11] + 6(2) - 2 = 76$$

HENCE  $Ve = VF$  (calculated from cluster formula)

The first approach is to consider the cluster  $Au_6L_6^{2+}$  as comprising of  $Au_6^{2+}$  fragment and 6L. The skeletal linkages of the naked fragment  $Au_6^{2+}$  subtracting the skeletal linkages of the cluster will give us the linkages remaining to bind the ligands.

The  $Au_6^{2+}$  fragment has a total of  $6[3.5] + 2(0.5) = 22$  linkages available. According to the calculation, 16 of those are utilized for the internal binding of the skeletal elements. Hence, the remaining linkages are available for the ligands. That is,  $KL = 22 - 16 = 6$ , This means there are 6 linkages available for 6 ligands distributed onto 6 gold skeletal elements as shown in N 69.

Alternatively, we can calculate the number of skeletal linkages available for every individual skeletal element as follows:

$K1 = 1[3.5] - 5(0.5) = 3.5 - 2.5 = 1$ ;  $K2$  is the same as  $K1 = 1 = K3 = K4 = K5 = K6$ . This information indicates that each skeletal element will be assigned to one ligand as indicated in N69. The ideal raw skeletal structure will have a 2-dimensional symmetry of  $D_{3h}$ . The outside circle in N69 is to assist in adding the ligands to the periphery gold atoms. The actual shape has been described as octahedral or edge-sharing bi-tetrahedral (Mingos, 1984). The two dimensional skeletal framework N69 looks like a star. The cluster valence electrons: The cluster valence electrons have been calculated using the series formula (Ve) and the result was compared with the one calculated from the cluster formula, VF. Always,  $Ve = VF$  indicating the authenticity of the series formula. Clearly, the skeletal structural frameworks of clusters follow an exact mathematical precision of  $4n$  cluster series.

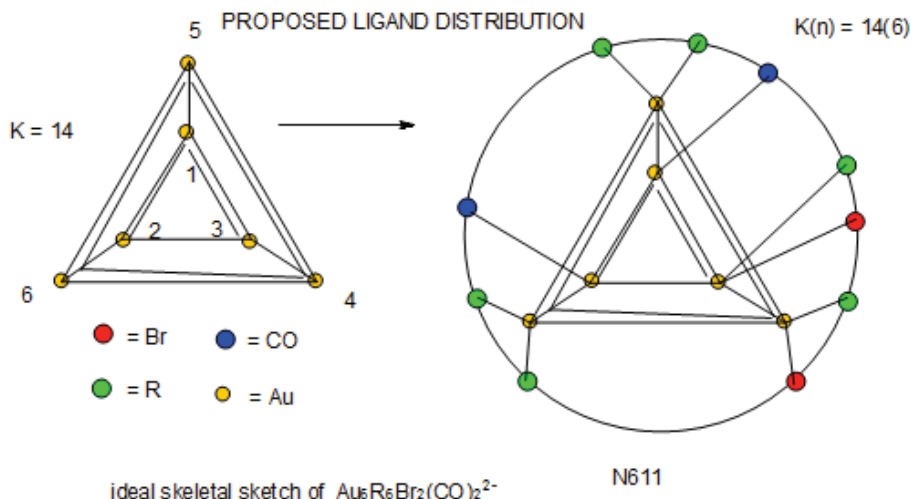
N611  $Au_5R_6Br_2(CO)_2^{2-}$  : R = CF<sub>3</sub> K = 6[3.5]-3-1-2-1 = 14, n = 6, K(n) = 14(6), S = 4n - 4, K<sub>p</sub> = C<sup>3</sup>C[M3]

V<sub>e</sub> = 14n - 4 = 14(6) - 4 = 80; V<sub>f</sub> = 6[11] + 6 + 2 + 4 + 2 = 80

The cluster has a nucleus of 3 skeletal elements surrounded by three capping skeletal elements.  
Possible skeletal shape as in figure N611

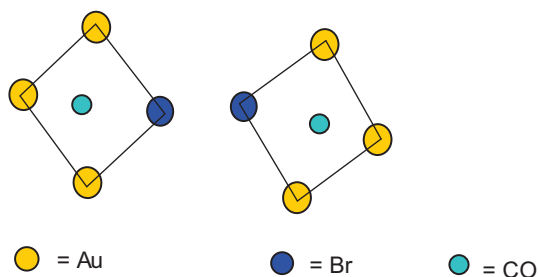
K<sub>1</sub> = 3.5 - 5(0.5) = 3.5 - 2.5 = 1; K<sub>2</sub> = 3.5 + 1(-.5) - 4(0.5) = 3.5 - 2.5 = 1; K<sub>3</sub> = K<sub>2</sub> = 1, K<sub>4</sub> = 3.5 - 5(0.5) = 1, K<sub>5</sub> = K<sub>4</sub> = 1, K<sub>6</sub> = K<sub>5</sub> = 1

Skeletal numbers: Au(K = 3.5, V = 7), R(K = -0.5), Br(K = -0.5), CO(K = -1), (-1)(K = -0.5)



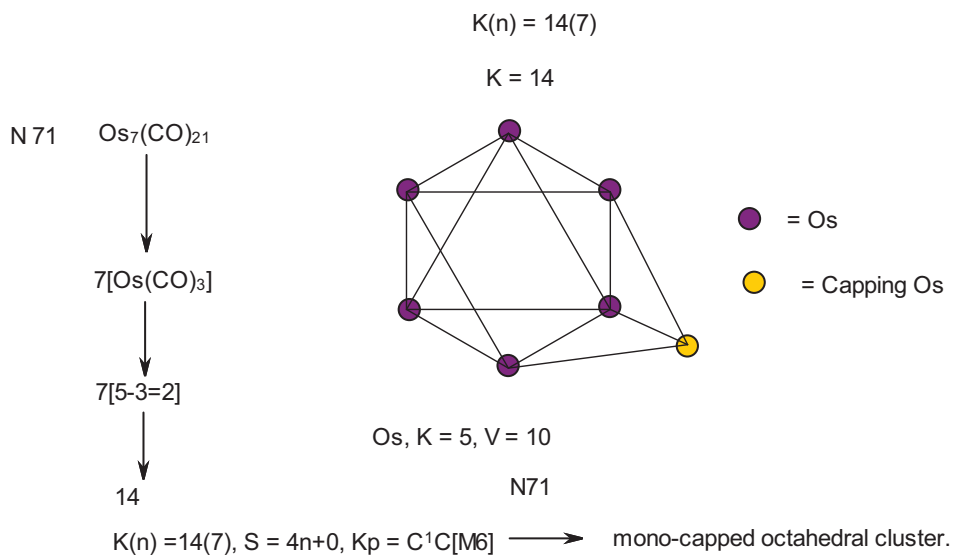
The series acts as a guide. Although the prediction is 3 skeletal elements capping on another set of three skeletal elements, what is observed is simply two sets of 3 golden skeletal elements as shown in N612.

K<sub>p</sub> = C<sup>3</sup>C[M3]



N612

N71 Os<sub>7</sub>(CO)<sub>21</sub>: Skeletal numbers; Os(K = 5, V = 10), CO(K = - 1), K = 7[5] - 21 = 14, n = 7, K(n) = 14(7), S = 4n + 0, K<sub>p</sub> = C<sup>1</sup>C[M6]. This symbol predicts a mono-capped octahedral complex and this is what is observed (Hughes & Wade, 200; Housecroft & Sharpe, 2005).



$Ve = 14n+0 = 14(7) + 0 = 98$ ; CHECK:  $VF = 7[8] + 21(2) = 98$

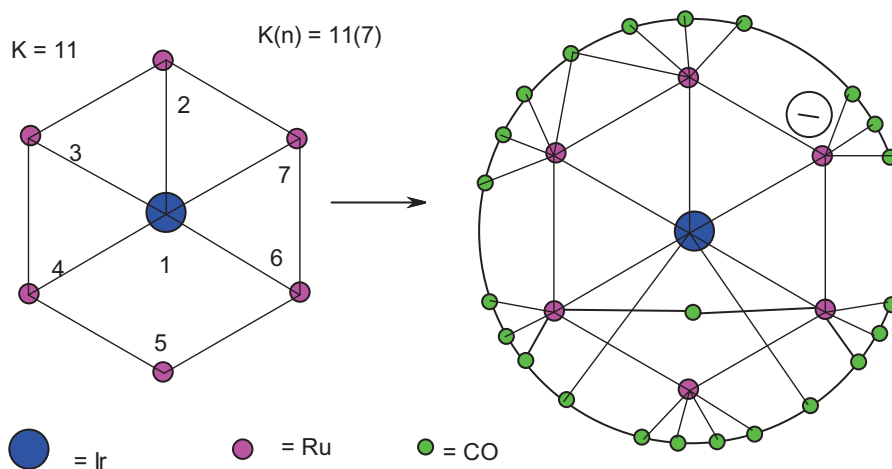
The cluster valence electrons number from the series formula (Ve) is the same as the number of valence electrons calculated from the cluster formula (VF) itself.

N 72  $IrRu_6(CO)_{23}^-$ :  $K = 1[4.5] + 6[5] - 23 \cdot 0.5 = 11$ ;  $K(n) = 11(7), S = 4n+6, K_p = C^{-2}C[M9]$

$Ve = 14n+6 = 14(7)+6 = 104$ ;  $VF = 1[9] + 6[8] + 23(2) + 1 = 104$

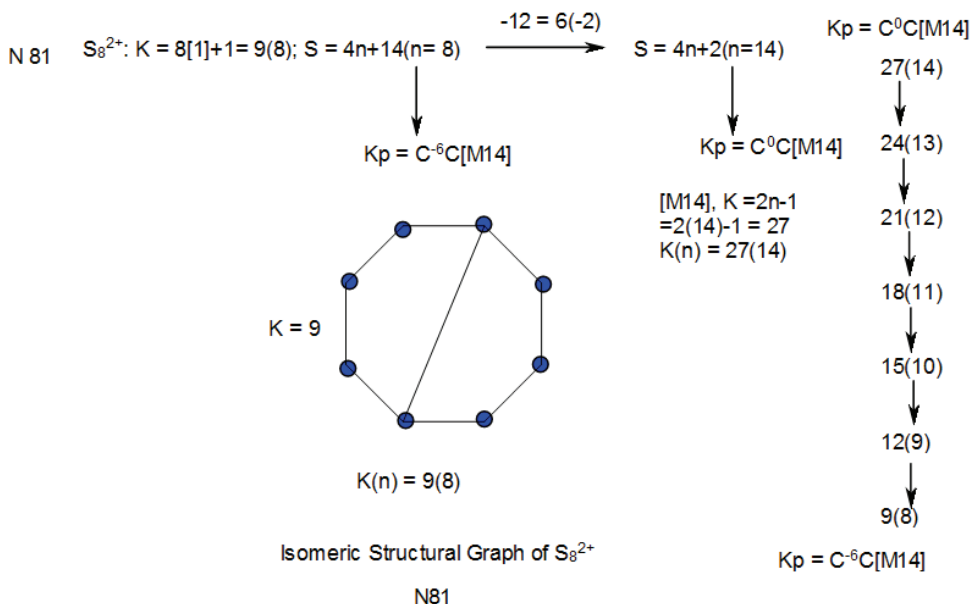
LIGAND DISTRIBUTION

$K_1 = 4.5 - 2.5 = 2$ ;  $K_2 = 5 - 1.5 = 3.5$ ;  $K_3 = 3.5$ ;  $K_4 = 3.5$ ;  $K_5 = 5 - 1 = 4$ ;  $K_6 = 3.5$ ;  $K_7 = 3.5$



Ideal skeletal sketch of  $IrRu_6(CO)_{23}^-$  (Adams, et al, 2011)

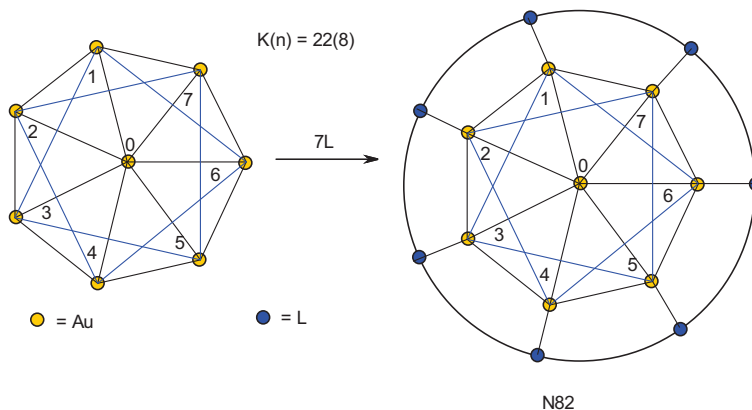
N72



Let us consider the first example G1  $S_8^{2+}$  cluster as an illustration. From the appendix 1, sulphur has a K value of 1. The K value of 8 S skeletal elements is simply  $8 \times 1 = 8$ . Also we know from series, that a unit of positive charge (+1) is assigned a K value of 0.5. So for 2+ charge the K value =  $2 \times 0.5 = 1$ . Hence the K value of  $S_8^{2+} = 8 + 1 = 9$ . Since there are 8 skeletal elements the K(n) parameter is  $K(n) = 9(8)$ . This means that the cluster will have 9 linkages and this has been found to be the case (Housecroft & Sharpe, 2005). We also know that  $K = 2n - \frac{1}{2}q$ ; hence  $9 = 2(8) - \frac{1}{2}q$  and this gives the value of  $q = 2[16-9] = 14$ . Since the cluster series  $S = 4n+q$ , this gives us  $S = 4n+14$ . We also know that there are a good number of isomers with  $K = 9$  (nine linkages) that can be constructed, but we can only sketch one. This is given in G1 below. Categorization of the cluster based on CLOSO ( $S = 4n+2$ ) vertical series ( $\Delta K = \pm 3, \Delta n = \pm 1$ ) has been developed. Since the cluster belongs to the series  $S = 4n+14(n=8)$ , it has to go through the stages  $4n+12(n=9) \rightarrow 4n+10(n=10) \rightarrow 4n+8(n=11) \rightarrow 4n+6(n=12) \rightarrow 4n+4(n=13) \rightarrow 4n+2(n=14)$ . Clearly, the cluster is 6 steps below the CLOSO step and hence its capping symbol can be expressed as  $K_p = C^{-6}C[M14]$ . Thus, the cluster belongs to the CLUSTER GROUP [M14] on the Rudolph type of numerical categorization (Rudolph, 1976). The symbol [M14] means that  $S = 4n+2$  and  $n = 14$ ;  $K = 2n-1 = 2(14)-1 = 27$ . Hence  $K(n) = 27(14)$ . The numerical series of this will be  $27(14) \rightarrow 24(13) \rightarrow 21(12) \rightarrow 18(11) \rightarrow 15(10) \rightarrow 12(9) \rightarrow 9(8)$ . Clearly, the cluster  $S_8^{2+}$ ,  $K(n) = 9(8)$  is numerically 6 steps below the Closo [M14] level. This cluster is graphically linked by 9 lines(linkages). According to the series, is it possible for us to say that cluster linkages are similar or identical to the conventional chemical bonds?

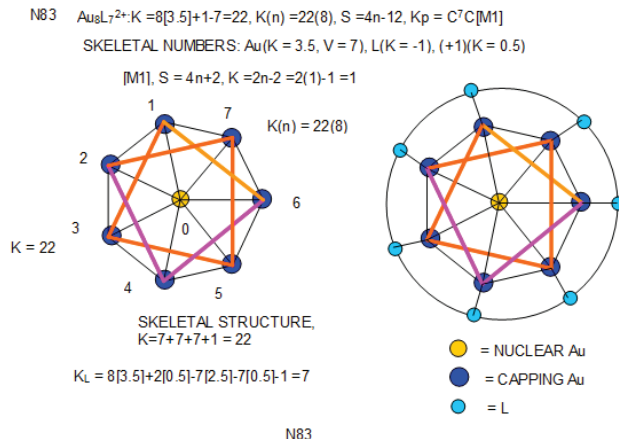
N82

$K_p = C^7C[M1]$  means there is 1 skeletal element in the nucleus surrounded by 7 others.



The  $Pt^+$  fragment has a K value is  $= 4+1(0.5)-7(0.5)-1 = 0$ . Since each of the periphery Au element is assumed to have a zero oxidation state, the positive charge can be assigned to the platinum element. In summary, each of the periphery Au

element will bind to a 2 electron donor ligand while the central Pt element will have no ligand. According to this model the ligand distribution is according to simple mathematical precision. The sketch is shown in N82.



THIS MEANS THERE ARE 7 LIGAND LINKAGES AVAILABLE FOR 7 LIGANDS.  
 $V_e = 14n - 12 = 14(8) - 12 = 100$ , STRUCTURE,  $V_e = 8[11] + 7(2) - 2 = 100$

LIGAND DISTRIBUTION  
 $K_1 = 3.5 - 5(0.5) = 3.5 - 2.5 = 1, K_2 = K_1 = 1, K_3 = K_1 = 1, K_4 = K_1 = 1, K_5 = K_1 = 1, K_6 = K_1 = 1, K_7 = K_1 = 1,$   
 $K_0 = 3.5 + 2(0.5) - 7(0.5) - 1 = 4.5 - 4.5 = 0$   
 THIS MEANS THAT EVERY PERIPHERY SKELETAL ELEMENT WILL BIND 1 TWO ELECTRON DONOR LIGAND. BUT THE NUCLEAR SKELETAL ELEMENT WILL BE NAKED.

Let us consider another example N83 :  $Au_8L_7^{2+} (L = PPh_3): K = 8[3.5] - 7 + 1 = 22; n = 8, K(n) = 22(8), K = 2n - \frac{1}{2} q, 22 = 2(8) - \frac{1}{2} q, \frac{1}{2} q = 16 - 22 = -6, q = -12, S = 4n - 12, K_p = C^7C[M1]$ . According to the series, the prediction is that this will be a cluster of 7 skeletal elements surrounding one skeletal element that is a member of CLOSO SERIES,  $S = 4n + 2, K = 2n - 1 = 2(1) - 1 = 1$ . Thus the closo nucleus has  $K(n)$  parameter = 1(1). The rest of the 7 skeletal elements will be capped around it. A capping fragment of the series has a formula  $S = 4n - 2, K = 2n + 1; n = 1, K = 2(1) + 1 = 3$ . This means the symbol  $C^7$  with seven cappings involves  $7(3) = 21$  linkages. This gives us a graphical guide of the diagram, N83. There are 7 linkages to the central closo skeletal nuclear element and 14 linkages on the periphery structure of the diagram giving a total of 21 linkages. Then the  $[M1]$  closo nucleus has 1 skeletal linkage ( $K = 1$ ) in its own right. This makes a grand total of 22 cluster linkages. This provides us with a graphical representation of  $Au_8$  skeletal elements in  $Au_8L_7^{2+}$  cluster. On a planar view point, the diagram has  $D_{7h}$  symmetry. How are the ligands distributed? This means that each of the periphery au will bind a 2 electron donor ligand such as  $pPh_3$ , while the nuclear au will have no ligands (naked) as sketched in the skeletal graph N83.

The outer circle just acts a guide to sketch ligands. Let us see the flow of  $K(n)$  numbers of  $K_p = C^7C[M1]; 1(1) \rightarrow 4(2) \rightarrow 7(3) \rightarrow 10(4) \rightarrow 13(5) \rightarrow 16(6) \rightarrow 19(7) \rightarrow 22(8)$ .



N84 Os<sub>8</sub>(CO)<sub>22</sub>z<sup>2-</sup>

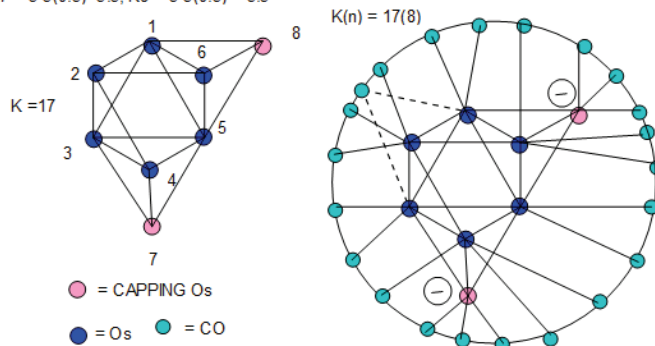
Os(K = 5, V = 10), CO(K = -1), (-1)(K = 0.5) ← Skeletal numbers  
 $K = 8[5] - 22(1) + 2(-0.5) = 17, n = 8, K(n) = 17(8), S = 4n - 2, K_p = C^2C[M6]$

$V_e = 14n - 2 = 14(8) - 2 = 110, V_f = 8[8] + 22(2) + 2 = 110$   
 $V_e$  = cluster valence electrons using series formula  
 $V_f$  = cluster valence electrons from the cluster formula

$K_p = C^2C[M6]$ , MEANS THAT THE CLUSTER IS A BI-CAPPED OCTAHEDRON.

LIGAND DISTRIBUTION

$K_1 = 5 - 5(0.5) = 2.5, K_2 = 5 - 2 = 3, K_3 = 5 - 5(0.5) = 2.5, K_4 = 5 - 4(0.5) = 3, K_5 = 5 - 6(0.5) = 2, K_6 = 5 - 4(0.5) = 3$   
 $K_7 = 5 - 3(0.5) = 3.5, K_8 = 5 - 3(0.5) = 3.5$



The capping symbol  $K_p = C^2C[M6]$  derived from the series predicts a bi-capped octahedral complex and this is what was found (Hughes and Wade, 2000).

N84 Os<sub>8</sub>(CO)<sub>22</sub>z<sup>2-</sup>

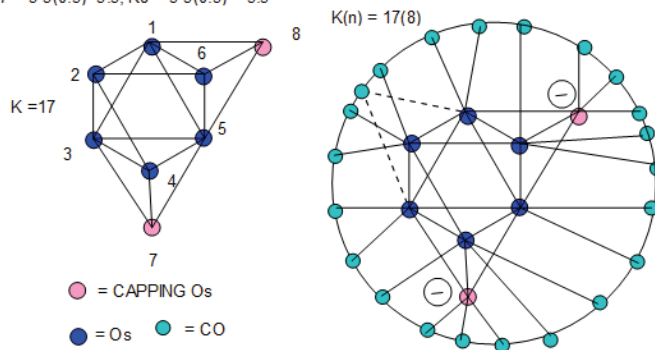
Os(K = 5, V = 10), CO(K = -1), (-1)(K = 0.5) ← Skeletal numbers  
 $K = 8[5] - 22(1) + 2(-0.5) = 17, n = 8, K(n) = 17(8), S = 4n - 2, K_p = C^2C[M6]$

$V_e = 14n - 2 = 14(8) - 2 = 110, V_f = 8[8] + 22(2) + 2 = 110$   
 $V_e$  = cluster valence electrons using series formula  
 $V_f$  = cluster valence electrons from the cluster formula

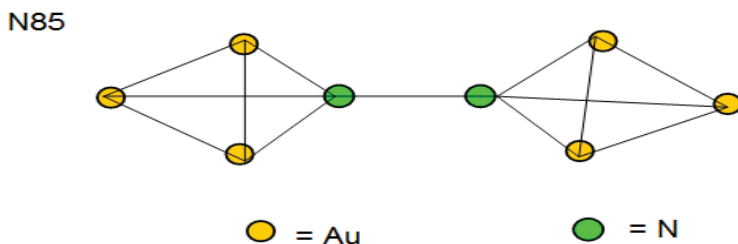
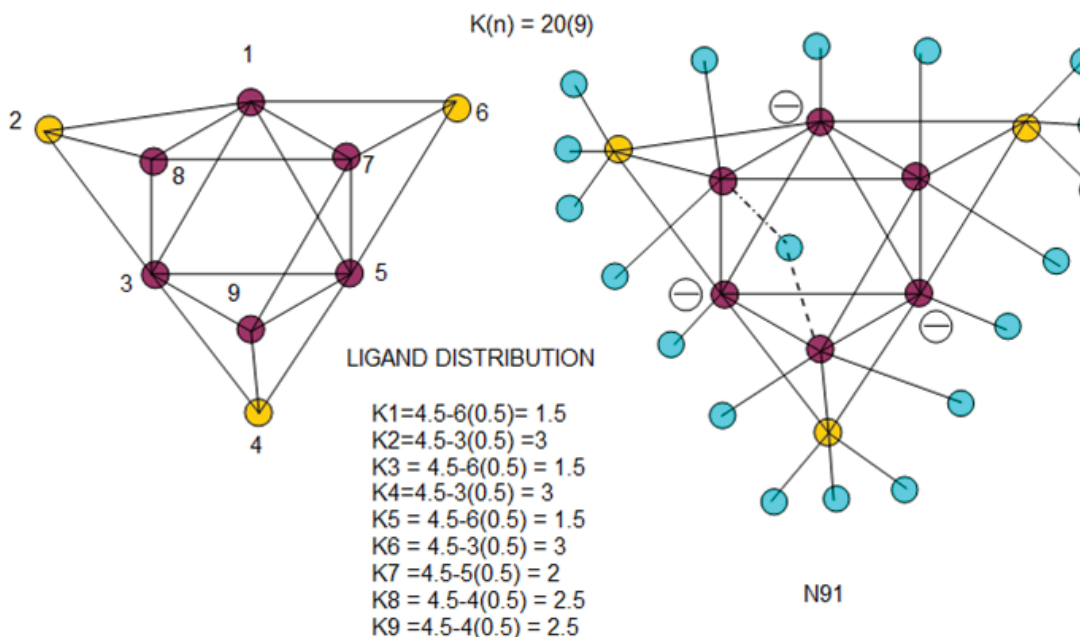
$K_p = C^2C[M6]$ , MEANS THAT THE CLUSTER IS A BI-CAPPED OCTAHEDRON.

LIGAND DISTRIBUTION

$K_1 = 5 - 5(0.5) = 2.5, K_2 = 5 - 2 = 3, K_3 = 5 - 5(0.5) = 2.5, K_4 = 5 - 4(0.5) = 3, K_5 = 5 - 6(0.5) = 2, K_6 = 5 - 4(0.5) = 3$   
 $K_7 = 5 - 3(0.5) = 3.5, K_8 = 5 - 3(0.5) = 3.5$

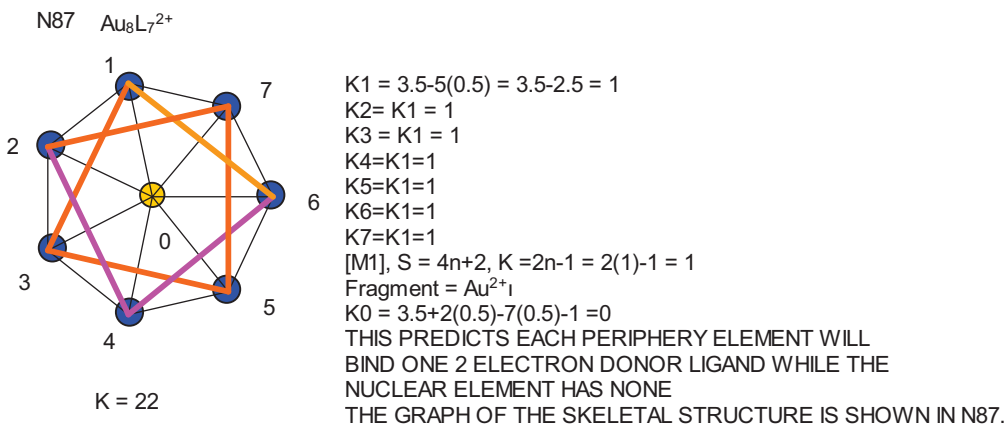


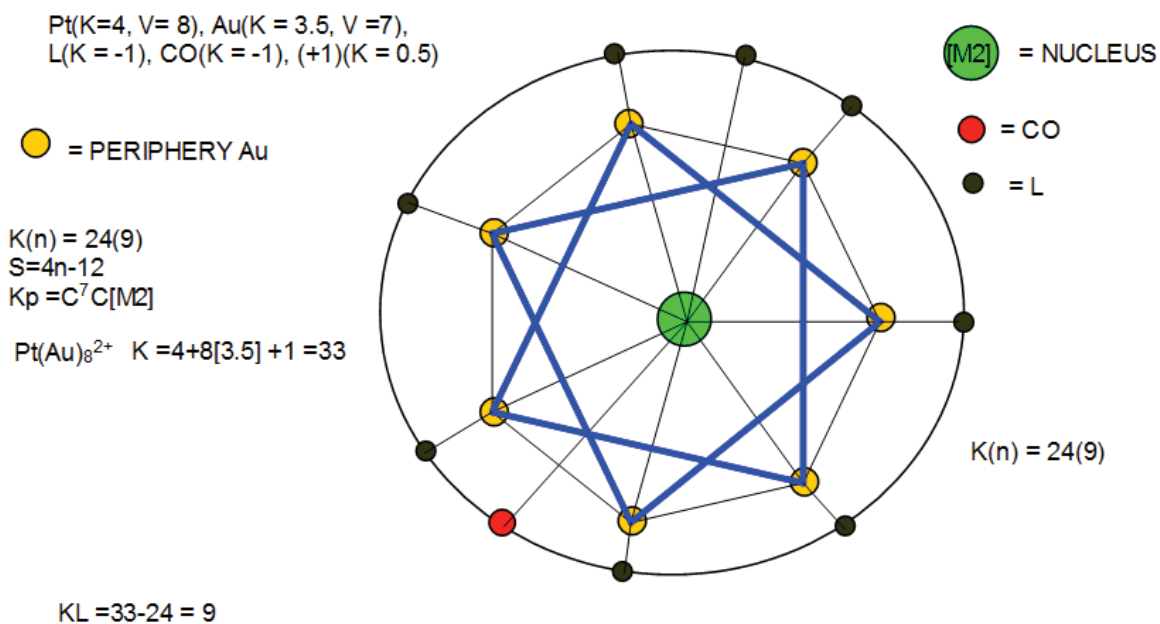
N91  $Rh_9(CO)_{19}^{3-}$ :  $K = 9[4.5] - 19 \cdot 1.5 = 20; K(n) = 20(9), S = 4n - 4, Kp = C^3C[M-6]$   
 $Rh(K = 4.5, V = 9), CO(K = -1), (-1)(K = -0.5)$



Skeletal sketch of  $N_2(AuL_6)^{2+}$  as observed (Gimeno, 2008)

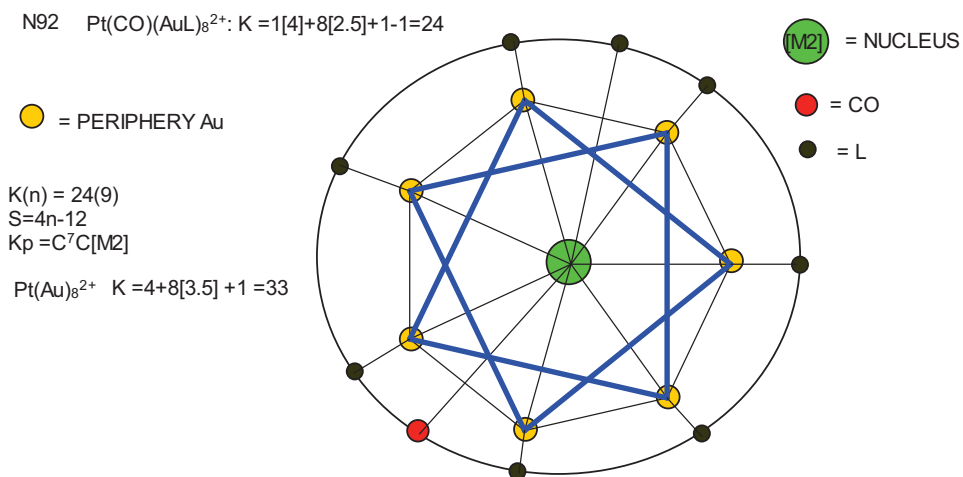
$Au_8L_7^{2+}$ :  $K = 22; Au_8^{2+}$ :  $K = 29, KL = 29 - 22 = 7$ . There will be 7 linkages available for 7 skeletal elements. The skeletal elements are the periphery ones as indicated in CC-25. This is in agreement with observation and is described as capped centered chair (Konishi). In 2 dimensional form, it forms a nice  $D_{7h}$  symmetry.





THIS IMPLIES THAT EACH SKELETAL ELEMENT WILL HAVE A LIGAND.

N92



$KL = 33 - 24 = 9$   
 THIS IMPLIES THAT EACH OF THE SKELETAL ELEMENT WILL HAVE A LIGAND.

$[M2], S = 4n + 2, K = 2n - 1 = 2(2) - 1 = 3$

LIGAND DISTRIBUTION

$N0 = [PtAu^{2+}]$

$K1 = 3.5 - 5(0.5) = 3.5 - 2.5 = 1$

$K2 = K1 = 1$

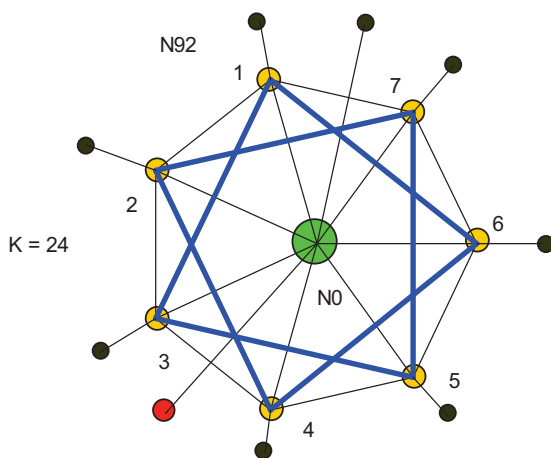
$K3 = K1 = 1$

$K4 = K1 = 1$

$K5 = K1 = 1$

$K6 = K1 = 1$

$K7 = K1 = 1$

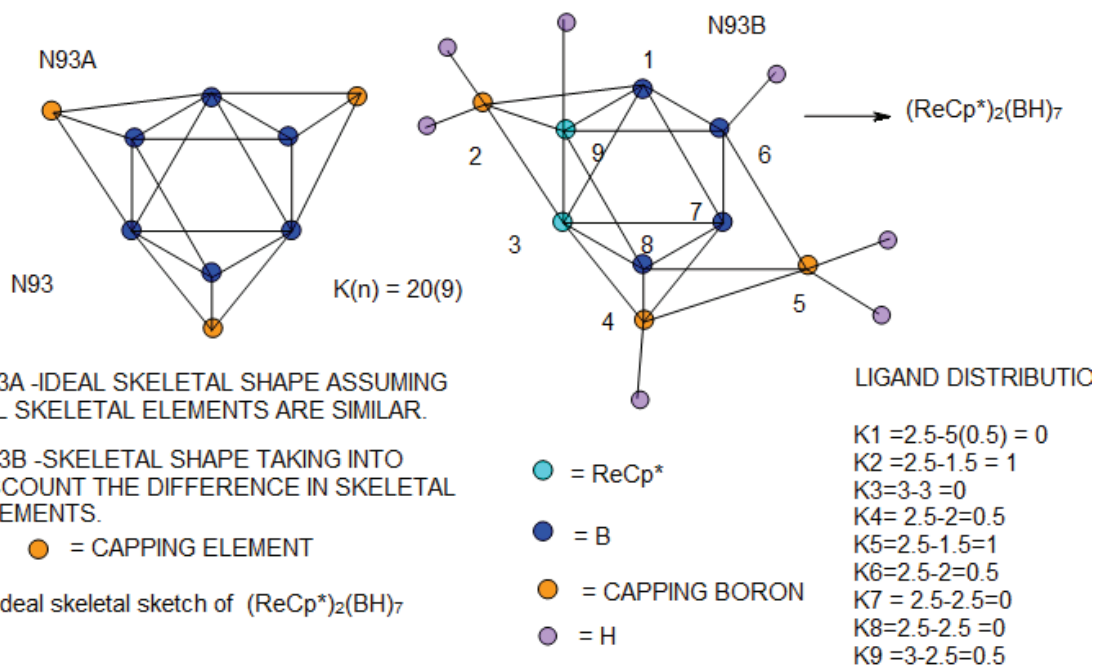


$KN0 = 1[4] + 1[3.5] + 2(0.5) - 7(0.5) - 3 = 2$   
 THIS MEANS THAT 2 LIGANDS WILL BE BOUND TO THE 2 NUCLEAR SKELETAL ELEMENTS AS IN N92

N93  $(\text{ReCp}^*)_2(\text{BH})_7$  :  $K = 2[5.5-2.5]+7[2.5-0.5] = 20$ ,  $n = 2+7 = 9$ ,  $K(n) = 20(9)$   
 $S = 4n-4$ ,  $K_p = \text{C}^3\text{C}[\text{M}6]$

$[\text{ReCp}^*]$ , ( $K = 5.5-2.5 = 3, V = 6$ )  
 $\text{B}$ , ( $K = 2.5, V = 5$ ),  $\text{H}(K = -0.5)$

The series predicts an ideal shape of a tri-capped octahedron.

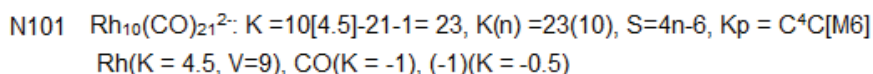


The rhenium homologous series are given by  $(\text{ReCp}^*)_2(\text{BH})_m$ ;  $m = 6-10$ . The increase from  $m = 6$  to  $m = 7$  is by 1[BH] fragment. If the cluster  $m = 6$  belongs to  $S = 4n-4$ , then the increase of 1[BH] = 1[C];  $S = 4n+0$ . The new series formula when the cluster changes from  $m = 6$  to  $m = 7$  will be given by  $S = [(4n-4)(n=6) + (4n+0)(n = 1) = 4n-4(n=7)]$ . Thus, the cluster series formula has remained the same despite  $n$  changing by 1. In other words, the series will still remain tri-capped;  $K_p = \text{C}^3\text{C}[\text{M}x]$ ,  $x = 5-9$ . This simply means, the capping index will remain the same, that is, same series but the nuclearity index will expand as it is observed (Fehlner & Halet, 2007).

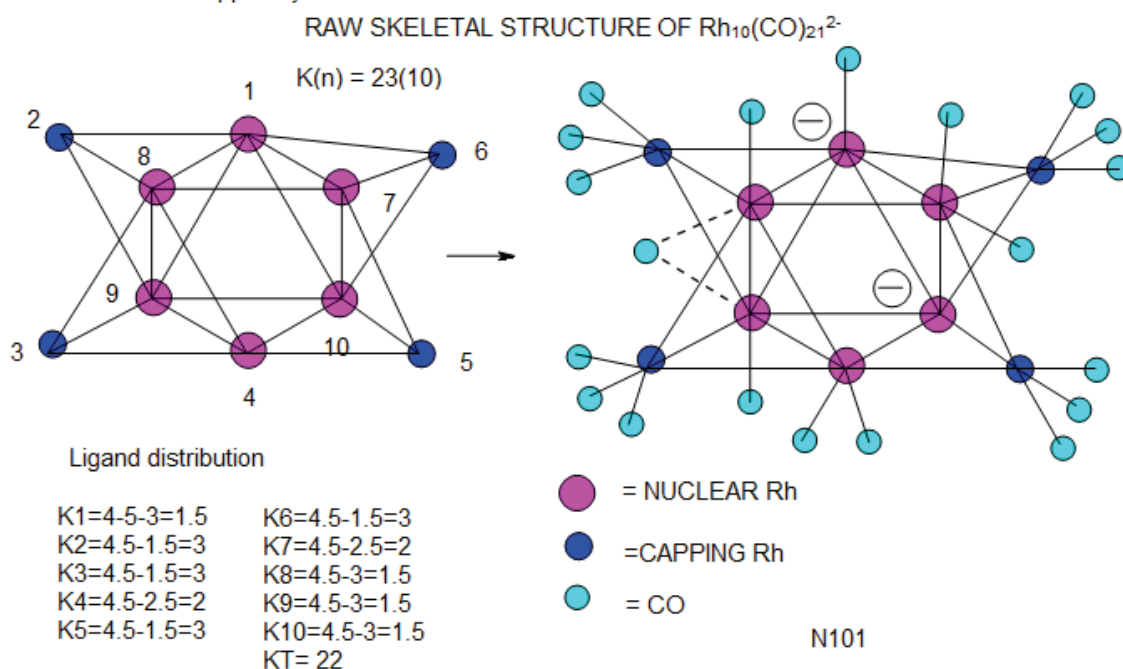
Periphery Au Elements: All Au elements are equal;  $K = 3.5 - 5(0.5) = 3.5 - 2.5 = 1$ , **Nuclear**  $\text{Au}^{3+}$ :  $K = 3.5 + 3(0.5) - 8(0.5) - 1 = 5 - 5 = 0$ . Each of the peripheral Au will carry 1 ligand while the nucleus will have none. There is another way of calculating the linkages available on the skeletal structure for binding the ligands.

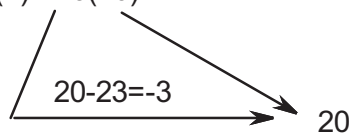
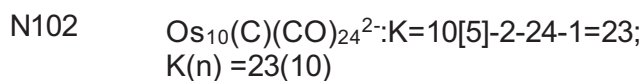
$\text{Au}_9\text{L}_8^{3+} \rightarrow \text{Au}_9^{3+} + 8\text{L}$ ;  $\text{Au}_9^{3+}$ ;  $K = 9[3.5] + 3(0.5) = 33$ . Some of these linkages will be used for binding the skeletal elements and the rest to bind the ligands. In the calculation above in CC-28,  $K = 25$ . This means that these are for binding the skeletal elements in the cluster. Therefore those remaining to bind the ligands will be given by  $KL = 33 - 25 = 8$ . As expected, this agrees with the cluster formula. These will be evenly distributed onto the periphery Au skeletal elements as indicated in N95. Note that the nuclear element [M1] obeys the closo series formula  $S = 4n + 2$ ,  $K = 2n - 1 = 2(1) - 1 = 1$ . Thus, the closo nuclear skeletal element in its own right has a K value of 1. We can also calculate the number of skeletal linkages available for binding ligand(s). As can be seen from the raw skeletal structure in N95, each peripheral Au skeletal element has 5 linkages. Each linkage behaves as a  $[\text{H}\cdot]$  ligand donating ONE electron to Au periphery skeletal atom. So we can calculate the respective K value as  $1[3.5] - 5(0.5) = 1$ . This shows that each peripheral Au skeletal element will bind ONE ligand as indicated in N95. The cluster of this formula has been described as bi-capped centered or crown centered (Konishi, 2014).

Let us illustrate these steps using the example of  $\text{Rh}_{10}(\text{CO})_{21}^{2-}$ :  $K = 23$ ,  $n = 10$ ;  $K(n) = 23(10)$ ;  $K = 2(10) - \frac{1}{2}q = 23$ ,  $q = -6$  and hence  $S = 4n - 6$ ,  $K_p = \text{C}^4\text{C}[\text{M}6]$ . The cluster has an octahedral CLOSO nucleus,  $S = 4n + 2$ ,  $K = 2n - 1 = 2(6) - 1 = 11$ . The ligand distributions have been indicated either numerically or diagrammatically or both.



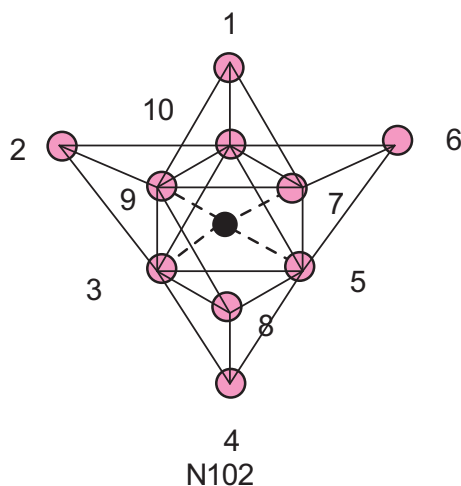
According to this information, it means that the cluster has an octahedral nucleus which is capped by 4 skeletal elements





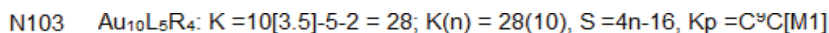
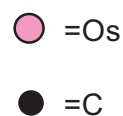
$q = -6 \longrightarrow S = 4n-6; K_p = \text{C}^4\text{C}[\text{M}6]$

THIS MEANS, THE CLUSTER WILL HAVE AN OCTAHEDRAL NUCLEUS  
 4 CAPPED BY 4 OTHER SKELETAL ELEMENTS



Ligand distribution

$K1=5-1.5=3.5$   
 $K2=3.5$   
 $K3=5-3.5=1.5$   
 $K4=3.5$   
 $K5=5-3.5=1.5$   
 $K6=3.5$   
 $K7=5-3=2$   
 $K8=5-2=3$   
 $K9=5-3.5=1.5$   
 $K10=5-3.5=1.5$   
 $KT=25$

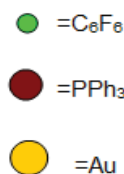
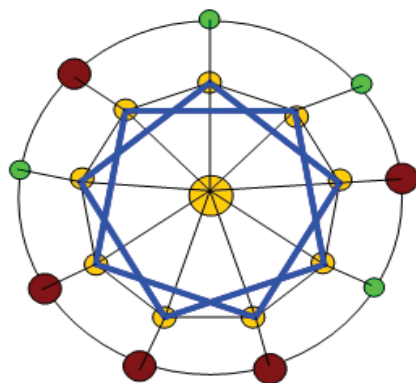


In this cluster, one skeletal element will be at the nucleus surrounded by 9 other skeletal elements.

In this case,  $L = \text{PPh}_3$  and  $R = \text{C}_6\text{F}_5$

$[\text{M}1], S = 4n+2, K=2n-1 = 2(1)-1 = 1$

$K = 28(10)$



LIGAND DISTRIBUTION

PERIPHERY:

$KL = 9[3.5]-9(2.5) = 9$

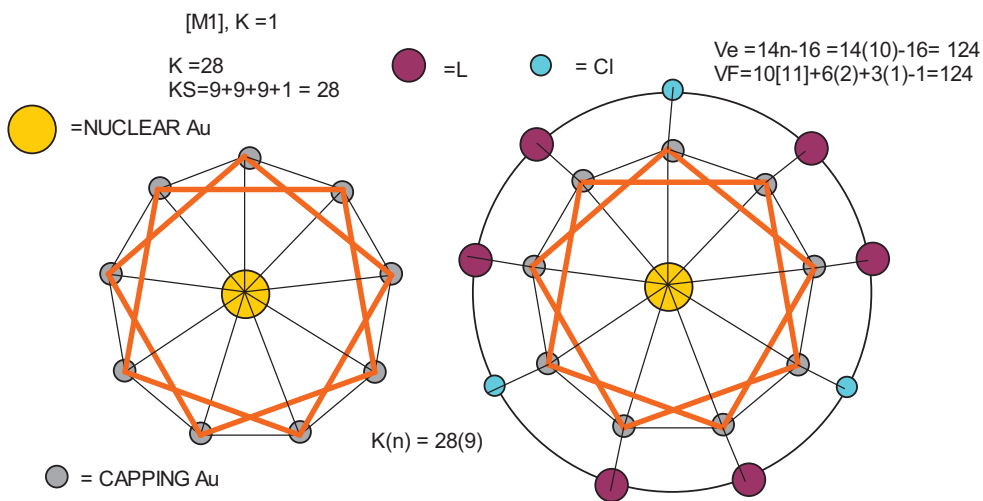
NUCLEUS:

$KN = 3.5-9(0.5)-1 = 3.5-5.5 = -2$

TOTAL =  $KL+KN = 9-2 = 7$

THIS MEANS THAT THE CLUSTER WILL ACCOMMODATE 7 TWO ELECTRON DONOR LIGANDS. WHAT WE HAVE ON THE CLUSTER =  $5L+4R = 5L + 2L = 7L$  SINCE  $2R = 1L$ . THUS THE LIGAND DISTRIBUTION FOLLOWS A SIMPLE MATHEMATICAL PRECISION.

N103  $Au_{10}Cl_3L_6^+ : K = 10[3.5] - 1.5 \cdot 6 + 0.5 = 28; K(n) = 28(9), S = 4n - 16, Kp = C^9C[M1]$   
 $Au(K=3.5, V=7), Cl(K=-0.5), L(K=-1), (+1)(K=0.5)$



$KL = 10[3.5] + 0.5 \cdot 9 - 9[2.5] - 9[0.5] - 1 = 7.5$   
 THERE ARE 7.5 LINKAGES AVAILABLE FOR 7.5 LIGANDS = 6L + 3Cl

LIGAND DISTRIBUTION

PERIPHERY:

$KP = 9[3.5] - 9(2.5) = 9$

NUCLEUS:

$KN = 3.5 + 1(0.5) - 9(0.5) - 1 = -1.5$

TOTAL =  $KP + KN = 9 - 1.5 = 7.5$

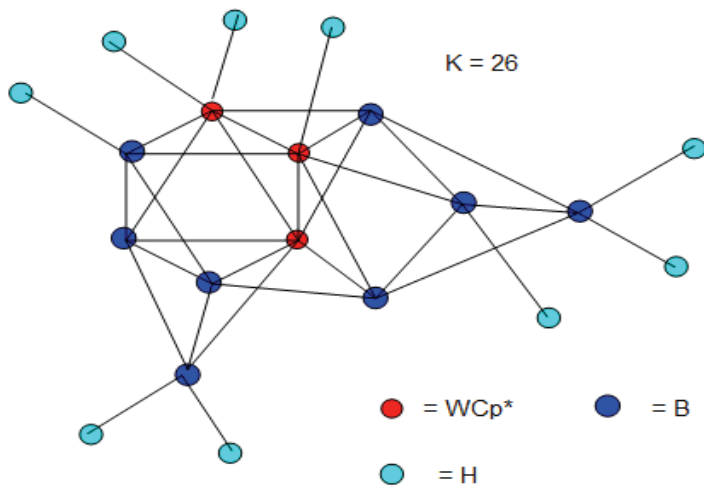
THIS MEANS THAT THE CLUSTER CAN ACCOMMODATE 7.5 TWO ELECTRON DONOR LIGANDS.

LIGANDS ON THE CLUSTER =  $6L + 3Cl = 6L + 1.5L = 7.5L$ , SINCE  $L = 2Cl$ .

N111  $(Cp^*W)_3B_8H_9 : K = 3[6 - 2.5] - 8[2.5] - 4.5 = 26, n = 3 + 8 = 11, K(n) = 26(11), S = 4n - 8, Kp = C^5C[6]$   
 Ideal shape is Penta-capped  $O_h$ .  
 $Ve = 4n - 8 + 3[10]$  for metal adjustment =  $4(11) - 8 + 30 = 66; VF = 3[5 + 6] + 8(3) + 9 = 66$

$WCp^* K=3.5, V=7 \quad B, K=2.5, V=5$

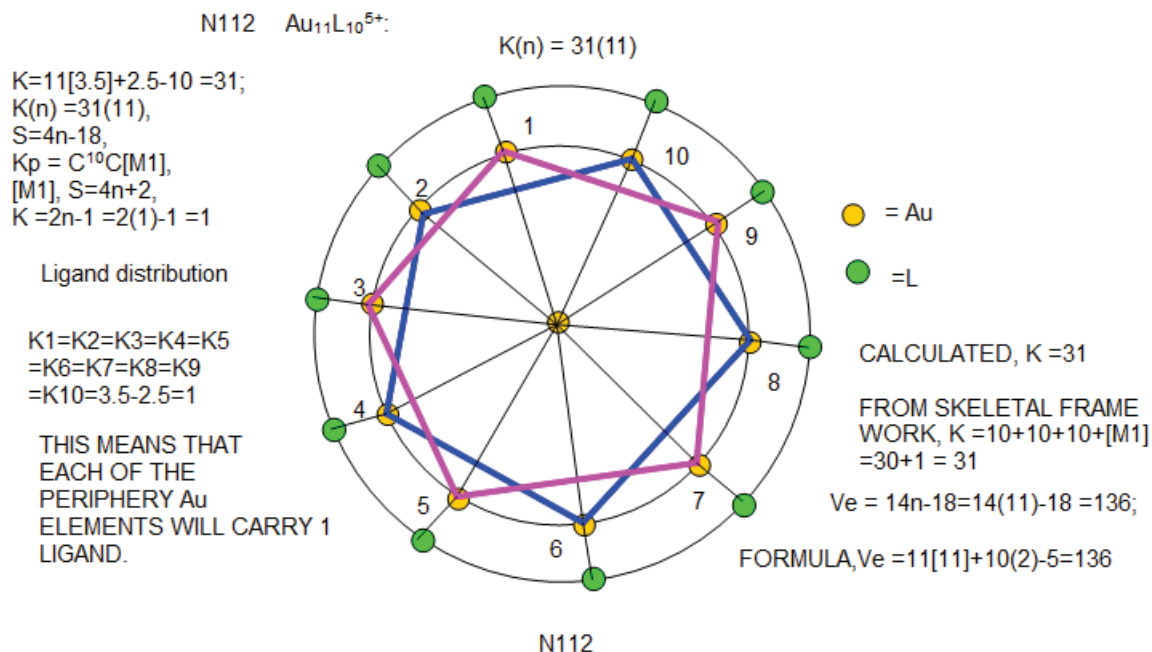
Ligand distribution has been done according to the law of the valence of the skeletal fragments in N111



Raw isomeric skeletal structure of  $(Cp^*W)_3B_8H_9$

N111





FROM THE SYMBOL  $K_p = C^{10}C[M1]$ , MEANS THAT THERE IS ONE SKELETAL ELEMENT AT THE NUCLEUS SURROUNDED BY 10 OTHER SKELETAL ELEMENTS.

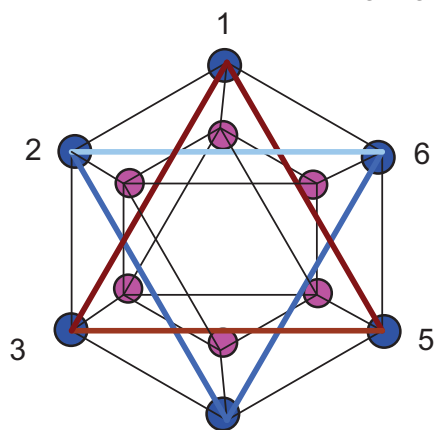
N121, N121 Cluster with a nucleus model



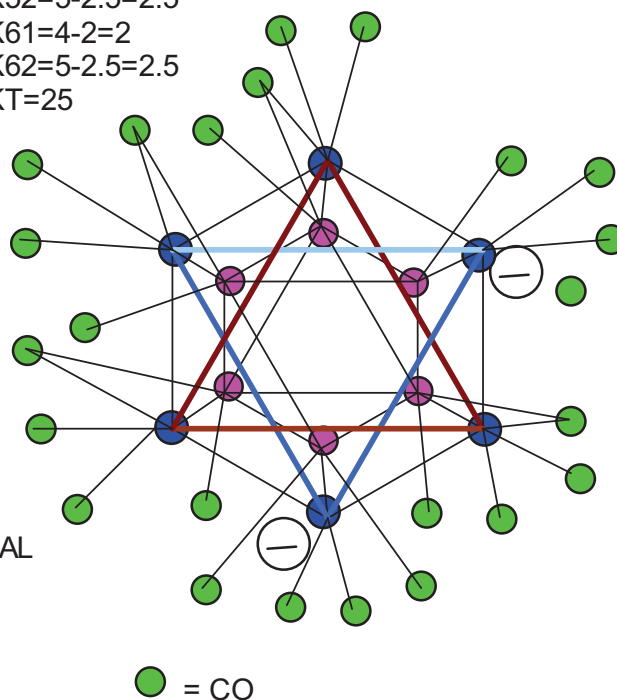
$K11=4-2.5=1.5$   
 $K12=5-2.5=2.5$   
 $K21=4-2.5=1.5$   
 $K22=5-2.5=2.5$

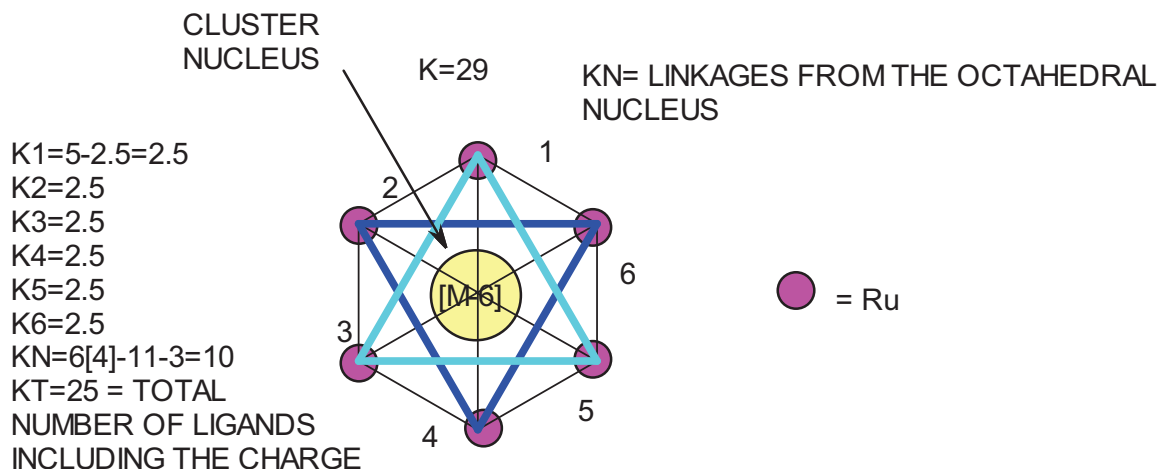
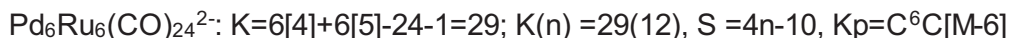
$K31=4-2.5=1.5$   
 $K32=5-2.5=2.5$   
 $K41=4-2=2$   
 $K42=5-2.5=2.5$

$K51=4-2.5=1.5$   
 $K52=5-2.5=2.5$   
 $K61=4-2=2$   
 $K62=5-2.5=2.5$   
 $KT=25$



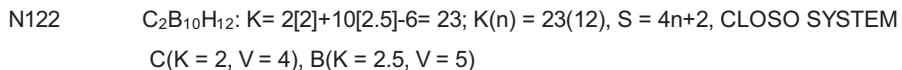
ISOMERIC SKELETAL STRUCTURES



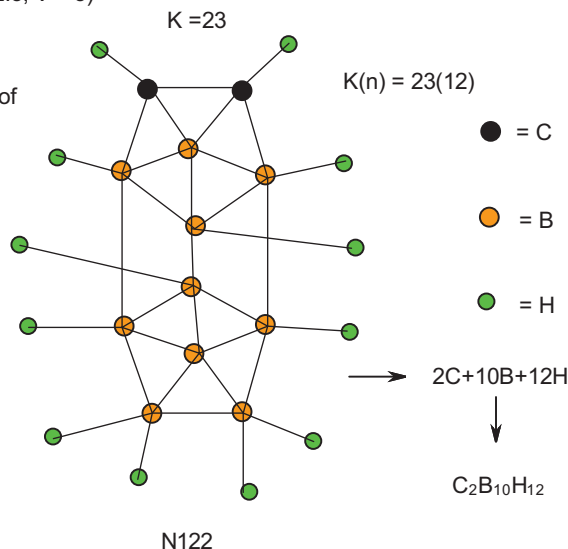


NUMBER OF LINKAGES FROM CLUSTER =  $6+6+6+11 = 29$

THE CLUSTER HAS AN OCTAHEDRAL NUCLEUS CAPPED BY 6 OTHER SKELETAL ELEMENTS. IT IS ASSUMED THAT THE ELEMENTS IN THE NUCLEUS ARE ALL Pd.



Ligand distribution  
 The ligands are added to the skeletal elements in such a way that the valence of each of the skeletal element is obeyed. Thus, the carbon element has a valence of 4, so it will have 4 connections to it including the H atoms. In the case of the B atom, there will be 5 connections to it including those from the H ligands if necessary. The valence rule of the skeletal element should be observed. When this is done correctly, the cluster formula derived from the sketch is usually in agreement with the original cluster formula. It is clear from N122 sketch that we have 2C, 10B and 12H corresponding to  $\text{C}_2\text{B}_{10}\text{H}_{12}$  cluster formula.

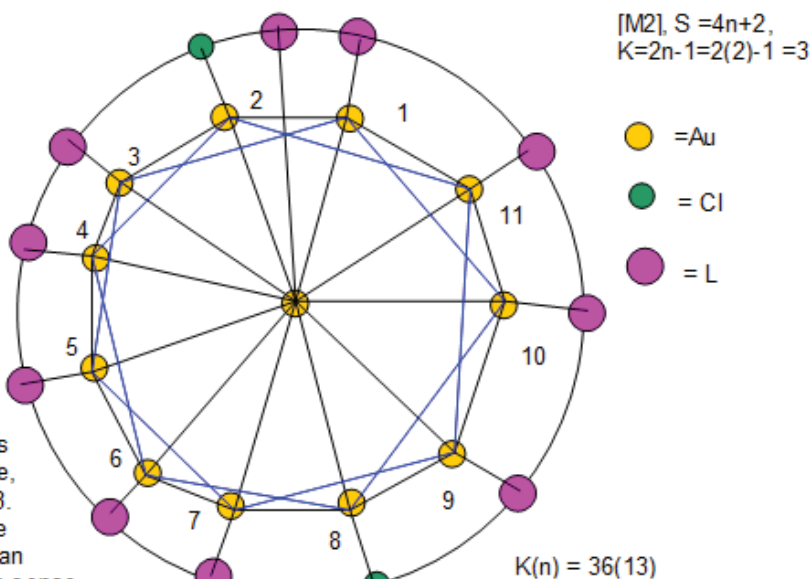


RAW ISOMERIC SKELETAL STRUCTURE OF  $\text{C}_2\text{B}_{10}\text{H}_{12}$

N131  $Au_{13}Cl_2L_{10}^{3+}$ :  $K = 13[3.5] + 3[0.5] - 2[0.5 - 10[1]] = 36$ ;  $K(n) = 36(13)$ ,  $S = 4n - 20$ ,  $K_p = C^{11}C[M2]$

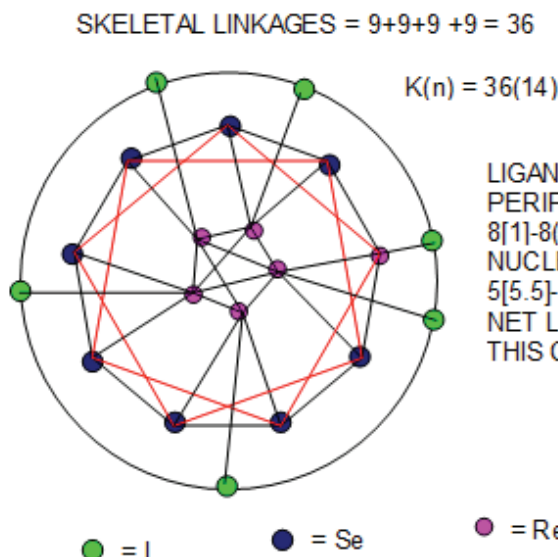
Available ligand linkages:  
**PERIPHERY**  
 There are 11 skeletal elements on the periphery each with  $K = 3.5$ . Also each skeletal element has 5 skeletal linkages each providing 1e. Hence, ligand available to each =  $1[3.5] - 5(0.5) = 1$ . In total there will  $11(1) = 11$  ligands.

**NUCLEUS**  
 [M2] means there are two skeletal elements at the nucleus which obey the closo series rule,  $S = 4n + 2$ ,  $K = 2n - 1 = 2(2) - 1 = 3$ . It was assumed that each of the periphery skeletal element has an oxidation state of zero. It makes sense to assign +3 to the two nuclear skeletal elements. Hence we may regard the nucleus to comprise of  $Au_2^{3+}$  fragment. This fragment has 11 single electron linkages in addition to the nuclear triple bond. Therefore the ligand linkages available at the nucleus =  $2[3.5] + 3(0.5) - 11(0.5) - 3 = 0$ . This predicts that there will be 2 nuclear skeletal elements which do not bear ligands. Only 11 ligands will be available to the periphery skeletal elements. This corresponds to 10 L + 2Cl ligands of the cluster. The 2Cl ligands are regarded as 1 electron donor while L is a 2 electron donor.



$Ve = 14n - 20 = 14(13) - 20 = 162$   
 $VF = 13[11] + 2[1] + 10[2] - 3 = 162$

N141  $Re_6Se_8I_6^{4-}$   $K = 6[5.5] + 8[8] - 3 - 2 = 36$ ,  $K(n) = 36(14)$ ,  $S = 4n - 16$ ,  $K_p = C^9C[M5]$



LIGAND LINKAGES  
**PERIPHERY:**  
 $8[1] - 8(2.5) + 1[5.5] - 1(2.5) = -9$   
**NUCLEAR LINKAGES:**  
 $5[5.5] - 9(0.5) - 4(0.5) - 9 = 12$   
**NET LIGAND LINKAGES =  $12 - 9 = 3$ ;**  
 THIS CORRESPONDS TO 6 IODINE LIGANDS.

9(5)  
 |  
 12(6)  
 |  
 15(7)  
 |  
 18(8)  
 |  
 21(9)  
 |  
 24(10)  
 |  
 27(11)  
 |  
 30(12)  
 |  
 33(13)  
 |  
 36(14)

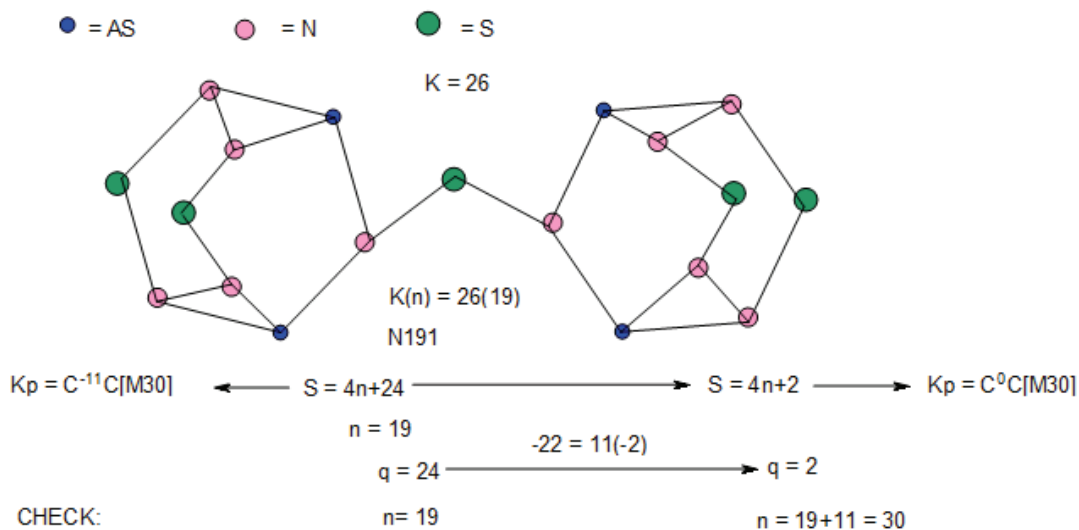
N141

**ISOMERIC STRUCTURAL GRAPH OF  $Re_6Se_8I_6^{4-}$**

Let us consider another cluster G3-  $Re_6Se_8I_6^{4-}$ :  $K = 6[5.5] + 8[1] - 6(0.5) - 4(0.5) = 36$ ;  $n = 14$ ,  $K(n) = 36(14)$ ,  $K = 2n - \frac{1}{2}q$ ,  $36 = 2(14) - \frac{1}{2}q$ ,  $q = -16$ ,  $S = 4n - 16$ ,  $K_p = C^9C[M5]$ . According to series, the cluster has a trigonal bipyramid nucleus surrounded by 9 capping skeletal elements. If we assume that the [M5] comprises of Re skeletal elements then 8 Se and

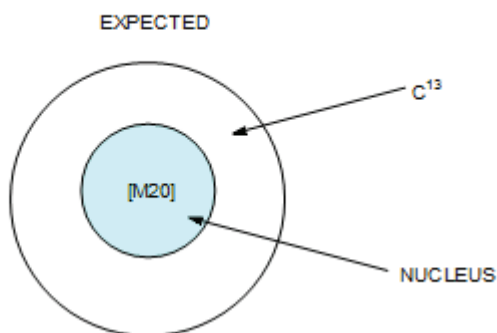
1 Re will be the capping elements. The  $C^9$  means there 9 cappings =  $9(3) = 27$  linkages. The [M5] nucleus has  $K = 2n-1 = 2(5)-1 = 9$  linkages. This gives us a grand total of  $27+9 = 36$  linkages. This is shown in sketch N141. Along with N141 is a calculation showing the net linkages available are 3. This means that the number of 2 electron donor ligands available are 3 or 6 single electron donor ligands. This agrees with the presence of 6 iodine ligands. What about the flow of  $K(n)$  numbers for [M5] series? For [M5] we have  $9(5) \rightarrow 12(6) \rightarrow 15(7) \rightarrow 18(8) \rightarrow 21(9) \rightarrow 24(10) \rightarrow 27(11) \rightarrow 30(12) \rightarrow 33(13) \rightarrow 36(14)$ . Clearly,  $36(14)$  is a member of [M5] series. What is observed for N141 is an octahedral cluster with 8 capping Se skeletal elements and 6 iodine ligands one on each Re skeletal elements in an octahedral nucleus (Fehlner & Halet, 2007). The graph of the cluster is sketched in N141. The construction of isomeric skeletal structures of clusters is in accordance with the  $4n$  series method and may be regarded to constitute the graph theory of the series approach.

N191  $N_{10}As_4S_5$ :  $K = 10[1.5]+4[1.5]+5[1] = 26$ ,  $n = 10+4+5 = 19$ ;  $K(n) = 26(19)$ ,  $S = 4n+24$ ,  $K = 2n-12=2(19)-12 = 26$   
 $Ve = 4n+24 = 4(19)+24 = 100$ ;  $VF = 10[5]+4[5]+5[6] = 100$



[M30],  $S = 4n+2$ ,  $K = 2n-1 = 2(30)-1 = 59$ ,  $K(n) = 59(30)$   
 $59(30), 56(29), 53(28), 50(27), 47(26), 44(25), 41(24), 38(23), 35(22), 32(21), 29(20), 26(19)$

N331  $N_{11}As_2S_1^{2-}$ :  $K = 12[4]+21[1.5]-1.5 = 78$ ;  $n = 12+21 = 33$ ,  $K(n) = 78(33)$ ;  $S = 4n-24$ ,  $K_p = C^{13}C[M20]$

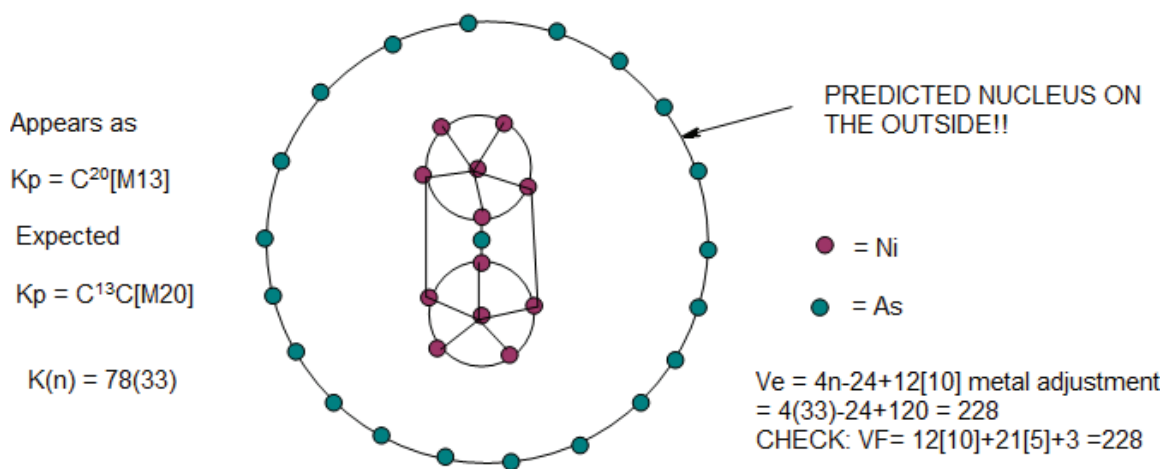


N331

$Ni_{12}As_{21}^{3-}$ :  $K = 12[4]+21[1.5]-1.5 = 78$ ;  $n = 12+21 = 33$ ,  $K(n) = 78(33)$ ;  $S = 4n-24$ ,  $Kp = C^{13}C[M20]$

This predicts a cluster of a nucleus comprising of 20 skeletal elements surrounded by 13 capping skeletal elements. THIS RESULT IS VERY FASCINATING INDEED. THIS IS BECAUSE THE 20 PREDICTED NUCLEAR ELEMENTS ARE ACTUALLY LOCATED ON THE OUTER LAYER COMPRISING OF As SKELETAL ELEMENTS AND THE 13 CAPPING ELEMENTS COMPRIZING OF 12 Ni INNER LAYER AND 1 As SITTING IN THE NUCLEUS. WHILE THE PREDICTION IS QUITE AMAZING, THE NATURAL FORCES HAVE DONE THE OPPOSITE..

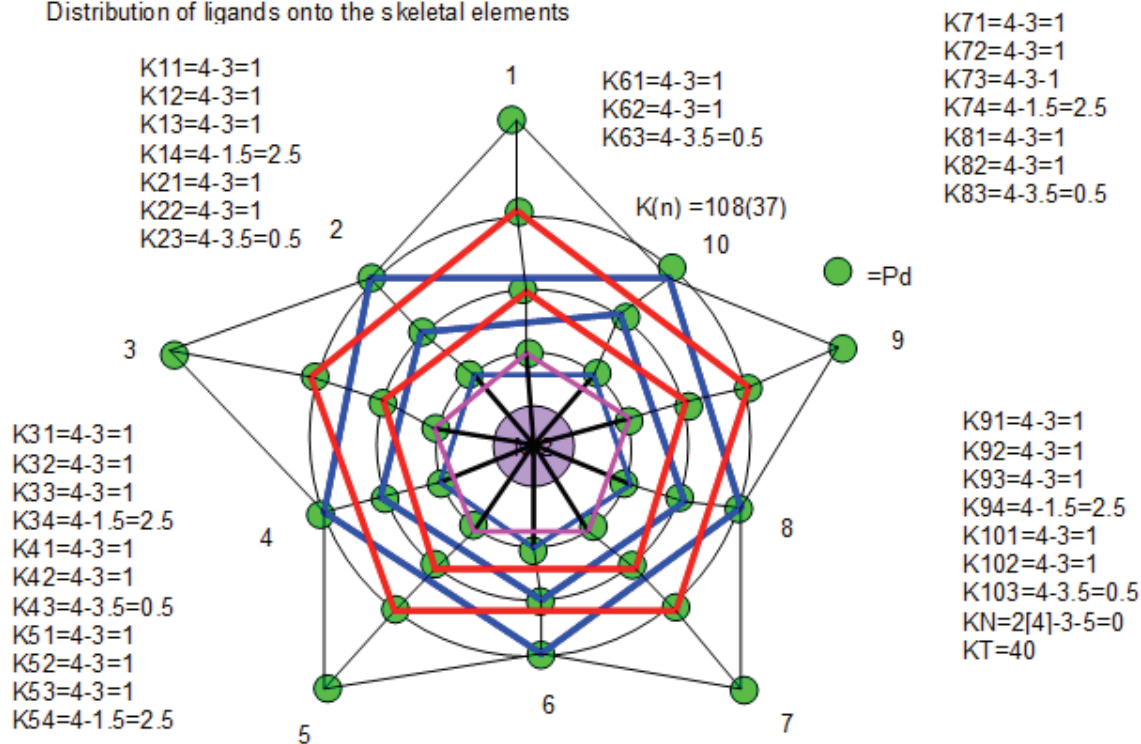
The observed skeletal structure can graphically be represented as indicated in FIGURE LG-1.



Graphical sketch of observed structure of  $Ni_{12}As_{21}^{3-}$

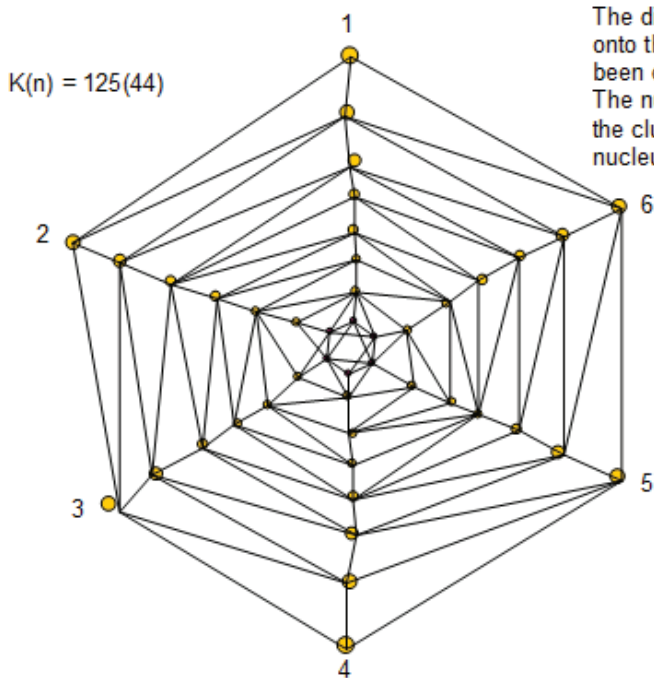
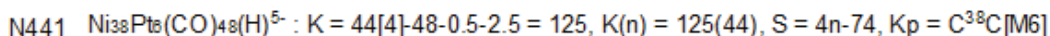
N37  $Pd_{37}(CO)_{28}L_{12}$ :  $K = 37[4]-28-12=108$ ;  $K(n) = 108(37)$ ,  $S = 4n-68$ ,  $Kp=C^{35}C[M-2]$

Distribution of ligands onto the skeletal elements



$K=108$ ; STRUCTURE,  $K=[M-2]+30+30+30+15 = 3+90+15=108$

According to the series method, the cluster  $Pd_{37}(CO)_{28}L_{12}$ ,  $K(n) = 108(37)$ ,  $S = 4n - 68$ ,  $K_p = C^{35}C[M2]$  reported in literature (Mednikov and Dahl, 2010) has central nucleus comprising of 2 skeletal elements with 35 capping skeletal elements based on series method.

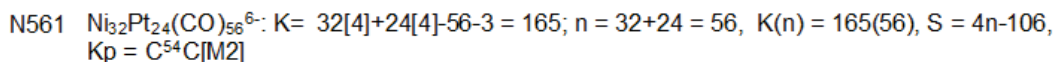


The distribution of the ligands onto the skeletal elements have been calculated and indicated numerically. The numbering of the cluster corners begin from the octahedral nucleus.

For example, k11 is at the nucleus while k18 is at the periphery. When the calculation is done correctly, the total numerical value should correspond to the total number of ligands on the cluster. All the connections to a skeletal point should be regarded as a single electron donor.

N441

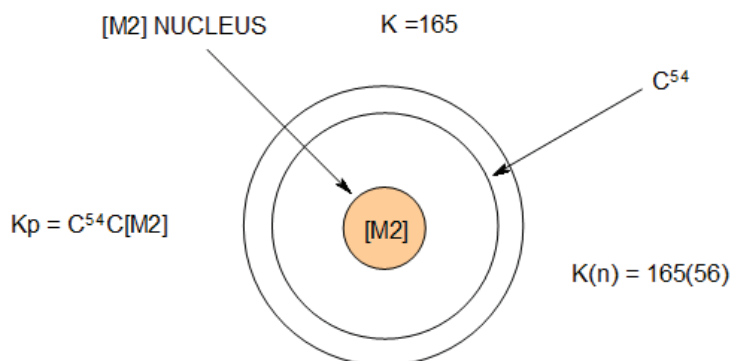
$K_{11} = 4 - 2.5 = 1.5$ , $k_{12} = 4 - 4 = 0$ <sup>↙</sup> $K_{13} = 4 - 2.5 = 1.5$ , $k_{14} = 4 - 3 = 1$ <sup>↙</sup> $K_{15} = 4 - 2.5 = 1.5$ , $k_{16} = 4 - 3 = 1$ <sup>↙</sup> $K_{17} = 4 - 3 = 1$ , $k_{18} = 4 - 1.5 = 2.5$ <sup>↙</sup> $K_{21} = 4 - 3 = 1$ , $k_{22} = 4 - 2 = 2$ <sup>↙</sup> $K_{23} = 4 - 3.5 = 0.5$ , $k_{24} = 4 - 3 = 1$ <sup>↙</sup> $K_{25} = 4 - 3.5 = 0.5$ , $k_{26} = 4 - 3 = 1$ <sup>↙</sup> $K_{27} = 4 - 2 = 2$ <sup>↙</sup> <b>TOTAL · 18</b> <sup>↙</sup>	$K_{31} = 4 - 3.5 = 0.5$ , $k_{32} = 4 - 2.5 = 1.5$ <sup>↙</sup> $K_{33} = 4 - 3 = 1$ , $k_{34} = 4 - 3 = 1$ <sup>↙</sup> $K_{35} = 4 - 3 = 1$ , $k_{36} = 4 - 3 = 1$ <sup>↙</sup> $k_{37} = 4 - 2.5 = 1.5$ <sup>↙</sup> $k_{41} = 4 - 2 = 2$ , $k_{42} = 4 - 3.5 = 0.5$ <sup>↙</sup> $k_{43} = 4 - 3 = 1$ , $k_{44} = 4 - 2.5 = 1.5$ <sup>↙</sup> $k_{45} = 4 - 3.5 = 0.5$ , $k_{46} = 4 - 3 = 1$ <sup>↙</sup> $k_{47} = 4 - 2.5 = 1.5$ , $k_{48} = 4 - 1.5 = 2.5$ <sup>↙</sup> <b>TOTAL · 18</b> <sup>↙</sup>	$K_{51} = 4 - 3.5 = 0.5$ , $k_{52} = 4 - 2.5 = 1.5$ <sup>↙</sup> $K_{53} = 4 - 2.5 = 1.5$ , $k_{54} = 4 - 4 = 0$ <sup>↙</sup> $K_{55} = 4 - 2.5 = 1.5$ , $k_{56} = 4 - 3 = 1$ <sup>↙</sup> $K_{57} = 4 - 2.5 = 1.5$ <sup>↙</sup> $K_{61} = 4 - 3 = 1$ , $k_{62} = 4 - 3 = 1$ <sup>↙</sup> $K_{63} = 4 - 3.5 = 0.5$ , $k_{64} = 4 - 2.5 = 1.5$ <sup>↙</sup> $K_{65} = 4 - 3 = 1$ , $k_{66} = 4 - 3 = 1$ <sup>↙</sup> $K_{67} = 4 - 2.5 = 1.5$ <sup>↙</sup> <b>TOTAL · 15</b> <sup>↙</sup> <b>GRAND TOTAL 51</b> <sup>↙</sup>
---	---	--



The capping symbol means that the cluster has 2 skeletal elements in the nucleus which belongs to CLOSO SERIES and is surrounded by 54 skeletal elements. It has been found that the capping for VERTICAL SERIES starts with the formation of a closo nucleus.

Cluster valence electrons are given by the series formula of transition metal clusters:  
 $\text{Ve} = 14n - 106 = 14(56) - 106 = 678$ ;  $\text{VF} = 32[10] + 24[10] + 56(2) + 6 = 678$

Using the broad cluster categorization, the cluster belongs to GROUP [M2] OF THE VERTICAL SERIES.



### 3.8 Numerical Periodic Table of Chemical Clusters

The examples of clusters given above cover a range of nuclearity index 1-56. By deriving the  $K(n)$  values of many clusters and carefully studying their relationship an interesting pattern was discerned. Firstly, the  $K(n)$  values of clusters covered an infinite range of  $4n$  series. That is,  $S = 4n + q$  [ $q = 2, 4, 6, 8, 10, 12, \dots$  (un-capping series);  $q = 0, -2, -4, -6, -8, -10, -12, \dots$  (capping series)]. This aspect has been illustrated in Table 1. In addition, a grid map shown in Table 2 was obtained. The  $K(n)$  values of the clusters derived from the  $4n$  series when carefully analyzed, are found to form an interesting series. A selected range of  $K(n)$  values from [M-10] through [M0] to [M14] are given in Table 2. This arrangement is similar to the usual X-axis of  $x = -10$  to  $x = +10$ . This array of  $K(n)$  values was discovered in earlier work (Kiremire, 2017a) but it is being re-introduced for the purpose of categorizing a vast range of capping chemical clusters.

The horizontal rows show the clusters arranged according to  $S = 4n + q$  where  $q$  is the same while the vertical columns indicate the cluster determinant  $q$  varies by  $\pm 2$ . Table 2 appears seemingly complex, but on close observation, it actually commences with one  $K(n)$  value. This is demonstrated in Scheme SC-4. Starting with point A of  $K(n) = 11(6)$ , the vertical movement upwards involves stepwise changes in  $K$  value by 3 units; while downward movements involves a decrease of  $K$  by the same amount of 3 units stepwise. Thus, the vertical axis can be extended in both directions indefinitely. Hence, new points B, C, D and E in scheme SC-4 are derived from A. Likewise, each of the points B, C, D and E can be handled in the same manner as a resulting in a seemingly complex cluster GRID MAP shown in Table 2. In a way, Table 2 is similar to an array of coordinates of a point  $P(x, y)$  except in this case we have the  $K(n)$  VALUES where  $K$  represents the number of cluster linkages corresponding to  $x$  value of the X-axis and  $n$  which represents the number of skeletal elements in a cluster corresponding to the  $y$  value of the Y axis in the Cartesian coordinate system. Thus, we have the correlation relationship  $P(x, y) \rightarrow (K, n)$  but expressed as  $K(n)$ . The base line has been chosen to correspond to the values of the horizontal clososeries,  $S = 4n + 2$ .

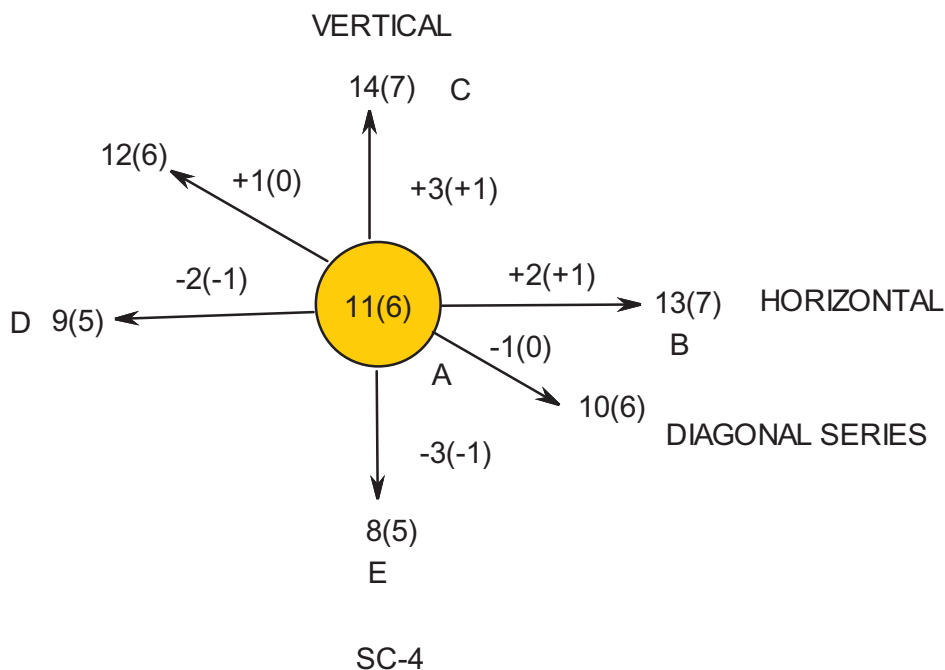


Table 2. The Grid Map of K(n) Series

TABLE 2A											
T-2 A	[M-10]	[M-9]	[M-8]	[M-7]	[M-6]	[M-5]	[M-4]	[M-3]	[M-2]	[M-1]	[M0]
4n-124	168(53)	170(54)	172(55)	174(56)	176(57)	178(58)	180(59)	182(60)	184(61)	186(62)	188(63)
4n-122	165(52)	167(53)	169(54)	171(55)	173(56)	175(57)	177(58)	179(59)	181(60)	183(61)	185(62)
4n-120	162(51)	164(52)	166(53)	168(54)	170(55)	172(56)	174(57)	176(58)	178(59)	180(60)	182(61)
4n-118	159(50)	161(51)	163(52)	165(53)	167(54)	169(55)	171(56)	173(57)	175(58)	177(59)	179(60)
4n-116	156(49)	158(50)	160(51)	162(52)	164(53)	166(54)	168(55)	170(56)	172(57)	174(58)	176(59)
4n-114	153(48)	155(49)	157(50)	159(51)	161(52)	163(53)	165(54)	167(55)	169(56)	171(57)	173(58)
4n-112	150(47)	152(48)	154(49)	156(50)	158(51)	160(52)	162(53)	164(54)	166(55)	168(56)	170(57)
4n-110	147(46)	149(47)	151(48)	153(49)	155(50)	157(51)	159(52)	161(53)	163(54)	165(55)	167(56)
4n-108	144(45)	146(46)	148(47)	150(48)	152(49)	154(50)	156(51)	158(52)	160(53)	162(54)	164(55)
4n-106	141(44)	143(45)	145(46)	147(47)	149(48)	151(49)	153(50)	155(51)	157(52)	159(53)	161(54)
4n-104	138(43)	140(44)	142(45)	144(46)	146(47)	148(48)	150(49)	152(50)	154(51)	156(52)	158(53)
4n-102	135(42)	137(43)	139(44)	141(45)	143(46)	145(47)	147(48)	149(49)	151(50)	153(51)	155(52)
4n-100	132(41)	134(42)	136(43)	138(44)	140(45)	142(46)	144(47)	146(48)	148(49)	150(50)	152(51)
4n-98	129(40)	131(41)	133(42)	135(43)	137(44)	139(45)	141(46)	143(47)	145(48)	147(49)	149(50)
4n-96	126(39)	128(40)	130(41)	132(42)	134(43)	136(44)	138(45)	140(46)	142(47)	144(48)	146(49)
4n-94	123(38)	125(39)	127(40)	129(41)	131(42)	133(43)	135(44)	137(45)	139(46)	141(47)	143(48)
4n-92	120(37)	122(38)	124(39)	126(40)	128(41)	130(42)	132(43)	134(44)	136(45)	138(46)	140(47)
4n-90	117(36)	119(37)	121(38)	123(39)	125(40)	127(41)	129(42)	131(43)	133(44)	135(45)	137(46)
4n-88	114(35)	116(36)	118(37)	120(38)	122(39)	124(40)	126(41)	128(42)	130(43)	132(44)	134(45)
4n-86	111(34)	113(35)	115(36)	117(37)	119(38)	121(39)	123(40)	125(41)	127(42)	129(43)	131(44)
4n-84	108(33)	110(34)	112(35)	114(36)	116(37)	118(38)	120(39)	122(40)	124(41)	126(42)	128(43)
4n-82	105(32)	107(33)	109(34)	111(35)	113(36)	115(37)	117(38)	119(39)	121(40)	123(41)	125(42)
4n-80	102(31)	104(32)	106(33)	108(34)	110(35)	112(36)	114(37)	116(38)	118(39)	120(40)	122(41)
4n-78	99(30)	101(31)	103(32)	105(33)	107(34)	109(35)	111(36)	113(37)	115(38)	117(39)	119(40)
4n-76	96(29)	98(30)	100(31)	102(32)	104(33)	106(34)	108(35)	110(36)	112(37)	114(38)	116(39)
4n-74	93(28)	95(29)	97(30)	99(31)	101(32)	103(33)	105(34)	107(35)	109(36)	111(37)	113(38)
4n-72	90(27)	92(28)	94(29)	96(30)	98(31)	100(32)	102(33)	104(34)	106(35)	108(36)	110(37)
4n-70	87(26)	89(27)	91(28)	93(29)	95(30)	97(31)	99(32)	101(33)	103(34)	105(35)	107(36)
4n-68	84(25)	86(26)	88(27)	90(28)	92(29)	94(30)	96(31)	98(32)	100(33)	102(34)	104(35)
4n-66	81(24)	83(25)	85(26)	87(27)	89(28)	91(29)	93(30)	95(31)	97(32)	99(33)	101(34)
	[M-10]	[M-9]	[M-8]	[M-7]	[M-6]	[M-5]	[M-4]	[M-3]	[M-2]	[M-1]	[M0]
4n-64	78(23)	80(24)	82(25)	84(26)	86(27)	88(28)	90(29)	92(30)	94(31)	96(32)	98(33)
4n-62	75(22)	77(23)	79(24)	81(25)	83(26)	85(27)	87(28)	89(29)	91(30)	93(31)	95(32)
4n-60	72(21)	74(22)	76(23)	78(24)	80(25)	82(26)	84(27)	86(28)	88(29)	90(30)	92(31)
4n-58	69(20)	71(21)	73(22)	75(23)	77(24)	79(25)	81(26)	83(27)	85(28)	87(29)	89(30)



4n-56	66(19)	68(20)	70(21)	72(22)	74(23)	76(24)	78(25)	80(26)	82(27)	84(28)	86(29)
4n-54	63(18)	65(19)	67(20)	69(21)	71(22)	73(23)	75(24)	77(25)	79(26)	81(27)	83(28)
4n-52	60(17)	62(18)	64(19)	66(20)	68(21)	70(22)	72(23)	74(24)	76(25)	78(26)	80(27)
4n-50	57(16)	59(17)	61(18)	63(19)	65(20)	67(21)	69(22)	71(23)	73(24)	75(25)	77(26)
4n-48	54(15)	56(16)	58(17)	60(18)	62(19)	64(20)	66(21)	68(22)	70(23)	72(24)	74(25)
4n-46	51(14)	53(15)	55(16)	57(17)	59(18)	61(19)	63(20)	65(21)	67(22)	69(23)	71(24)
4n-44	48(13)	50(14)	52(15)	54(16)	56(17)	58(18)	60(19)	62(20)	64(21)	66(22)	68(23)
4n-42	45(12)	47(13)	49(14)	51(15)	53(16)	55(17)	57(18)	59(19)	61(20)	63(21)	65(22)
4n-40	42(11)	44(12)	46(13)	48(14)	50(15)	52(16)	54(17)	56(18)	58(19)	60(20)	62(21)
4n-38	39(10)	41(11)	43(12)	45(13)	47(14)	49(15)	51(16)	53(17)	55(18)	57(19)	59(20)
4n-36	36(9)	38(10)	40(11)	42(12)	44(13)	46(14)	48(15)	50(16)	52(17)	54(18)	56(19)
4n-34	33(8)	35(9)	37(10)	39(11)	41(12)	43(13)	45(14)	47(15)	49(16)	51(17)	53(18)
4n-32	30(7)	32(8)	34(9)	36(10)	38(11)	40(12)	42(13)	44(14)	46(15)	48(16)	50(17)
4n-30	27(6)	29(7)	31(8)	33(9)	35(10)	37(11)	39(12)	41(13)	43(14)	45(15)	47(16)
4n-28	24(5)	26(6)	28(7)	30(8)	32(9)	34(10)	36(11)	38(12)	40(13)	42(14)	44(15)
4n-26	21(4)	23(5)	25(6)	27(7)	29(8)	31(9)	33(10)	35(11)	37(12)	39(13)	41(14)
4n-24	18(3)	20(4)	22(5)	24(6)	26(7)	28(8)	30(9)	32(10)	34(11)	36(12)	38(13)
4n-22	15(2)	17(3)	19(4)	21(5)	23(6)	25(7)	27(8)	29(9)	31(10)	33(11)	35(12)
4n-20	12(1)	14(2)	16(3)	18(4)	20(5)	22(6)	24(7)	26(8)	28(9)	30(10)	32(11)
4n-18	9(0)	11(1)	13(2)	15(3)	17(4)	19(5)	21(6)	23(7)	25(8)	27(9)	29(10)
4n-16	6(-1)	8(0)	10(1)	12(2)	14(3)	16(4)	18(5)	20(6)	22(7)	24(8)	26(9)
4n-14	3(-2)	5(-1)	7(0)	9(1)	11(2)	13(3)	15(4)	17(5)	19(6)	21(7)	23(8)
4n-12	0(-3)	2(-2)	4(-1)	6(0)	8(1)	10(2)	12(3)	14(4)	16(5)	18(6)	20(7)
4n-10	-3(-4)	-1(-3)	1(-2)	3(-1)	5(0)	7(1)	9(2)	11(3)	13(4)	15(5)	17(6)
4n-8	-6(-5)	-4(-4)	-2(-3)	0(-2)	2(-1)	4(0)	6(1)	8(2)	10(3)	12(4)	14(5)
4n-6	-9(-6)	-7(-5)	-5(-4)	-3(-3)	-1(-2)	1(-1)	3(0)	5(1)	7(2)	9(3)	11(4)
4n-4	-12(-7)	-10(-6)	-8(-5)	-6(-4)	-4(-3)	-2(-2)	0(-1)	2(0)	4(1)	6(2)	8(3)
4n-2	-15(-8)	-13(-7)	-11(-6)	-9(-5)	-7(-4)	-5(-3)	-3(-2)	-1(-1)	1(0)	3(1)	5(2)
4n+0	-18(-9)	-16(-8)	-14(-7)	-12(-6)	-10(-5)	-8(-4)	-6(-3)	-4(-2)	-2(-1)	0(0)	2(1)
4n+2	-21(-10)	-19(-9)	-17(-8)	-15(-7)	-13(-6)	-11(-5)	-9(-4)	-7(-3)	-5(-2)	-3(-1)	-1(0)
	[M-10]	[M-9]	[M-8]	[M-7]	[M-6]	[M-5]	[M-4]	[M-3]	[M-2]	[M-1]	[M0]

TABLE 2B												
T-2B	[M1]	[M2]	[M3]	[M4]	[M5]	[M6]	[M7]	[M8]	[M9]	[M10]	[M11]	[M12]
4n-114	175(59)	177(60)	179(61)	181(62)	<b>183(63)</b>	<b>185(64)</b>	187(65)	189(66)	191(67)	193(68)	195(69)	197(70)
4n-112	172(58)	174(59)	176(60)	178(61)	<b>180(62)</b>	<b>182(63)</b>	184(64)	186(65)	188(66)	190(67)	192(68)	194(69)
4n-110	169(57)	171(58)	173(59)	175(60)	<b>177(61)</b>	<b>179(62)</b>	181(63)	183(64)	185(65)	187(66)	189(67)	191(68)
4n-108	166(56)	168(57)	170(58)	172(59)	<b>174(60)</b>	<b>176(61)</b>	178(62)	180(63)	182(64)	184(65)	186(66)	188(67)
4n-106	163(55)	<b>165(56)</b>	167(57)	169(58)	<b>171(59)</b>	<b>173(60)</b>	175(61)	177(62)	179(63)	181(64)	183(65)	185(66)
4n-104	160(54)	162(55)	164(56)	166(57)	<b>168(58)</b>	<b>170(59)</b>	172(60)	174(61)	176(62)	178(63)	180(64)	182(65)
4n-102	157(53)	159(54)	161(55)	163(56)	<b>165(57)</b>	<b>167(58)</b>	169(59)	171(60)	173(61)	175(62)	177(63)	179(64)
4n-100	154(52)	156(53)	158(54)	160(55)	<b>162(56)</b>	<b>164(57)</b>	166(58)	168(59)	170(60)	172(61)	174(62)	176(63)
4n-98	151(51)	153(52)	155(53)	157(54)	<b>159(55)</b>	<b>161(56)</b>	163(57)	165(58)	167(59)	169(60)	171(61)	173(62)
4n-96	148(50)	150(51)	152(52)	154(53)	<b>156(54)</b>	<b>158(55)</b>	160(56)	162(57)	164(58)	166(59)	168(60)	170(61)
4n-94	145(49)	147(50)	149(51)	151(52)	<b>153(53)</b>	<b>155(54)</b>	157(55)	159(56)	161(57)	163(58)	165(59)	167(60)
4n-92	142(48)	144(49)	146(50)	148(51)	<b>150(52)</b>	<b>152(53)</b>	154(54)	156(55)	158(56)	160(57)	162(58)	164(59)
4n-90	139(47)	141(48)	143(49)	145(50)	<b>147(51)</b>	<b>149(52)</b>	151(53)	153(54)	155(55)	157(56)	159(57)	161(58)
4n-88	136(46)	138(47)	140(48)	142(49)	<b>144(50)</b>	<b>146(51)</b>	148(52)	150(53)	152(54)	154(55)	156(56)	158(57)
4n-86	133(45)	135(46)	137(47)	139(48)	<b>141(49)</b>	<b>143(50)</b>	145(51)	147(52)	149(53)	151(54)	153(55)	155(56)
4n-84	130(44)	132(45)	134(46)	136(47)	<b>138(48)</b>	<b>140(49)</b>	142(50)	144(51)	146(52)	148(53)	150(54)	152(55)
4n-82	127(43)	129(44)	131(45)	133(46)	<b>135(47)</b>	<b>137(48)</b>	139(49)	141(50)	143(51)	145(52)	147(53)	149(54)
4n-80	124(42)	126(43)	128(44)	130(45)	<b>132(46)</b>	<b>134(47)</b>	136(48)	138(49)	140(50)	142(51)	144(52)	146(53)
4n-78	121(41)	123(42)	125(43)	127(44)	<b>129(45)</b>	<b>131(46)</b>	133(47)	135(48)	137(49)	139(50)	141(51)	143(52)
4n-76	118(40)	120(41)	122(42)	124(43)	<b>126(44)</b>	<b>128(45)</b>	130(46)	132(47)	134(48)	136(49)	138(50)	140(51)
4n-74	115(39)	117(40)	119(41)	121(42)	<b>123(43)</b>	<b>125(44)</b>	127(45)	129(46)	131(47)	133(48)	135(49)	137(50)
4n-72	112(38)	114(39)	116(40)	118(41)	<b>120(42)</b>	<b>122(43)</b>	124(44)	126(45)	128(46)	130(47)	132(48)	134(49)
4n-70	109(37)	111(38)	113(39)	115(40)	<b>117(41)</b>	<b>119(42)</b>	121(43)	123(44)	125(45)	127(46)	129(47)	131(48)
	[M1]	[M2]	[M3]	[M4]	[M5]	[M6]	[M7]	[M8]	[M9]	[M10]	[M11]	[M12]
4n-68	106(36)	108(37)	110(38)	112(39)	<b>114(40)</b>	<b>116(41)</b>	118(42)	120(43)	122(44)	124(45)	126(46)	128(47)
4n-66	103(35)	105(36)	107(37)	<b>109(38)</b>	<b>111(39)</b>	<b>113(40)</b>	115(41)	117(42)	119(43)	121(44)	123(45)	125(46)
4n-64	100(34)	102(35)	104(36)	106(37)	<b>108(38)</b>	<b>110(39)</b>	112(40)	114(41)	116(42)	118(43)	120(44)	122(45)
4n-62	97(33)	99(34)	101(35)	103(36)	<b>105(37)</b>	<b>107(38)</b>	109(39)	111(40)	113(41)	115(42)	117(43)	119(44)
4n-60	94(32)	96(33)	98(34)	100(35)	<b>102(36)</b>	<b>104(37)</b>	106(38)	108(39)	110(40)	112(41)	114(42)	116(43)
4n-58	91(31)	93(32)	95(33)	97(34)	<b>99(35)</b>	<b>101(36)</b>	103(37)	105(38)	107(39)	109(40)	111(41)	113(42)

4n-56	88(30)	90(31)	92(32)	94(33)	<b>96(34)</b>	<b>98(35)</b>	100(36)	102(37)	104(38)	106(39)	108(40)	110(41)
4n-54	85(29)	87(30)	89(31)	91(32)	<b>93(33)</b>	<b>95(34)</b>	97(35)	99(36)	101(37)	103(38)	105(39)	107(40)
4n-52	82(28)	84(29)	86(30)	88(31)	<b>90(32)</b>	<b>92(33)</b>	94(34)	96(35)	98(36)	100(37)	102(38)	104(39)
4n-50	79(27)	81(28)	83(29)	85(30)	<b>87(31)</b>	<b>89(32)</b>	91(33)	93(34)	95(35)	97(36)	99(37)	101(38)
4n-48	76(26)	78(27)	80(28)	82(29)	<b>84(30)</b>	<b>86(31)</b>	88(32)	90(33)	92(34)	94(35)	96(36)	98(37)
4n-46	73(25)	75(26)	77(27)	79(28)	<b>81(29)</b>	<b>83(30)</b>	85(31)	87(32)	89(33)	91(34)	93(35)	95(36)
4n-44	70(24)	72(25)	74(26)	76(27)	<b>78(28)</b>	<b>80(29)</b>	82(30)	84(31)	86(32)	88(33)	90(34)	92(35)
4n-42	67(23)	69(24)	71(25)	73(26)	<b>75(27)</b>	<b>77(28)</b>	79(29)	81(30)	83(31)	85(32)	87(33)	89(34)
4n-40	64(22)	66(23)	68(24)	70(25)	<b>72(26)</b>	<b>74(27)</b>	76(28)	78(29)	80(30)	82(31)	84(32)	86(33)
4n-38	61(21)	63(22)	65(23)	67(24)	<b>69(25)</b>	<b>71(26)</b>	73(27)	75(28)	77(29)	79(30)	81(31)	83(32)
4n-36	58(20)	60(21)	62(22)	64(23)	<b>66(24)</b>	<b>68(25)</b>	70(26)	72(27)	74(28)	76(29)	78(30)	80(31)
4n-34	55(19)	57(20)	59(21)	61(22)	<b>63(23)</b>	<b>65(24)</b>	67(25)	69(26)	71(27)	73(28)	75(29)	77(30)
4n-32	52(18)	54(19)	56(20)	58(21)	<b>60(22)</b>	<b>62(23)</b>	64(24)	66(25)	68(26)	70(27)	72(28)	74(29)
4n-30	49(17)	51(18)	53(19)	55(20)	<b>57(21)</b>	<b>59(22)</b>	61(23)	63(24)	65(25)	67(26)	69(27)	71(28)
	<b>[M1]</b>	<b>[M2]</b>	<b>[M3]</b>	<b>[M4]</b>	<b>[M5]</b>	<b>[M6]</b>	<b>[M7]</b>	<b>[M8]</b>	<b>[M9]</b>	<b>[M10]</b>	<b>[M11]</b>	<b>[M12]</b>
4n-28	46(16)	48(17)	50(18)	52(19)	<b>54(20)</b>	<b>56(21)</b>	58(22)	60(23)	62(24)	64(25)	66(26)	68(27)
4n-26	43(15)	45(16)	47(17)	49(18)	<b>51(19)</b>	<b>53(20)</b>	55(21)	57(22)	59(23)	61(24)	63(25)	65(26)
4n-24	40(14)	42(15)	44(16)	46(17)	<b>48(18)</b>	<b>50(19)</b>	52(20)	54(21)	56(22)	58(23)	60(24)	62(25)
4n-22	37(13)	39(14)	41(15)	43(16)	<b>45(17)</b>	<b>47(18)</b>	49(19)	51(20)	53(21)	55(22)	57(23)	59(24)
4n-20	34(12)	36(13)	38(14)	40(15)	<b>42(16)</b>	<b>44(17)</b>	46(18)	48(19)	50(20)	52(21)	54(22)	56(23)
4n-18	31(11)	33(12)	35(13)	37(14)	<b>39(15)</b>	<b>41(16)</b>	43(17)	45(18)	47(19)	49(20)	51(21)	53(22)
4n-16	28(10)	30(11)	32(12)	34(13)	<b>36(14)</b>	<b>38(15)</b>	40(16)	42(17)	44(18)	46(19)	48(20)	50(21)
4n-14	25(9)	27(10)	29(11)	31(12)	<b>33(13)</b>	35(14)	37(15)	39(16)	41(17)	43(18)	45(19)	47(20)
	<b>[M1]</b>	<b>[M2]</b>	<b>[M3]</b>	<b>[M4]</b>	<b>[M5]</b>	<b>[M6]</b>	<b>[M7]</b>	<b>[M8]</b>	<b>[M9]</b>	<b>[M10]</b>	<b>[M11]</b>	<b>[M12]</b>
4n-12	22(8)	24(9)	26(10)	28(11)	<b>30(12)</b>	32(13)	34(14)	36(15)	38(16)	40(17)	42(18)	44(19)
4n-10	19(7)	21(8)	23(9)	25(10)	<b>27(11)</b>	29(12)	31(13)	33(14)	35(15)	37(16)	39(17)	41(18)
4n-8	<b>16(6)</b>	18(7)	20(8)	22(9)	<b>24(10)</b>	26(11)	28(12)	30(13)	32(14)	34(15)	36(16)	38(17)
4n-6	13(5)	<b>15(6)</b>	17(7)	19(8)	<b>21(9)</b>	23(10)	25(11)	27(12)	29(13)	31(14)	33(15)	35(16)
4n-4	10(4)	12(5)	<b>14(6)</b>	16(7)	<b>18(8)</b>	20(9)	22(10)	24(11)	26(12)	28(13)	30(14)	32(15)
4n-2	7(3)	9(4)	11(5)	<b>13(6)</b>	<b>15(7)</b>	17(8)	19(9)	21(10)	23(11)	25(12)	27(13)	29(14)
4n+0	4(2)	6(3)	8(4)	10(5)	<b>12(6)</b>	14(7)	16(8)	18(9)	20(10)	22(11)	24(12)	26(13)

TABLE 2C												
RUDOLPH SYSTEM: BORANES AND RELATIVES												
T-2C	[M1]	[M2]	[M3]	[M4]	[M5]	[M6]	[M7]	[M8]	[M9]	[M10]	[M11]	[M12]
4n+2	<b>1(1)</b>	<b>3(2)</b>	<b>5(3)</b>	<b>7(4)</b>	<b>9(5)</b>	<b>11(6)</b>	<b>13(7)</b>	<b>15(8)</b>	<b>17(9)</b>	<b>19(10)</b>	<b>21(11)</b>	<b>23(12)</b>
4n+4		0(1)	<b>2(2)</b>	4(3)	6(4)	8(5)	<b>10(6)</b>	12(7)	14(8)	16(9)	18(10)	20(11)
4n+6				<b>1(2)</b>	3(3)	5(4)	7(5)	<b>9(6)</b>	11(7)	13(8)	15(9)	17(10)
4n+8					0(2)	2(3)	4(4)	6(5)	<b>8(6)</b>	10(7)	12(8)	14(9)
4n+10							1(3)	3(4)	5(5)	<b>7(6)</b>	9(7)	11(8)
								0(3)	2(4)	4(5)	<b>6(6)</b>	8(7)
										1(4)	3(5)	<b>5(6)</b>
											0(4)	2(5)

TABLE 2D					
T-2D					
		[M11]	[M12]	[M13]	[M14]
C <sup>26</sup>	4n-50	99(37)	101(38)	103(39)	105(40)
C <sup>25</sup>	4n-48	96(36)	98(37)	100(38)	102(39)
C <sup>24</sup>	4n-46	93(35)	93(35)	95(35)	97(36)
C <sup>23</sup>	4n-44	90(34)	92(35)	94(36)	96(37)
C <sup>22</sup>	4n-42	87(33)	89(34)	91(35)	93(36)
C <sup>21</sup>	4n-40	84(32)	86(33)	88(34)	90(35)
C <sup>20</sup>	4n-38	82(31)	84(32)	86(33)	88(34)
C <sup>19</sup>	4n-36	78(30)	80(31)	82(32)	84(33)
C <sup>18</sup>	4n-34	75(29)	77(30)	79(31)	81(32)
C <sup>17</sup>	4n-32	72(28)	74(29)	76(30)	78(31)
C <sup>16</sup>	4n-30	69(27)	71(28)	73(29)	75(30)
C <sup>15</sup>	4n-28	66(26)	68(27)	70(28)	72(29)
C <sup>14</sup>	4n-26	63(25)	65(26)	67(27)	69(28)
C <sup>13</sup>	4n-24	60(24)	62(25)	64(26)	66(28)
C <sup>12</sup>	4n-22	57(23)	59(24)	61(25)	63(26)
C <sup>11</sup>	4n-20	54(22)	56(23)	58(24)	60(25)

C <sup>10</sup>	4n-18	51(21)	53(22)	55(23)	57(24)
C <sup>9</sup>	4n-16	48(20)	50(21)	52(22)	46(19)
C <sup>8</sup>	4n-14	45(19)	47(20)	49(21)	51(22)
C <sup>7</sup>	4n-12	42(18)	44(19)	46(20)	48(21)
C <sup>6</sup>	4n-10	39(17)	41(18)	43(19)	45(20)
C <sup>5</sup>	4n-8	36(16)	38(17)	40(18)	42(19)
C <sup>4</sup>	4n-6	33(15)	35(16)	37(17)	39(18)
C <sup>3</sup>	4n-4	30(14)	32(15)	34(16)	36(17)
C <sup>2</sup>	4n-2	27(13)	29(14)	31(15)	33(16)
C <sup>1</sup>	4n+0	24(12)	26(13)	28(14)	30(15)
<b>C<sup>0</sup></b>	<b>4n+2</b>	<b>21(11)</b>	<b>23(12)</b>	<b>25(13)</b>	<b>27(14)</b>
C <sup>-1</sup>	4n+4	18(10)	20(11)	22(12)	24(13)
C <sup>-2</sup>	4n+6	15(9)	17(10)	19(11)	21(10)
C <sup>-3</sup>	4n+8	12(8)	14(9)	16(10)	18(11)
C <sup>-4</sup>	4n+10	9(7)	11(8)	13(9)	15(10)
C <sup>-5</sup>		6(6)	8(7)	10(8)	12(9)
C <sup>-6</sup>		3(5)	5(6)	7(7)	9(8)

T-2 = TABLE 2, P = PAGE

### 3.9 Outstanding Derivatives from Table 2

#### • THE BROAD MEANING OF TABLE 2

The table is extremely important. It represents K(n) values of chemical clusters comprising of a single (n=1) skeletal element to seventy(n=70) skeletal elements. Let us illustrate this with clusters which have whole number K values starting from small ones to large ones. The K(n) = 1(1): this will represent all the elements such as O(K=1), K(n) = 1(1); S(K=1), Se(K=1) and Te in group 6(16) in the periodic table (see Appendix 1). The K(n) = 2(1) will be the carbon group 4(14); K(n) = 3(1) → Be group 2(12) or Zn group 12 (see Appendix 2), K(n) = 4(1) → Ni group 10 and K(n) = 5(1) → Fe group 8 in the periodic table (see Appendix 2). The K(n)=1(2) represents clusters such as X<sub>2</sub>( group 17, X = F, Cl), M<sub>2</sub>(CO)<sub>10</sub>(M=Mn, Tc, Re); Co<sub>2</sub>(CO)<sub>8</sub>, Mo<sub>2</sub>(Cp)<sub>2</sub>(CO)<sub>6</sub>; 2(2) → O<sub>2</sub>, C<sub>2</sub>H<sub>4</sub>, Rh<sub>2</sub>(Cp)<sub>2</sub>(CO)<sub>2</sub>; 3(2) → N<sub>2</sub>, C<sub>2</sub>H<sub>2</sub>, Mo<sub>2</sub>(Cp)<sub>2</sub>(CO)<sub>4</sub>; 3(3) → C<sub>3</sub>H<sub>6</sub>, Os<sub>3</sub>(CO)<sub>12</sub>; 6(4) → C<sub>4</sub>R<sub>4</sub>, M<sub>4</sub>(CO)<sub>12</sub>(M=Co, Rh, Ir); 8(5) → B<sub>5</sub>H<sub>5</sub><sup>2-</sup>, Sn<sub>5</sub><sup>2-</sup>, Os<sub>5</sub>(CO)<sub>16</sub>; 11(6) → B<sub>6</sub>H<sub>6</sub><sup>2-</sup>, Rh<sub>6</sub>(CO)<sub>16</sub>, Co<sub>6</sub>(C)(CO)<sub>14</sub><sup>-</sup>.

#### • CAPPING CONCEPT FROM SERIES ELABORATED

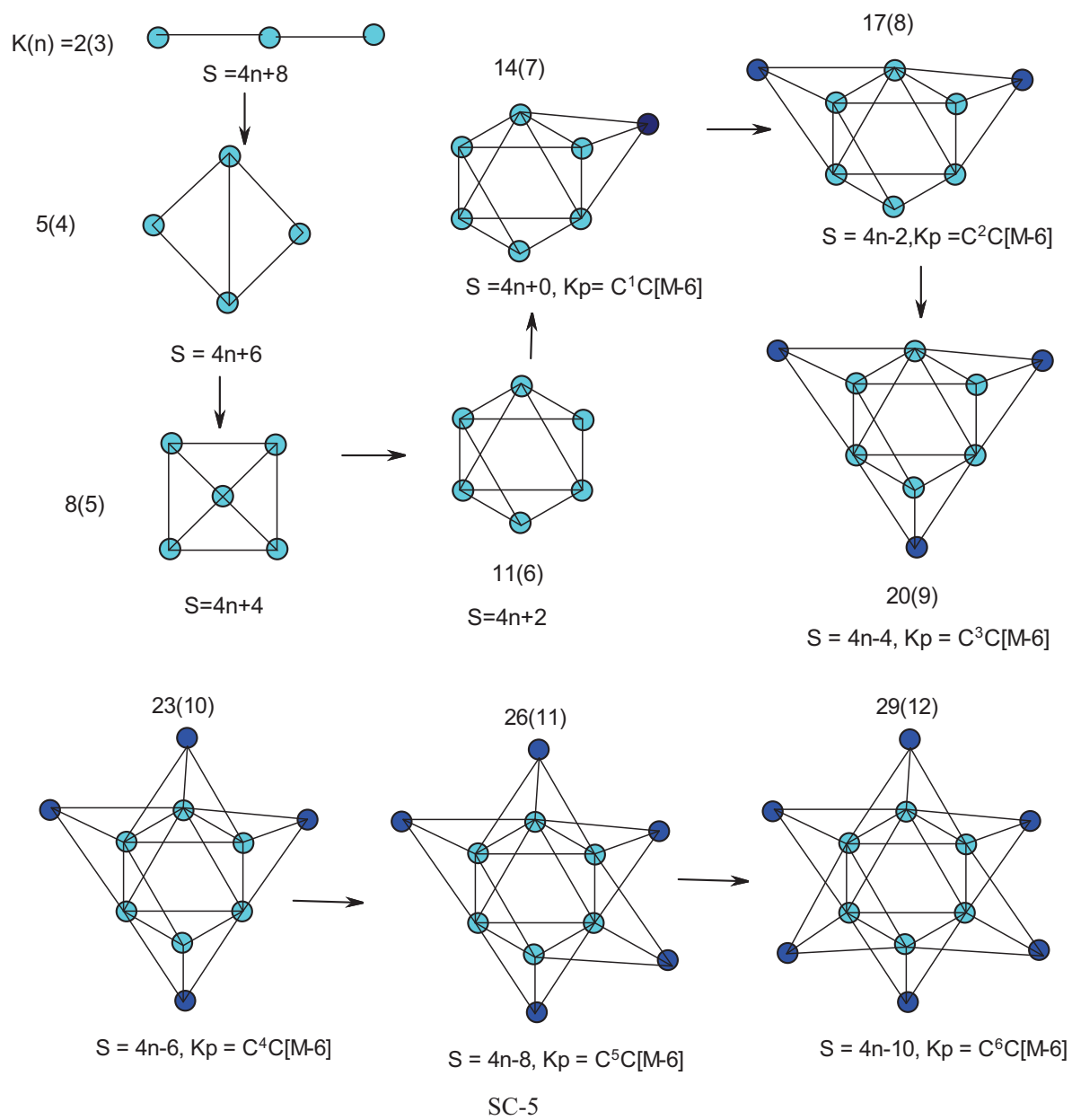
The capping symbol K<sub>p</sub> = C<sup>y</sup>C[M<sub>x</sub>] that has been developed is very useful in explain the capping concept. The letter y (capping index) represents the number of capping skeletal elements outside the cluster nucleus [M<sub>x</sub>] (x = nuclear index), represents the number of the skeletal elements in the nucleus of a cluster. If Table 2 were displayed on a larger space, it would cover the [M<sub>x</sub>] range x = -10 to x = +14 expressed as [M-10] to [M14]. The construction of the table shows that the un-capped series commence at x = 2 upwards, that is, x ≥ 2. However, there are no un-capped series for x ≤ 1. Therefore, the Rudolph concept of correlation of geometrical structures is more meaningful for clusters x ≥ 2. A section of Table 2 has been numerically demarcated and labeled Table 2C(T-2C). If we focus on the close base-line, S = 4n + 2. As a reference, then clusters with genuine skeletal elements in the nucleus commence with [M1]. This means, these will be clusters which have a single element in the nucleus. This is the foundation of golden clusters referred to as toroidal clusters. According to the series in Table 2, the starting cluster on the vertical grid-line is numerically represented as [M1], K(n) = 1(1) and belongs to the CLOSO family of series S = 4n + 2. The selected vertical range of K(n) numbers are:

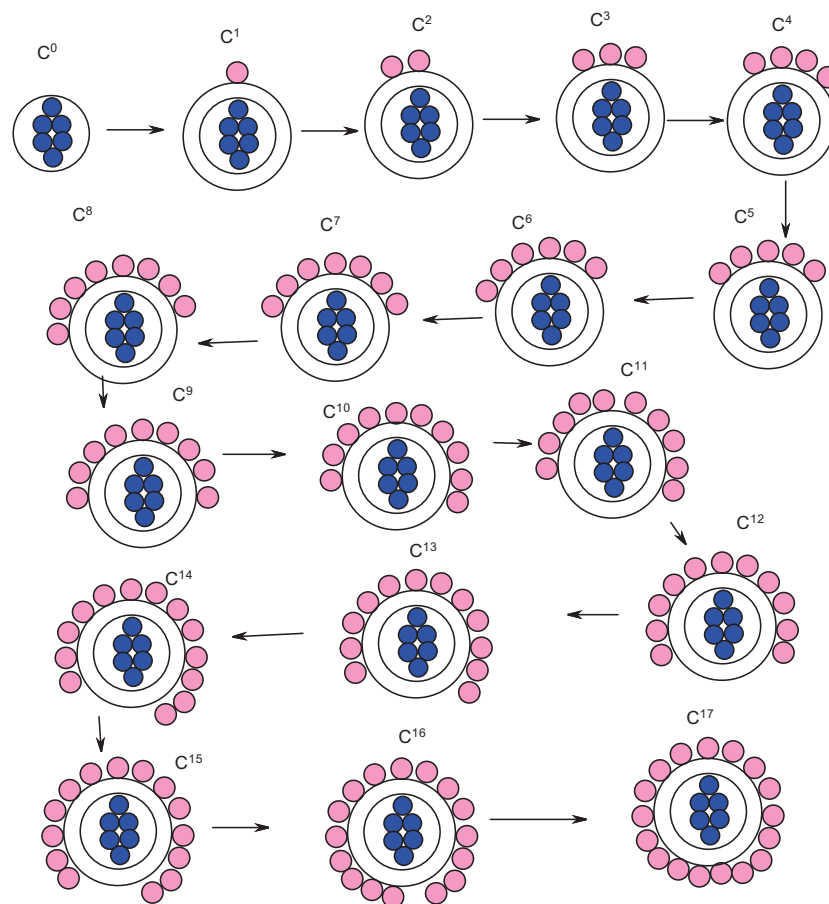
K(n):[M1]SERIES

→ 1(1) → 4(2) → 7(3) → 10(4) → 13(5) → 16(6) → 19(7) → 22(8) → 25(9) → 28(10) → 31(11) → 34(12) → 37(13).

Let us look at the following golden clusters: Au<sub>6</sub>L<sub>6</sub><sup>2+</sup>: K(n) = **16(6)**, S = 4n - 8, K<sub>p</sub> = C<sup>5</sup>C[M1]; Au<sub>8</sub>L<sub>7</sub><sup>2+</sup>: K(n) = **22(8)**, S = 4n - 12, K<sub>p</sub> = C<sup>7</sup>C[M1]; Au<sub>9</sub>L<sub>8</sub><sup>3+</sup>: K(n) = **25(9)**, S = 4n - 14, K<sub>p</sub> = C<sup>8</sup>C[M1]; Au<sub>10</sub>L<sub>5</sub>R<sub>4</sub>: K(n) = **28(10)**, S = 4n - 16, K<sub>p</sub> = C<sup>9</sup>C[M1]; Au<sub>10</sub>Cl<sub>3</sub>L<sub>6</sub><sup>+1</sup>: K(n) = **28(10)**, S = 4n - 16, K<sub>p</sub> = C<sup>9</sup>C[M1]; Au<sub>11</sub>L<sub>10</sub><sup>5+</sup>: K(n) = **31(11)**, S = 4n - 18, K<sub>p</sub> = C<sup>10</sup>C[M1]. All these clusters belong to the [M1] SERIES, that is, they belong to GROUP [M1] CLUSTERS. As mentioned earlier, these clusters are referred to as toroidal clusters (Mingos, 1984).

According to Table 2, the genuine un-capping series commences from [M2] and increases in the sequence [M3] → [M4] → [M5] → [M6] → [M7] → [M8] → [M9] → [M10] → [M11] → [M12]. If we use [M6] to illustrate capping, there will be un-capping series below it as can be seen from Table 2C. The clusters below [M6] can be regarded as 'build-up' clusters before reaching [M6] close base-line. When we reach [M6], then we reach a zero capping base line, K<sub>p</sub> = C<sup>0</sup>C[M6]. Moving vertically along [M6], then we get capped clusters of an octahedral nucleus. This idea of capping based on an octahedral nucleus can be illustrated in Schemes SC-5 and SC-6 and the Grid-line SC-7 (BLUE LINE). The scheme SC-7 also indicates the capping series of [M2] (GREEN LINE) and [M1] (ORANGE LINE) series.





SC-6

• CATEGORIZATION OF CLUSTERS BASED ON CLOSO GRID-LINES

Let us illustrate this by monitoring some of the  $K(n)$  values based on the CLOSO VERTICAL LINE [M6],  $K(n) = 11(6)$ ,  $S = 4n+2$ . We can simply refer to this as [M6] grid-line. This is indicated in BLUE in the scheme SC-5. The vertical numerical sequence starting with [M6], will be  $K(n) = \{11(6), 4n+2, K_p = C^0C[M6]\}; \{14(7), 4n+0, K_p = C^1C[M6]\}; \{17(8); 4n-2, C^2C[M6]\}; \{20(9), 4n-4, C^3C[M6]\}$ , and so on. We may call all these clusters which line up on [M6] grid-line as CLUSTER GROUP 6. If we include clusters below [M6],  $S = 4n+2$  base-line, then we will create Rudolph type of correlation. The cluster series below [M6] will include,  $\{8(5), 4n+4, C^{-1}C[M6], \text{nido clusters}\}$ ,  $\{5(4), 4n+6, C^{-2}C[M6], \text{arachno clusters}\}$ ,  $\{2(3), 4n+8, C^{-3}C[M6], \text{hypho clusters}\}$  and so on. The horizontal movement below [M6], we get [M5], this corresponds to  $S = 4n+2$  and  $K(n) = 9(5)$ . The borane closo cluster that corresponds to this point is  $B_5H_5^{2-}$ . The numerical movement upwards from 9(5), we get 12(6), 15(7), 18(8), 21(9), and so on. We can refer to these clusters as GROUP 5 clusters, [M5]. Continuing the horizontal movement left-wise, we get [M4], 7(4),  $S = 4n+2$ ; then [M3], 5(3),  $4n+2$ ; [M2], 3(2),  $4n+2$ . It has been found that a good range of golden clusters belong to GROUP 2, [M2]. Accordingly, their vertical [M2] numerical series will be; 3(2), 6(3), 9(4), 12(5), and so on. The group 2 clusters lie along the grid-line shown in GREEN in SC-7. These golden clusters which are [M2]-based have been referred to as SPHERICAL while those which are [M1]-based with a single element in the nucleus were referred to as TORROIDAL (Mingos, 1984). A good example of spherical golden cluster is  $Au_9L_8^+$ :  $K=9[3.5]-8+0.5 = 24, K(n) = 24(9), S = 4n-12, K_p = C^7C[M2]$ . On the other hand the cluster of the same nuclearity index,  $Au_9L_8^{3+}$ : has a  $K$  value 25,  $K(n) = 25(9), S = 4n-14, K_p = C^8C[M1]$  is described as torroidal. The transformation from  $Au_9L_8^+$  to  $Au_9L_8^{3+}$  results in the increase in  $K$  value by 1. The increase in  $K$  value of a capping cluster by 1 results in the increase of the corresponding skeletal elements by 1. That additional capping element is extracted from the nucleus. Hence, the [M2] (two skeletal elements in the nucleus) now becomes [M1] (one skeletal element in the nucleus). The group 2 clusters lie along the [M1] orange grid-line in SC-7.

3.10 Categorization of Un-Capping Series

This is simply the categorization of clusters below the closo [M6] grid-line (SC-7). The closo cluster [M6],  $S = 4n+2, n$

= 6,  $K=2n-1 = 2(6)-1 = 11$ ,  $K(n) = 11(6)$ ,  $K_p = C^0C[M6]$ . If we use the grid-line SC-7 as a reference, upward movement by one step gives  $K(n) = 14(7)$ ,  $S = 4n+0$ ,  $K_p = C^1C[M6]$ . This will be a mono-capped octahedron. The next movement upwards by another one step will give us  $K(n) = 17(8)$ ,  $S = 4n-2$ ,  $K_p = C^2C[M6]$ . This is a bi-capped octahedron. Let us consider the movement downwards (opposite direction) on [M6] grid-line. This is numerically expressed as  $K(n) = 11(6)\{S = 4n+2, K_p = C^0C[M6]\} \rightarrow 8(5)\{S = 4n+4, K_p = C^{-1}C[M6], \text{nido series}\}$ ; the next movement from nido series by one step will give us  $K(n) = 5(4)$ ,  $S = 4n+6$ ,  $K_p = C^{-2}C[M6]$ , arachno series}. Since the movement is downwards from the closo base-line, the use of the negative capping index,  $C^{-1}$  and  $C^{-2}$  makes sense. Thus, we can categorize both the capping and de-capping clusters using the capping symbol  $K_p = C^yC[Mx]$ , where  $y$  can have positive or negative values. A selected sample of clusters categorized like this is shown in Table 3.

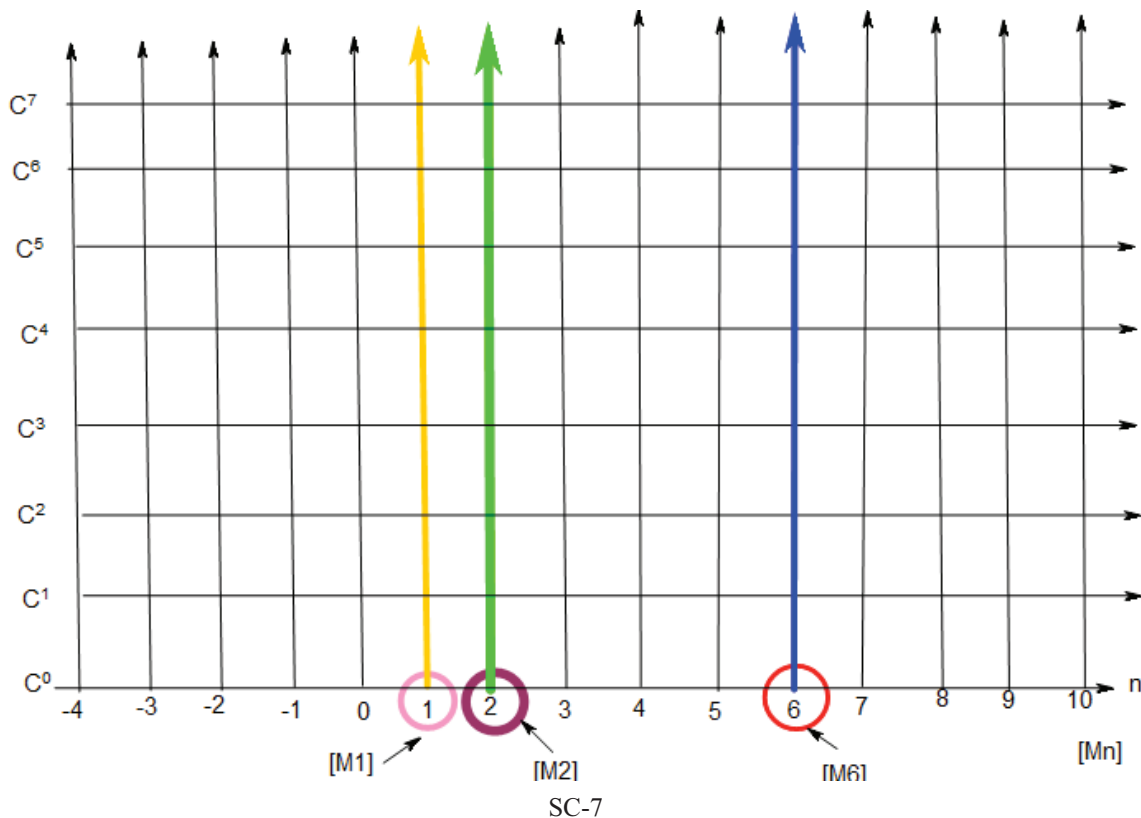


Table 3. Selected Examples Illustrating the Concept of Categorizing Clusters into their Closo Nuclearity Index

CLUSTER	$K(n)$	SERIES	NAME, $K_p = C^yC[Mx]$	[Mx]
$Pd_{59}(CO)_{32}L_{21}$	183(59)	$4n-130$	$C^{66}C[M-7]$	[M-7]
$Pd_{66}(CO)_{45}L_{16}$	203(66)	$4n-142$	$C^{72}C[M-6]$	[M-6]
$Pd_{52}(CO)_{36}L_{14}$	158(52)	$4n-108$	$C^{55}C[M-3]$	[M-3]
$Pd_{54}(CO)_{40}L_{14}$	162(54)	$4n-108$	$C^{55}C[M-1]$	[M-1]
$Pd_{39}(CO)_{23}L_{16}$	117(39)	$4n-78$	$C^{40}C[M-1]$	[M-1]
$Pd_3(CO)_3L_4$	5(3)	$4n+2$	$C^0C[M3](\text{closo})$	[M3]
$Pd_4(CO)_5L_4$	7(4)	$4n+2$	$C^0C[M3](\text{closo})$	[M3]
$Au_4L_4$	10(4)	$4n-4$	$C^3C[M1]$	[M1]
$Au_6L_6^{2+}$	16(6)	$4n-8$	$C^5C[M1]$	[M1]
$Au_6L_4Cl_2$	16(6)	$4n-8$	$C^5C[M1]$	[M1]
$Au_8L_7^{2+}$	22(8)	$4n-12$	$C^7C[M1]$	[M1]
$Au_9L_8^{3+}$	25(9)	$4n-14$	$C^8C[M1]$	[M1]
$Au_{11}L_{10}^{5+}$	31(11)	$4n-18$	$C^{10}C[M1]$	[M1]
$Pd_{34}(CO)_{24}L_{12}$	100(34)	$4n-64$	$C^{33}C[M1]$	[M1]
$Re_5(C)(H)(CO)_{12}^{2-}$	12(5)	$4n-4$	$C^3C[M2]$	[M2]
$Au_9L_8^+$	24(9)	$4n-12$	$C^7C[M2]$	[M2]
$Os_{17}(CO)_{36}^{2-}$	48(17)	$4n-28$	$C^{15}C[M2]$	[M2]
$Pd_{35}(CO)_{23}L_{15}$	102(35)	$4n-64$	$C^{33}C[M2]$	[M2]
$Pd_{37}(CO)_{28}L_{12}$	108(37)	$4n-68$	$C^{35}C[M2]$	[M2]
$B_2H_6$	2(2)	$4n+4$	$C^{-1}C[M3]$	[M3]
$Re_2H_2(CO)_8$	2(2)	$4n+4$	$C^{-1}C[M3]$	[M3]

Re <sub>4</sub> H <sub>4</sub> (CO) <sub>12</sub>	8(4)	4n+0	C <sup>1</sup> C[M3]	[M3]
Os <sub>2</sub> (CO) <sub>9</sub>	1(2)	4n+6	C <sup>2</sup> C[M4]	[M4]
Re <sub>3</sub> H <sub>3</sub> (CO) <sub>10</sub> <sup>2-</sup>	4(3)	4n+4	C <sup>-1</sup> C[M4]	[M4]
B <sub>4</sub> H <sub>4</sub> <sup>2+</sup>	7(4)	4n+2	C <sup>0</sup> C[M4]	[M4]
Pd <sub>6</sub> (CO) <sub>4</sub> L <sub>7</sub>	13(6)	4n-2	C <sup>2</sup> C[M4]	[M4]
Pt <sub>19</sub> (CO) <sub>22</sub> <sup>4+</sup>	52(19)	4n-28	C <sup>15</sup> C[M4]	[M4]
Pd <sub>16</sub> Ni <sub>4</sub> (CO) <sub>22</sub> L <sub>2</sub> <sup>2-</sup>	55(20)	4n-30	C <sup>16</sup> C[M4]	[M4]
(Au)Pd <sub>22</sub> (CO) <sub>20</sub> L <sub>8</sub> <sup>2+</sup>	64(23)	4n-36	C <sup>19</sup> C[M4]	[M4]
Pd <sub>23</sub> (CO) <sub>20</sub> L <sub>8</sub>	64(23)	4n-36	C <sup>19</sup> C[M4]	[M4]
Pd <sub>28</sub> Pt <sub>13</sub> L <sub>13</sub>	118(41)	4n-72	C <sup>37</sup> C[M4]	[M4]
Au <sub>39</sub> L <sub>14</sub> Cl <sub>6</sub> <sup>+</sup>	120(39)	4n-84	C <sup>43</sup> C[M4]	[M4]
Os <sub>3</sub> (CO) <sub>12</sub>	3(3)	4n+6	C <sup>-2</sup> C[M5]	[M5]
B <sub>3</sub> H <sub>6</sub>	3(3)	4n+6	C <sup>-2</sup> C[M5]	[M5]
Os <sub>4</sub> (CO) <sub>14</sub>	6(4)	4n+4	C <sup>-1</sup> C[M5]	[M5]
Os <sub>4</sub> H <sub>2</sub> (CO) <sub>12</sub> <sup>2-</sup>	6(4)	4n+4	C <sup>-1</sup> C[M5]	[M5]
Rh <sub>4</sub> (CO) <sub>12</sub>	6(4)	4n+4	C <sup>-1</sup> C[M5]	[M5]
Re <sub>4</sub> H <sub>4</sub> (CO) <sub>13</sub> <sup>2-</sup>	6(4)	4n+4	C <sup>-1</sup> C[M5]	[M5]
B <sub>4</sub> H <sub>8</sub>	6(4)	4n+4	C <sup>-1</sup> C[M5]	[M5]
CB <sub>4</sub> H <sub>10</sub>	9(5)	4n+2	C <sup>0</sup> C[M5]	[M5]
B <sub>3</sub> C <sub>2</sub> H <sub>5</sub>	9(5)	4n+2	C <sup>0</sup> C[M5]	[M5]
Os <sub>5</sub> H(CO) <sub>15</sub> <sup>-</sup>	9(5)	4n+2	C <sup>0</sup> C[M5]	[M5]
Os <sub>6</sub> (CO) <sub>18</sub>	12(6)	4n+0	C <sup>1</sup> C[M5]	[M5]
Os <sub>10</sub> (CO)(CO) <sub>24</sub>	24(10)	4n-8	C <sup>5</sup> C[M5]	[M5]
Rh <sub>14</sub> (CO) <sub>25</sub> <sup>4-</sup>	36(14)	4n-16	C <sup>9</sup> C[M5]	[M5]
Rh <sub>15</sub> (CO) <sub>27</sub> <sup>3-</sup>	39(15)	4n-18	C <sup>10</sup> C[M5]	[M5]
Pd <sub>16</sub> (CO) <sub>13</sub> L <sub>9</sub>	42(16)	4n-20	C <sup>11</sup> C[M5]	[M5]
Rh <sub>17</sub> (CO) <sub>30</sub> <sup>3-</sup>	45(17)	4n-22	C <sup>12</sup> C[M5]	[M5]
Rh <sub>22</sub> (CO) <sub>37</sub> <sup>4-</sup>	60(22)	4n-32	C <sup>17</sup> C[M5]	[M5]
Os <sub>4</sub> (CO) <sub>15</sub>	5(4)	4n+6	C <sup>-2</sup> C[M6]	[M6]
B <sub>4</sub> H <sub>10</sub>	5(4)	4n+6	C <sup>-2</sup> C[M6]	[M6]
Os <sub>5</sub> H <sub>2</sub> (CO) <sub>18</sub>	8(5)	4n+4	C <sup>-1</sup> C[M6]	[M6]
B <sub>4</sub> H <sub>8</sub> (CoCp)	8(5)	4n+4	C <sup>-1</sup> C[M6]	[M6]
B <sub>5</sub> H <sub>9</sub>	8(5)	4n+4	C <sup>-1</sup> C[M6]	[M6]
B <sub>4</sub> H <sub>8</sub> Fe(CO) <sub>3</sub>	8(5)	4n+4	C <sup>-1</sup> C[M6]	[M6]
Os <sub>6</sub> (CO) <sub>18</sub> <sup>2-</sup>	11(6)	4n+2	C <sup>0</sup> C[M6]	[M6]
Rh <sub>5</sub> Pt(CO) <sub>15</sub> <sup>-</sup>	11(6)	4n+2	C <sup>0</sup> C[M6]	[M6]
Re <sub>6</sub> C(CO) <sub>19</sub> <sup>2-</sup>	11(6)	4n+2	C <sup>0</sup> C[M6]	[M6]
B <sub>4</sub> C <sub>2</sub> H <sub>6</sub>	11(6)	4n+2	C <sup>0</sup> C[M6]	[M6]
Pd <sub>7</sub> (CO) <sub>7</sub> L <sub>7</sub>	14(7)	4n+0	C <sup>1</sup> C[M6]	[M6]
Os <sub>7</sub> (CO) <sub>21</sub>	14(7)	4n+0	C <sup>1</sup> C[M6]	[M6]
Rh <sub>7</sub> (CO) <sub>16</sub> <sup>3-</sup>	14(7)	4n+0	C <sup>1</sup> C[M6]	[M6]
Re <sub>7</sub> C(CO) <sub>21</sub> <sup>3-</sup>	14(7)	4n+0	C <sup>1</sup> C[M6]	[M6]
Pd <sub>8</sub> (CO) <sub>8</sub> L <sub>7</sub>	17(8)	4n-2	C <sup>2</sup> C[M6]	[M6]
Re <sub>8</sub> C(CO) <sub>24</sub> <sup>2-</sup>	17(8)	4n-2	C <sup>2</sup> C[M6]	[M6]
Os <sub>8</sub> (CO) <sub>22</sub> <sup>2-</sup>	17(8)	4n-2	C <sup>2</sup> C[M6]	[M6]
Os <sub>9</sub> H(CO) <sub>24</sub> <sup>-</sup>	20(9)	4n-4	C <sup>3</sup> C[M6]	[M6]
Rh <sub>9</sub> (CO) <sub>19</sub> <sup>3-</sup>	20(9)	4n-4	C <sup>3</sup> C[M6]	[M6]
Os <sub>10</sub> (CO) <sub>26</sub> <sup>2-</sup>	23(10)	4n-6	C <sup>4</sup> C[M6]	[M6]
Rh <sub>10</sub> (CO) <sub>21</sub> <sup>2-</sup>	23(10)	4n-6	C <sup>4</sup> C[M6]	[M6]
Os <sub>10</sub> H <sub>2</sub> (C)(CO) <sub>24</sub>	23(10)	4n-6	C <sup>4</sup> C[M6]	[M6]
Rh <sub>13</sub> (CO) <sub>24</sub> H <sub>2</sub> <sup>3-</sup>	32(13)	4n-12	C <sup>7</sup> C[M6]	[M6]
Pd <sub>16</sub> Ni <sub>4</sub> (CO) <sub>22</sub> L <sub>4</sub> <sup>2-</sup>	53(20)	4n-26	C <sup>14</sup> C[M6]	[M6]
Pd <sub>23</sub> (CO) <sub>20</sub> L <sub>10</sub>	62(23)	4n-32	C <sup>17</sup> C[M6]	[M6]
Pt <sub>24</sub> (CO) <sub>30</sub> <sup>2-</sup>	65(24)	4n-34	C <sup>18</sup> C[M6]	[M6]
Pd <sub>29</sub> (CO) <sub>28</sub> L <sub>7</sub> <sup>2-</sup>	80(29)	4n-44	C <sup>23</sup> C[M6]	[M6]
HPd <sub>30</sub> (CO) <sub>26</sub> L <sub>10</sub> <sup>-</sup>	83(30)	4n-46	C <sup>24</sup> C[M6]	[M6]
Au <sub>2</sub> Pd <sub>28</sub> (CO) <sub>26</sub> L <sub>10</sub>	83(30)	4n-46	C <sup>24</sup> C[M6]	[M6]
Pt <sub>38</sub> (CO) <sub>44</sub> <sup>2-</sup>	107(38)	4n-62	C <sup>32</sup> C[M6]	[M6]
Pd <sub>33</sub> Ni <sub>9</sub> (CO) <sub>41</sub> L <sub>6</sub> <sup>4-</sup>	119(42)	4n-70	C <sup>36</sup> C[M6]	[M6]
Pd <sub>8</sub> Ni <sub>56</sub> (CO) <sub>48</sub> <sup>6-</sup>	125(44)	4n-74	C <sup>38</sup> C[M6]	[M6]
Ni <sub>35</sub> Pt <sub>9</sub> (CO) <sub>48</sub> <sup>6-</sup>	125(44)	4n-74	C <sup>38</sup> C[M6]	[M6]
Ni <sub>38</sub> Pt <sub>6</sub> (CO) <sub>48</sub> H <sup>5-</sup>	125(44)	4n-74	C <sup>38</sup> C[M6]	[M6]
Os <sub>4</sub> (CO) <sub>16</sub>	4(4)	4n+8	C <sup>-3</sup> C[M7]	[M7]
Os <sub>5</sub> (CO) <sub>18</sub>	7(5)	4n+6	C <sup>-2</sup> C[M7]	[M7]

Rh <sub>5</sub> (CO) <sub>15</sub> <sup>-</sup>	7(5)	4n+6	C <sup>-2</sup> C[M7]	[M7]
B <sub>5</sub> H <sub>11</sub>	7(5)	4n+6	C <sup>-2</sup> C[M7]	[M7]
B <sub>6</sub> H <sub>10</sub>	10(6)	4n+4	C <sup>-1</sup> C[M7]	[M7]
Os <sub>7</sub> H <sub>2</sub> (CO) <sub>19</sub>	13(7)	4n+2	C <sup>0</sup> C[M7]	[M7]
Os <sub>10</sub> (C)(CO) <sub>24</sub> <sup>4-</sup>	22(10)	4n-4	C <sup>3</sup> C[M7]	[M7]
Pd <sub>10</sub> (CO) <sub>12</sub> L <sub>6</sub>	22(10)	4n-4	C <sup>3</sup> C[M7]	[M7]
Rh <sub>11</sub> (CO) <sub>23</sub> <sup>3-</sup>	25(11)	4n-6	C <sup>4</sup> C[M7]	[M7]
Pd <sub>9</sub> Ni <sub>9</sub> (CO) <sub>17</sub> L <sub>9</sub>	46(18)	4n-20	C <sup>11</sup> C[M7]	[M7]
Ni <sub>14</sub> Pt <sub>10</sub> (CO) <sub>30</sub> <sup>4-</sup>	64(24)	4n-32	C <sup>17</sup> C[M7]	[M7]
Au <sub>4</sub> Pd <sub>28</sub> (CO) <sub>22</sub> L <sub>16</sub>	88(32)	4n-48	C <sup>25</sup> C[M7]	[M7]
Au <sub>4</sub> Pd <sub>32</sub> (CO) <sub>28</sub> L <sub>14</sub>	100(36)	4n-56	C <sup>29</sup> C[M7]	[M7]
Pd <sub>36</sub> (C)(CO) <sub>28</sub> L <sub>14</sub>	100(36)	4n-56	C <sup>29</sup> C[M7]	[M7]
Ni <sub>24</sub> Pt <sub>14</sub> (CO) <sub>44</sub> <sup>4-</sup>	106(38)	4n-60	C <sup>31</sup> C[M7]	[M7]
Os <sub>5</sub> (CO) <sub>19</sub>	6(5)	4n+8	C <sup>-3</sup> C[M8]	[M8]
Os <sub>6</sub> (CO) <sub>21</sub>	9(6)	4n+6	C <sup>-2</sup> C[M8]	[M8]
CB <sub>5</sub> H <sub>11</sub>	9(6)	4n+6	C <sup>-2</sup> C[M8]	[M8]
B <sub>6</sub> H <sub>12</sub>	9(6)	4n+6	C <sup>-2</sup> C[M8]	[M8]
B <sub>6</sub> C <sub>2</sub> H <sub>8</sub>	15(8)	4n+2	C <sup>0</sup> C[M8]	[M8]
Rh <sub>8</sub> C(CO) <sub>19</sub>	15(8)	4n+2	C <sup>0</sup> C[M8]	[M8]
B <sub>8</sub> H <sub>12</sub>	14(8)	4n+4	C <sup>-1</sup> C[M9]	[M9]
Rh <sub>9</sub> P(CO) <sub>21</sub> <sup>2-</sup>	16(9)	4n+4	C <sup>-1</sup> C[M9]	[M10]
B <sub>10</sub> H <sub>10</sub> <sup>2-</sup>	19(10)	4n+2	C <sup>0</sup> C[M10]	[M10]
B <sub>10</sub> H <sub>14</sub>	18(10)	4n+4	C <sup>-1</sup> C[M11]	[M11]
SB <sub>9</sub> H <sub>11</sub>	18(10)	4n+4	C <sup>-1</sup> C[M11]	[M11]
Au <sub>6</sub> Ni <sub>32</sub> (CO) <sub>44</sub> <sup>6-</sup>	102(38)	4n-52	C <sup>27</sup> C[M11]	[M11]
B <sub>8</sub> H <sub>18</sub>	11(8)	4n+10	C <sup>-4</sup> C[M12]	[M12]
B <sub>9</sub> C <sub>2</sub> H <sub>12</sub> <sup>-</sup>	20(11)	4n+4	C <sup>-2</sup> C[M12]	[M12]
B <sub>12</sub> H <sub>12</sub> <sup>2-</sup>	23(12)	4n+2	C <sup>0</sup> C[M12]	[M12]
B <sub>10</sub> C <sub>2</sub> H <sub>12</sub>	23(12)	4n+2	C <sup>0</sup> C[M12]	[M12]

- THE EXISTANCE OF THE NUCLEUS IN CAPPING CLUSTERS

All the capped clusters with a CLOSO nucleus are expressed as  $Kp = C^yC[Mx]$  ( $x$ = nuclear index,  $y$ = capping index). Using the series method, a wide range of clusters have been found to possess CLOSO nuclei in capping clusters. For instance, the cluster  $Ru_6Pd_6(CO)_{24}^{2-}$ ;  $K(n) = 29(12)$ ,  $S = 4n-10$ ,  $Kp = C^6C[M6]$  was found to have a distorted octahedral nucleus of palladium skeletal elements capped by six ruthenium skeletal elements (Brivio, et al, 1994). Let us consider the giant cluster  $Ni_{38}Pt_6(CO)_{48}(H)^{5-}$ :  $K = 125(44)$ ,  $S = 4n-74$ ,  $Kp = C^{38}C[M6]$ . The series analysis tells us that this huge cluster has an octahedral nucleus surrounded by 38 capping elements. In actual fact, it was found that the octahedral nucleus comprised of platinum elements surrounded by 38 nickel skeletal elements by x-ray analysis (Rossi, Zanello, 2011). The golden clusters,  $Au_8L_7^{2+}$ :  $K = 8[3.5]-7+1 = 22$ ,  $K(n) = 22(8)$ ,  $S = 4n-12$ ,  $Kp = C^7C[M1]$ ,  $Au_9L_8^{3+}$ :  $K = 9[3.5]-8+1.5 = 25$ ,  $K(n) = 25(9)$ ,  $S = 4n-14$ ,  $Kp = C^8C[M1]$ , and  $Au_{10}Cl_3L_6^{+1}$ :  $K = 10[3.5]-1.5-6+0.5 = 28$ ,  $K(n) = 28(10)$ ,  $S = 4n-16$ ,  $Kp = C^9C[M1]$  were found to possess mono-skeletal nuclei as predicted by the series method (Mingos, 1984).

- A SET OF ALL CLUSTERS WHICH POSSESS  $K(n)$  VALUES

Let us take  $K(n) = 11(6)$  as an illustration. With the help of skeletal numbers, the clusters with  $K(n) = 11(6)$  are readily identified. The Table 4 gives a sample of about 50 clusters identified in this way. Many more can be added to the table. The  $K(n)$  parameter acts as a 'car-park' in which clusters of  $n$  skeletal elements and same  $K$  values can be accommodated endlessly. This implies that each  $K(n)$  parameter in the CLUSTER TABLE represents a large number of clusters known and unknown. As for the ideal skeletal shapes and their isomers, in the case of  $K(n) = 11(6) \rightarrow$  octahedral,  $9(5) \rightarrow$  trigonal bipyramid,  $8(5) \rightarrow$  square pyramid and  $6(4) \rightarrow$  tetrahedral.

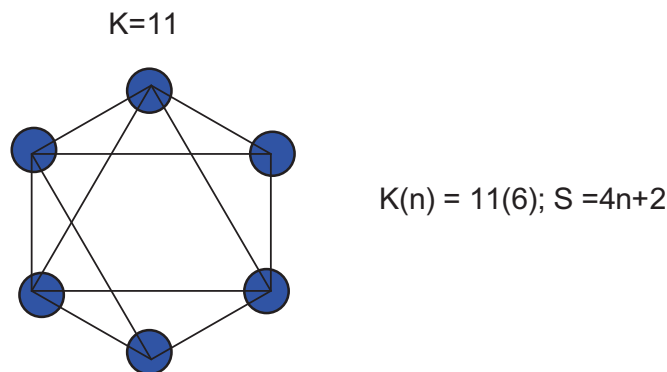


Table 4. Selected sample of clusters with an ideal octahedral symmetry ( $O_h$ )

	K(n)=11(6)					
	CLUSTER	K	K(n)	SERIES, S	VALENCE ELECTRONS, Ve	CLASSIFICATION
1	$Os_6(CO)_{18}^{2-}$	6[5]-18-1=11	11(6)	4n+2	14n+2=14(6)+2=86	CLOSO, $C^0C[M6]$
2	$Os_6(H)(CO)_{18}^-$	11	11(6)	4n+2	14n+2=14(6)+2=86	CLOSO, $C^0C[M6]$
3	$Rh_6(CO)_{16}$	6[4.5]-16=11	11(6)	4n+2	14n+2=14(6)+2=86	CLOSO, $C^0C[M6]$
4	$B_6H_6^{2-}$	6[2.5]-3-1=11	11(6)	4n+2	4n+2=4(6)+2=26	CLOSO, $C^0C[M6]$
5	$(CoCp)_3B_3H_5$	3[4.5-2.5]+3[2.5]-2.5=11	11(6)	4n+2	26+3[10]=56	CLOSO, $C^0C[M6]$
6	$C_2B_4H_6$	2[2]+4[2.5]-3=11	11(6)	4n+2	4n+2=4(6)+2=26	CLOSO, $C^0C[M6]$
7	$B_4H_6(CoCp)_2$	4[2.5]+2[4.5-2.5]-3=11	11(6)	4n+2	26+2[10]=46	CLOSO, $C^0C[M6]$
8	$C_2B_3H_5Fe(CO)_3$	2[2]+3[2.5]+1[5]-2.5-3=11	11(6)	4n+2	26+1[10]=36	CLOSO, $C^0C[M6]$
9	$Ru_6(C)(CO)_{17}$	6[5]-2-17=11	11(6)	4n+2	14n+2=14(6)+2=86	CLOSO, $C^0C[M6]$
10	$Ir_6(CO)_{16}$	11	11(6)	4n+2	14n+2=14(6)+2=86	CLOSO, $C^0C[M6]$
11	$Co_6(CO)_{13}(N)^-$	6[4.5]-13-2.5-0.5=11	11(6)	4n+2	14n+2=14(6)+2=86	CLOSO, $C^0C[M6]$
12	$Ru_6(CO)_{17}(B)^-$	6[5]-17-1.5-0.5=11	11(6)	4n+2	14n+2=14(6)+2=86	CLOSO, $C^0C[M6]$
13	$Ru_6(C)(CO)_{16}^{2-}$	6[5]-2-16-1=11	11(6)	4n+2	14n+2=14(6)+2=86	CLOSO, $C^0C[M6]$
14	$Ru_6(C)(CO)_{17}$	6[5]-2-17=11	11(6)	4n+2	14n+2=14(6)+2=86	CLOSO, $C^0C[M6]$
15	$Fe_6(N)(CO)_{15}^{3-}$	6[5]-2.5-15-1.5=11	11(6)	4n+2	14n+2=14(6)+2=86	CLOSO, $C^0C[M6]$
16	$Co_6(C)(CO)_{13}^{2-}$	6[4.5]-2-13-1=11	11(6)	4n+2	14n+2=14(6)+2=86	CLOSO, $C^0C[M6]$
17	$Fe_6(C)(CO)_{16}^{2-}$	6[5]-2-16-1=11	11(6)	4n+2	14n+2=14(6)+2=86	CLOSO, $C^0C[M6]$
18	$SFe_3Ru_3(CO)_{14}^{2-}$	1[1]+2[5]+3[5]-14-1=11	11(6)	4n+2	26+3[10]=56	CLOSO, $C^0C[M6]$
19	$Se_2Mn_4(CO)_{12}^{2-}$	2[1]+4[5.5]-12-1=11	11(6)	4n+2	26+4[10]=66	CLOSO, $C^0C[M6]$
20	$Te_2Ru_4(CO)_{10}^{2-}$	2[1]+4[5]-10-1=11	11(6)	4n+2	26+4[10]=66	CLOSO, $C^0C[M6]$
21	$Te_2Ru_4(CO)_{11}$	2[1]+4[5]-11=11	11(6)	4n+2	26+4[10]=66	CLOSO, $C^0C[M6]$
22	$Ru_6H(CO)_{18}^-$	6[5]-0.5-18-0.5=11	11(6)	4n+2	14n+2=14(6)+2=86	CLOSO, $C^0C[M6]$
23	$Re_6(C)(CO)_{19}^{2-}$	11	11(6)	4n+2	14n+2=14(6)+2=86	CLOSO, $C^0C[M6]$
24	$Re_6(C)(CO)_{19}(H)^-$	11	11(6)	4n+2	14n+2=14(6)+2=86	CLOSO, $C^0C[M6]$
25	$Re_6(C)(CO)_{18}^{3-}$	11	11(6)	4n+2	14n+2=14(6)+2=86	CLOSO, $C^0C[M6]$
26	$Re_6(C)(CO)_{18}(H)_2^{2-}$	11	11(6)	4n+2	14n+2=14(6)+2=86	CLOSO, $C^0C[M6]$
27	$Rh_6(CO)_{13}(C)^{2-}$	11	11(6)	4n+2	14n+2=14(6)+2=86	CLOSO, $C^0C[M6]$
28	$Ru_5Pd(C)(CO)_{16}$	11	11(6)	4n+2	14n+2=14(6)+2=86	CLOSO, $C^0C[M6]$
29	$Ru_5Co(C)(CO)_{16}^-$	11	11(6)	4n+2	14n+2=14(6)+2=86	CLOSO, $C^0C[M6]$
30	$Ru_4(H)Co_2(C)(CO)_{15}^-$	11	11(6)	4n+2	14n+2=14(6)+2=86	CLOSO, $C^0C[M6]$
31	$Ru_6(CO)_{18}^{2-}$	11	11(6)	4n+2	14n+2=14(6)+2=86	CLOSO, $C^0C[M6]$
32	$Ni_6(CO)_{12}^{2-}$	11	11(6)	4n+2	14n+2=14(6)+2=86	CLOSO, $C^0C[M6]$
33	$Ge_6R_2$	11	11(6)	4n+2	4n+2=4(6)+2=26	CLOSO, $C^0C[M6]$
34	$C_3B_3H_7$	11	11(6)	4n+2	4n+2=4(6)+2=26	CLOSO, $C^0C[M6]$
35	$Co_6(CO)_{16}$	11	11(6)	4n+2	14n+2=14(6)+2=86	CLOSO, $C^0C[M6]$
36	$Rh_2Fe_4(B)(CO)_{16}^-$	11	11(6)	4n+2	14n+2=14(6)+2=86	CLOSO, $C^0C[M6]$
37	$CB_3H_7$	11	11(6)	4n+2	4n+2=4(6)+2=26	CLOSO, $C^0C[M6]$
38	$(CoCp)C_2B_3H_5$	11	11(6)	4n+2	4n+2=4(6)+2+1[10]=36	CLOSO, $C^0C[M6]$
39	$Ir_6(CO)_{15}^{2-}$	11	11(6)	4n+2	14n+2=14(6)+2=86	CLOSO, $C^0C[M6]$
40	$Pt_6(CO)_{12}^{2-}$	11	11(6)	4n+2	14n+2=14(6)+2=86	CLOSO, $C^0C[M6]$
41	$Ru_4(CO)_9L_2$	11	11(6)	4n+2	14n+2=14(6)+2=86	CLOSO, $C^0C[M6]$
42	$Fe_2Rh_4(CO)_{16}^{2-}$	11	11(6)	4n+2	14n+2=14(6)+2=86	CLOSO, $C^0C[M6]$
43	$FeRh_5(CO)_{16}^-$	11	11(6)	4n+2	14n+2=14(6)+2=86	CLOSO, $C^0C[M6]$
44	$Rh_5Pt(CO)_{15}^-$	11	11(6)	4n+2	14n+2=14(6)+2=86	CLOSO, $C^0C[M6]$
45	$Fe_3Rh(N)(CO)_{15}^{2-}$	11	11(6)	4n+2	14n+2=14(6)+2=86	CLOSO, $C^0C[M6]$
46	$Ru_6(C)(CO)_{16}(L)$	11	11(6)	4n+2	14n+2=14(6)+2=86	CLOSO, $C^0C[M6]$
47	$Fe_4Rh_2(N)(CO)_{15}^-$	11	11(6)	4n+2	14n+2=14(6)+2=86	CLOSO, $C^0C[M6]$
48	$Fe_3Ir(N)(CO)_{15}^{2-}$	11	11(6)	4n+2	14n+2=14(6)+2=86	CLOSO, $C^0C[M6]$
49	$Rh_2Os_4(CO)_{18}$	11	11(6)	4n+2	14n+2=14(6)+2=86	CLOSO, $C^0C[M6]$
50	$Ni_6(CO)_{13}$	11	11(6)	4n+2	14n+2=14(6)+2=86	CLOSO, $C^0C[M6]$
51	$Co_6(C)(CO)_{12}^{4-}$	11	11(6)	4n+2	14n+2=14(6)+2=86	CLOSO, $C^0C[M6]$

- IDENTICAL OR SIMILAR GEOMETRY

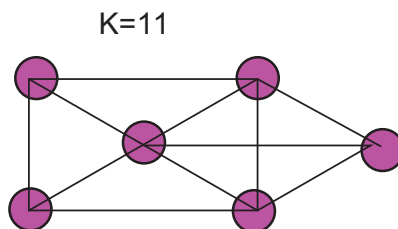
Taking the  $K(n) = 11(6)$  example, the ideal shape of this parameter is  $O_h$  symmetry. This is sketched in Figure F-1.



### IDEAL OCTAHEDRAL SKELETAL SHAPE BASED ON 4n SERIES

#### F-1

However, in special cases, K-isomerism occurs and a different shape with the same K value is observed. A good example is  $\text{H}_2\text{Os}_6(\text{CO})_{18}$ ;  $K(n) = 11(6)$  which portrays a capped square pyramid shape as sketched in Figure F-2 (Hughes and Wade, 2000).



#### • CLUSTER INTERCONVERSIONS

Let us remain with  $K(n) = 11(6)$  as an example. This parameter belongs to  $S = 4n+2(\text{CLOSO})$  series. If we need to determine the borane equivalent of the series, then we use the  $[\text{BH}]$  fragment which has a content of 4 electrons which will replace the [4] position in the series formula and then  $n = 6$  and 2 will be the 2 electrons for closo systems. Hence, the borane cluster will be given by  $\text{FB} = [\text{BH}](6) + 2e = \text{B}_6\text{H}_6^{2-}$ . In order to derive the osmium equivalent cluster, we have to use the [14] electron content. Thus,  $S = 14n+2$ ;  $\text{F}_{\text{Os}} = [\text{Os}(\text{CO})_3](6) + 2e = \text{Os}_6(\text{CO})_{18}^{2-}$ . We can also use it to derive the rhodium analogue:  $\text{F}_{\text{Rh}} = [\text{Rh}(\text{H})(\text{CO})_2](6) + \text{CO} = \text{Rh}_6(\text{H})_6(\text{CO})_{12} + \text{CO} = \text{Rh}_6(\text{CO})_3(\text{CO})_{12} + \text{CO} = \text{Rh}_6(\text{CO})_{16}$ . The clusters,  $\text{B}_6\text{H}_6^{2-}$ ,  $\text{Os}_6(\text{CO})_{18}^{2-}$  and  $\text{Rh}_6(\text{CO})_{16}$  are well known (Housecroft & Sharpe, 2005). In the case of rhenium,  $\text{F}_{\text{Re}} = [\text{Re}(\text{H})(\text{CO})_3](6) + \text{CO} = \text{Re}_6(\text{H})_6(\text{CO})_{18} + \text{CO} = \text{Re}_6(\text{CO})_3(\text{CO})_{18} + \text{CO} = \text{Re}_6(\text{CO})_{22}$ . One of the rhenium octahedral clusters has the formula  $\text{Re}_6(\text{C})(\text{CO})_{19}^{2-}$  (Hughes & Wade, 2000). According to the series method, this is the same as  $\text{Re}_6(\text{CO})_{22}$ . What about Zintl clusters? Consider group 14 cluster such as lead:  $\text{F}_{\text{Pb}} = 4n+2 = [\text{Pb}](6) + 2e = \text{Pb}_6^{2-}$ . What type of ideal Zintl cluster of bismuth with  $K(n) = 11(6)$  can we expect? In this case, we have to remove ONE electron from bismuth to conform to a 4n electron system. Hence,  $\text{Bi}-1e = \text{Bi}^+$ . Applying the series formula,  $S = 4n+2(n=6)$ ;  $\text{F}_{\text{Bi}} = [\text{Bi}^+](6) + 2e = \text{Bi}_6^{6+} + 2e = \text{Bi}_6^{4+}$ . This cluster has the K value  $= 6[1.5] + 2 = 11$ ;  $K(n) = 11(6)$ . Most of the information we can derive from the  $K(n)$  parameter is summarized in the sketch shown in Figure SC-8.

#### • CLUSTER VALENCE ELECTRONS

The calculation of cluster number K has already been explained in the chemical clusters CC-1 to CC-15 as well as in the examples given in Table 2. The skeletal numbers of elements are obtained from the appendices 1 and 2. When the K value and the number of skeletal elements are known, then this gives us the  $K(n)$  parameter of the cluster from which the series formula is derived as summarized in the scheme SC-2 (page 14). The valence electrons of the cluster are directly calculated using the same series equation  $S = 4n+q$  [ $\text{Ve} = 4n+q$  for the main group element clusters or  $\text{Ve} = 14n+q$  for transition metal clusters]. When the cluster comprises of both main group and transition metal elements, the calculation is adjusted to take into account the presence of transition metal elements due to the isolobal series relationship [ $S = 4n+q \leftrightarrow S = 10n+q$ ] observed in previous work (Kiremire, 2015C).

- (a)  $\text{B}_6\text{H}_6^{2-}$ :  $K = 6[2.5] - 3 - 1 = 11$ ;  $K(n) = 11(6)$ ,  $K = 2n - \frac{1}{2}q = 11 = 2(6) - \frac{1}{2}q$ ,  $\frac{1}{2}q = 12 - 11 = 1$ ,  $q = 2$ ;  $S = 4n+q = 4n+2$ . Fortunately, the number of cluster valence electrons (Ve) is directly obtained by using the same series formula

by simply substituting the value of  $n$  in the series formula. In this case,  $n = 6$  (number of boron skeletal elements) and hence,  $Ve = 4(6) + 2 = 26$ . This number of cluster valence electrons can be checked from the valence electrons calculated from the cluster formula itself; thus  $VF = 6[3] + 6(1) + 2 = 18 + 6 + 2 = 26$ . In case of transition metal clusters,  $S = 14n + q$  and the cluster valence electrons will be given by  $Ve = 14n + q$ . This is illustrated in the following example of the osmium cluster.

- (b)  $Os_6(CO)_{18}^{2-}$ :  $K = 6[5] - 18 - 1 = 11$ ,  $K(n) = 11(6)$ ,  $S = 4n + 2$ ,  $Ve = 14n + 2 = 14(6) + 2 = 86$ . This value can be compared to the value obtained from the cluster formula,  $VF = 6[8] + 18(2) + 2 = 86$ . The following example is a boron cluster with one metal skeletal element. The series formula is derived in the usual way and the valence electrons are determined by making an adjustment of one transition metal atom.
- (c)  $B_4H_8(CoCp)$ :  $K = 4[2.5] - 4 + 1[4.5 - 2.5] = 8$ ,  $K(n) = 8(5)$ ,  $S = 4n + 4$ ;  $Ve = 4n + 4 + 1[10] = 4(5) + 2 + 10 = 32$
- (d)  $P_2Co_2(CO)_6$ :  $K = 2[1.5] + 2[4.5] - 6 = 6$ ;  $n = 2 + 2 = 4$ ;  $K(n) = 6(4)$ ;  $K = 2n - \frac{1}{2}q = 6 - 2(4) - \frac{1}{2}q$ ,  $\frac{1}{2}q = 4$ ; hence  $S = 4n + 4$ . In this example, the cluster valence electrons will be calculated by assuming that all the skeletal elements are main group elements,  $Ve = 4n + 4 + 2[10] = 4(4) + 4 + 20 = 40$ . Thus, the adjustment for the 2 transition metals is taken into account, giving us  $Ve = 20 + 20 = 40$ . This value can be checked from the calculation using the cluster formula,  $VF = 2[5] + 2[9] + 6(2) = 10 + 18 + 12 = 40$ .

- LIGAND DISTRIBUTIONS

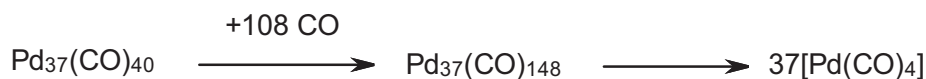
Skeletal numbers are very useful in the distribution of ligands among skeletal elements. This concept has been applied in many examples in this paper. Other examples can be found in literature (Kiremire, 2016b, 2017).

- DOUBLE MEANING OF  $K(n)$

Ex-3: Let us consider  $Os_6(CO)_{18}^{2-}$  example;  $K = 6[5] - 18 - 1 = 11$ ;  $K(n) = 11(6)$ ,  $S = 4n + 2$ . The parameter  $K(n) = 11(6)$  represents an octahedral shape. This means the skeletal elements are linked by 11 lines as in F-1. At the same time, it represents the number of electron pairs that will decompose the cluster into mono-skeletal fragments each of which will obey the 18 electron rule. This is illustrated in equation (i).



Thus 6 complexes of  $Os(CO)_5$  are generated each of which obeys the 18 electron rule. This principle applies to even huge clusters. Let us consider  $Pd_{37}(CO)_{28}L_{12}$ :  $K = 108$  (as calculated above);  $K(n) = 108(37)$ ;  $S = 4n - 74$ ,  $K_p = C^{35}C[M_2]$ . According to the series method, the giant cluster of 37 skeletal elements is bound by 108 skeletal linkages. It also has a nucleus of two skeletal elements  $[M_2]$  surrounded by 35 capping skeletal elements. This cluster, according to the series method, requires 108 electron pairs to be dismantled into individual mono-skeletal fragments each of which obeys the 18 electron rule. Since the CO ligand and L each donates 2 electrons to the skeletal elements, they are regarded as being equivalent. For simplicity, let us represent all of them by CO ligands. Then the cluster can be written as  $Pd_{37}(CO)_{40}$ . Since each CO ligand is 1 electron pair donor, then  $K = 108$  will be equivalent to 108 CO ligands. This is illustrated in equation (ii).

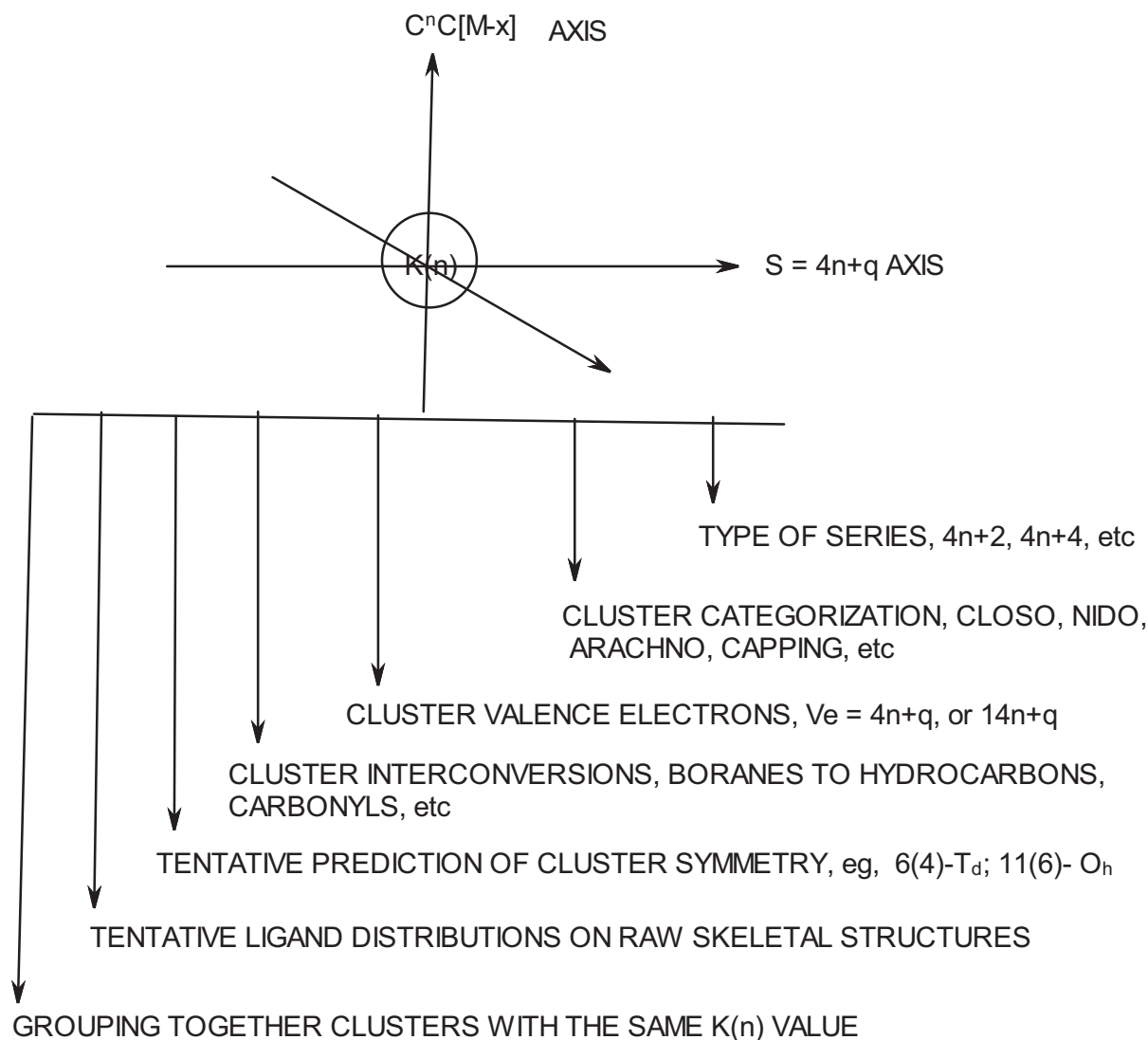


In this example, the addition of 108 CO ligands to the cluster results in the formation of 37 fragments of  $[Pd(CO)_4]$  each of which obeys the 18 electron rule.

Since each CO ligand carries a pair of electrons for donation as a ligand, then in the case of rhodium cluster,  $Rh_6(CO)_{16} + 11CO \rightarrow Rh_6(CO)_{27} \rightarrow 6[Rh(CO)_{4.5}]$ . Each fragment  $Rh(CO)_{4.5}$  obeys the 18 electron rule. Consider the cluster system:  $Te_2Ru_4(CO)_{11} + 9CO + 4H \rightarrow 4[Ru(CO)_5] + 2TeH_2$ . In this example,  $Ru(CO)_5$  obeys the 18 electron rule while  $TeH_2$  molecule obeys the 8 electron rule. The  $9CO + 4H$  donate an equivalent of 11 pairs of electrons when acting as ligands. Let us consider the last example  $B_6H_6^{2-} + 11(2H) \rightarrow B_6H_{30}^{2-} \equiv B_6H_{30} \rightarrow 6[BH_5]$ . The fragment  $BH_5$  obeys the 8 electron rule. In general, based on series analysis, the  $k(n)$  parameter represents both the number of  $k$  linkages that bind a cluster of  $n$  skeletal elements on one hand, and a shortage of  $k$  electron pairs needed for each of the skeletal elements concerned to attain a noble gas configuration, on the other hand.

- Summary of information derived from  $k(n)$  parameter

Most of the important information that can be derived from the  $K(n)$  parameter is summarized in Figure SC-8. This includes, among others, the type of series, the cluster valence electrons, the possible shape of a cluster, and so on.



## SC-8

## 3.11 The Diagonal Series and the Shrinking Nucleus

The diagonal series of clusters are also very interesting. Let us consider  $\text{Rh}_6(\text{CO})_{16}$  as an illustration. This cluster as we know has an octahedral symmetry with  $K(n)=11(6)$  parameter. It is a family member of the closo series,  $S=4n+2$ . Its cluster valence electrons are given by  $V_e = 14n+2 = 14(6)+2 = 86$ . If we remove a CO ligand we will get  $\text{Rh}_6(\text{CO})_{15}$  with a  $K(n)=12(6)$ . This belongs to the series  $S=4n+0$  with  $K_p = C^1C[M5]$ . Its cluster valence electron content is given by  $V_e = 14n+0 = 14(6)+0 = 84$ . The removal of the next CO ligand we will get  $\text{Rh}_6(\text{CO})_{14}$  with a corresponding  $K(n)$  value of 13(6). This belongs to the series  $S = 4n-2$  with  $K_p = C^2C[M4]$ . The cluster valence content will be  $V_e = 14n-2 = 14(6)-2 = 82$ . The cluster becomes a bi-capped closo tetrahedron. The next cluster will be  $\text{Rh}_6(\text{CO})_{13}$  with  $K(n) = 14(6)$ . The corresponding series for this is  $S = 4n-4$ . This cluster will have a capping symbol  $K_p = C^3C[M3]$ . This is a tri-capped closo triangle. The next cluster of the series is  $\text{Rh}_6(\text{CO})_{12}$ . This has a  $K(n)$  parameter of 15(6). It belongs to the series  $S=4n-6$ ,  $K_p = C^4C[M2]$ . According to the series, the cluster will have 2 of its skeletal elements in the nucleus and 4 capping skeletal elements. The next fragment is  $\text{Rh}_6(\text{CO})_{11}$  with  $K = 16$ . Its cluster parameter is  $K(n) = 16(6)$ . Its cluster series will be  $S = 4n-8$  and  $K_p = C^5C[M1]$ . This is a cluster with a single skeletal element at the nucleus with 5 capping skeletal elements. The entire sequence of  $K(n)$  numbers will be:  $11(6)[\text{Rh}_6(\text{CO})_{16}] \rightarrow 12(6)[\text{Rh}_6(\text{CO})_{15}] \rightarrow 13(6)[\text{Rh}_6(\text{CO})_{14}] \rightarrow 14(6)[\text{Rh}_6(\text{CO})_{13}] \rightarrow 15(6)[\text{Rh}_6(\text{CO})_{12}] \rightarrow 16(6)[\text{Rh}_6(\text{CO})_{11}] \rightarrow 17(6)[\text{Rh}_6(\text{CO})_{10}] \rightarrow 18(6)[\text{Rh}_6(\text{CO})_9] \rightarrow 19(6)[\text{Rh}_6(\text{CO})_8] \rightarrow 20(6)[\text{Rh}_6(\text{CO})_7] \rightarrow 21(6)[\text{Rh}_6(\text{CO})_6] \rightarrow 22(6)[\text{Rh}_6(\text{CO})_5] \rightarrow 23(6)[\text{Rh}_6(\text{CO})_4] \rightarrow 24(6)[\text{Rh}_6(\text{CO})_3] \rightarrow 25(6)[\text{Rh}_6(\text{CO})_2] \rightarrow 26(6)[\text{Rh}_6(\text{CO})_1] \rightarrow 27(6)[\text{Rh}_6(\text{CO})_0]$  [ $S = 4n-30$ ]. These diagonal  $K(n)$  numbers are highlighted in RED in Table 2 and converted into series in Table 5. This movement

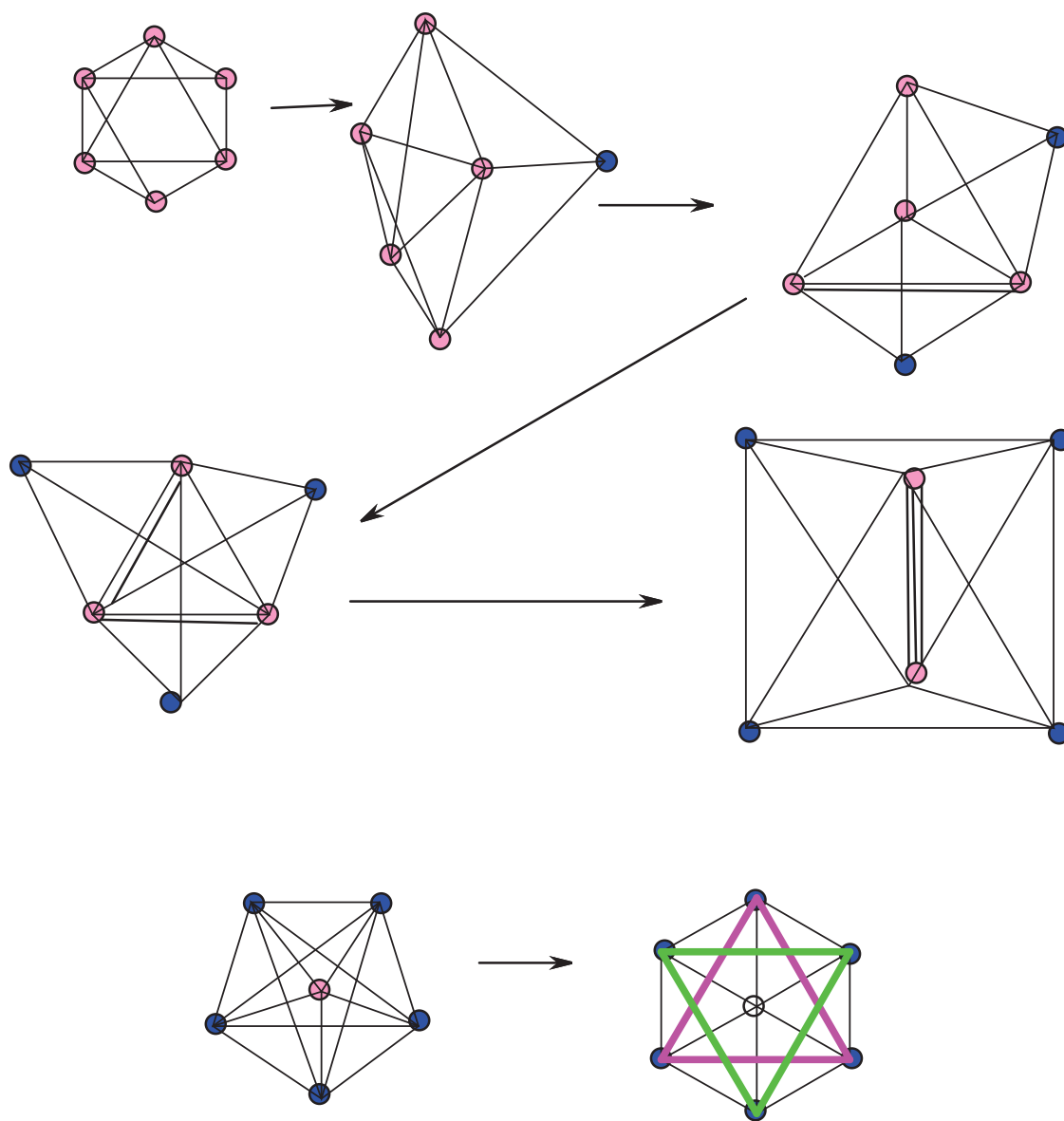
involving the removal of a co ligand step-wise may be described as stripping series. In the stripping series  $K_p = C^yC[M_x]$ , both the nuclear index  $x$  and the capping index  $y$  change as we move from one step to the next. We also notice that as  $y$  increases,  $x$  decreases and vice versa. In the example of the octahedral cluster  $Rh_6(CO)_{16}$ , the nuclear index  $x$  goes from 6 to 0 where all the 6 rhodium skeletal elements are capped. These changes are diagrammatically expressed in figure SC-17 below. Using the rhodium carbonyl cluster,  $Rh_6(CO)_{16}$  as a reference for illustration, the cluster is a member of the CLOSO family,  $S = 4n+2$ ,  $K(n) = 12(6)$  and  $K_p = C^0C[M6]$ . This is a 'borderline' cluster with zero capping skeletal element. When a CO ligand is removed via stripping, it becomes  $Rh_6(CO)_{15}$ ,  $K = 12(6)$ ,  $K_p = C^1C[M5]$ . This represents a mono-capped trigonal bipyramid geometry. The next stripping of a CO ligand creates,  $K_p = C^2C[M4]$  which is a bi-capped tetrahedral cluster. The next stripping gives us  $K_p = C^3C[M3]$  cluster which is a triangular tri-capped cluster. This is followed by a tetra-capped cluster with a two bi-skeletal nuclear cluster,  $K_p = C^4C[M2]$ . Further stripping generates  $K_p = C^5C[M1]$  which is a penta-capped mono-skeletal nuclear cluster. The next stripping creates a cluster  $K_p = C^6C[M0]$  where all the skeletal elements are capping and the nucleus is empty.

#### Blackholes in the Nucleus and Ghost Skeletal Elements

Further stripping creates clusters with negative nuclear indices. Thus, the cluster number 8 in Table 5,  $Rh_6(CO)_9$ ;  $K(n) = 18(6)$ ,  $K_p = C^7C[M-1]$ ; shows that it has 7 capped skeletal elements. However in reality, the cluster has 6 skeletal elements not 7. Hence, we can regard the seventh elements as fictitious and just a creation of the series. We may call such an element created by the series as a hole or a ghost skeletal element. A closer look at Table 5 shows that the capping elements are being taken from the nucleus. When  $[M0]$  becomes  $[M-1]$ , it means the capping fictitious element has been 'borrowed' from a nucleus which did not have any at all, hence  $[M_x]$ ,  $x = -1$  or according to series,  $n = -1$  at the nucleus. Since the nucleus is a member of CLOSO family,  $S = 4n+2$  and  $K = 2n-1 = 2(-1)-1 = -3$ . This means the cluster nucleus is indebted with -3 cluster linkages. As  $x$  in  $[M_x]$  becomes  $x \leq 0$ , the number of nuclear skeletal linkages becomes more and more negative. We may regard such nuclei as having BLACK HOLES since they seem to be swallowing skeletal linkages. When all the CO ligands have been removed from  $Rh_6(CO)_{16}$  to become completely naked, cluster number 17 Table 5,  $Rh_6$ ;  $K(n) = 27(6)$ ; and  $K_p = C^{16}C[M-10]$ . We can interpret this to mean that there are 16 capping skeletal elements, 6 genuine ones and 10 ghost ones borrowed from the cluster nucleus which develops a huge black-hole of  $n = -10$  and  $K = 2n-1 = 2(-10)-1 = -21$  skeletal linkages. Can we then regard a cluster with a nucleus possessing a black-hole and ghost capping skeletal elements as a characteristic of a metallic character of a cluster? The nuclear changes in the stripping series of  $Rh_6(CO)_{16}$  up to  $[M0]$  are illustrated in SC-9. The decomposition fragments of  $Rh_6(CO)_{16}$  are shown in Table 5.

On the other hand, the addition of CO ligands to the  $Rh_6(CO)_{16}$  cluster reduces the K value from  $K = 11$  to finally  $K = 5$ , the limiting K value when the cluster behaves as a saturated hydrocarbon analogue.

The cluster  $Pd_{23}(CO)_{20}L_{10}$ ;  $K(n) = 62(23)$ ;  $S = 4n-32$ ,  $K_p = C^{17}C[M6]$ ; was chemically converted into  $Pd_{23}(CO)_{20}L_8$ ;  $K(n) = 64(23)$ ;  $S = 4n-36$ ,  $K_p = C^{19}C[M4]$ . The two clusters were found to have different skeletal structures (Mednikov and Dahl, 2010). The former is described to have a  $Pd_{19}$  pseudo octahedral while the latter has a  $Pd_{15}$  kernel hexa-capped cubic with 8 capping Pd elements. The transformation can be explained using series in that  $Pd_{23}(CO)_{20}L_{10}$  has a K value of 62 with an octahedral nucleus  $[M6]$  while the cluster  $Pd_{23}(CO)_{20}L_8$  has a K value of 64 with a tetrahedral nucleus. According to the series method, the two clusters of the same nuclearity differ by 2 electron donor ligands and hence as expected as in line with the case of rhodium clusters discussed in SC-17, the removal of a ligand from a cluster of the same nuclearity results in the increase of K value and increase in the degree of capping. In the case of capping clusters, the increase in the capping corresponds to the decrease of the number of atoms in the nucleus. An increase in K value by 1 is accompanied by a decrease in the number of nuclear skeletal elements by 1. What was also found to be exciting is the discovery that the series method predicts that the clusters  $Pt_{38}(CO)_{44}^{2-}\{C^{32}C[M6]\}$ ,  $H_{6-n}Pt_6Ni_{38}(CO)_{48}^{n-}\{C^{38}C[M6]\}$ ,  $Pt_9Ni_{35}(CO)_{48}^{6-}\{C^{38}C[M6]\}$ , and  $Pd_8Ni_{36}(CO)_{48}^{6-}\{C^{38}C[M6]\}$  possess an octahedral nucleus and indeed they have all been described to have octahedral cores (Mednikov and Dahl, 2010). The series method can also be useful in rapid categorization of the products encountered in EDESI-MS work (Bucher, 2003). An illustration is given in Table 6.



SC-9

Table 5. Illustration of the Shrinking Nucleus of Diagonal Series

	CLUSTER	K	K(n)	SERIES, S	Kp
1	Rh <sub>6</sub> (CO) <sub>16</sub>	6[4.5]-16 =11	11(6)	4n+2	C <sup>0</sup> C[M6]
2	Rh <sub>6</sub> (CO) <sub>15</sub>	6[4.5]-15 =12	12(6)	4n+0	C <sup>1</sup> C[M5]
3	Rh <sub>6</sub> (CO) <sub>14</sub>	6[4.5]-14 =13	13(6)	4n-2	C <sup>2</sup> C[M4]
4	Rh <sub>6</sub> (CO) <sub>13</sub>	6[4.5]-13 =14	14(6)	4n-4	C <sup>3</sup> C[M3]
5	Rh <sub>6</sub> (CO) <sub>12</sub>	6[4.5]-12 =15	15(6)	4n-6	C <sup>4</sup> C[M2]
6	Rh <sub>6</sub> (CO) <sub>11</sub>	6[4.5]-11 =16	16(6)	4n-8	C <sup>5</sup> C[M1]
7	Rh <sub>6</sub> (CO) <sub>10</sub>	6[4.5]-10 =17	17(6)	4n-10	C <sup>6</sup> C[M0]
8	Rh <sub>6</sub> (CO) <sub>9</sub>	6[4.5]-9 =18	18(6)	4n-12	C <sup>7</sup> C[M-1]
9	Rh <sub>6</sub> (CO) <sub>8</sub>	6[4.5]-8 =19	19(6)	4n-14	C <sup>8</sup> C[M-2]
10	Rh <sub>6</sub> (CO) <sub>7</sub>	6[4.5]-7 =20	20(6)	4n-16	C <sup>9</sup> C[M-3]
11	Rh <sub>6</sub> (CO) <sub>6</sub>	6[4.5]-6 =21	21(6)	4n-18	C <sup>10</sup> C[M-4]
12	Rh <sub>6</sub> (CO) <sub>5</sub>	6[4.5]-5 =22	22(6)	4n-20	C <sup>11</sup> C[M-5]
13	Rh <sub>6</sub> (CO) <sub>4</sub>	6[4.5]-4 =23	23(6)	4n-22	C <sup>12</sup> C[M-6]
14	Rh <sub>6</sub> (CO) <sub>3</sub>	6[4.5]-3 =24	24(6)	4n-24	C <sup>13</sup> C[M-7]
15	Rh <sub>6</sub> (CO) <sub>2</sub>	26[4.5]-2 =25	25(6)	4n-26	C <sup>14</sup> C[M-8]
16	Rh <sub>6</sub> (CO) <sub>1</sub>	6[4.5]-1 =26	26(6)	4n-28	C <sup>15</sup> C[M-9]
17	Rh <sub>6</sub>	6[4.5]-0 =27	27(6)	4n-30	C <sup>16</sup> C[M-10]
	CLUSTER	K	K(n)	SERIES, S	Kp
	Rh <sub>6</sub> (CO) <sub>16</sub>	6[4.5]-16 =11	11(6)	4n+2	C <sup>0</sup> C[M6]
	Rh <sub>6</sub> (CO) <sub>17</sub>	6[4.5]-17 =10	10(6)	4n+4	C <sup>-1</sup> C[M7]
	Rh <sub>6</sub> (CO) <sub>18</sub>	6[4.5]-18 =9	9(6)	4n+6	C <sup>-2</sup> C[M8]
	Rh <sub>6</sub> (CO) <sub>19</sub>	6[4.5]-19 =8	8(6)	4n+8	C <sup>-3</sup> C[M9]
	Rh <sub>6</sub> (CO) <sub>20</sub>	6[4.5]-20 =7	7(6)	4n+10	C <sup>-4</sup> C[M10]
	Rh <sub>6</sub> (CO) <sub>21</sub>	6[4.5]-21 =6	6(6)	4n+12	C <sup>-5</sup> C[M11]
	Rh <sub>6</sub> (CO) <sub>22</sub>	6[4.5]-22 =5	5(6)	4n+14	C <sup>-6</sup> C[M12]

Table 6. Application of Series to Categorize the decomposition clusters from literature\*

Ru <sub>3</sub> (CO) <sub>12</sub> Decomposition products						
	K	n	K(n)	SERIES, S	Kp	Lit.
Ru <sub>6</sub> (CO) <sub>21</sub> <sup>2-</sup>	6[5]-21-1=8	6	8(6)	4n+8	C <sup>-3</sup> C[M9]	Raft
Ru <sub>6</sub> (CO) <sub>20</sub> <sup>2-</sup>	6[5]-20-1=9	6	9(6)	4n+6	C <sup>-2</sup> C[M8]	Raft
Ru <sub>7</sub> (CO) <sub>20</sub> <sup>2-</sup>	7[5]-20-1=14	7	14(7)	4n+0	C <sup>-1</sup> C[M6]	Mono-cap O <sub>h</sub>
Ru <sub>6</sub> (CO) <sub>18</sub> <sup>2-</sup>	6[5]-18-1=11	6	11(6)	4n+2	C <sup>0</sup> C[M6]	O <sub>h</sub>
Ru <sub>9</sub> (CO) <sub>23</sub> <sup>2-</sup>	9[5]-23-1=21	9	21(9)	4n-6	C <sup>4</sup> C[M5]	Tri-cap O <sub>h</sub>
Ru <sub>8</sub> (CO) <sub>21</sub> <sup>2-</sup>	8[5]-21-1= 18	8	18(8)	4n-4	C <sup>3</sup> C[M5]	Bi-cap O <sub>h</sub>
Ru <sub>7</sub> (CO) <sub>19</sub> <sup>2-</sup>	7[5]-19-1=15	7	15(7)	4n-2	C <sup>2</sup> C[M5]	Mono-cap O <sub>h</sub>
Ru <sub>6</sub> (CO) <sub>17</sub> <sup>2-</sup>	6[5]-17-1=12	6	12(6)	4n+0	C <sup>1</sup> C[M5]	Bi-cap T <sub>d</sub>
Ru <sub>5</sub> (CO) <sub>15</sub> <sup>2-</sup>	5[5]-15-1=9	5	9(5)	4n+2	C <sup>0</sup> C[M5]	Trigonalbipy
Ru <sub>4</sub> (CO) <sub>13</sub> <sup>2-</sup>	4[5]-13-1=6	4	6(4)	4n+4	C <sup>-1</sup> C[M5]	T <sub>d</sub>
Ru <sub>3</sub> (CO) <sub>11</sub> <sup>2-</sup>	3[5]-11-1=3	3	3(3)	4n+6	C <sup>-2</sup> C[M5]	Triangle
Ru <sub>9</sub> (CO) <sub>22</sub> <sup>2-</sup>	9[5]-22-1 =22	9	22(9)	4n-8	C <sup>5</sup> C[M4]	Tri-cap O <sub>h</sub>
Ru <sub>8</sub> (CO) <sub>20</sub> <sup>2-</sup>	8[5]-20-1=19	8	19(8)	4n-6	C <sup>4</sup> C[M4]	Bi-cap O <sub>h</sub>
Ru <sub>7</sub> (CO) <sub>18</sub> <sup>2-</sup>	7[5]-18-1=16	7	16(7)	4n-4	C <sup>3</sup> C[M4]	Mono-cap O <sub>h</sub>
Ru <sub>6</sub> (CO) <sub>16</sub> <sup>2-</sup>	6[5]-16-1=13	6	13(6)	4n-2	C <sup>2</sup> C[M4]	Bi-cap T <sub>d</sub>
Ru <sub>5</sub> (CO) <sub>14</sub> <sup>2-</sup>	5[5]-14-1=10	5	10(5)	4n+0	C <sup>1</sup> C[M4]	Trigonalbipy
Ru <sub>4</sub> (CO) <sub>12</sub> <sup>2-</sup>	4[5]-12-1=7	4	7(4)	4n+2	C <sup>0</sup> C[M4]	T <sub>d</sub>
Ru <sub>3</sub> (CO) <sub>10</sub> <sup>2-</sup>	3[5]-10-1=4	3	4(3)	4n+4	C <sup>-1</sup> C[M4]	Triangle
Ru <sub>6</sub> (CO) <sub>15</sub> <sup>2-</sup>	6[5]-15-1=14	6	14(6)	4n-4	C <sup>3</sup> C[M3]	Bi-cap T <sub>d</sub>
Ru <sub>5</sub> (CO) <sub>13</sub> <sup>2-</sup>	5[5]-13-1=11	5	11(5)	4n-2	C <sup>2</sup> C[M3]	Trigonalbipy
Ru <sub>3</sub> (CO) <sub>9</sub> <sup>2-</sup>	3[5]-9-1=5	3	5(3)	4n+2	C <sup>0</sup> C[M3]	Triangle
Ru <sub>6</sub> (CO) <sub>14</sub> <sup>2-</sup>	6[5]-14-1=15	6	15(6)	4n-6	C <sup>4</sup> C[M2]	Bi-cap T <sub>d</sub>

• Butcher, et al, 2003

## DIFFERENCES BETWEEN THE 4n SERIES METHOD AND THE SEP METHOD

Arising from the applications of the 4n series method, some salient features of the differences between the method and the existing SEP method have emerged.

## • TOOLS OF ANALYSIS OF CLUSTERS

The SEP method utilizes SEP and vertices concept to analyze the clusters while the 4n method utilizes the SKELETAL NUMBERS and the 4n series to analyze and categorize the clusters of skeletal elements from the main group and transition metals.

- CAPPING AND NON-CAPPING CLUSTERS

According to the  $4n$  series method, all clusters comprising of skeletal elements from the MAIN GROUP or TRANSITION METALS are interrelated and can all be analyzed using the skeletal numbers and the  $4n$  series method.

The series  $S = 4n+q(q \geq 2)$  are non-capping types while  $S = 4n+q(q \leq 0)$  represent capping clusters. The SEP method breaks clusters into groups such as  $4n$ ,  $5n$  and  $6n$  and finds some clusters which are described as “rule-breakers”. On the other hand, there are no rule-breakers in the  $4n$  series method.

- CLUSTER VALENCE ELECTRONS(cve)

The series method provides an easy method of calculating the cluster valence electrons directly from the series formula.

- INTER-CONVERSION OF CLUSTERS

The series formula can be used to generate analogous clusters in line with  $K(n)$  parameter. For instance,  $K(n) = 11(6)$ ,  $S = 4n+2(n=6)$  can be used to derive any appropriate octahedral cluster such as  $B_6H_6^{2-}$ ,  $Rh_6(CO)_{16}$  and  $Os_6(CO)_{18}^{2-}$ .

- THE  $K(n)$  PARAMETER WITH DOUBLE MEANING

The series method gives us a cluster number  $K$  which has a double meaning. For instance the oxygen atom has a  $K$  value of 1;  $O(K=1)$ . This means it has the potential of contributing 1 bond in its chemical activity.

Hence,  $O(K=1)+O(K=1) \rightarrow O_2(K=2)$ , that is, an oxygen molecule with a double bond,  $O=O$ . At the same time, for the single oxygen atom,  $K=1$ , which means it has a shortage of 1 electron pair so as to attain the octet rule;  $O+2e \rightarrow O^{2-}$ . The  $[O^{2-}]$  fragment obeys the octet rule. In the case of  $O_2(K=2)$  with a double bond, it also means this diatomic molecule needs 2 pairs of electrons so that each of the 2 skeletal atoms obey the octet rule, that is,  $O_2+2(2e) \rightarrow 2[O^{2-}]$ . According to the series,  $[H\bullet]$  and  $[1e]$  or  $[-1]$  are equivalent. Therefore the electron donations could take the form of hydrogen atoms:

$O+2H \rightarrow H_2O$ ;  $O_2+4H \rightarrow 2[H_2O]$ . Similarly,  $N(K=1.5)+3H \rightarrow NH_3$ ;  $N_2(K=3) \rightarrow N \equiv N$ ;  $N_2+3[2H] \rightarrow 2NH_3$  and  $[NH_3]$  molecule obeys the octet rule. This concept also applies equally well to large clusters. For instance,  $B_5H_9[K=5(2.5)-4.5=8]$ . This means that the 5 skeletal elements of B are bound by 8 linkages as shown in N51. The 8 linkages according to series also means that the cluster requires 8 pairs of electrons given directly as  $8(2e^-)$  or  $8(2H)$  atoms as ligands. That is,

$B_5H_9+8(2H) \rightarrow B_5H_{25} \rightarrow 5[BH_5]$ . The  $[BH_5]$  fragment obeys the octet rule. The  $[BH_5]$  fragment normally occurs in the form of  $[BH_4^-]$  cluster ion. Since the skeletal number of boron,  $K=2.5$ , its skeletal valence is 5 and this leads us to distribute the H ligands of  $B_5H_9$  to generate a raw skeletal structure as in F-2 and then propose a rearranged skeletal one in F-3 as is normally observed from x-ray structural analysis.

- BROAD CATEGORIZATION OF CLUSTERS

By analyzing the cluster series, it has been possible to identify 3 broader clusters series, namely, the vertical, diagonal and horizontal ones. With this knowledge, it has now been possible to categorize all the clusters derived from the main group/transition metals according to their respective closo family members,  $[M0]$ ,  $[M1]$ ,  $[M2]$ , and  $[M3]$  and so on. Being able to categorize clusters into groups, means that we have created a system of literally categorizing every cluster comprising of main group/transition metals with the help of a larger type of Rudolph system that operates numerically.

- CATEGORIZATION OF GOLDEN CLUSTERS

The series method has penetrated the golden clusters and showed that they all obey the cluster laws. As much as possible detailed analysis of each cluster regarding consistency with skeletal linkages and ligand distribution are explained for each cluster.

- THE STRIPPING SERIES OF CLUSTERS

The analysis and categorization of stripping series of clusters may assist in improvement of understanding and appreciation of the work by Butcher and his research groups (Butcher, et al, 2003).

- CATALYSIS

The concept can readily be applied in enhancing deeper understanding and selection of cluster catalysts such as the carbonyls. Selected examples of carbonyl tried for catalysis (Gates, 1995) are given in Table7. As can easily be seen from Table7, most of the clusters that have been tried in catalytic work belong to CLUSTER GROUP 5 OR GROUP 6. Furthermore, there is no sample of positive capping index,  $K_p = C^yC(y \geq 1)$  on the table list.



Table 7. Selected carbonyl clusters that have been tested for catalysis

T-7 CLUSTER	CATALYSIS K	n	K(n)	SERIES, S	CATEGORIZATION, Kp
Fe <sub>3</sub> (CO) <sub>12</sub>	3[5]-12 = 3	3	3(3)	4n+6	C <sup>-2</sup> C[M5]
Co <sub>4</sub> (CO) <sub>12</sub>	4[4.5]-12=6	4	6(4)	4n+4	C <sup>-1</sup> C[M5]
Os <sub>3</sub> (CO) <sub>12</sub>	3[5]-12 = 3	3	3(3)	4n+6	C <sup>-2</sup> C[M5]
Ir <sub>4</sub> (CO) <sub>12</sub>	4[4.5]-12=6	4	6(4)	4n+4	C <sup>-1</sup> C[M5]
Pt <sub>15</sub> (CO) <sub>30</sub> <sup>2-</sup>	15[4]-30-1 = 29	15	29(15)	4n+2	C <sup>0</sup> C[M15]
HFe <sub>3</sub> (CO) <sub>11</sub> <sup>-</sup>	3[5]-0.5-11-0.5=3	3	3(3)	4n+6	C <sup>-2</sup> C[M5]
H <sub>3</sub> Os <sub>4</sub> (CO) <sub>12</sub> <sup>-</sup>	4[5]-1.5-12-0.5=6	4	6(4)	4n+4	C <sup>-1</sup> C[M5]
HIr <sub>4</sub> (CO) <sub>11</sub> <sup>-</sup>	4[4.5]-0.5-11-0.5=6	4	6(4)	4n+4	C <sup>-1</sup> C[M5]
Ir <sub>6</sub> (CO) <sub>15</sub> <sup>2-</sup>	6[4.5]-15-1 = 11	6	11(6)	4n+2	C <sup>0</sup> C[M6]
Ru <sub>6</sub> (C)(CO) <sub>16</sub> <sup>2-</sup>	6[5]-2-16-1 = 11	6	11(6)	4n+2	C <sup>0</sup> C[M6]
Rh <sub>6</sub> (CO) <sub>16</sub>	6[4.5]-16 = 11	6	11(6)	4n+2	C <sup>0</sup> C[M6]
Os <sub>5</sub> (C)(CO) <sub>14</sub> <sup>2-</sup>	5[5]-2-14-1 = 8	5	8(5)	4n+4	C <sup>-1</sup> C[M6]
Os <sub>10</sub> (C)(CO) <sub>24</sub> <sup>2-</sup>	10[5]-2-24-1 = 23	10	23(10)	4n-6	C <sup>4</sup> C[M6]
Rh <sub>5</sub> (CO) <sub>15</sub> <sup>-</sup>	5[4.5]-15-0.5 = 7	5	7(5)	4n+6	C <sup>-2</sup> C[M7]
Pt <sub>6</sub> (CO) <sub>12</sub> <sup>2-</sup>	6[4]-12-1 = 11	6	11(6)	4n+2	C <sup>0</sup> C[M6]
Pt <sub>9</sub> (CO) <sub>18</sub> <sup>2-</sup>	9[4]-18-1 = 17	9	17(9)	4n+2	C <sup>0</sup> C[M9]
Pt <sub>12</sub> (CO) <sub>24</sub> <sup>2-</sup>	12[4]-24-1 = 23	12	23(12)	4n+2	C <sup>0</sup> C[M12]
H <sub>4</sub> Os <sub>4</sub> (CO) <sub>12</sub>	4[5]-2-12 = 6	4	6(4)	4n+4	C <sup>-1</sup> C[M5]
Ir <sub>6</sub> (CO) <sub>16</sub>	6[4.5]-16 = 11	6	11(6)	4n+2	C <sup>0</sup> C[M6]
Fe <sub>2</sub> (CO) <sub>6</sub> S <sub>2</sub>	2[5]+2[1]-6 = 6	4	6(4)	4n+4	C <sup>-1</sup> C[M5]
Fe <sub>3</sub> (CO) <sub>9</sub> S <sub>2</sub>	3[5]+2[1]-9 = 8	5	8(5)	4n+4	C <sup>-1</sup> C[M6]
Pt <sub>30</sub> (CO) <sub>60</sub> <sup>2-</sup>	30[4]-60-1 = 59	30	59(30)	4n+2	C <sup>0</sup> C[M30]

CLUSTER	K	n	K(n)	SERIES, S	CATEGORIZATION, Kp
Co <sub>2</sub> Ru <sub>2</sub> (CO) <sub>13</sub>	2[4.5]+2[5]-13 = 6	4	6(4)	4n+4	C <sup>-1</sup> C[M5]
Co <sub>3</sub> Ru(H)(CO) <sub>12</sub>	3[4.5]+1[5]-0.5-12=6	4	6(4)	4n+4	C <sup>-1</sup> C[M5]
Co <sub>2</sub> Ru <sub>2</sub> (CO) <sub>12</sub> H <sub>2</sub>	2[4.5]+2[5]-12-1 = 6	4	6(4)	4n+4	C <sup>-1</sup> C[M5]
CoRu <sub>3</sub> (CO) <sub>12</sub> H <sub>3</sub>	1[4.5]+3[5]-12-1.5 = 6	4	6(4)	4n+4	C <sup>-1</sup> C[M5]
Ru <sub>4</sub> H <sub>4</sub> (CO) <sub>12</sub>	4[5]-2-12 = 6	4	6(4)	4n+4	C <sup>-1</sup> C[M5]
Co <sub>3</sub> Rh(CO) <sub>12</sub>	3[4.5]+1[4.5]-12 = 6	4	6(4)	4n+4	C <sup>-1</sup> C[M5]
Co <sub>2</sub> Rh <sub>2</sub> (CO) <sub>12</sub>	2[4.5]+2[4.5]-12 = 6	4	6(4)	4n+4	C <sup>-1</sup> C[M5]
Rh <sub>4</sub> (CO) <sub>12</sub>	4[4.5]-12 = 6	4	6(4)	4n+4	C <sup>-1</sup> C[M5]
H <sub>3</sub> Re <sub>3</sub> (CO) <sub>12</sub>	3[5.5]-1.5-12=3	3	3(3)	4n+6	C <sup>-2</sup> C[M5]
Re <sub>2</sub> Pt(CO) <sub>12</sub>	2[5.5]+1[4]-12 = 3	3	3(3)	4n+6	C <sup>-2</sup> C[M5]

• POLYMERIZATION OF CLUSTERS

Let us consider two similar hypothetical reactions.

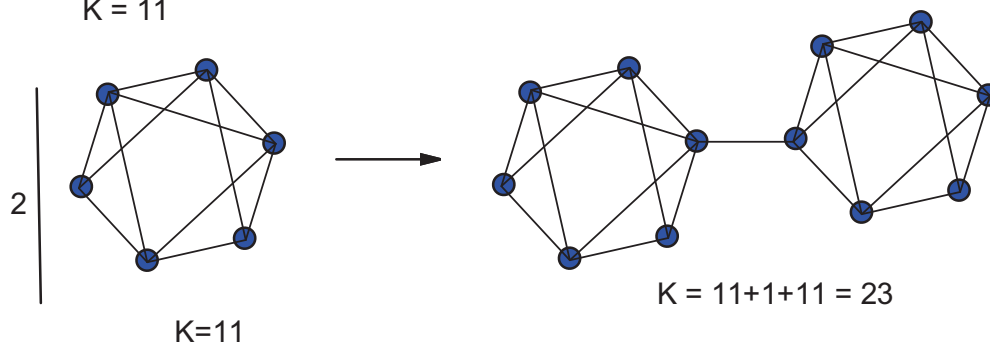
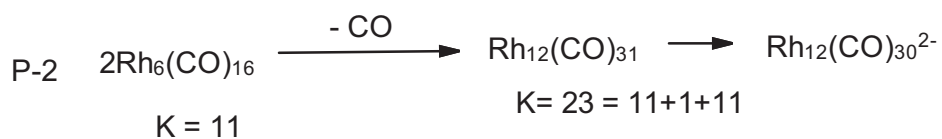
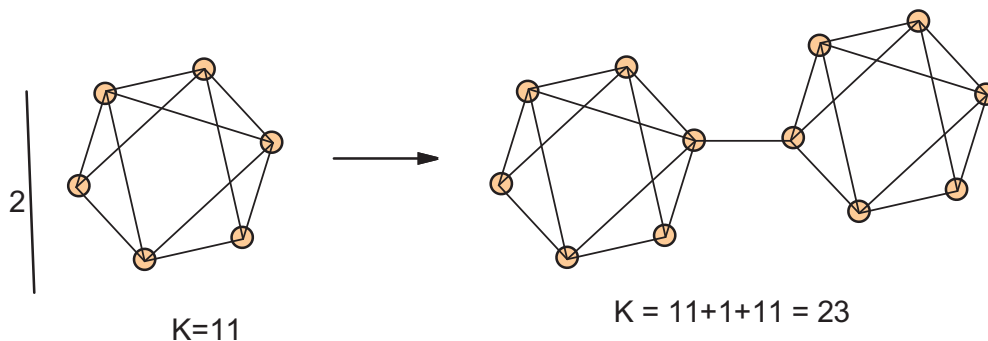
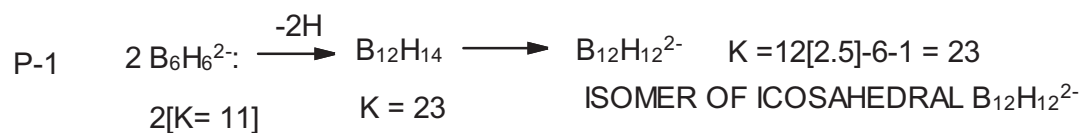
The dimerization of B<sub>6</sub>H<sub>6</sub><sup>2-</sup> (B<sub>6</sub>H<sub>8</sub>) to form B<sub>12</sub>H<sub>14</sub> in the form of (B<sub>12</sub>H<sub>12</sub><sup>2-</sup>) known product (Housecroft & Sharpe, 2005). In the case of the rhodium cluster Rh<sub>6</sub>(CO)<sub>16</sub>, the removal of a CO ligand creates an additional linkage for binding the two fragments, the cluster K value goes from 11 to 23 for the combined 2 fragments (11+1+11=23) according to the series to generate the dimeric cluster, Rh<sub>12</sub>(CO)<sub>31</sub> in the form Rh<sub>12</sub>(CO)<sub>30</sub><sup>2-</sup> (Housecroft & Sharpe, 2005). The hypothetical mechanism for the processes is given in P-1 and P-2. The possible extension of rhodium polymerization to produce longer chains is sketched in P-3.

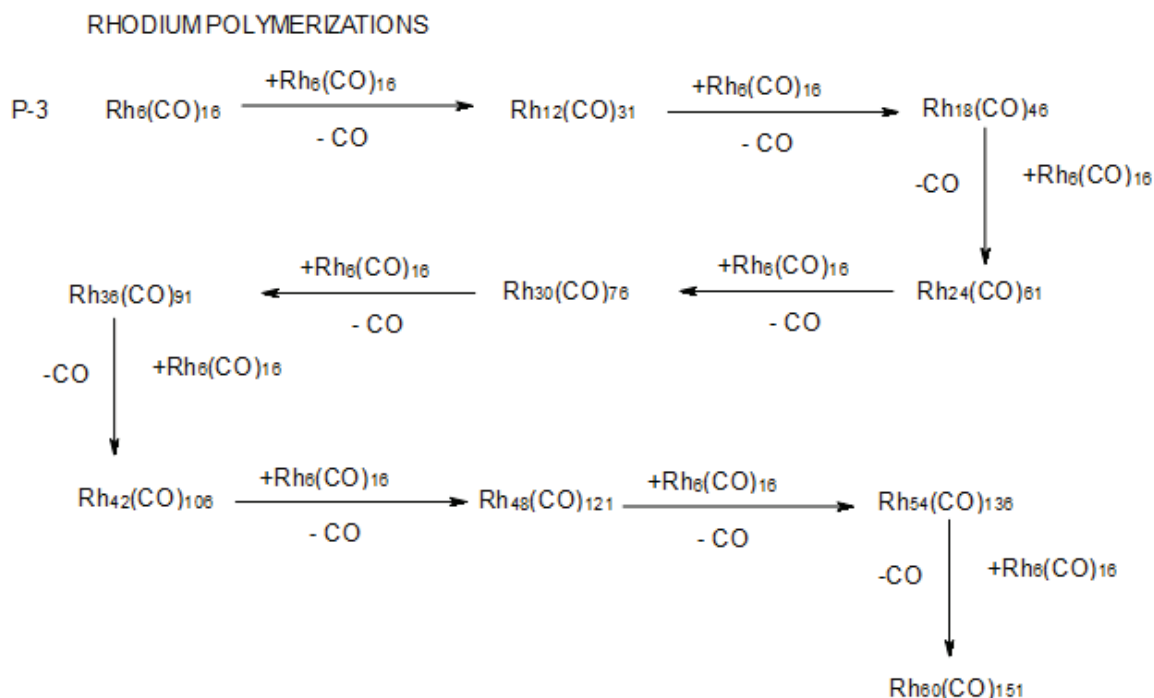
### 3.12 Unique Capping Clusters

Predicting the structures of clusters or unique structures: This may be illustrated by the two examples, Au<sub>6</sub>R<sub>6</sub>Br<sub>2</sub>(CO)<sub>2</sub><sup>2-</sup>, R = CF<sub>3</sub>; K = 6[3.5]-6(0.5)-2(0.5)-2(0.5) = 14, n = 6, K(n) = 14(6), S = 4n-4, Kp = C<sup>3</sup>C[M3]. This predicts a cluster of 3 closo skeletal nucleus surrounded by 3 other skeletal elements. According to series approach, the prediction is a closo nucleus of 3 skeletal elements surrounded by 3 capping skeletal elements. However what is observed are two sets of separate trinuclear clusters (Martinez-Salvado et al, 2015). This is sketched in N611. A similar prediction is found in the dinitrogenhexagolden cluster N<sub>2</sub>(AuL)<sub>6</sub><sup>2+</sup>: K = 2[1.5]+6[3.5-1]+1 = 19; n=2+6 = 8, K(n) = 19(8), S = 4n-6, Kp = C<sup>4</sup>C[M4]. Again two sets of 4 skeletal elements were observed (Gimeno, 2008). The predicted skeletal sketch and the observed one for N<sub>2</sub>(AuL)<sub>6</sub><sup>2+</sup> are sketched in N85. Another interesting cluster is Ni<sub>12</sub>As<sub>21</sub><sup>3-</sup>. The capping series Kp = C<sup>13</sup>C[M20] predicts a nucleus of 20 skeletal elements surrounded by 13 capping skeletal elements. However, what is observed is the other way round; a dome of 20 skeletal elements encapsulating 13 others. The sketch of the cluster is given in N331. The last cluster on this list is the rhenium selenium cluster Re<sub>6</sub>Se<sub>8</sub>I<sub>6</sub><sup>4-</sup>: It has a capping symbol Kp = C<sup>9</sup>C[M5]. The prediction here is that the cluster has a trigonal bipyramid nucleus surrounded by 9 capping elements.

The x-ray analytical interpretation of the structure is 8 selenium capping elements with an octahedral nucleus. This revelation is quite fascinating as the prediction is 9 skeletal elements by the series and the observed are 8. Since the series acts as a 'deaf and dumb' guide, this result is good enough and gives more confidence in understanding the language of the series method deeper. The cluster is sketched in N141.

### POLYMERIZATIONS





APPENDIX 1. SKELETAL NUMBERS OF MAIN GROUP ELEMENTS								
V*	7	6	5	4	3	2	1	0
K*(n=1)	3.5	3	2.5	2	1.5	1	0.5	0
K*	2n+1.5	2n+1	2n+0.5	2n+0	2n-0.5	2n-1	2n-1.5	2n-2
S	4n-3	4n-2	4n-1	4n+0	4n+1	4n+2	4n+3	4n+4
Ve*	1	2	3	4	5	6	7	8
	Li	Be	B	C	N	O	F	Ne
	Na	Mg	Al	Si	P	S	Cl	Ar
	K	Ca	Ga	Ge	As	Se	Br	Kr
	Rb	Sr	In	Sn	Sb	Te	I	Xe
	Cs	Ba	Tl	Pb	Bi	Po		Rn

V\* = skeletal valence, K\* = skeletal number, Ve\* = valence electrons, S = series

APPENDIX 2. SKELETAL NUMBERS OF TRANSITION METALS										
V*	15	14	13	12	11	10	9	8	7	6
K*(n=1)	7.5	7	6.5	6	5.5	5	4.5	4	3.5	3
K*	2n+5.5	2n+5	2n+4.5	2n+4	2n+3.5	2n+3	2n+2.5	2n+2	2n+1.5	2n+1
S	4n-11	4n-10	4n-9	4n-8	4n-7	4n-6	4n-5	4n-4	4n-3	4n-2
Ve*	3	4	5	6	7	8	9	10	11	12
E*	Sc	Ti	V	Cr	Mn	Fe	Co	Ni	Cu	Zn
	Y	Zr	Nb	Mo	Tc	Ru	Rh	Pd	Ag	Cd
	La	Hf	Ta	W	Re	Os	Ir	Pt	Au	Hg

V\* = skeletal valence, K\* = skeletal number, Ve\* = valence electrons, S = series

#### 4. Conclusion

Using skeletal numbers and the series method, chemical clusters have been divided into periodic groups. A capping symbol for non-capping clusters has been introduced. Sketching of clusters strictly following the rules of skeletal numbers and their valences according to series has been emphasized. This procedure has been termed "a simple graph theory of capping clusters". A wide range clusters have been sketched and tentative ligand distribution proposed. The golden clusters have generated very interesting and fascinating two dimensional geometrical structural frameworks. The grouping of clusters based on closo nuclear index will promote further understanding and possible synthesis of novel clusters and their applications.

#### Acknowledgement

The continued encouragement by Mrs. Merab Kambamu Kiremire to write up this paper and the editing assistance of Dr. P.E.T. Kiremire are greatly appreciated.

## References

- Brivio, E., Cariotti, A., Pergola, R. D., Garlaschalli, L., Demartin, F., Manassero, M., Sansoni, M., & Zanello, P. (1994). Synthesis and Solid-state structure of  $\text{Pd}_6\text{Ru}_6(\text{CO})_{24}^{2-}$ . *J. Chem. Soc.*, 3237-3231.
- Butcher, C. P. G., Dyson, P. J., Johnson, B. F. G., Khimiyak, J., & McIndoe, J. S. (2003). Fragmentation of Transition Metal Carbonyl Clusters Anions: Structural Insights from Mass Spectrometry. *Chem. Eur. J.*, 9(4), 944-950. <https://doi.org/10.1002/chem.200390116>
- Ciabatti, I. (2015). PhD Thesis. Homo- and Hetero-metal carbonyl Nanoclusters.
- Dyson, P. J., Hearley, A. K., Johnson, B. F. G., McIndoe, J. S., & Whyte, P. R. L. S. C. (2001). Combining energy-dependent electrospray ionization with tandem mass spectrometry for the analysis of inorganic compounds. *Rapid Comm. Mass Spec.*, 15, 885-897. <https://doi.org/10.1002/rcm.314>
- Fehlner, T. P., & Halet, J. F. (2007). *Molecular Clusters*, Cambridge University Press, UK. <https://doi.org/10.1017/CBO9780511628887>
- Gates, B. C. (1995). Supported metal clusters: Synthesis, Structure, and Catalysis. *Chem. Rev.*, 95, 511-522. <https://doi.org/10.1021/cr00035a003>
- Gimeno, M. C. (2008). *Modern Supramolecular Gold-Metal Interactive and Applications*. Edited A. Laguna, 2008. Wiley-VCH, Weinheim
- Greenwood, N. N., & Earnshaw, A. (1998). *Chemistry of the Elements*, 2<sup>nd</sup> Ed. Butterworth, Oxford.
- Housecroft, C. E., & Sharpe, A. G. (2005). *Inorganic Chemistry*, 2<sup>nd</sup> Ed., Pearson, Prentice Hall, Harlow, England
- Hughes, A. K., & Wade, K. (2000). Metal-metal and metal-ligand strengths in metal carbonyl clusters. *Coord. Chem. Rev.*, 197, 191-229. [https://doi.org/10.1016/S0010-8545\(99\)00208-8](https://doi.org/10.1016/S0010-8545(99)00208-8)
- Jemmis, E. D. (2005). Building relationships between polyhedral boranes and elemental boron. *Inorg. Chem.* 18, 620-628.
- Jemmis, E. D., & Prasad, D. L. V. K. (2008). Unknowns in the chemistry of Boron. *Current Science*, 95(10), 1277-1283.
- Jemmis, E. D., Jayasree, E. G., & Parameswaran, P. (2006). Hypercarbons in polyhedral structures. *Chem. Soc. Rev.*, 35, 157-168. <https://doi.org/10.1039/B310618G>
- Kiremire, E. M. (2014). Validation and verification of the Expanded Table for Transition Metal Carbonyl and Main Group Element Cluster Series which obey the 18-Electron and the 8-Electron Rules Respectively. *Orient. J. Chem.*, 30(4), 1475-1495. <https://doi.org/10.13005/ojc/300404>
- Kiremire, E. M. (2015a). Classification of Transition Metal Carbonyl Clusters Using the 14n Rule Derived from Number Theory. *Orient. J. Chem.*, 31(2), 605-618. <https://doi.org/10.13005/ojc/310201>
- Kiremire, E. M. (2015b). Categorization and Structural Determination of Simple and More Complex Carbonyl Clusters of Rhenium and Osmium Using K-values and the Cluster Table. *Orient. J. Chem.*, 31(1), 293-302. <https://doi.org/10.13005/ojc/310133>
- Kiremire, E. M. (2015c). Isolobal Series of Chemical Fragments. *Orient. J. Chem.*, 31(spl. Edn), 59-70.
- Kiremire, E. M. (2015d). Classification of Transition Metal Carbonyl Clusters Using the 14n Rule Derived from Number Theory. *Orient. J. Chem.*, 31(2), 605-618. <https://doi.org/10.13005/ojc/310201>
- Kiremire, E. M. R. (2016a). The categorization and Structural Prediction of Transition Metal Carbonyl Clusters Using the 14n Series Numerical Matrix. *Int. J. Chem.* 8(1), 109-125. <https://doi.org/10.5539/ijc.v8n1p109>
- Kiremire, E. M. R. (2016b). A Hypothetical Model for the Formation of Transition Metal Carbonyl Clusters Based Upon 4n Series Skeletal Numbers. *Int. J. Chem.*, 8(4), 78-110. <https://doi.org/10.5539/ijc.v8n4p78>
- Kiremire, E. M. R. (2016c). The Application of the 4n Series Method to Categorize Metalloboranes. *Int. J. Chem.*, 8(3), 62-73. <https://doi.org/10.5539/ijc.v8n3p62>
- Kiremire, E. M. R. (2016d). Classification of Zintl Ion Clusters Using 4n Series Approach. *Orient. J. Chem.*, 32(4), 1731-1738. <https://doi.org/10.13005/ojc/320401>
- Kiremire, E. M. R. (2017a). The Six Silent Laws of Chemical Clusters. *Amer. J. Chem.* 7(2), 21-47.
- Kiremire, E. M. R. (2017b). Outstanding Applications of Skeletal Numbers to Chemical Clusters. *Int. J. Chem.*, 9(3), 28-48. <https://doi.org/10.5539/ijc.v9n3p28>
- Kiremire, E. M. R. (2017c). Boranes, Carboranes, Metalloboranes, Transition Metal Carbonyls, and Other Cluster

- Formulas Obey the Law of Skeletal Numbers and Their Valences. *Amer. J. Chem.*, 7(4), 113-144.
- Kiremire, E. M. R. (2017d). Numerical Characterization of Chemical Fragments, Molecules, and Clusters Using Skeletal Numbers and Nuclearity Trees. *Amer. J. Chem.*, 7(3), 73-96.
- Konishi, K. (2014). Phosphine-coordinated Pure Gold-Clusters and Unique Optical Properties/Responses. *Structure and Bonding*, 161, 49-86. [https://doi.org/10.1007/430\\_2014\\_143](https://doi.org/10.1007/430_2014_143)
- Lipscomb, W. N. (1963). *Boron Hydrides*. W. A. Benjamin, Inc., New York.
- Luquin, A., Cerrada, E., & Laguna, M. (2009). Pentafluorophenyl gold complexes. *Gold Chemistry*, Edited, Mohr, F., Wiley-VCH, Wuppertal, Germany. <https://doi.org/10.1002/9783527626724.ch3>
- Martinez-Salvado, S., Falvello, L. R., Martin, A., & Menjón, B. (2015). A Hexanuclear gold carbonyl Cluster. *Chem. Sci.*, 6, 5506-5510. <https://doi.org/10.1039/C5SC01578B>
- McIndoe, J. S., & Henderson, M. S. (2013). Gas-phase reactivity of iron penta-carbonyls with anionic clusters. *Inter. J. Mass Spec.*, 354-355, 257-262.
- Mednikov, E. G., & Dahl, L. F. (2010). Synthesis, structures and properties of primarily nano-sized homo/hetero metallic palladium CO/PR<sub>3</sub> ligated clusters. *Phil., Trans., R. Soc. A*, 368, 1301-1332. <https://doi.org/10.1098/rsta.2009.0272>
- Mingos, D. M. P. (1972). A General Theory for Cluster and Ring Compounds of the Main Group and Transition Elements. *Nature(London), Phys. Sci.*, 236, 99-102. <https://doi.org/10.1038/physci236099a0>
- Mingos, D. M. P. (1984). Gold Cluster Compounds: Are they materials in miniature? *Gold Bull.*, 17(1), 5-12. <https://doi.org/10.1007/BF03214670>
- Mingos, D. M. P. (1987). Complementary spherical electron density model for coordination compounds. *Pure and Appl. Chem.*, 59(2), 145-154. <https://doi.org/10.1351/pac198759020145>
- Pergola, R. D., & Garlaschelli, L. (1990). *J. Chem. Soc., Dalton Trans.*, 127-135. <https://doi.org/10.1039/DT9900000127>
- Rossi, F., & Zanello, P. (2011). Electron Reservoir Activity of High-Nuclearity Transition Metal Carbonyl Clusters. *Portugaliae Electrochimica Acta*, 29(5), 309-327. <https://doi.org/10.4152/pea.201105309>
- Rudolph, R. W. (1976). Boranes and heteroboranes: a paradigm for the electron requirements of clusters? *Acc. Chem. Res.*, 9(12), 446-452. <https://doi.org/10.1021/ar50108a004>
- Teo, B. K., Longoni, G., & Chung, F. R. K. (1984). Applications of Topological Electron-Counting Theory to Polyhedral Metal Clusters. *Inorg. Chem.*, 23(9), 1257-1266. <https://doi.org/10.1021/ic00177a018>
- Wade, A. (1976). Structural and Bonding Patterns in Cluster Chemistry. *Adv. Inorg. Chem. Radiochem.*, 18, 1-66. [https://doi.org/10.1016/S0065-2792\(08\)60027-8](https://doi.org/10.1016/S0065-2792(08)60027-8)
- Wade, K. (1971). The structural significance of the number of skeletal bonding electron-pairs in carboranes, the higher boranes and borane ions and various transition metal carbonyl cluster compounds. *Chem. Commun.*, 792-793. <https://doi.org/10.1039/c29710000792>
- Welch, A. J. (2013). The significance of Wade's rules. *Chem. Commun.*, 49, 3615-3616. <https://doi.org/10.1039/c3cc00069a>
- Yvon, K. (2004). Transition Metal Hydride Complexes. *Encyclopedia of Materials and Science Technology*, 1-9.

## Copyrights

Copyright for this article is retained by the author(s), with first publication rights granted to the journal.

This is an open-access article distributed under the terms and conditions of the Creative Commons Attribution license (<http://creativecommons.org/licenses/by/4.0/>).

# Green Preparation of Sulfonated Polystyrene/Polyaniline/Silver Composites with Enhanced Anticorrosive Properties

Guangfu Liao

Correspondence: Guangfu Liao, Hubei Collaborative Innovation Center for Advanced Organic Chemical Materials, Ministry of Education Key Laboratory for The Green Preparation and Application of Functional Materials, Hubei University, Wuhan, Hubei 430062, China. E-mail:lgfhubu@163.com

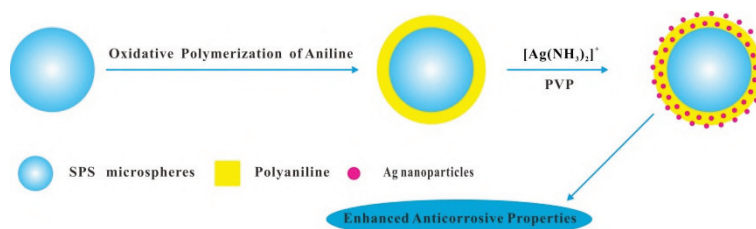
Received: December 22, 2017 Accepted: January 15, 2018 Online Published: January 25, 2018

doi:10.5539/ijc.v10n1p81

URL: <https://doi.org/10.5539/ijc.v10n1p81>

## Abstract

Sulfonated polystyrene/polyaniline/silver (SPS/PANI/Ag) composites with enhanced anticorrosive properties have been successfully prepared by using SPS microspheres as substrates and utilizing polyvinylpyrrolidone (PVP) as reducing agent and stabilizing agent. Our method is an environmentally friendly method because of the absence of any toxic reagents in the whole process. Fourier transform infrared Spectrum (FTIR), field emission scanning electron microscopy (FESEM), and energy disperse spectroscopy (EDX) results confirmed the formation of pure PANI, SPS/PANI composites, and SPS/PANI/Ag composites. Powder X-ray diffraction (XRD) patterns indicate that the obtained Ag nanoparticles are crystalline. The anticorrosive studies indicate that both SPS/PANI composites and SPS/PANI/Ag composites have enhanced anticorrosive properties in comparison to pure PANI in various corrosive environments.



**Keywords:** sulfonated polystyrene, polyaniline, silver, enhanced anticorrosive properties

## 1. Introduction

Polyaniline (PANI) is now regarded as a prominent anticorrosive material due to its low cost, unique oxidation–reduction chemistry, and environmental stability.( Kim, Lee, In, & Park, 2014) ( Yang et al., 2015) (Han et al., 2017) (Yuan et al., 2013) However, using single PANI particles as corrosive material have a series of problems such as poor processability, easy aggregation, dissatisfactory anticorrosive properties, etc.( Yang, Cao, & Tan, 2014) To solve the problem, many different approaches have been attempted, and a significant attempt to overcome these drawbacks is that using sulfonated polystyrene (SPS) microspheres as substrates to prepare SPS/PANI composites.( Liu et al., 2008) Using SPS microspheres as substrates can significantly improve the processability of PANI as well as reduce aggregation of PANI because SPS is similar to amphiphilic polymer.( Dai et al., 2011) In addition, the incorporation of silver (Ag) nanoparticles in PANI can obviously promote the anticorrosive properties of PANI because Ag nanoparticles exhibit excellent environmental stability and anticorrosive properties. (Zhao et al., 2005)

Combined with the above, in this work, we present a green approach to prepare SPS/PANI/Ag composites with enhanced anticorrosive properties through using SPS microspheres as substrates and utilizing PVP as reducing agent and stabilizing agent. Anticorrosive studies show that the prepared SPS/PANI/Ag composites have enhanced anticorrosive properties in comparison to pure PANI and SPS/PANI composites in various corrosive environments.

## 2. Materials and Methods

### 2.1 Materials

Polyvinylpyrrolidone (PVP, Mw=40000mol/g), absolute ethanol, silver nitrate ( $\text{AgNO}_3$ ,  $\geq 99.8\%$ ), sulfuric acid ( $\text{H}_2\text{SO}_4$ , 98%), hydrochloric acid (HCl), ammonia, Aniline (An), ammonium persulfate (APS) and waterborne alkyd resin (WAR) were purchased from Sinopharm Chemical Reagent Co., Ltd, China. Aniline was used after distillation. Monodisperse SPS microspheres were prepared according to the method of Deng.( Deng et al., 2012).

## 2.2 Preparation of Pure PANI

0.5 g of aniline and 20 mL of 2M HCl were added into 100 mL three-necked flask, and then the mixture of aniline and HCl was stirred in an ice bath for 5 h, finally added 1.2 g of APS (dissolved in 20 mL deionized water) aqueous solution by dropping slowly. The polymerization had been proceeding for 24 h by stirring slowly at 0 °C. The product was centrifuged, washed with deionized water and absolute ethanol several times, and then dried in vacuum at 50 °C for 24 h.

## 2.3 Preparation of SPS/PANI Composites

SPS powder (0.3 g) and aniline (0.05 g) monomer were dispersed in deionized water (40 mL) and 2 mL of 2M HCl with the aid of ultrasonic. The mixture of aniline and SPS was stirred in an ice bath for 5 h, and then added 0.12 g of APS (dissolved in 2 mL deionized water) aqueous solution by dropping slowly. The polymerization had been proceeding for 24 h by stirring slowly at 0 °C. The product was centrifuged, washed with deionized water and absolute ethanol several times, and then dried in vacuum at 50 °C for 24 h.

## 2.4 Preparation of SPS/PANI/Ag Composites

SPS/PANI composites (0.13 g) and PVP (1 g) was mixed with deionized water (50 mL) with the aid of ultrasonic. Then, 10 mL of freshly prepared aqueous solution of  $[\text{Ag}(\text{NH}_3)_2]^+$  (0.2 M) was quickly added into the above dispersion, magnetically stirred at room temperature for 1 h. Finally, this mixture was kept at 70 °C and stirred for 7 h under the atmosphere of nitrogen. The product was separated by centrifugation, and washed with deionized water several times, and then dried in vacuum at 50 °C for 24 h.

## 2.5 Characterization

Fourier transform infrared spectroscopy (FTIR) analysis of the samples was taken on a Spectrum One FTIR spectrometer (Perkin-Elmer Co., USA). Crystal structures of the samples were performed on an X-ray diffraction (XRD, D/MAX-IIIC, Japan), taken from 5° to 90°. The morphology and component of the samples were determined by Field emission scanning electron microscopy (FESEM, JSM7100F, Japan) and corresponding energy-dispersive X-ray spectroscopy (EDX).

## 2.6 Anticorrosion Tests

Throughout this work, Tafel plots were performed using an electrochemical workstation (CHI660D, CH Instruments Inc.) and carried out using a conventional three-electrode electrochemical cell with a Pt plate as counter electrode and an Ag/AgCl as reference electrode. The working electrode was the tinplate sample. The room temperature (25 °C) is the experimental temperature. Four tinplate samples were prepared, tinplate coated with waterborne alkyd resin, waterborne alkyd resin with 1% (w/w) PANI, waterborne alkyd resin with 1% (w/w) SPS/PANI and waterborne alkyd resin with 1% (w/w) SPS/PANI/Ag, coded as WAR, WAR/P, WAR/SP and WAR/SPA, respectively. NaCl 0.6M, NaOH 1M, and HCl 1M electrolytes were used as corrosive environment, respectively. During potentiodynamic polarization, the scanning voltage range was -0.1 ~ 0.1 V and the scan rate was 1 mV/s.

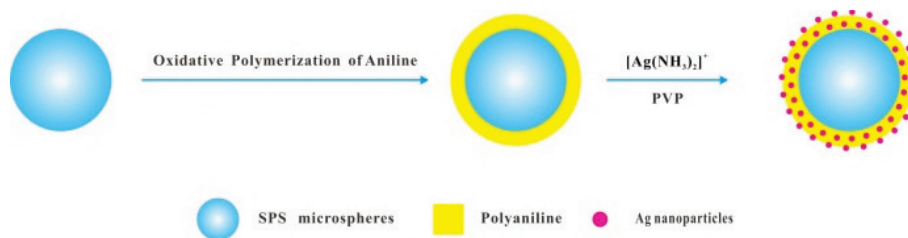


Figure 1. Schematic illustration of the formation of SPS/PANI/Ag composites

## 3. Results and Discussion

The detailed preparation process of SPS/PANI/Ag composites is illustrated in Figure 1. Firstly, aniline monomer is added into the SPS microspheres aqueous solution and then it is adsorbed onto the surfaces of the SPS microspheres. In this case, SPS/PANI composites are formed by polymerization of aniline on the surface of SPS microspheres. Then,  $[\text{Ag}(\text{NH}_3)_2]^+$  aqueous solution is added into the SPS/PANI composites aqueous solution and then it is adsorbed onto the surfaces of SPS/PANI composites. In this case, SPS/PANI/Ag composites are formed by the reduction of  $[\text{Ag}(\text{NH}_3)_2]^+$  ions with PVP. Neither additional reducing agent nor toxic organic solvents are added in the whole process. Therefore, our preparative method is environmentally friendly.

The FTIR spectra of pure PANI, SPS/PANI composites, and SPS/PANI/Ag composites is shown in Figure 2. The typical PANI absorption bands at 1597  $\text{cm}^{-1}$ , 1487  $\text{cm}^{-1}$ , 1300  $\text{cm}^{-1}$ , 1164  $\text{cm}^{-1}$ , 843  $\text{cm}^{-1}$  can be clearly seen in Figure 1a-c. The typical PS absorption bands at 3047  $\text{cm}^{-1}$ , 2929  $\text{cm}^{-1}$ , 1440  $\text{cm}^{-1}$ , 761  $\text{cm}^{-1}$ , 697  $\text{cm}^{-1}$  can be clearly seen in Figure

1b–c. The band at  $1042\text{ cm}^{-1}$  is related with  $-\text{SO}_3\text{H}$  groups can be clearly seen in Figure 1b-c, but this peak intensity is weak due to hydrolysis of  $-\text{SO}_3\text{H}$  groups. In addition, the characteristic peak of SPS/PANI and SPS/PANI/Ag is similar, but the peak intensity of SPS/PANI is greater than SPS/PANI/Ag. This phenomenon may be attributed to Ag nanoparticles making the peak intensity of SPS/PANI weaker. These results confirm the formation of pure PANI, SPS/PANI composites, and SPS/PANI/Ag composites.

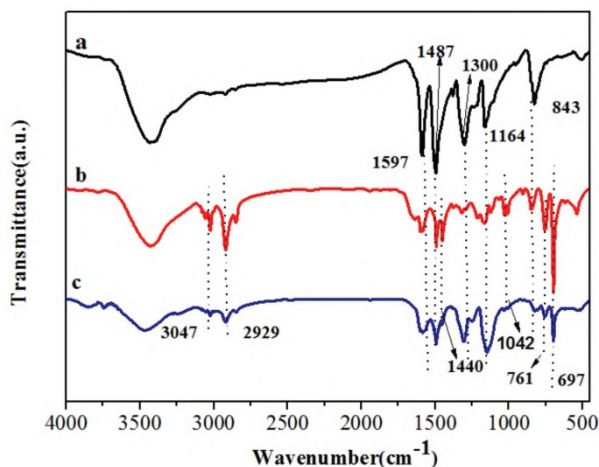


Figure 2. FTIR spectra of (a) pure PANI, (b) SPS/PANI composites, and (c) SPS/PANI/Ag composites

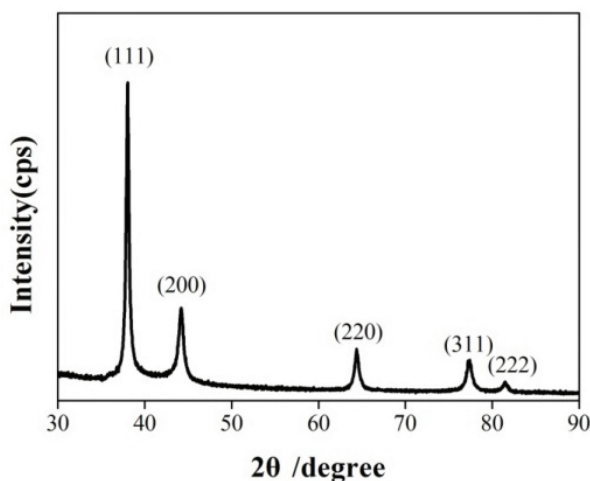


Figure 3. XRD patterns of SPS/PANI/Ag composites

The XRD patterns of SPS/PANI/Ag composites is shown in Figure 3. The XRD patterns of the SPS/PANI/Ag nanocomposites exhibits the sharp peaks at  $2\theta$  angles of  $38.0^\circ$ ,  $44.1^\circ$ ,  $64.3^\circ$ ,  $77.2^\circ$ , and  $81.5^\circ$ , which corresponds to (111), (200), (220), (311), and (222) crystal planes of Ag (JCPDS No.04–0783). (Liao et al., 2016) (Liao et al., 2017) (Liao et al., 2018) (Liao et al., 2017) This indicates that the Ag nanocrystallites have been obtained through the reduction of  $[\text{Ag}(\text{NH}_3)_2]^+$  ions with PVP.

The FESEM images and corresponding EDX spectra of pure PANI, SPS/PANI composites, and SPS/PANI/Ag composites have been shown in Figure 4. Figure 4a shows pure PANI particles are agglomerated. Figure 4b shows the SPS/PANI composites have many bulges on the surface of SPS microspheres. This indicates that PANI overlayer has formed on surface of SPS microspheres, but the PANI overlayer is not totally covered on the surface of SPS microspheres. It may be attributed to two possible reasons. First, the absence of strong electrostatic interaction between PANI and SPS. Second, PANI is a kind of rigid material, it is impossible to use PANI overlayer to cover completely SPS microspheres. Ag nanoparticles are found on the surfaces of the SPS/PANI composites with its size ranging from 50 to 70 nm (Figure S2c). Corresponding EDX spectra is shown in Figure 4d, Figure 4e, and Figure 4f. Note, Si element signals in high intensity observed in the all EDX spectra are originated silica wafer. As shown in Figure 4d, C and N element signals are observed in the EDX spectra of pure PANI. As shown in Figure 4e, C, O, S, and N element



signals are observed in the EDX spectra of SPS/PANI composites. As shown in Figure 4f, C, O, S, N, and Ag element signals are observed in the EDX spectra of SPS/PANI/Ag composites. These evidences demonstrate these products have been successfully prepared.

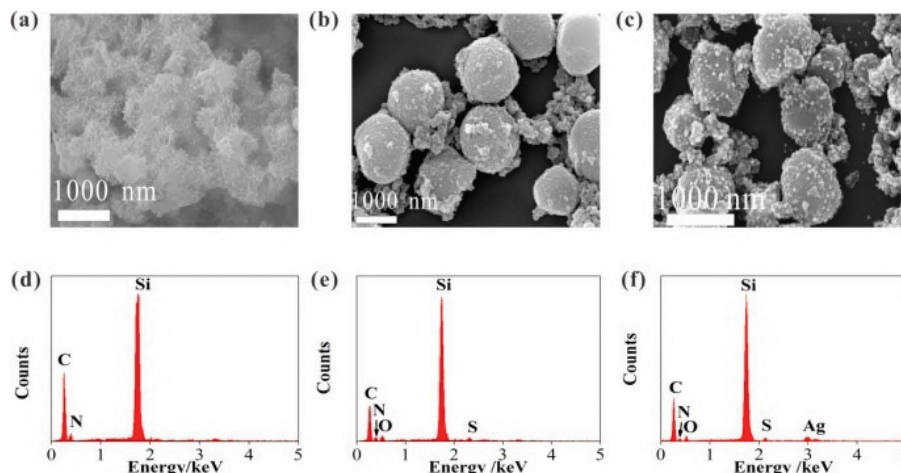


Figure 4. FESEM images and the corresponding EDX spectra of (a, d) pure PANI, (b, e) SPS/PANI composites, and (c, f) SPS/PANI/Ag composites

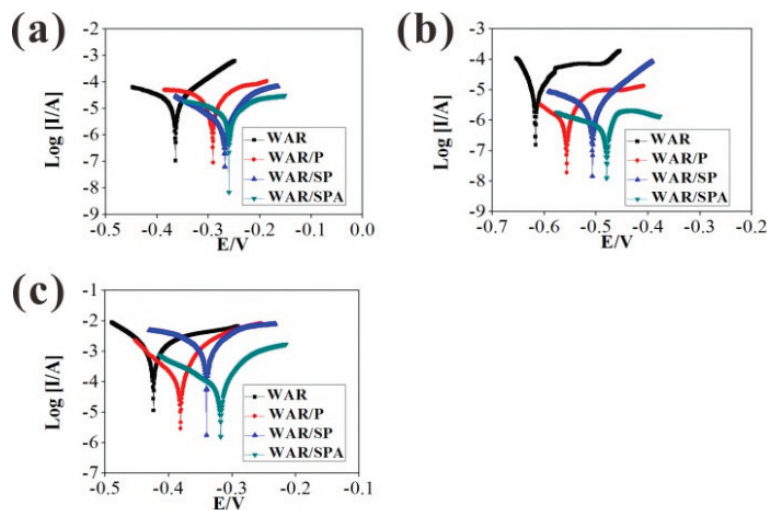


Figure 5. Tafel plots of WAR, WAR/P, WAR/SP, and WAR/SPA in NaCl 0.6M solutions (a), NaOH 1M solutions (b), and HCl 1M solutions (c), respectively

The Tafel plots analysis is used to evaluate the anticorrosive performance of WAR, WAR/P, WAR/SP and WAR/SPA. Figure 5 and Table 1 show that the corrosion potential of WAR/SPA is the highest, secondarily is WAR/SP, next is WAR/P, and the lowest is WAR in the following several corrosive environments. In other words, the anticorrosive properties of WAR/SPA is the best, secondarily is WAR/SP, next is WAR/P, and the worst is WAR in the following several corrosive environments. This result indicates that both WAR/SP and WAR/SPA exhibit improved enhanced anticorrosive properties. Moreover, WAR/SPA have better anticorrosive properties than WAR/SP. The enhancement is mainly attributed to the following two reasons. First, SPS microspheres are used as substrates can reduce aggregation of PANI particles. (Yang et al., 2005) Second, Ag nanoparticles have excellent environmental stability and anticorrosion property. (Liu et al., 2015)

Table 1. Corrosion current ( $I_{\text{corr}}$ ), corrosion potential ( $E_{\text{corr}}$ ) of WAR, WAR/P, WAR/SP, and WAR/SPA in NaCl 3.5% (w/w), NaOH 1M, and HCl 1M solutions, respectively

Corrosive environment	Sample	$E_{\text{corr}}$ (V)	$I_{\text{corr}}$ (mA)
NaCl 0.6M	WAR	-0.363	$6.607 \times 10^{-6}$
	WAR/P	-0.291	$3.467 \times 10^{-6}$
	WAR/SP	-0.268	$0.125 \times 10^{-6}$
	WAR/SPA	-0.259	$2.259 \times 10^{-7}$
NaOH 1M	WAR	-0.616	$2.291 \times 10^{-6}$
	WAR/P	-0.556	$1.819 \times 10^{-6}$
	WAR/SP	-0.507	$1.380 \times 10^{-6}$
	WAR/SPA	-0.479	$1.023 \times 10^{-6}$
HCl 1M	WAR	-0.423	$1.175 \times 10^{-3}$
	WAR/P	-0.381	$2.571 \times 10^{-4}$
	WAR/SP	-0.339	$1.622 \times 10^{-4}$
	WAR/SPA	-0.317	$1.355 \times 10^{-4}$

#### 4. Conclusion

In summary, we present a green approach to prepare SPS/PANI/Ag composites with enhanced anticorrosive properties through using SPS microspheres as substrates and utilizing PVP as reducing agent and stabilizing agent. FTIR, FESEM, and EDX results have confirmed the formation of pure PANI, SPS/PANI composites, and SPS/PANI/Ag composites. XRD patterns indicate that the obtained Ag nanoparticles are crystalline. Anticorrosive studies show that both SPS/PANI and SPS/PANI/Ag composites have enhanced anticorrosive properties in comparison to pure PANI in various corrosive environments.

#### Acknowledgements

We would like to acknowledge the Ministry of Education Key Laboratory for the Green Preparation and Application of Functional Materials for providing necessary facilities.

#### References

- Kim, S., M., Lee, J., In, I., & Park, S. Y. (2014). Formulation of Silver Nanowire–Polyaniline Hybrid Transparent Electrodes by Using Catechol-enriched Polyaniline. *Chem. Lett.*, *43*, 1453-1455. <https://doi.org/10.1246/cl.140527>
- Yang, C., Wei, H., Guan, L., Guo, J., Wang, Y., & Yan, X. (2015). Polymer nanocomposites for energy storage, energy saving, and anticorrosion. *J. Mater. Chem. A*, *3*, 14929-14941. <https://doi.org/10.1039/C5TA02707A>
- Han, J., Wang, M., Hu, Y., Zhou, C., & Guo, R. (2017). Conducting polymer-noble metal nanoparticle hybrids: Synthesis mechanism application. *Prog. Polym. Sci.*, *70*, 52-91. <https://doi.org/10.1016/j.progpolymsci.2017.04.002>
- Yuan, C., Xu, Y., Zhong, L., Zhang, L., Yang, C., & Jiang, B. (2013). Heterogeneous silver-polyaniline nanocomposites with tunable morphology and controllable catalytic properties. *Nanotechnology*, *24*, 185602-185611. <https://doi.org/10.1088/0957-4484/24/18/185602>
- Yang, M., Cao, L., & Tan, L. (2014). Synthesis of sea urchin-like polystyrene/polyaniline microspheres by seeded swelling polymerization and their catalytic application. *Colloid. Surf. A*, *441*, 678-684. <https://doi.org/10.1016/j.colsurfa.2013.10.034>
- Liu, Y., Feng, X., Shen, J., Zhu, J., & Hou, W. (2008). Fabrication of a novel glucose biosensor based on a highly electroactive polystyrene/polyaniline/Au nanocomposite. *J. Phys. Chem. B*, *112*, 9237-9242. <https://doi.org/10.1021/jp801938w>
- Dai, X., Zhang, X., Meng, Y., & Shen, P. (2011) Preparation of hollow carbon spheres by carbonization of polystyrene/polyaniline core-shell polymer particles. *New Carbon Mater.*, *26*, 389-395. [https://doi.org/10.1016/S1872-5805\(11\)60089-9](https://doi.org/10.1016/S1872-5805(11)60089-9)

- Zhao, Q., Liu, Y., & Wang, C. (2005). Development and evaluation of electroless Ag-PTFE composite coatings with anti-microbial and anti-corrosion properties. *Appl. Surf. Sci.*, *252*, 1620-1627. <https://doi.org/10.1016/j.apsusc.2005.02.098>
- Deng, Z., Zhu, H., Peng, B., Chen, H., Sun, Y., & Gang, X. (2012). Synthesis of PS/Ag nanocomposite spheres with catalytic and antibacterial activities. *ACS Appl. Mater. Inter.*, *4*, 5625-5632. <https://doi.org/10.1021/am3015313>
- Liao, G., Chen, J., Zeng, W., Yu, C., Yi, C., & Xu, Z. (2016). Facile Preparation of Uniform Nanocomposite Spheres with Loading Silver Nanoparticles on Polystyrene-methyl Acrylic Acid Spheres for Catalytic Reduction of 4-Nitrophenol. *J. Phys. Chem. C*, *120*, 25935-25944. <https://doi.org/10.1021/acs.jpcc.6b09356>
- Liao, G., Zhao, W., Li, Q., Pang, Q., & Xu, Z. (2017). Novel Poly(acrylic acid)-modified Tourmaline/Silver Composites for Adsorption Removal of Cu(II) ions and Catalytic Reduction of Methylene Blue in Water. *Chem. Lett.*, *46*, 1631-1634. <https://doi.org/10.1246/cl.170785>
- Liao, G., Li, Q., Zhao, W., Pang, Q., Gao, H., & Xu, Z. (2018). In-situ construction of novel silver nanoparticle decorated polymeric spheres as highly active and stable catalysts for reduction of methylene blue dye. *Appl. Catal. A*, *549*, 102-111. <https://doi.org/10.1016/j.apcata.2017.09.034>
- Liao, G., Gong, Y., Yi, C., & Xu, Z. (2017). Soluble, Antibacterial, and Anticorrosion Studies of Sulfonated Polystyrene/Polyaniline/Silver Nanocomposites Prepared with the Sulfonated Polystyrene Template. *Chin. J. Chem.*, *35*, 1157-1164. <https://doi.org/10.1002/cjoc.201600816>
- Yang, Y., Chu, Y., Yang, F., & Zhang, Y. (2005). Uniform hollow conductive polymer microspheres synthesized with the sulfonated polystyrene template. *Mater. Chem. Phys.*, *92*, 164-171. <https://doi.org/10.1016/j.matchemphys.2005.01.007>
- Liu, Y., Gao, H., Chen, S., & Wang, D. (2015). Ag Nanoparticle-Loaded Hierarchical Superamphiphobic Surface on an Al Substrate with Enhanced Anticorrosion and Antibacterial Properties. *J. Phys. Chem. C*, *119*, 25449-25456. <https://doi.org/10.1021/acs.jpcc.5b08679>

## Copyrights

Copyright for this article is retained by the author(s), with first publication rights granted to the journal.

This is an open-access article distributed under the terms and conditions of the Creative Commons Attribution license (<http://creativecommons.org/licenses/by/4.0/>).

# Graph Theory of Capping Golden Clusters

Enos Masheija Rwantale Kiremire

Correspondence: Enos Masheija Rwantale Kiremire, Professor of Chemistry, University of Namibia. Hochland Park, P. O. Box, 98013, Pelican Square, Tauben Glen, Windhoek, Namibia. E-mail: kiremire15@yahoo.com

Received: December 1, 2017 Accepted: January 23, 2018 Online Published: January 25, 2018

doi:10.5539/ijc.v10n1p87

URL: <https://doi.org/10.5539/ijc.v10n1p87>

## Abstract

Skeletal numbers and their valences have been extremely useful in analyzing and categorizing clusters especially boranes, carbonyls, and Zintl ions. This approach is being extended to the analysis and categorization of golden clusters. The newly introduced concept of graphing will also be applied to the clusters. The capping symbol  $K_p = C^Y C[M_x]$  which has been restricted to post-closo clusters will be adapted for pre-closo cluster series. The concept of the existence of black holes in the nuclei of capping golden clusters will be introduced and explained.

**Keywords:** golden clusters, black holes, capping series, de-capping series, skeletal numbers,  $K(n)$  series, nuclearity index

## 1. Introduction

The first golden cluster to be synthesized was  $Au_{11}I_3L_7$  in 1968 (Mingos, 1984). Since then many more clusters have been synthesized (Cotton & Wilkinson, 1980; Greenwood & Earnshaw, 1998; Gimeno, 2008; Kilmartin, 2010; Kwok-Ming, 2011; Konishi, 2014). The golden clusters have attracted immense interest among many scientists in terms of trying to understand their geometrical shapes, bonding and potential applications in catalysis and nanotechnology (Corti, et al, 2005; Zhang, et al, 2014). The fascinating shapes of gold have been described by a number of ways, for instance,  $Au_4I_2L_4$ , tetrahedral;  $Au_6L_6^{2+}$ , ( $L = PPh_3$ ), octahedral;  $Au_8L_8^{2+}$ , chair-like centered hexagon;  $Au_{13}Cl_2L_{10}^{3+}$ , ( $L = PMe_2Ph$ ); icosahedron;  $Au_8L_7^{2+}$  and  $Au_9L_8^{3+}$ ; flat, ring, torus or doughnut-shaped (Cotton & Wilkinson, 1980; Greenwood & Earnshaw, 1998). Further descriptions include, centered polyhedral, non-centered polyhedral and exo-attached polyhedral clusters (Konishi, 2014). The recent application of the  $4n$  series method to the analysis and categorization of golden clusters indicated almost all the clusters with nuclearity index 4 and above belong to the CAPPING SERIES (Kiremire, 2016, 2017). With the development of skeletal numbers and the concept of graph theory of capping series (Kiremire, 2017b, 2017c), it will be interesting to investigate how the golden cluster structures look like under the series graph theory.

## 2. Results and Discussion

In order to be able to compare and contrast the structures of gold as compared to other clusters, let us compare and contrast the structures of two hypothetical clusters, namely  $C_6H_{10}$  and  $Au_6H_{10}$ . The  $K$  value of  $C_6H_{10}$ :  $K = 6[2]-5 = 7$ ;  $K(n) = 7(6)$ ,  $S = 4n+10$ . In the case of  $Au_6H_{10}$ :  $K = 6[3.5]-5 = 16$ ;  $K(n) = 16(6)$ ,  $S = 4n-8$ ,  $K_p = C^5C[M1]$ . The calculation of skeletal linkages of clusters has been discussed extensively (Kiremire, 2017d). Let us analyze these cases one at a time.

Ex-1:  $C_6H_{10}$ :  $K = 6[2]-5 = 7$ ;  $K(n) = 7(6)$ ,  $S = 4n+10$ . The symbol  $K(n) = 7(6)$  means that the 6 carbon skeletal atoms in the formula are joined by 7 linkages or bonds. One of the possible skeletal isomers is shown as F-1. The skeletal number of carbon [C],  $K = 2$ , gold, [Au],  $K = 3.5$ , [H] as a ligand,  $K = -0.5$  since it is a 1 electron donor (refer to appendixes 1 and 2). The number of valence electrons can also be derived from the series formula:  $Ve = 4n+10 = 4(6) + 10 = 34$ . This figure can be confirmed from the cluster formula itself:  $VF = 6[4] + 10 = 34$ .

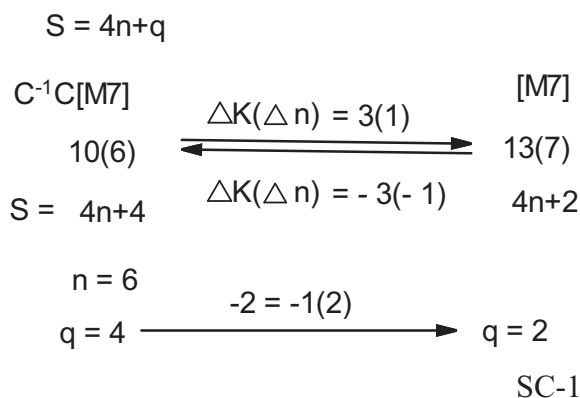
Ex-2:  $Au_6H_{10}$ :  $K = 6[3.5]-5 = 16$ ,  $K(n) = 16(6)$ ,  $S = 4n-8$ ,  $K_p = C^5C[M1]$ . This symbol means that the cluster is capped in such a way that 5 skeletal elements are surrounding 1 central skeletal atom at the nucleus. In addition, the skeletal framework of 6 golden elements is bound by 16 linkages. Since each capping skeletal element uses 3 linkages, the 5 capping elements means utilizing 15 of the skeletal linkages out of the 16. Since the cluster has one skeletal element  $\{[M1]; n=1\}$ , then the element obeys the CLOSO series formula  $S = 4n+2$  and  $K = 2n-1 = 2(1)-1 = 1$ . Thus, the skeletal element in the nucleus utilizes 1 skeletal element and the 5 capping atoms consume 15 skeletal elements giving us a total of  $15+1 = 16$ . For categorization, we can use  $S = 4n+q$  for main group and transition elements. However for calculating the number of valence electrons we have to use  $Ve = 14n+q$  equation. In this case, the number of valence electrons will be given by  $Ve = 14n-8 = 14(6)-8 = 76$ . We can verify this from the cluster formula  $F = Au_6H_{10}$ ;  $VF =$

6[11] + 10 = 76. Since  $K_p = C^5C[M1]$ , the capping symbol can guide us to sketch a skeletal isomeric structure, F-2.

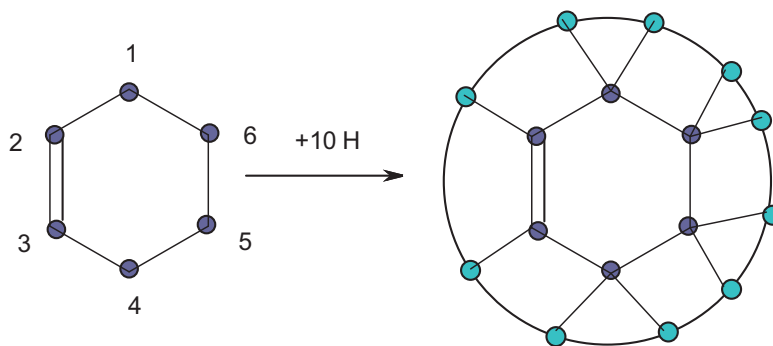
Ex-3:  $Zn_6H_{10}$ :  $K = 6[3]-5 = 13$ ;  $K(n) = 13(6)$ ,  $S = 4n-2$ ,  $K_p = C^2C[M4]$ . This is a bi-capped tetrahedron. Its possible isomeric structure has been proposed F-3.

Ex-4:  $B_6H_{10}$ :  $K = 6[2.5]-5 = 10$ ;  $K(n) = 10(6)$ ,  $S = 4n+4$  ( $q = 4$ ). The closo series is given by  $S = 4n+2$  ( $q = 2$ ). Since the ordinary series,  $q$  runs in the multiples of 2,  $S = 4n+4$  is a step before  $S = 4n+2$ . If we follow the Rudolph type of capping series, then the closo above  $B_6H_{10}$  will have a  $K$  value of 13 and  $n = 7$ . Hence, its closo cluster parameter will be  $K(n) = 13(7) = [M7]$ . Since capping clusters after  $[M7]$  are expressed as  $K_p = C^yC[Mx]$ , then the de-capping series can be expressed as  $K_p = C^{-y}C[Mx]$ . Therefore, the cluster  $K(n) = 10(6)$ , can be expressed as  $K_p = C^{-1}C[M7]$ . According to this approach, this symbol means, its  $K(n)$  is one step below the closo base, that is,  $\Delta K = -3$ , and  $\Delta n = -1 \equiv \Delta K(\Delta n) = -3(-1)$ . We can express this idea diagrammatically, SC-1. This means that by comparing the  $q$  value of a cluster and that of the 'standard reference' closo system, we can determine the relative positions of the  $K(n)$  values and hence numerically categorize the cluster, in this case  $10(6)$ ,  $K_p = C^{-1}C[M7]$ .

Ex-5:  $B_5H_9$  and Ex-6:  $B_4H_{10}$  were numerically categorized in the same way.



$C_6H_{10}$ :  $K=6[2]-10(0.5) = 7$ ,  $K(n) = 7(6)$ ,  $S = 4n+10$ ;  $V_e = 4(6)+10 = 34$ ,  $V_f = 6[4]+10 = 34$



$K1 = 2-1 = 1 = 2H$   
 $K2 = 2-1.5 = 0.5 = 1H$   
 $K3 = 2-1.5 = 0.5 = 1H$   
 $K4 = 2-1 = 1 = 2H$   
 $K5 = 2-1 = 1 = 2H$   
 $K6 = 2-1 = 1 = 2H$

● = C  
● = H

Ex-1:  $C_6H_{10}$

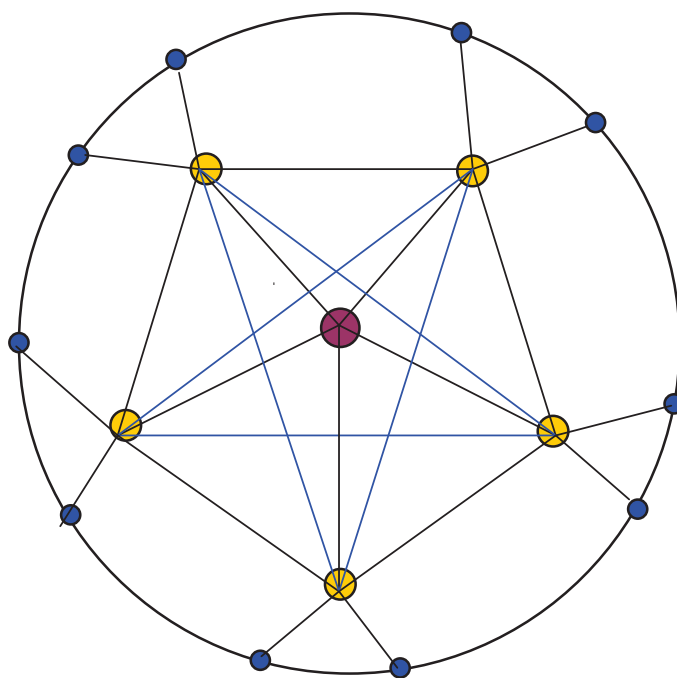
Without Hydrogen Ligands

Is  $K(n) = 10(6)$  below [M7]? We can test this by a simple check on the flow of  $K(n)$  numbers.

[M7] means,  $S = 4n+2(n = 7)$ . Hence  $K = 2n-1 = 2(7)-1 = 13$  and so  $K(n) = 13(7)$  for [M7].

[M7] lower series will be as follows starting with [M7] =  $13(7) \rightarrow 10(6) \rightarrow 7(5) \rightarrow 4(4) \rightarrow 1(3)$ . According to the historical terminology 13(7) will correspond to a CLOSO system, 10(6), NIDO; 7(5), ARACHNO; 4(4), HYPHO; and 1(3), KLADO system. The symbol [M7] will also represent the borane cluster  $B_7H_7^{2-}$ . Hence,  $K(n) = 10(6)$  is just one step below the closo system [M7] and corresponds to a nidoborane cluster  $B_6H_{10}$ .

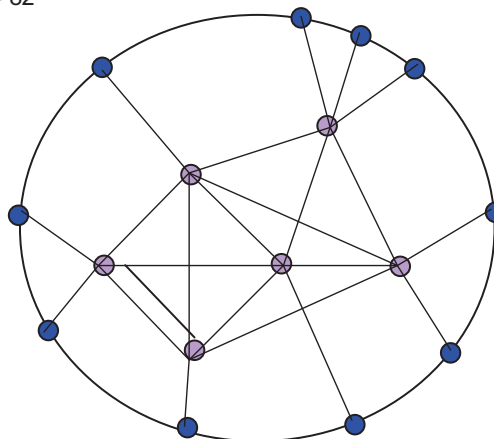
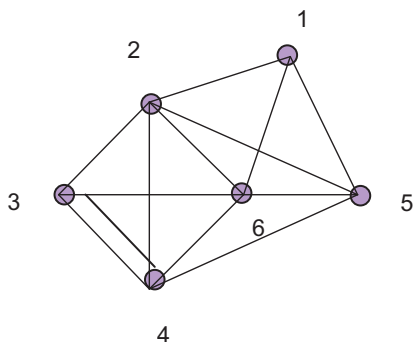
According to the series method,  $K(n) = 16(6)$ ,  $K_p = C^5C[M1]$ . This means it belongs to the group or a clan of clusters which have got 1 skeletal element in the nucleus. Thus,  $K(n) = 16(6)$  parameter will be found to be a member of [M1] - based numbers. This can be seen to be the case as indicated in the [M1] series.



$Zn_6H_{10}$ :  $K = 6[3]-5 = 13$ ;  $K(n) = 13(6)$ ,  $S = 4n-2$ ,  $Kp = C^2C[M4]$

$Ve = 14n-2 = 14(6)-2 = 82$ ,  $VF = 6[12]+10 = 82$

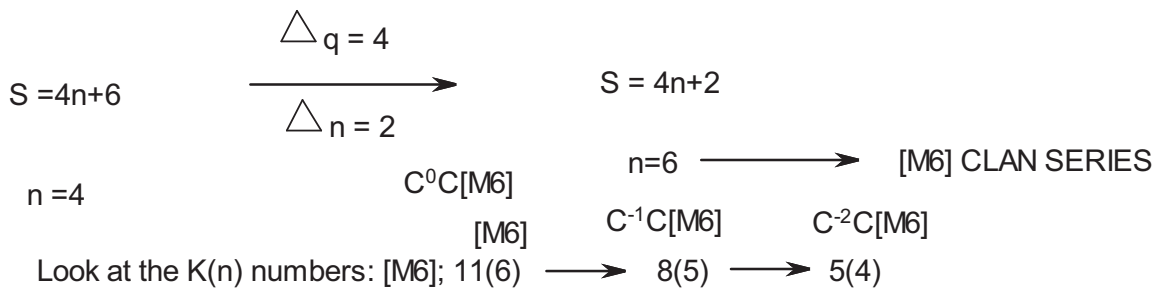
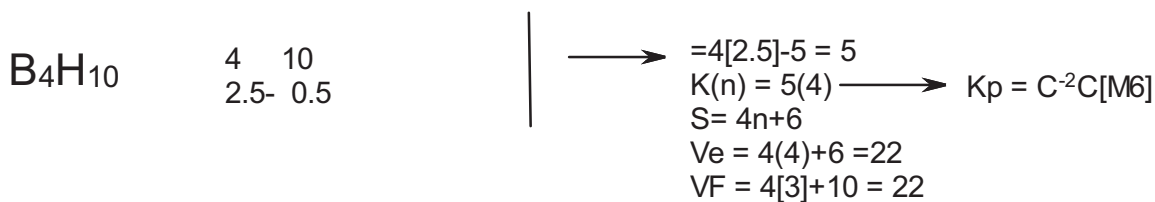
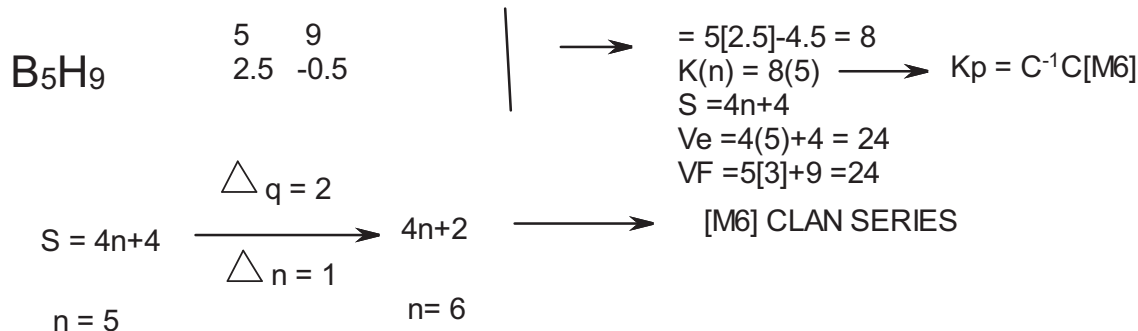
$[M4]$ ,  $K=2n-1 = 2(4)-1 = 7$

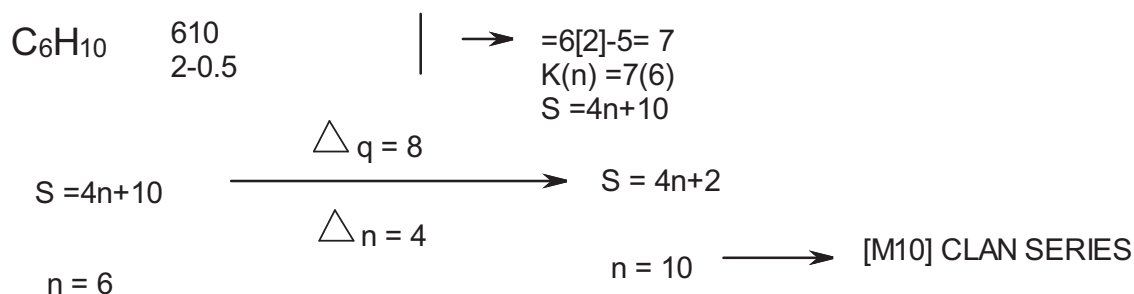


$K1=1[3]-1.5=1.5 = 3H$   
 $K2=1[3]-2.5=0.5 = 1H$   
 $K3=1[3]-2 = 1 = 2H$   
 $K4=1[3]-2.5 = 0.5 = 1H$   
 $K5=1[3]-2 = 1 = 2H$   
 $K6=1[3]-2.5 = 0.5 = 1H$

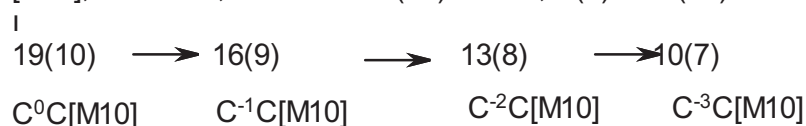
Is  $K(n) = 13(6)$  a member of  $[M4]$  series of numbers?. Let us check it out.

$K(n) = 13(6)\{S = 4n-2, Kp = C^2C[M4]\} \rightarrow 10(5)\{S = 4n+0, Kp = C^1C[M5]\} \rightarrow 7(4)\{S = 4n+2\}$ . The parameter  $K(n) = 7(4) = [M4]$ .





[M10];  $S = 4n+2$ ,  $K = 2n-1 = 2(10)-1 = 19$ ,  $K(n) = 19(10)$

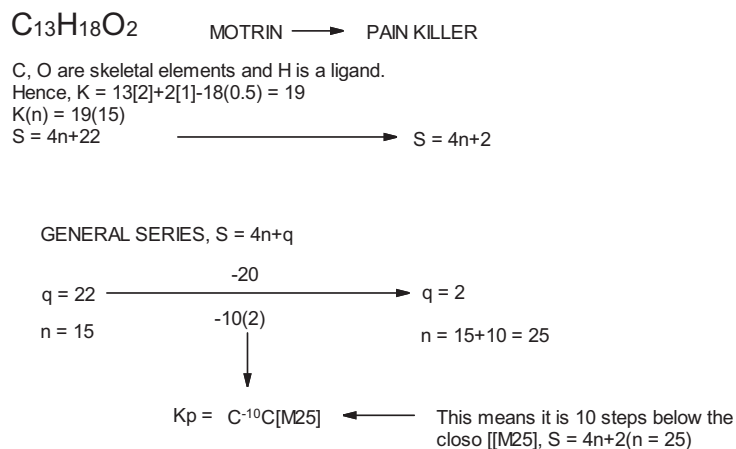


### SC-2

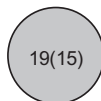
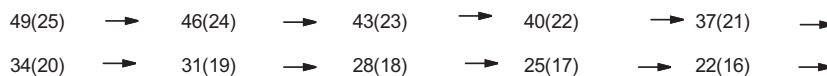
#### The flow of K(n) numbers: the clan series (and families)

Since the main group and transition metal elements have been assigned skeletal numbers, this means that any cluster small or large that comprises these elements can naturally be assigned a cluster number parameter K(n) and hence be categorized. Take the examples:

1-1: MOTRIN – PAIN KILLER, FORMULA:  $\text{C}^{13}\text{H}_{18}\text{O}_2$ ; in this example, [C] and [O] are regarded as skeletal elements and [H] as a ligand. Its categorization is given in SC-3



[M25];  $S = 4n+2$ ;  $K = 2n-1 = 2(25)-1 = 49$ ,  $K(n) = 49(25)$



### SC-3



1-2: ASPIRIN- PAIN KILLER, FORMULA, C<sub>9</sub>H<sub>8</sub>O<sub>4</sub>

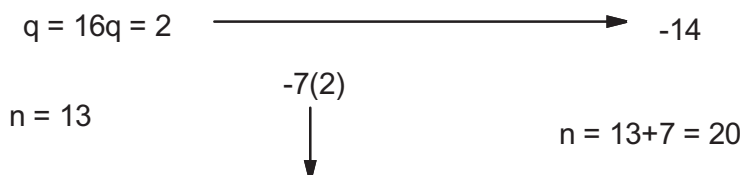
SKELETAL ELEMENTS, [C], [O] AND [H] LIGAND

I

$$K = 9[2] + 4[1] - 8(0.5) = 18$$

$$K(n) = 18(13)$$

$$S = 4n + 16(n = 13)$$



$K_p = C^{-7}C[M20]$  ← This means the cluster is 7 steps below [M20] CLOSO SYSTEM.

[M20],  $K = 2n - 1 = 2(20) - 1 = 39$ ,  $K(n) = 39(20) \rightarrow 36(19) \rightarrow 33(18) \rightarrow 30(17) \rightarrow 27(16) \rightarrow 24(15) \rightarrow 21(14) \rightarrow 18(13)$   
SC-4

1-3: QUININE - C<sub>20</sub>H<sub>24</sub>N<sub>2</sub>O<sub>2</sub>

In this example, let us consider [H] as a ligand and the rest as skeletal elements. Its K value is given by  $K = 20[2] + 2[1.5] + 2[1] - 24(0.5) = 33$ ;  $K(n) = 33(24)$ ,  $S = 4n + 30$ . In this case  $q = 30$  and we have to compare this with  $q = 2$  for a closo system. That is,

$q = 30 \rightarrow q = 2$ . The gap is 28 or we must subtract 28 from 30 to arrive at  $q = 2$ . Hence  $\Delta q = -28 = -14(2)$ . In terms of series, it means we have to go down numerically by 14 steps corresponding to an increase in  $n$  value by 14. Hence, the new  $n = 24 + 14 = 38$ . This means the CLOSO system will correspond to  $n = 38 \rightarrow [M38]$ . Similarly, the quinine formula itself will be at 14 steps below the [M38] closo system. Therefore its symbol is appropriately set at  $K_p = C^{-14}C[M38]$ . We can test this from the flow of [M38]  $K(n)$  numbers, SC-5;

[M38]  $\rightarrow 75(38) \rightarrow 72(37) \rightarrow 69(36) \rightarrow 66(35) \rightarrow 63(34) \rightarrow 60(33) \rightarrow 57(32) \rightarrow 54(31) \rightarrow 51(30) \rightarrow 48(29) \rightarrow 45(28) \rightarrow 42(27) \rightarrow 39(26) \rightarrow 36(25) \rightarrow \mathbf{33(24)}$

## SC-5

The rest of the examples we can just demonstrate the categorization and the flow of  $K(n)$  number series.

1-4: Cp<sub>4</sub>Ni<sub>4</sub>B<sub>4</sub>H<sub>4</sub>;  $K = 4[4] + 4[2.5] - 4(2.5) - 4(0.5) = 14$ ,  $K(n) = 14(8)$ ,  $S = 4n + 4$ ;  $q = 4 \rightarrow q = 2$ . This means, the cluster is one step below the CLOSO system. Hence,  $K_p = C^{-1}C[M9]$ . This is a NIDO cluster.

1-5: Al<sub>77</sub>R<sub>10</sub><sup>-</sup>:  $K = 77[2.5] - 5 - 0.5 = 187$ ;  $K(n) = 187(77)$ ,  $S = 4n - 66$ ,  $K_p = C^{34}C[M43]$ . This is a huge cluster with a large nucleus of 43 skeletal elements capped by 34 skeletal elements. Now, let us see the flow of the  $K(n)$  numbers downwards, SC-6.

187(77)  $\rightarrow$  184(76)  $\rightarrow$  181(75)  $\rightarrow$  178(74)  $\rightarrow$  175(73)  $\rightarrow$  172(72)  $\rightarrow$  169(71)  $\rightarrow$  166(70)  $\rightarrow$  163(69)  $\rightarrow$  160(68)  $\rightarrow$  157(67)  $\rightarrow$  154(66)  $\rightarrow$  151(65)  $\rightarrow$  148(64)  $\rightarrow$  145(63)  $\rightarrow$  142(62)  $\rightarrow$  139(61)  $\rightarrow$  136(60)  $\rightarrow$  133(59)  $\rightarrow$  130(58)  $\rightarrow$  127(57)  $\rightarrow$  124(56)  $\rightarrow$  121(55)  $\rightarrow$  118(54)  $\rightarrow$  115(53)  $\rightarrow$  112(52)  $\rightarrow$  109(51)  $\rightarrow$  106(50)  $\rightarrow$  103(49)  $\rightarrow$  100(48)  $\rightarrow$  97(47)  $\rightarrow$  94(46)  $\rightarrow$  91(45)  $\rightarrow$  88(44)  $\rightarrow$  **85(43)**

$K(n) = 85(43)$ ,  $S = 4n + 2$ ; CLOSO SYSTEM. Hence,  $K(n) = 187(77) \rightarrow K_p = C^{34}C[M43]$  is in line with the  $K(n)$  number series.

## SC-6

1-6: Sb<sub>7</sub>Ni<sub>3</sub>(CO)<sub>3</sub><sup>3-</sup>:  $K = 7[1.5] + 3[4] - 3 - 1.5 = 18$ ;  $K(n) = 18(10)$ ,  $S = 4n + 4$ ;  $K_p = C^{-1}C[M11]$ . This is a NIDO cluster – a derivative from [M11] which corresponds to B<sub>11</sub>H<sub>11</sub><sup>2-</sup> closo cluster.

1-7: Rh<sub>13</sub>H<sub>3</sub>(CO)<sub>24</sub><sup>2-</sup>:  $K = 13[4.5] - 1.5 - 24 - 1 = 32$ ;  $K(n) = 32(13)$ ,  $S = 4n - 12$ ,  $K_p = C^7C[M6]$ . Let us look at the flow of the  $K(n)$  numbers and then the skeletal graph of the cluster.

32(13)  $\rightarrow$  29(12)  $\rightarrow$  26(11)  $\rightarrow$  23(10)  $\rightarrow$  20(9)  $\rightarrow$  17(8)  $\rightarrow$  14(7)  $\rightarrow$  **11(6)**

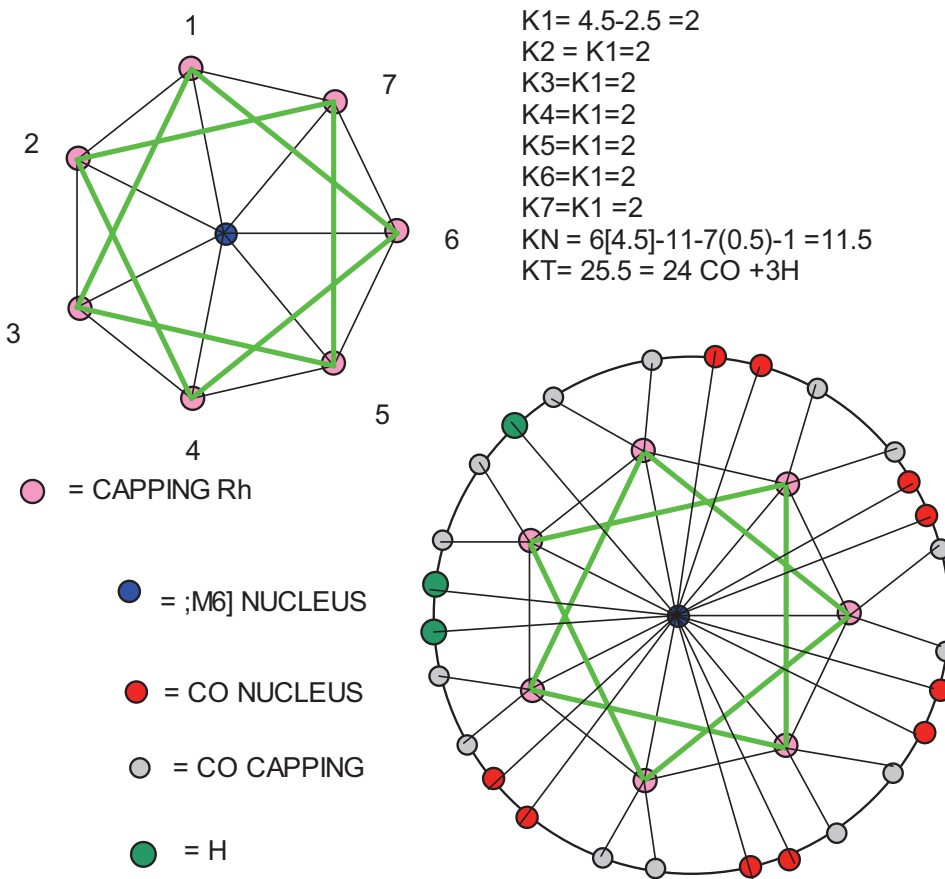
This clearly agrees with the flow of the K(n) numbers and with the [M6] series below. The cluster symbol  $K_p = C^7C[M6]$  means that the overall cluster has an  $O_h$  nucleus of 6 skeletal elements surrounded by 7 capping skeletal elements. The sketch of the possible isomeric skeletal graph F-5

$$Rh_{13}H_3(CO)_{24}^{2-}: K = 32, K(n) = 32(13), S = 4n - 12, K_p = C^7C[M6]$$

$$[M6], K = 2n - 1 = 2(6) - 1 = 11$$

$$Rh(K=4.5, V=9)$$

$$SKELETAL LINKAGES = 7 + 7 + 7 + [M6] = 21 + 11 = 32$$



When we analyze more closely, it is quite clear that chemical elements, fragments, molecular formulas and clusters comprising of the main group and transition metals can readily be categorized using skeletal numbers. Therefore the clusters such as boranes, carboranes, metalloboranes, transition metal carbonyls, Zintl ion clusters and others all belong to one universe of clusters which obey a simple cluster formula  $S = 4n + q$  ( $q > 0$ , non-capping clusters;  $q \leq 0$ , capping clusters) and a simple parameter  $K(n)$ . It has been proposed that the clusters are best grouped according to the CLOSO NUCLEAR SYSTEM  $[M_x]$ . Although the golden clusters are usually centered around the closo nuclei  $[M_1]$  and  $[M_2]$  series, a number of examples of  $[M_x]$  series have been provided to allow readers to have familiarity with the beautiful flow of  $K(n)$  numbers. The important Rudolph correlation system set up about 40 years ago is a subset of the universe of  $K(n)$  numbers. A sample of selected  $[M_x]$  series SRS -1 are given below for illustrations and a selected collection of golden clusters are analyzed using skeletal numbers and their skeletal graphs mixed with a few non-golden clusters for comparison are shown F-6 to F-34

[M0]Series:

-1(0)→2(1)  
 →5(2)→8(3)→11(4)→14(5)→17(6)→20(7)→23(8)→26(9)→29(10)→32(11)→35(12)→38(13)→41(14)→44(15)→47(16)→50(17)→53(18)→56(19)→59(20)→62(21)→65(22)→68(23)→71(24)→74(25)→77(26)→80(27),...

BELOW [M0]

NEGATIVE K(n) VALUES

[M1]Series:1(1)→4(2)→7(3)→10(4)→13(5)→16(6)→19(7)→22(8)→25(9)→28(10)→31(11)→34(12)→37(13)→40(14)→43(15)→46(16)→49(17)→52(18)→55(19)→58(20)→61(21)→64(22)→67(23)→70(24),.....

BELOW [M1]

NEGATIVE K(n) VALUES

[M2] Series:

3(2)→6(3)→9(4)→12(5)→15(6)→18(7)→21(8)→24(9)→27(10)→30(11)→33(12)→36(13)→39(14)→42(15)→45(16)→48(17)→51(18)→54(19)→57(20)→60(21)→63(22)→66(23)→69(24)→72(25), ....

BELOW [M2]

3(2)→0(1)

[M3]Series

5(3)→8(4) →11(5) →14(6) →17(7)  
 →20(8)→23(9)→26(10)→29(11)→32(12)→35(13)→38(14)→41(15)→44(16)→47(17)→50(18)→53(19)→56(20)→59(21)→62(22)→65(23)→68(24)→71(25),....

BELOW [M3]

5(3)→2(2)

[M4]Series

7(4)→10(5)→13(6)→16(7)→19(8)→22(9)→25(10)→28(11)→31(12)→34(13)→37(14)→40(15)→43(16)→46(17)→49(18)→52(19)→55(20)→58(21)→61(22)→64(23)→67(24)→70(25), .....

BELOW [M4]

7(4)→4(3)→1(2)

[M5]Series:

9(5)→12(6)→15(7)→18(8)→21(9)→24(10)→27(11)→30(12)→33(13)→36(14)→39(15)→42(16)→45(17)→48(18)→51(19)→54(20)→57(21)→60(22)→63(23)→66(24)→69(25)→71(26)→74(27)→77(28)→80(29), ...

BELOW [M5]

9(5)→6(4)→3(3)→0(2)

[M6]Series:

11(6)→14(7)→17(8)→20(9)→23(10)→26(11)→29(12)→32(13)→35(14)→38(15)→41(16)→44(17)→47(18)→50(19)→53(20)→56(21)→59(22)→62(23)→65(24)→68(25)→71(26)→74(27)→77(28)→80(29),....

BELOW [M6]

11(6)→8(5)→5(4)→2(3)

[M7]Series:

13(7)→16(8)→19(9)→22(10)→25(11)→28(12)→31(13)→34(14)→37(15)→40(16)→43(17)→46(18)→49(19)→52(20)→55(21)→58(22)→61(23)→64(24)→67(25)→70(26)→73(27)→76(28)→79(29)→82(30), ...

BELOW [M7]

13(7)→10(6)→7(5)→4(4)→1(3)

[M8]Series:

15(8)→18(9)→21(10)→24(11)→27(12)→30(13)→33(14)→36(15)→39(16)→42(17)→45(18)→48(19)→51(20)→54(21)→57(22)→60(23)→63(24)→66(25)→69(26)→72(27)→75(28)→78(29)→81(30), ..

BELOW [M8]

15(8)→12(7)→9(6)→6(5)→3(4)→0(3)

[M9]Series:

**17(9)**→20(10)→23(11)→26(12)→29(13)→32(14)→35(15)→38(16)→41(17)→44(18)→47(19)→50(20)→53(21)→56(22)→59(23)→62(24)→65(25)→68(26)→71(27)→74(28)→77(29)→80(30),...

BELOW [M9]

17(9)→14(8)→11(7)→8(6)→5(5)→2(4)

[M10]Series:

**19(10)**→22(11)→25(12)→28(13)→31(14)→34(15)→37(16)→40(17)→43(18)→46(19)→49(20)→52(21)→55(22)→58(23)→61(24)→64(25)→67(26)→70(27)→73(28)→76(29)→79(30)→82(31),...

BELOW [M10]

19(10)→16(9)→13(8)→10(7)→7(6)→4(5)→1(4)

[M11]Series:

**21(11)**→24(12)→27(13)→30(14)→33(15)→36(16)→39(17)→42(18)→45(19)→48(20)→51(21)→54(22)→57(23)→60(24), ...

BELOW [M11]

21(11)→18(10)→15(9)→12(8)→9(7)→6(6)→3(5)→0(4)

[M12]Series:

**23(12)**→26(13)→29(14)→32(15)→35(16)→38(17)→41(18)→44(19)→47(20)→50(21), ...

BELOW [M12]

23(12)→20(11)→17(10)→14(9)→11(8)→8(7)→5(6)→2(5)

[M13]Series

**25(13)**→28(14)→31(15)→34(16)→37(17)→40(18)→43(19)→46(20)→49(21)→52(22),...

BELOW [M13]

25(13)→22(12)→19(11)→16(10)→13(9)→10(8)→7(7)→4(6)→1(5)

[M-1] Series

**-3(-1)**→0(0)→3(1)→6(2)→9(3)→12(4)→15(5)→18(6)→21(7)→24(8)→27(9)→30(10),....

[M-2] Series

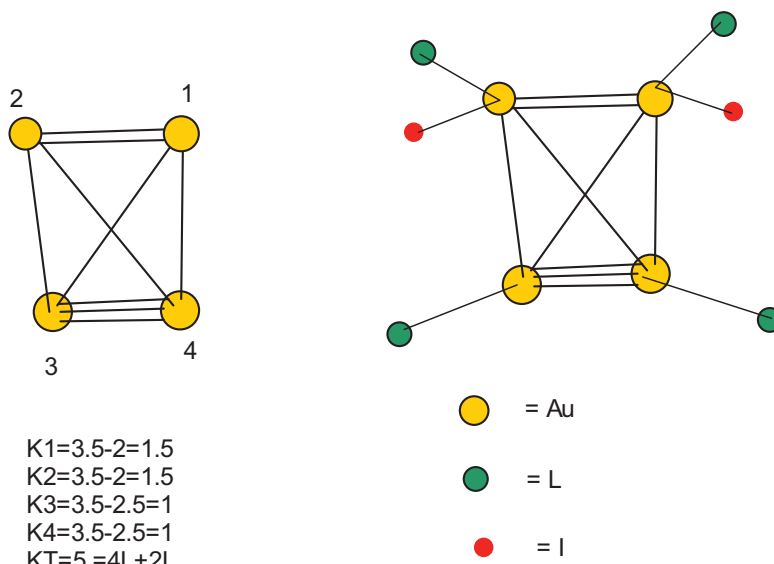
**-5(-2)**→--2(-1)→5(0)→7(1)→10(2)→13(3)→16(4)→19(5)→21(6)→24(7)→27(8)→30(9)→33(10), ...

[M-3] Series

**-7(-3)**→-4(-2)→-1(-1)→2(0)→5(1)→8(2)→11(3)→14(4)→17(5)→20(6)→23(7)→26(8)→29(9)→32(10), ....

SRS-1

$Au_4L_4I_2$ :  $K = 4[3.5]-4-1 = 9$ ;  $K(n) = 9(4)$ ,  $S = 4n-2$ ,  $Kp = C^2C[M2]$

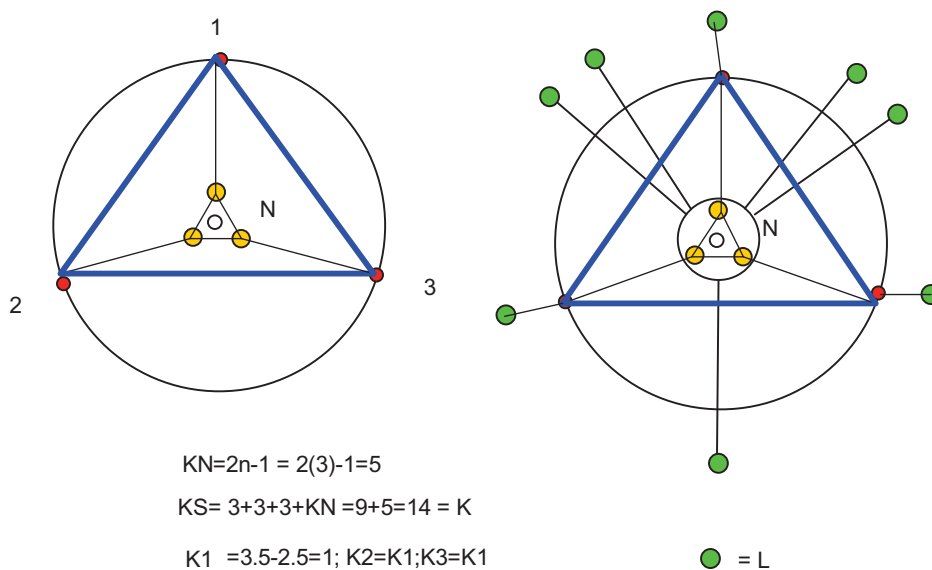


$Ve = 14n-2 = 14(4)-2 = 54$ ;  $VF = 4[11]+8+2 = 54$

Ve = valence electrons, VF = valence electrons from cluster formula

$K(n) = 9(4)$  belongs to [M2] series.

$Au_6L_8^{2+}$ :  $K = 14$ ;  $Kp = C^3C[M3]$



$Au_3^{2+}$ :  $KNL = 3[3.5]+1-3(0.5)-5=5$   
 $KLT = 3+5=8 = 8L$

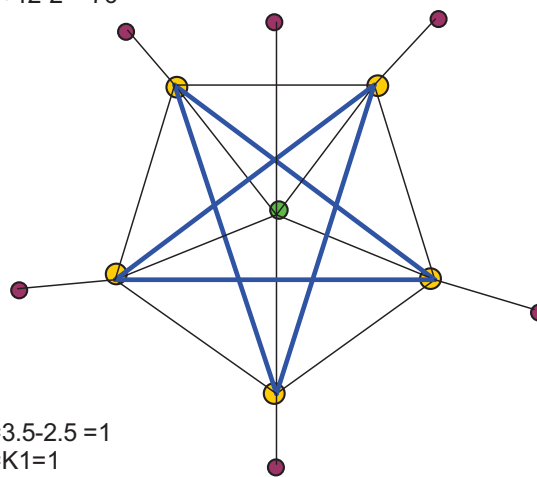
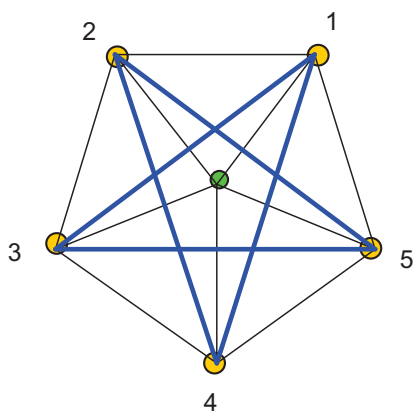
$K(n) = 14(6)$  belongs to [M3] series

$Au_6L_6^{2+}$ :  $K = 6[3.5]-6+1 = 16$ ;  $K(n) = 16(6)$ ,  $S = 4n-8$ ,  $Kp = C^5C[M1]$

$Ve = 14n-8 = 14(6)-8 = 76$ ;  $VF = 6[11]+12-2 = 76$

$[M1]$ ,  $S = 4n+2$ ,  $K = 2n-1 = 2(1)-1 = 1$

$SL = 5+5+5+1 = 16$



$K1 = 3.5 - 2.5 = 1$

$K2 = K1 = 1$

$K3 = K1 = 1$

$K4 = K1 = 1$

$K5 = K1 = 1$

$KN = 1[3.5+1-2.5-1] = 1$

$KT = 6 = 6L$

● = CAPPING Au

● = NUCLEAR Au

● = L

$K(n) = 16(6)$  belongs to  $[M1]$  series

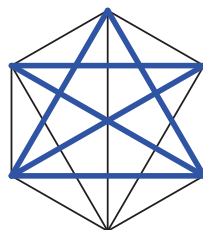
### ISOMERIC STRUCTURE OF $Au_6L_6^{2+}$

$K = 6[3.5]-6+1 = 16$

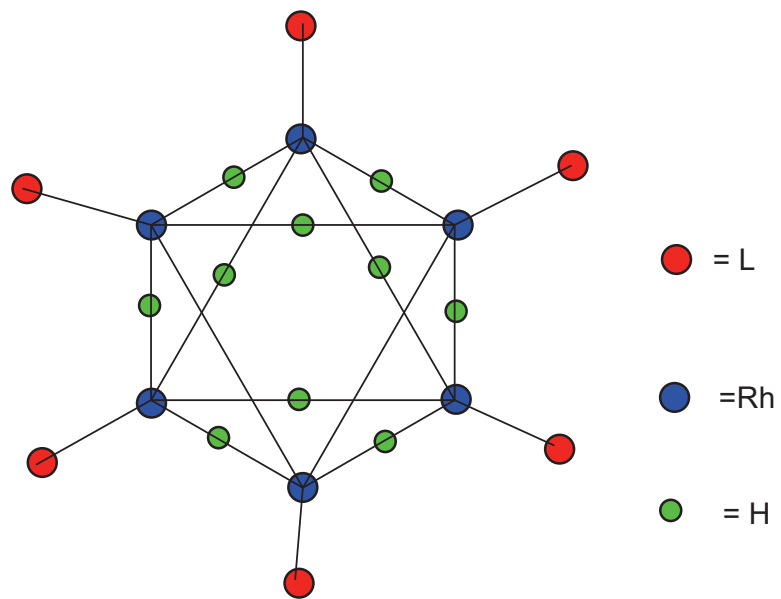
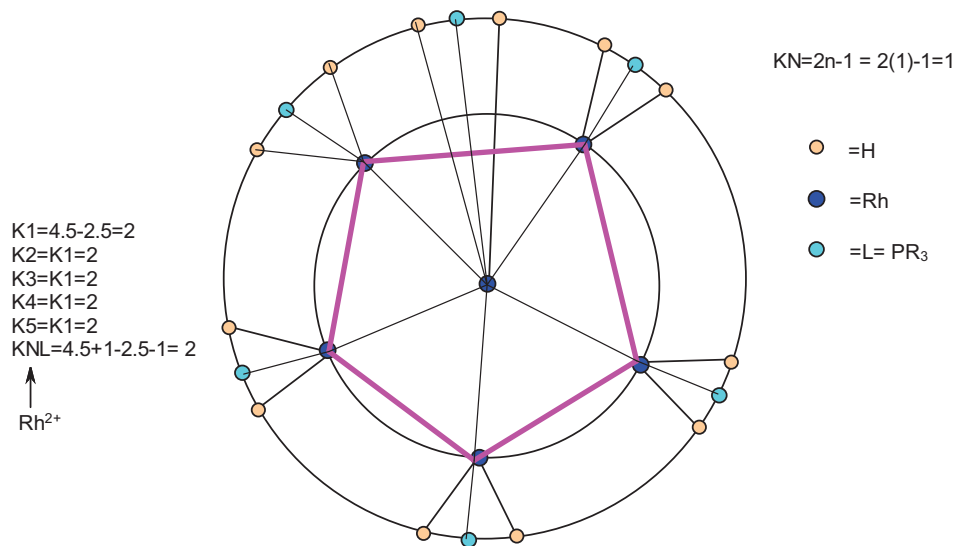
$K(n) = 16(6)$

$S = 4n-8$

$Kp = C^5C[M1]$



$Rh_6L_6H_{12}^{2+}$ :  $K = 6[4.5]-6-6+1 = 16$ ,  $K(n) = 16(6)$ ,  $S = 4n-8$ ,  $Kp = C^5C[M1]$   
 $Ve = 14n-8 = 14(6)-8 = 76$ ,  $VF = 6[9]+12+12-2 = 76$



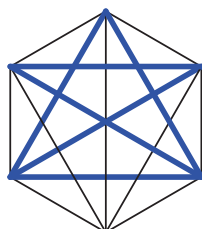
ISOMERIC SKELETAL SHAPE OF  $Rh_6L_6H_{12}^{2+}$ .

$$K = 6[3.5]-6+1 = 16$$

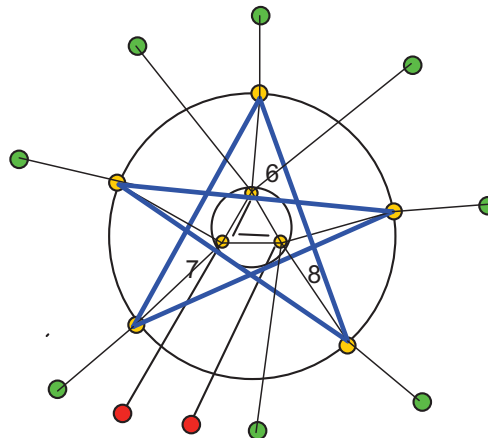
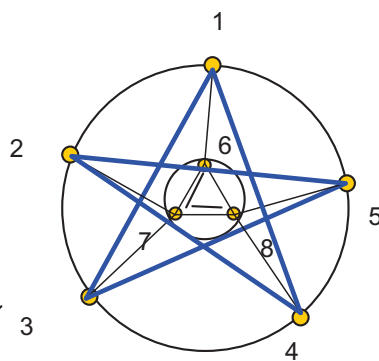
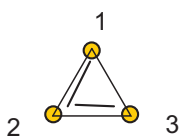
$$K(n) = 16(6)$$

$$S = 4n-8$$

$$K_p = C^5C[M1]$$



$Au_8L_8Cl_2^{2+}$ :  $K(n) = 20(8)$ ,  $K_p = C^5C[M3]$



$$K1=3.5-1.5=2$$

$$K2=3.5-2=1.5$$

$$K3=3.5-1.5=2$$

$$K1=3.5-2.5=1$$

$$K2=K1=1$$

$$K3=K1=1$$

$$K4=K1=1$$

$$K5=K1=1$$

$$K6=4-2=2$$

$$K7=3.5-3=0.5$$

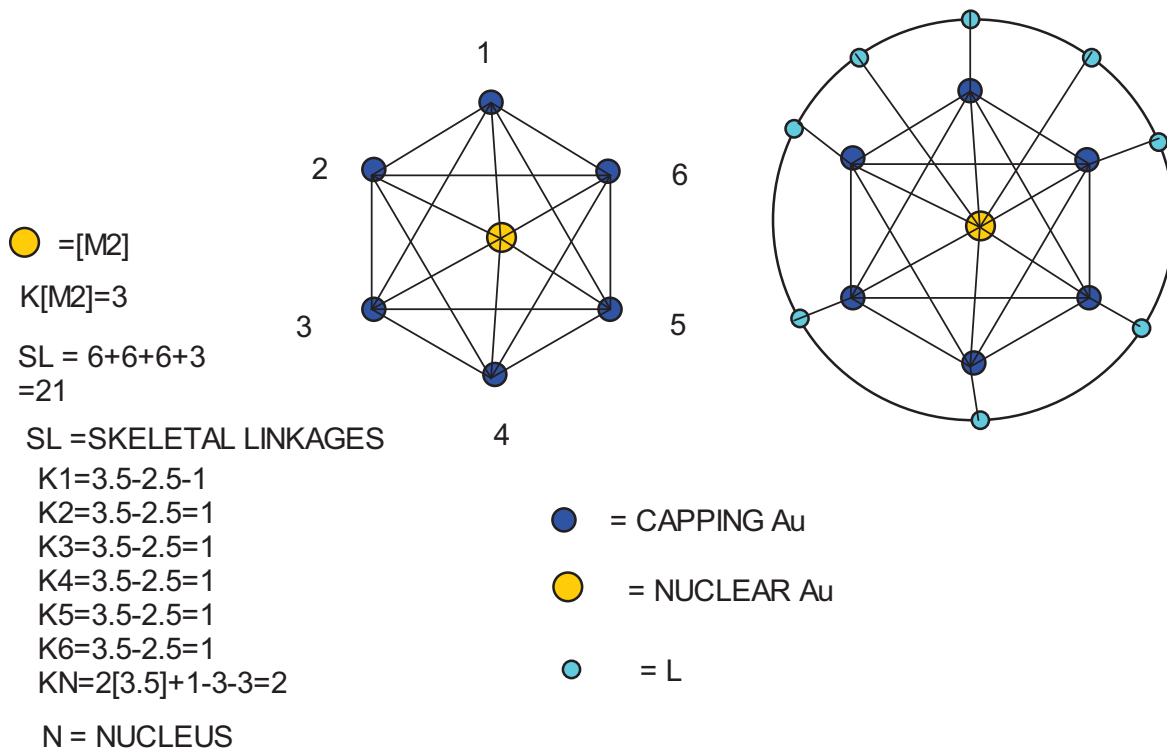
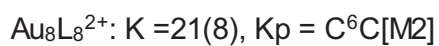
$$K8=4-2.5=1.5$$

$$KT=9$$

- =L
- = Au
- =Cl

$K(n) = 20(8)$  belongs to [M3] series



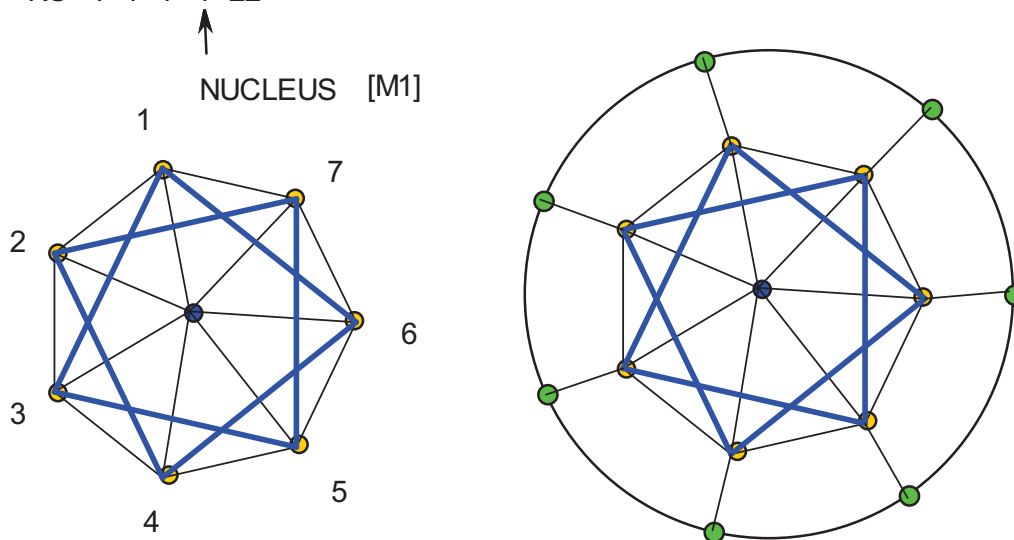


$K(n) = 21(8)$  belongs to [M2] series

$Au_8L_7^{2+}$ :  $K(n) = 22(8)$ ,  $K_p = C^7C[M1]$  [M1],  $S = 4n+2$ ,  $K=2n-1 = 2(1)-1 = 1$

$K_1=3.5-2.5=1$ ,  $K_2=1$ ,  $K_3=1$ ,  $K_4=1$ ,  $K_5=1$ ,  $K_6=1$ ,  $K_7=1$

$KS = 7+7+7+1=22$  ← SKELETAL LINKAGES



$KN = 1[3.5]+1-3.5-1 = 0$

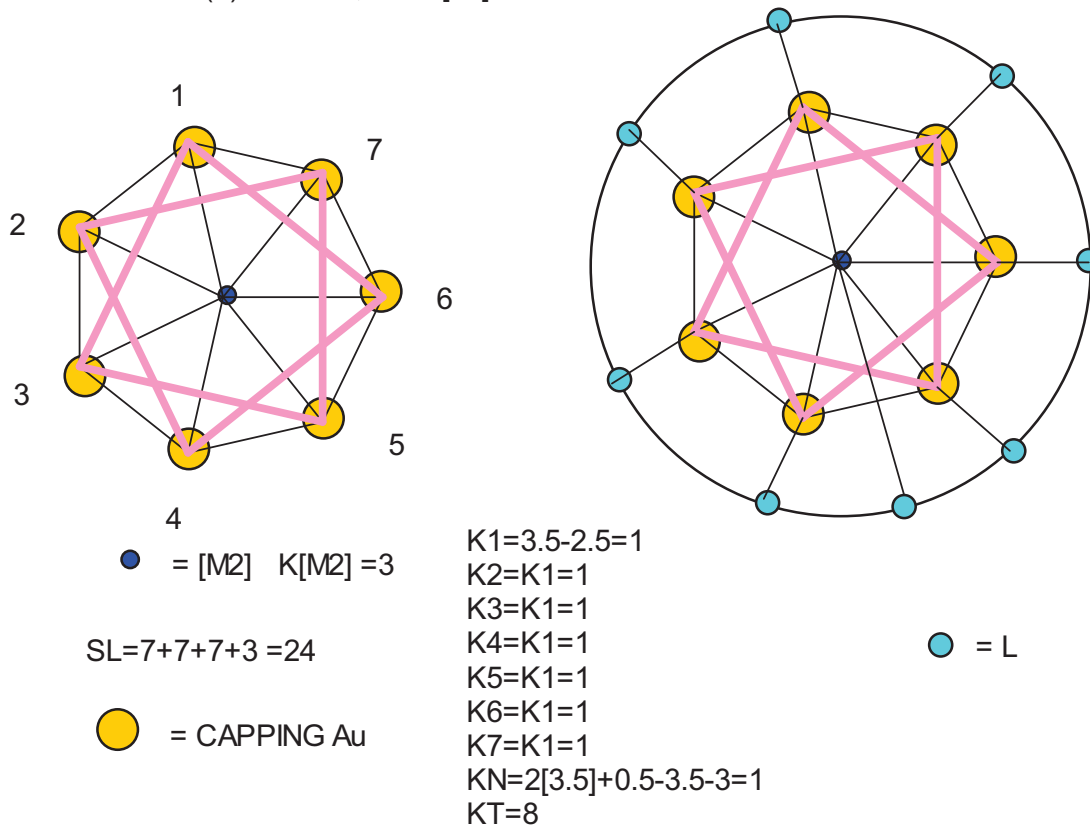
● = CAPPING Au

● = L

$K(n) = 22(8)$  belongs to [M1] series

$Au_9L_8^{+1}$ :  $K = 9[3.5] - 8 + 0.5 = 24$ ;  $K(n) = 24(9)$ ,  $S = 4n - 12$ ,  $Kp = C^7C[M2]$

$Ve = 14n - 12 = 14(9) - 12 = 114$ ;  $VF = 9[11] + 16 - 1 = 114$

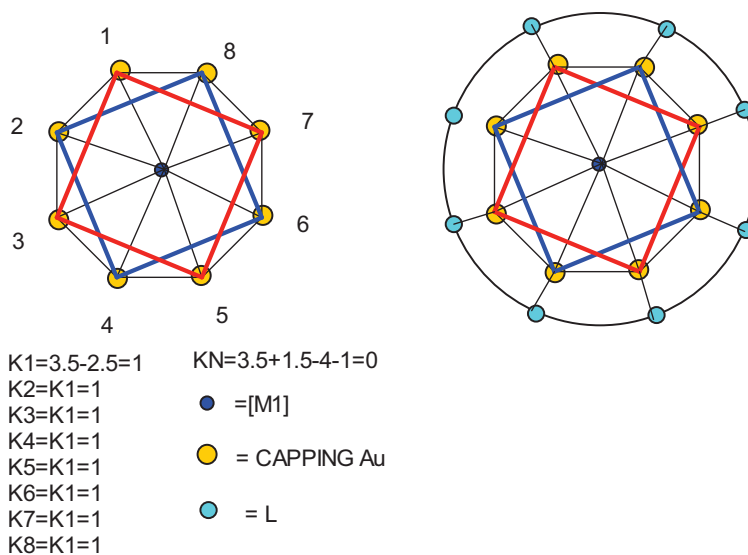


**$K(n) = 24(9)$  belongs to [M2] series.**

$Au_9L_8^{3+}$ :  $K = 9[3.5] - 8 + 1.5 = 25$ ;  $K(n) = 25(9)$ ,  $S = 4n - 14$ ,  $Kp = C^8C[M1]$

$Ve = 14n - 14 = 14(9) - 14 = 112$ ,  $VF = 9[11] + 16 - 3 = 112$       [M1],  $S = 4n + 2$ ,  $K = 2n - 1 = 2(9) - 1 = 17$

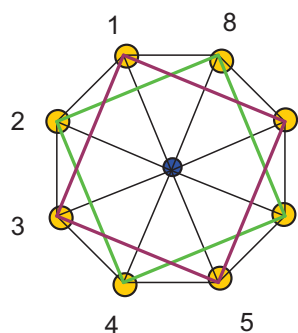
$SL = 8 + 8 + 8 + 1 = 25$



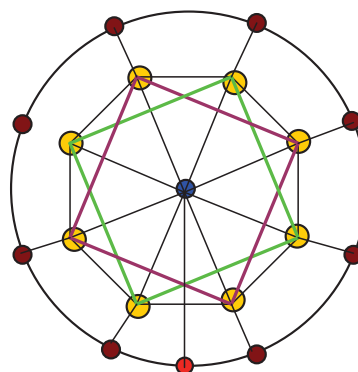
**$K(n) = 25(9)$  belongs to [M1] series**

$Au_{10}L_8Cl^{+1}$ :  $K = 10[3.5] - 8 - 0.5 + 0.5 = 27$ ;  $K(n) = 27(10)$ ,  $S = 4n - 14$ ,  $K_p = C^8C[M2]$

$[M2]$ ,  $S = 4n + 2$ ,  $K = 2n - 1$   
 $= 2(2) - 1 = 3$



$K1 = 3.5 - 2.5 = 1$   
 $K2 = K1 = 1$   
 $K3 = K1 = 1$   
 $K4 = K1 = 1$   
 $K5 = K1 = 1$   
 $K6 = K1 = 1$   
 $K7 = K1 = 1$   
 $K8 = K1 = 1$   
 $KN = 2[3.5] + 0.5 - 4 - 3 = 0.5$   
 $KT = 8.5$

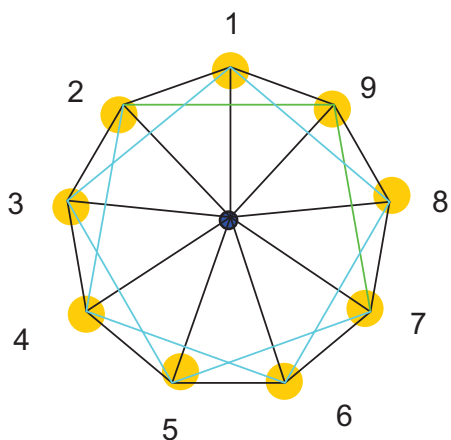


- = [M2]
- = L
- = CAPPING Au
- = Cl

$K(n) = 27(10)$  belongs to  $[M2]$  series.

$Au_{10}L_6Cl_3^{+1}$ :  $K = 10[3.5]-6-1.5+0.5 = 28(10)$ ,  $S = 4n-16$ ,  $Kp = C^9C[M1]$  [M1],  $K = 1$

$Ve = 14n-16 = 14(10)-16 = 124$ ;  $VF = 10[11]+12+3-1 = 124$



$SL = 9+9+9+1 = 28$

- = [M1]
- = CAPPING Au

$K1 = 3.5 - 2.5 = 1$

$K2 = K1 = 1$

$K3 = K1 = 1$

$K4 = K1 = 1$

$K5 = K1 = 1$

$K6 = K1 = 1$

$K7 = K1 = 1$

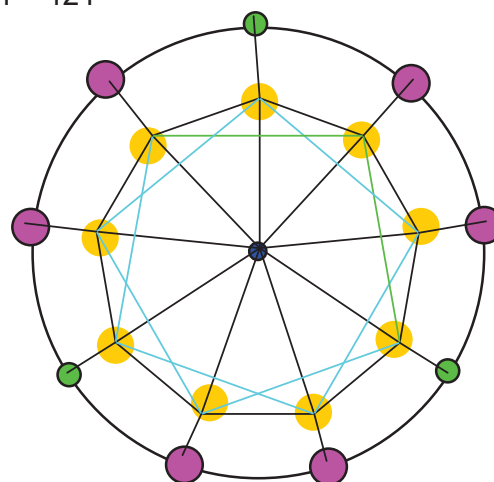
$K8 = K1 = 1$

$K9 = K1 = 1$

$K10 = K1 = 1$

$KN = 3.5 + 0.5 - 4.5 - 1 = -1.5$

$KT = 9 - 1.5 = 7.5 = 6L + 3Cl$



● = L

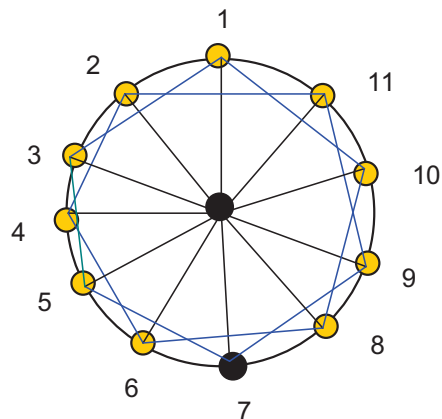
● = Cl

← BLACKHOLE NUCLEUS

$K(n) = 28(10)$  belongs to [M1] series.

$Au_{10}L_3R_4: K = 10[3.5]-3-2= 30(10), S=4n-20, Kp =C^{11}C[M-1]$

$Ve = 14n-20 = 14(10)-20 =120, VF= 10[11]+6+4= 120$   
 $[M-1], S =4n+2, K =2n-1 = 2(-1)-1 = -3$



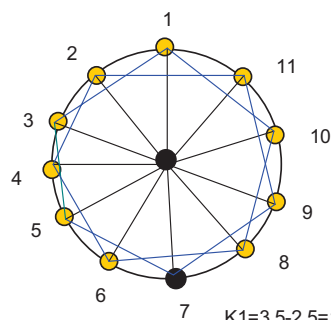
$K1=3.5-2.5=1$   
 $K2=K1=1$   
 $K3=K1=1$   
 $K4=K1=1$   
 $K5=K1=1$   
 $K6=K1=1$   
 $K7=K1=1$   
 $K8=K1=1$   
 $K9=K1=1$   
 $K10=K1=1$   
 $K11=K1=1$   
 $KN= -[3.5]-5.5-(-3)= -6$  ← BLACK HOLE NUCLEUS  
 $KT=11-6 =5 = 3L+4R$

$SL =11+11+11+[M-1]$   
 $= 33+(-3) = 30$

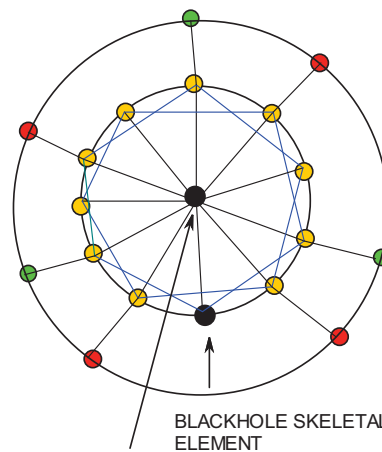
● = BLACK HOLE NUCLES/SKELETAL ELEMENT

● = CAPPING Au

$K(n) = 30(10)$  belongs to  $[M-1]$  series.



$K1=3.5-2.5=1$   
 $K2=K1=1$   
 $K3=K1=1$   
 $K4=K1=1$   
 $K5=K1=1$   
 $K6=K1=1$   
 $K7=K1=1$   
 $K8=K1=1$   
 $K9=K1=1$   
 $K10=K1=1$   
 $K11=K1=1$   
 $KN= -[3.5]-5.5-(-3)= -6$   
 $KT=11-6 =5 = 3L+4R$



BLACKHOLE SKELETAL ELEMENT

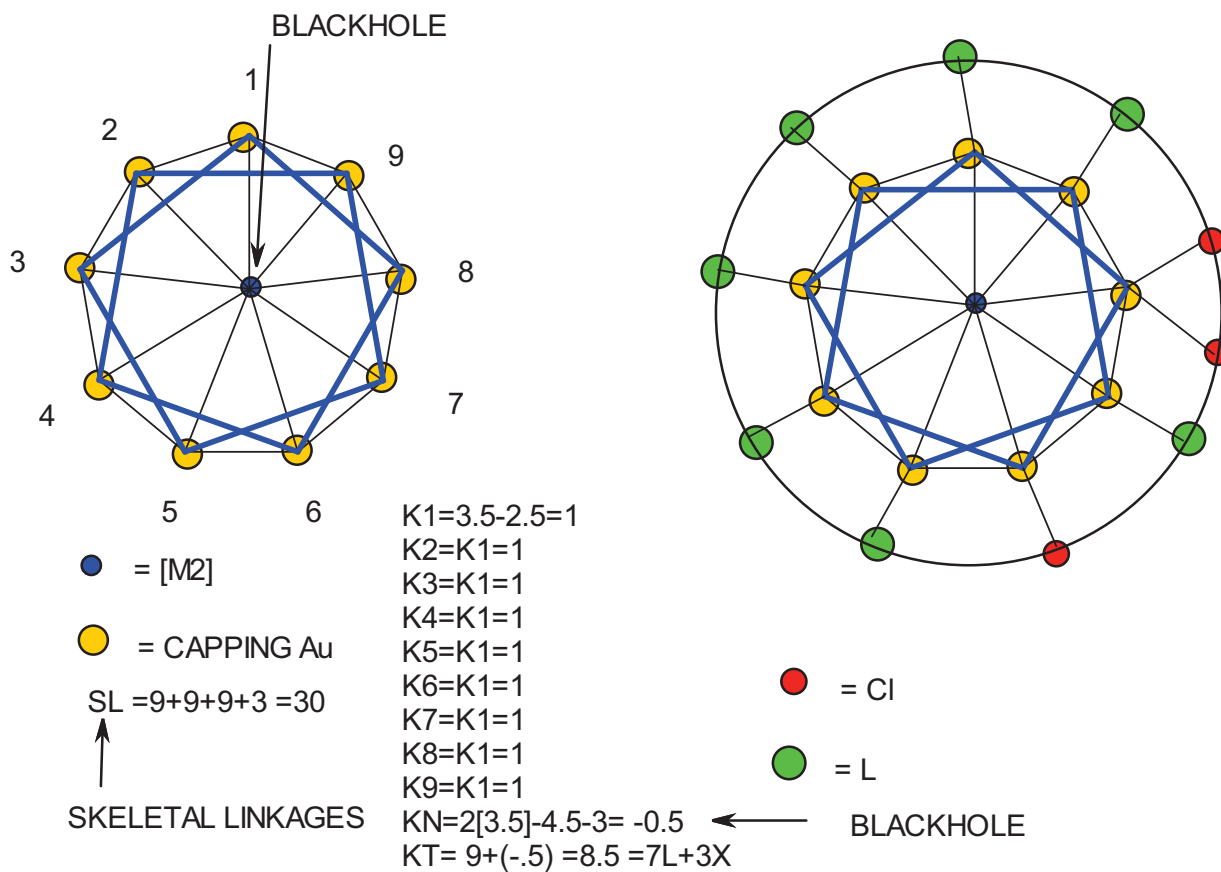
BLACKHOLE NUCLEUS

● = R

● = L

$Au_{11}L_7X_3$ :  $K = 11[3.5]-7-1.5 = 30$ ,  $K(n) = 30(11)$ ,  $S = 4n-16$ ,  $Kp = C^9C[M2]$

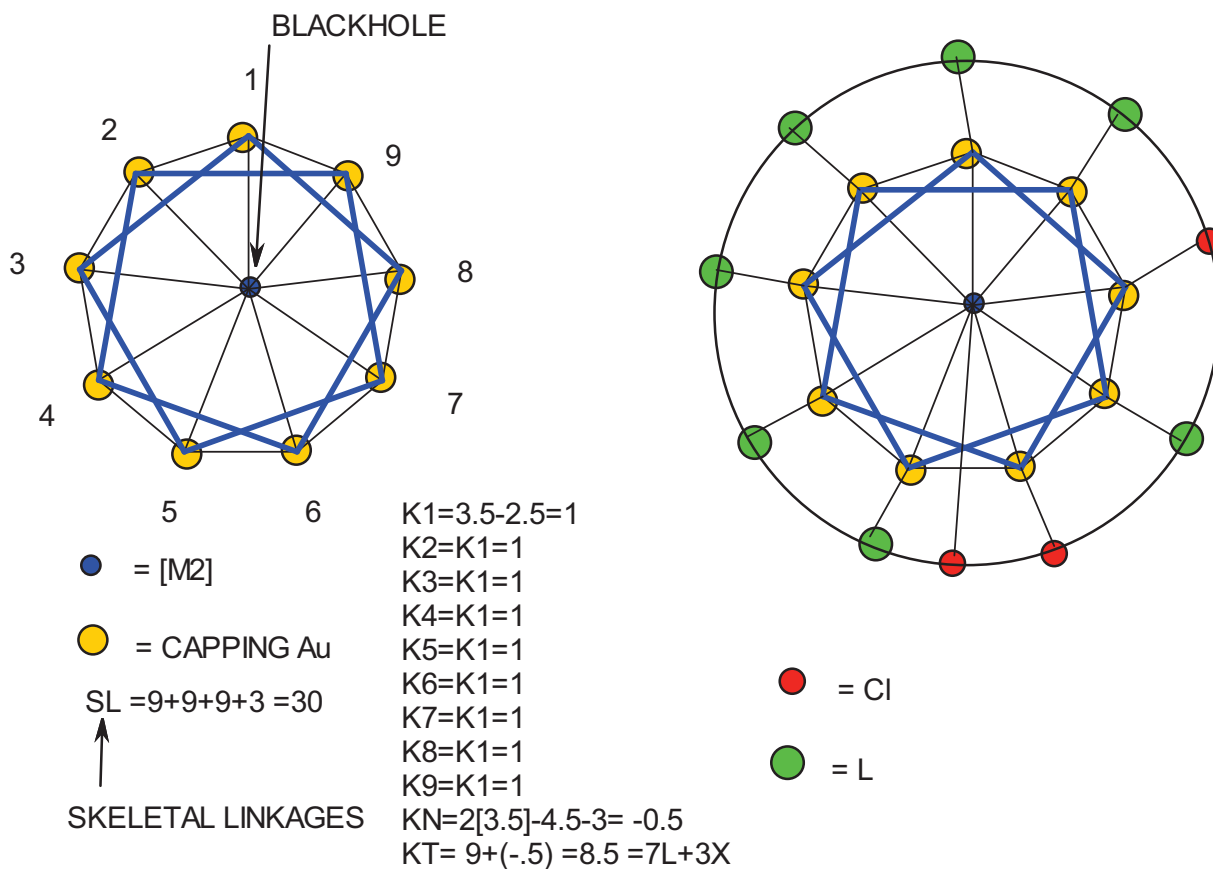
$Ve = 14n-16 = 14(11)-16 = 138$ ,  $\sqrt{VF} = 11[11]+14+3 = 138$ ;  $K[M2] = 3$



$K(n) = 30(11)$  belongs to [M2] series.

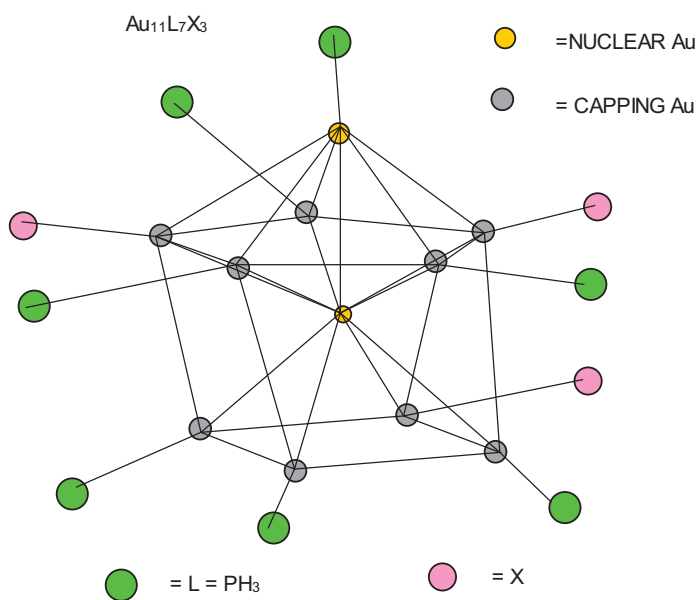
$Au_{11}L_7X_3$ :  $K = 11[3.5]-7-1.5 = 30$ ,  $K(n) = 30(11)$ ,  $S = 4n-16$ ,  $K_p = C^9C[M2]$

$V_e = 14n-16 = 14(11)-16 = 138$ ,  $V_f = 11[11]+14+3 = 138$ ;  $K[M2] = 3$



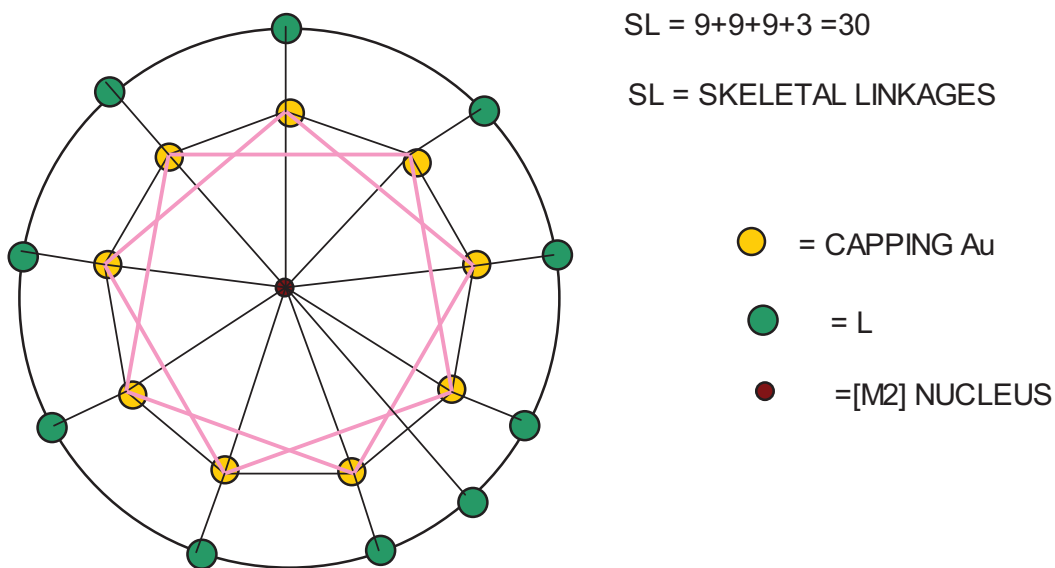
ISOMERISM





SKETCH OF THE OBSERVED STRUCTURE

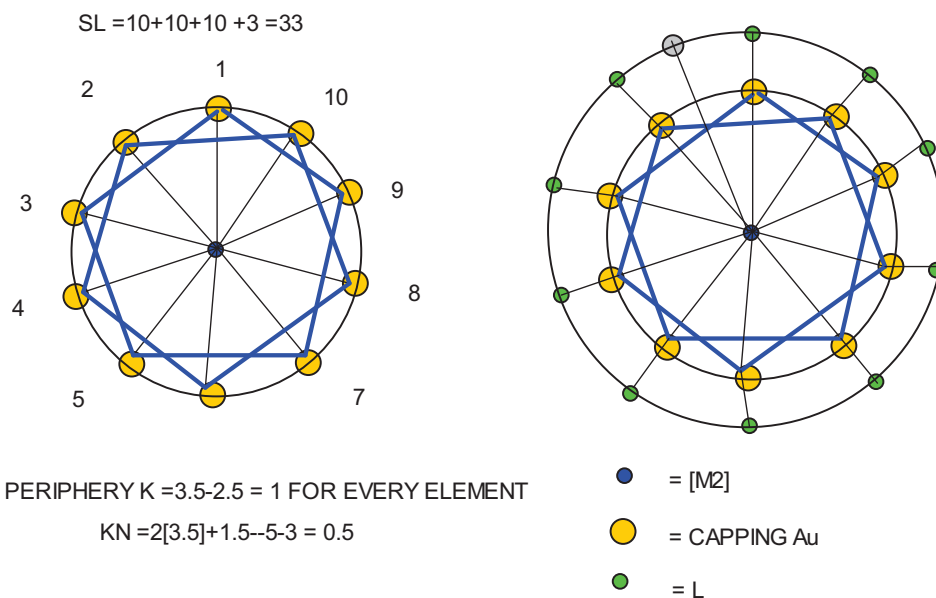
$Au_{11}L_{10}^{3+}$ :  $K = 11[3.5] - 10 + 1.5 = 30$ ;  $K(n) = 30(11)$ ,  $S = 4n - 16$ ,  $K_p = C^9C[M2]$   
 $Ve = 14n - 16 = 14(11) - 16 = 138$ ;  $VF = 11[11] + 20 - 3 = 138$



PERIPHERY,  $K = 1$   
 $KT = 9$   
 TOTAL K VALUES =  $KT$

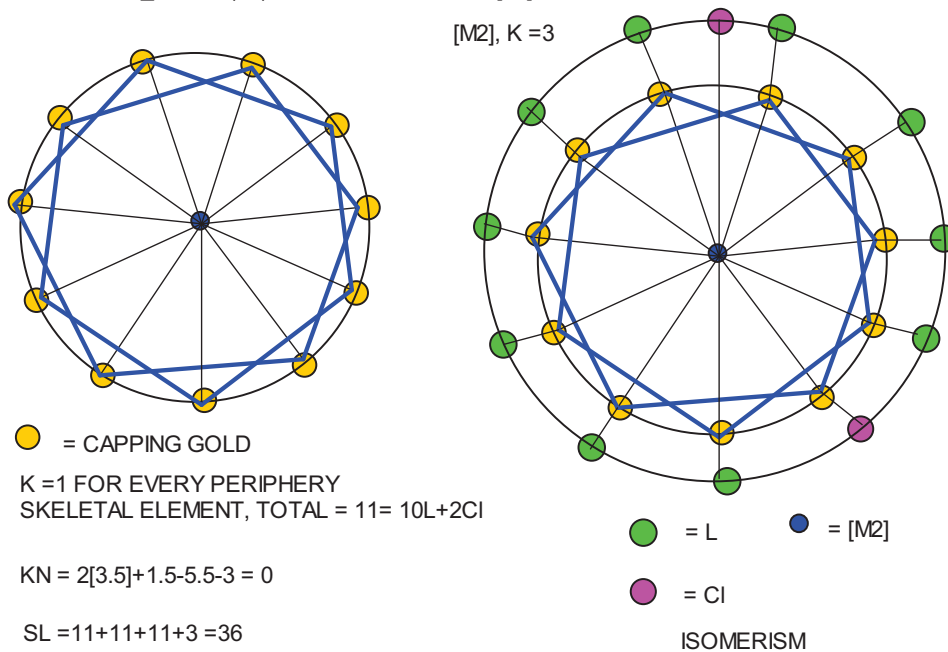
$KN = 2[3.5] + 1.5 - 4.5 - 3 = 1$   
 $GRD\ TOTAL = 9 + 1 = 10$

$Au_{12}L_{10}Cl^{3+}$ :  $K = 12[3.5]-10-0.5+1.5 = 33$ ;  $K(n) = 33(12)$ ,  $S = 4n-18$ ,  $Kp = C^{10}C[M2]$   
 $Ve = 14n-18 = 14(12)-18 = 150$ ;  $VF = 12[11]+20+1-3 = 150$  [M2],  $K = 3$



$K(n) = 33(12)$  belongs to [M2] series

$Au_{13}L_{10}Cl_2^{3+}$ :  $K = 13[3.5]-10-1+1.5 = 36$ ;  $K(n) = 36(13)$ ,  $S = 4n-20$ ,  $Kp = C^{11}C[M2]$   
 $Ve = 14n_{20} = 14(13)-20 = 162$   $VF = 13[11]+20+2-3 =$

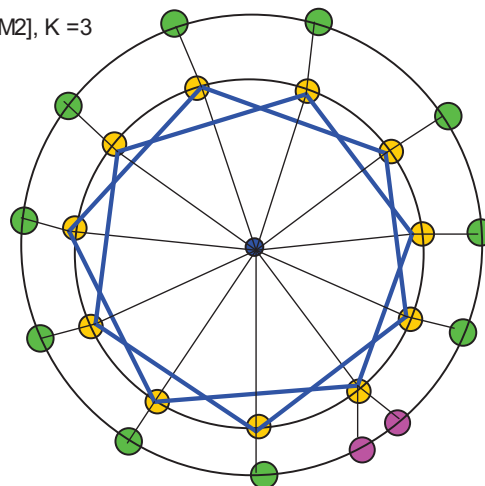
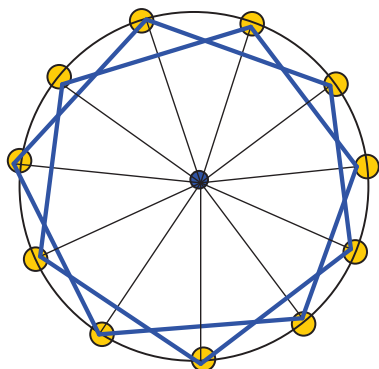


$K(n) = 36(13)$  belongs to [M2] series.

$Au_{13}L_{10}Cl_2^{3+}$ :  $K = 13[3.5] - 10 - 1 + 1.5 = 36$ ;  $K(n) = 36(13)$ ,  $S = 4n - 20$ ,  $K_p = C^{11}C[M2]$

$Ve = 14n_{20} = 14(13) - 20 = 162$        $VF = 13[11] + 20 + 2 - 3 =$

$[M2], K = 3$



● = CAPPING GOLD

$K = 1$  FOR EVERY PERIPHERY  
SKELETAL ELEMENT, TOTAL =  $11 = 10L + 2Cl$

$KN = 2[3.5] + 1.5 - 5.5 - 3 = 0$

$SL = 11 + 11 + 11 + 3 = 36$

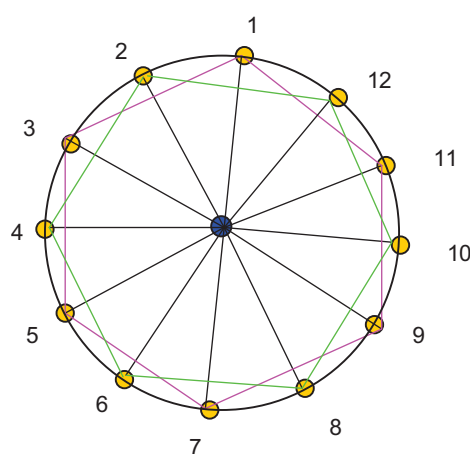
● = L      ● = [M2]  
● = Cl

ISOMERISM

$Au_{15}L_{12}(Cl)(H)^{3+}$ :  $K = 15[3.5] - 12 - 1 + 1.5 = 41$ ;  $K(n) = 41(15)$ ,  $S = 4n - 22$ ,  $K_p = C^{12}C[M3]$

$Ve = 14n - 22 = 14(15) - 22 = 188$ ;  $VF = 15[11] + 24 + 2 - 3 = 188$

$[M3], K = 2n - 1 = 2(3) - 1 = 5$

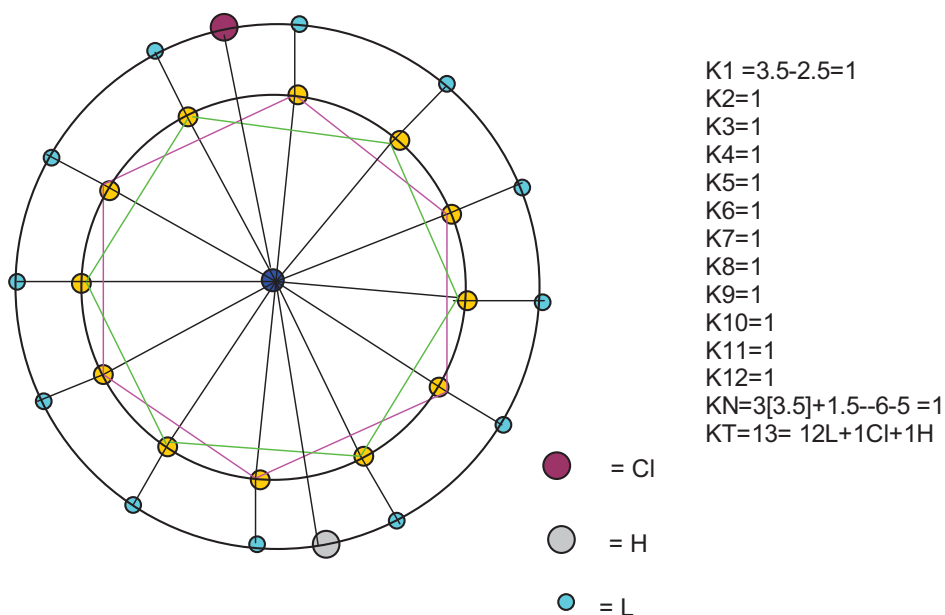


$K1 = 3.5 - 2.5 = 1$   
 $K2 = 1$   
 $K3 = 1$   
 $K4 = 1$   
 $K5 = 1$   
 $K6 = 1$   
 $K7 = 1$   
 $K8 = 1$   
 $K9 = 1$   
 $K10 = 1$   
 $K11 = 1$   
 $K12 = 1$   
 $KN = 3[3.5] + 1.5 - 6 - 5 = 1$   
 $KT = 13 = 12L + 1Cl + 1H$

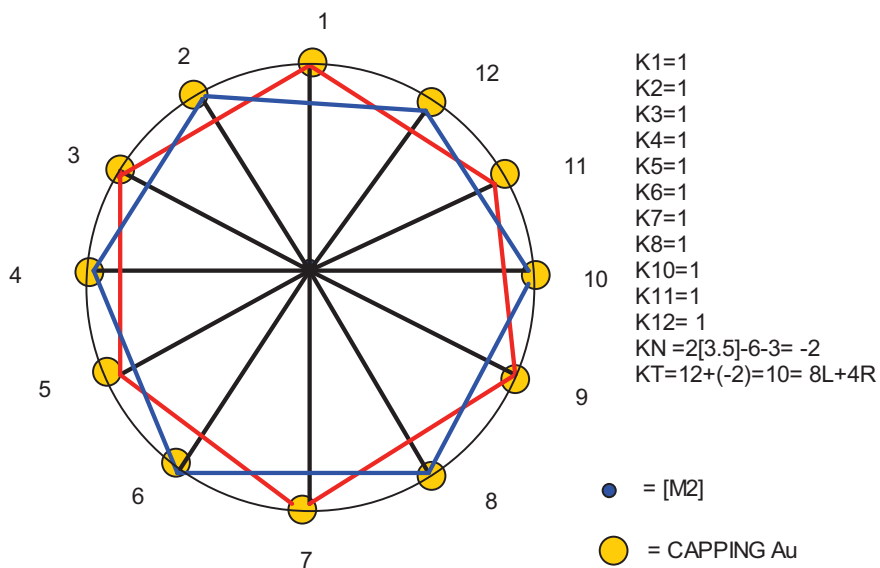
$SL = 12 + 12 + 12 + 5 = 41$

● = [M3]  
● = CAPPING Au

$K(n) = 41(15)$  belongs to [M3] series.



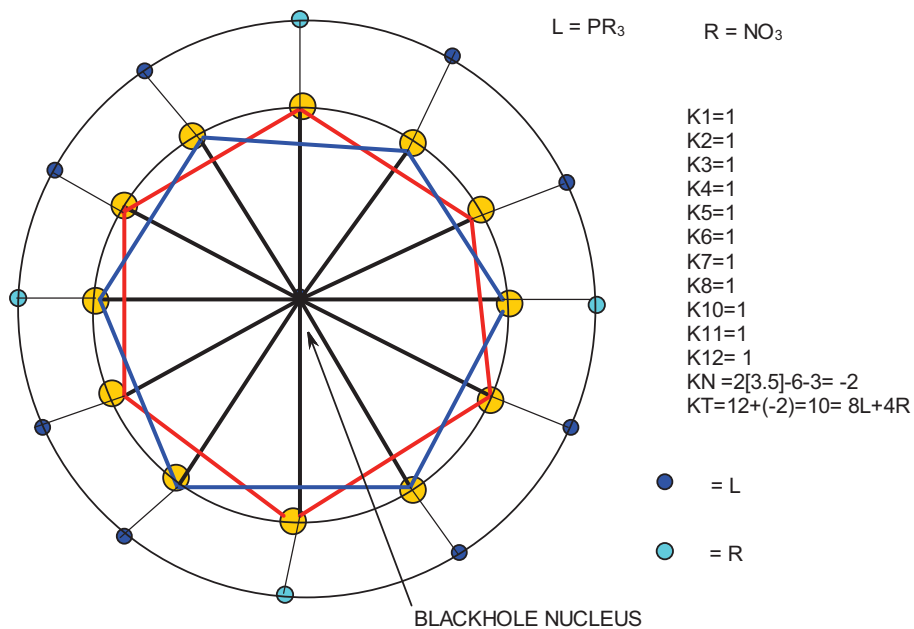
$Au_{14}L_8R_4$ :  $K = 14[3.5] - 8 - 2 = 39$ ,  $K(n) = 39(14)$ ,  $S = 4n - 22$ ,  $Kp = C^{12}C[M2]$   
 $Ve = 14n - 22 = 14(14) - 22 = 174$ ;  $VF = 14[11] + 16 + 4 = 174$  [M2],  $K = 3$



$SL = 12 + 12 + 12 + 3 = 39$

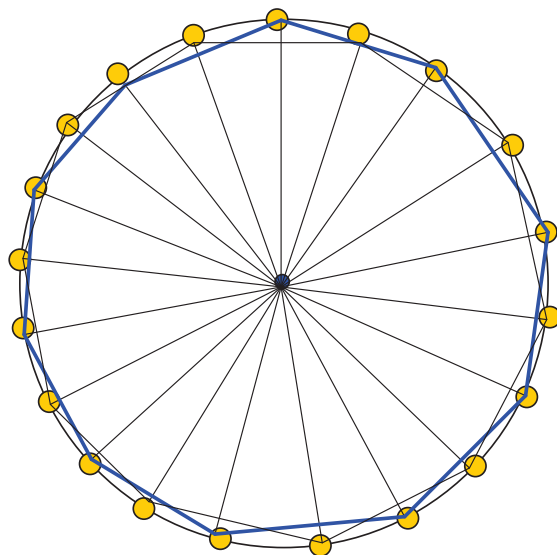
$K(n) = 39(14)$  belongs to [M2] series.

$Au_{14}L_8R_4$ :  $K = 14[3.5] - 8 - 2 = 39$ ,  $K(n) = 39(14)$ ,  $S = 4n - 22$ ,  $K_p = C^{12}C[M2]$



$K(n) = 59(20)$  belongs to  $[M0]$  series.

$Au_{20}L_{10}Cl_4^{2+}$ :  $K = 20[3.5] - 10 - 2 + 1 = 59$ ,  $K(n) = 59(20)$ ,  $S = 4n - 38$ ,  $K_p = C^{20}C[M0]$   
 $V_e = 14n - 38 = 14(20) - 38 = 242$ ,  $V_f = 20[11] + 20 + 4 - 2 = 242$



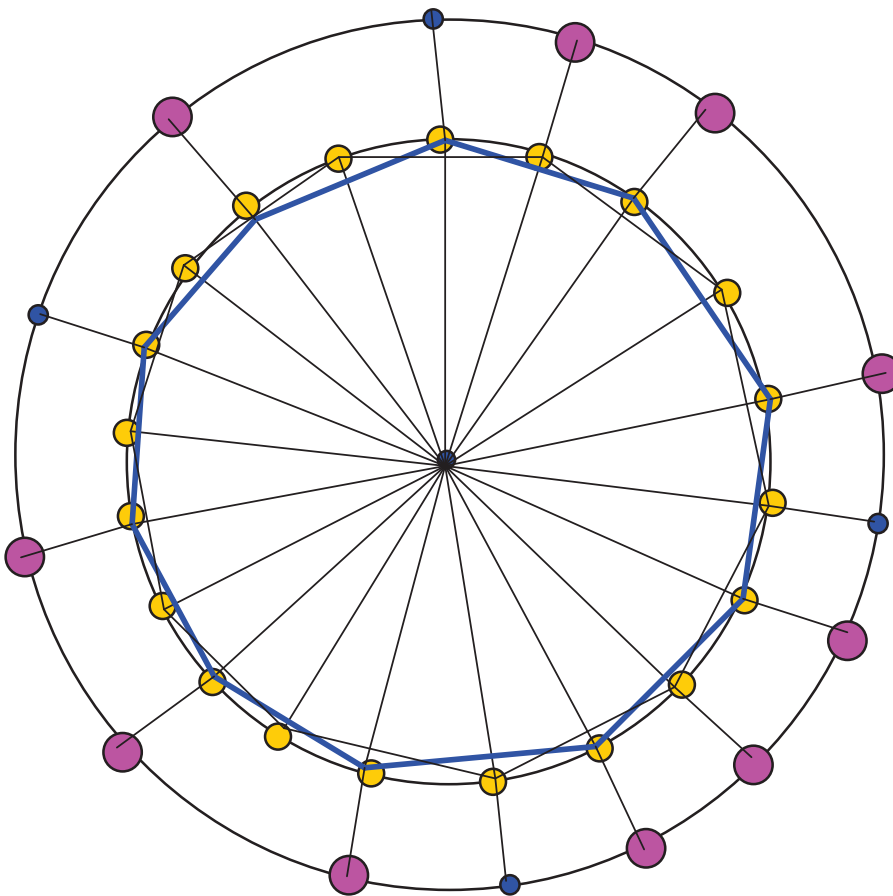
$SL = 20 + 20 + 20 + [M0]$

$[M0]$ ,  $K = 2n - 1 = 2(0) - 1 = -1$   
 $KT = 60 - 1 = 59$

$PL = 20[3.5] - 20(2.5) = 20$   
 $KNL = 0(3.5) + 1 - 20(0.5) - [-1] = 1 - 10 + 1 = -8$   
 $NET = 20 - 8 = 12 = 10L + 4Cl$   
 |

$$\text{Au}_{20}\text{L}_{10}\text{Cl}_4^{2+}: K = 20[3.5] - 10 - 2 + 1 = 59, K(n) = 59(20), S = 4n - 38, K_p = C^{20}C[M_0]$$

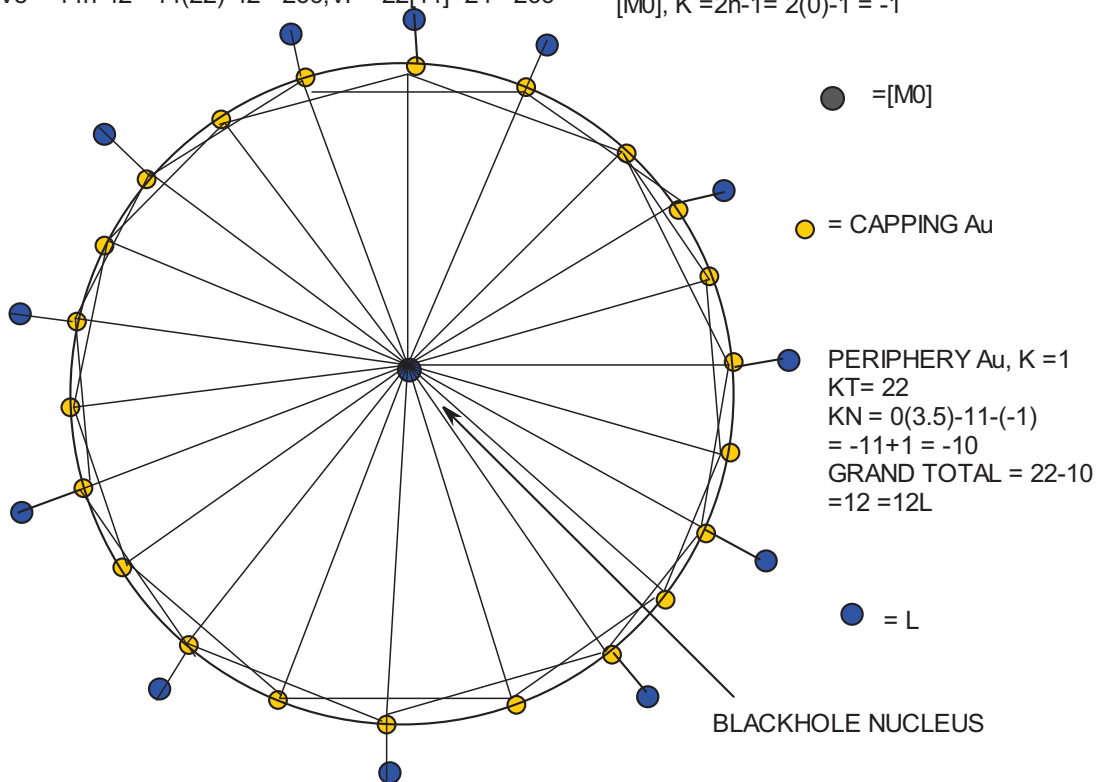
$$V_e = 14n - 38 = 14(20) - 38 = 242, V_f = 20[11] + 20 + 4 - 2 = 242$$



$Au_{22}L_{12}$ :  $K = 22[3.5]-12=65; K(n) = 65(22)$ ,  $S = 4n-42$ ,  $Kp = C^{22}C[M0]$

$Ve = 14n-42 = 14(22)-42 = 266; VF = 22[11]+24 = 266$

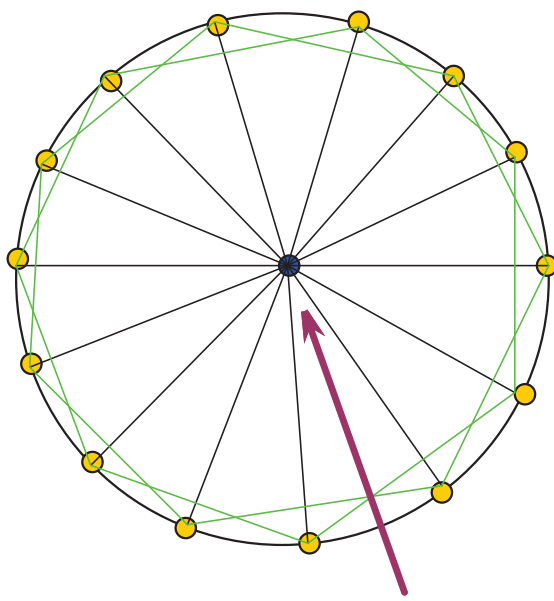
$[M0], K = 2n-1 = 2(0)-1 = -1$



$K(n) = 65(22)$  belongs to  $[M0]$  series.

$$\text{Au}_{16}\text{L}_8\text{Cl}_6: K = 16[3.5]-8-3 = 45; K(n) = 45(16), S = 4n-26, Kp = C^{14}C[M2]$$

SKELETAL LINKAGES =  $14+14+14+3 = 45$   
 3 ARE FROM [M2],  $S = 4n+2, K = 2n-1$   
 $= 2(16)-1 = 3$



Ligand linkage distribution  
 Periphery =  $14[3.5]-14(2.5) = 14$   
 Nucleus =  $2[3.5]-14(0.5)-3 = -3$   
 This means that the nucleus has negative nuclear linkages for ligands-BLACKHOLE.  
 The NET linkages available for ligands =  $14+(-3) = 8$ . This is the same as  $8l + 6Cl$ .

- = [M2] BLACKHOLE NUCLEUS
- = CAPPING Au

BLACKHOLE

$K(n) = 45(16)$  belongs to [M2] series.

The categorization of  $K(n)$  values of the golden clusters into respective [Mx] clan groups can easily be verified using the appropriate series given in SRS-1. The calculation of  $K$  values and respective valence electrons from the series formula,  $Ve$  and the cluster formula,  $VF$  are given in Table 1. The clusters were regrouped according to [Mx] series and are presented in Table 2. In order to emphasize the idea of grouping the clusters according to [Mx] series, cluster group trees of selected clusters were constructed F-35 to F-37 for selected clusters of [M1], [M2] and [M6]. A proposed scheme for broad grouping of clusters is shown GR-1.

Table 1. Deducing  $K(n)$  Parameter and Deriving the Series of Golden Clusters

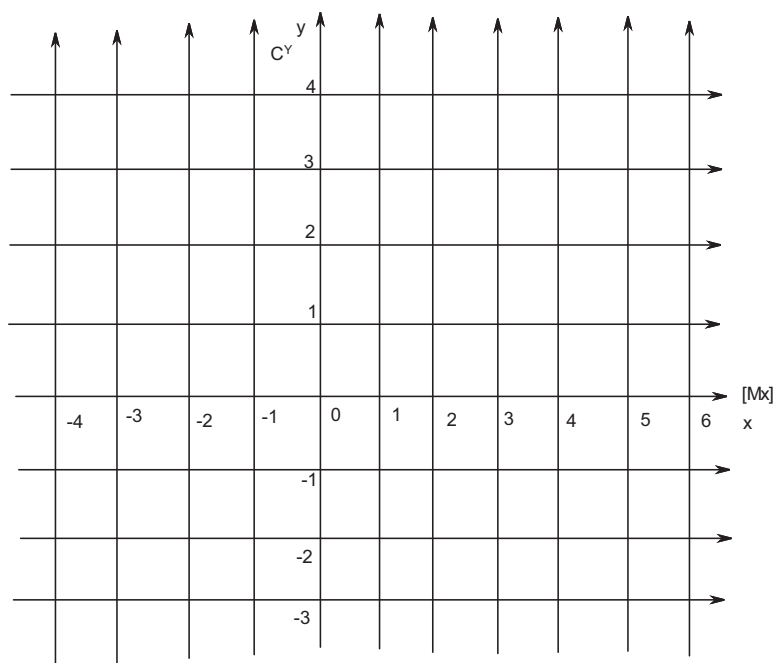
CLUSTER	n	K VALUE	K(n)	SERIES $S = 4n+q$	$Kp$ $= C^qC[Mx]$	$Ve$ $Ve = 14n+q$	VF
$\text{Au}_4\text{L}_2\text{L}_4$	4	$4[3.5]-1-4 = 9$	9(4)	$4n-2$	$C^2C[M2]$	$14(4)-2=54$	$4[11]+2+8 = 54$
$\text{Au}_6\text{L}_8^{2+}$	6	$6[3.5]-8+1 = 14$	14(6)	$4n-4$	$C^3C[M3]$	$14(6)-4=80$	$6[11]+8(2)-2=80$
$\text{Au}_6\text{L}_6^{2+}$	6	$6[3.5]-6+1 = 16$	16(6)	$4n-8$	$C^5C[M1]$	$14(6)-8=76$	$6[11]+6(2)-2=76$
$\text{Au}_7\text{L}_7^{+1}$	7	$7[3.5]-7+0.5=18$	18(7)	$4n-8$	$C^5C[M2]$	$14(7)-8=90$	$7[11]+14-1=90$
$\text{Au}_8\text{L}_8\text{Cl}_2^{2+}$	8	$8[3.5]-8-1+1 = 20$	20(8)	$4n-8$	$C^5C[M3]$	$14(8)-8=104$	$8[11]+8(2)+2-2=104$
$\text{Au}_8\text{L}_8^{2+}$	8	$8[3.5]-8+1=21$	21(8)	$4n-10$	$C^6C[M2]$	$14(8)-10 = 102$	$8[11]+8(2)-2 = 102$
$\text{Au}_8\text{L}_7^{2+}$	8	$8[3.5]-7+1 = 22$	22(8)	$4n-12$	$C^7C[M1]$	$14(8)-12=100$	$8[11]+7(2)-2=100$
$\text{Au}_9\text{L}_8^{+}$	9	$9[3.5]-8+0.5=24$	24(9)	$4n-12$	$C^7C[M2]$	$14(9)-12=114$	$9[11]+16-1 = 114$
$\text{Au}_9\text{L}_8^{3+}$	9	$9[3.5]-8+1.5=25$	25(9)	$4n-14$	$C^8C[M1]$	$14(9)-14= 112$	$9[11]+8(2)-3=112$
L=Par3							
$\text{Au}_{10}\text{L}_8\text{Cl}^+$	10	$10[3.5]-8-0.5+0.5=27$	27(10)	$4n-14$	$C^8C[M2]$	$14(10)-14=126$	$10[11]+16+1-1=126$
$\text{Au}_{10}\text{L}_6\text{Cl}_3^+$	10	$10[3.5]-6-1.5+0.5=28$	28(10)	$4n-16$	$C^9C[M1]$	$14(10)-16=124$	$10[11]+6(2)+3-1 = 124$
$\text{Au}_{10}\text{L}_3\text{R}_4$	10	$10[3.5]-3-2=30$	30(10)	$4n-20$	$C^{11}C[M-1]$	$14(10)-20=120$	$10[11]+3(2)+4 = 120$
$\text{Au}_{11}\text{L}_{12}^{3+}$	11	$11[3.5]-12+1.5=28$	28(11)	$4n-12$	$C^7C[M4]$	$14(11)-12=142$	$11[11]+12(2)-3 = 142$
$\text{Au}_{11}\text{L}_8\text{Cl}_3$		$11[3.5]-8-1.5=29$	29(11)	$4n-14$	$C^8C[M3]$	$14(11)-14=140$	$11[11]+8(2)+3=140$
$\text{Au}_{11}\text{L}_7\text{X}_3$	11	$11[3.5]-7-1.5=30$	30(11)	$4n-16$	$C^9C[M2]$	$14(11)-16=138$	$11[11]+7(2)+3 = 138$
L=PAR <sub>3</sub> X= Cl							
$\text{Au}_{11}\text{L}_8\text{Cl}_2^+$	11	$11[3.5]-8-1+0.5=30$	30(11)	$4n-16$	$C^9C[M2]$	$14(11)-16=138$	$11[11]+8(2)+2-1=138$



Au <sub>11</sub> L <sub>10</sub> <sup>3+</sup>	11	11[3.5]-10+1.5=30	30(11)	4n-16	C <sup>9</sup> C[M2]	14(11)-16=138	11[11]+10(2)-3=138
Au <sub>12</sub> L <sub>10</sub> Cl <sub>2</sub> <sup>3+</sup>	12	12[3.5]-10-0.5+1.5=33	33(12)	4n-18	C <sup>10</sup> C[M2]	14(12)-18=150	12[11]+20+1-3=150
Au <sub>13</sub> L <sub>10</sub> Cl <sub>2</sub> <sup>3+</sup>	13	13[3.5]-10-1+1.5=36	36(13)	4n-20	C <sup>11</sup> C[M2]	14(13)-20=162	13[11]+10(2)+2-3=162
Au <sub>13</sub> L <sub>8</sub> Cl <sub>4</sub> <sup>+</sup>	13	13[3.5]-8-2+0.5=36	36(13)	4n-20	C <sup>11</sup> C[M2]	14(13)-20=162	13[11]+10(2)+2-3=162
Au <sub>15</sub> L <sub>12</sub> Cl(H) <sup>3+</sup>	15	15[3.5]-12-0.5-0.5+1.5=41	41(15)	4n-22	C <sup>12</sup> C[M3]	14(15)-22=188	15[11]+24+2-3=188
Au <sub>16</sub> L <sub>8</sub> X <sub>8</sub>	16	16[3.5]-8-4=44	44(16)	4n-24	C <sup>13</sup> C[M3]	14(16)-24=200	16[11]+16+8=200
Au <sub>20</sub> L <sub>10</sub> Cl <sub>4</sub> <sup>2+</sup>	20	20[3.5]-10-2+1=59	59(20)	4n-38	C <sup>20</sup> C[M0]	14(20)-38=242	20[11]+10(2)+4-2=242
Au <sub>22</sub> L <sub>12</sub>	22	22[3.5]-12=65	65(22)	4n-42	C <sup>22</sup> C[M0]	14(22)-42=266	22[11]+12(2)=266
Au <sub>24</sub> L <sub>10</sub> R <sub>5</sub> X <sub>2</sub> <sup>+1</sup>	24	24[3.5]-10-2.5-1+0.5=71	71(24)	4n-46	C <sup>24</sup> C[M0]	14(24)-46=290	24[11]+20+5+2-1=290
Au <sub>25</sub> L <sub>10</sub> (SR) <sub>5</sub> <sup>2+</sup>	25	25[3.5]-10-2.5+1=76	76(25)	4n-52	C <sup>27</sup> C[M-2]	14(25)-52=298	25[11]+10(2)+5-2=298
Au <sub>36</sub> R <sub>34</sub>	36	36[3.5]-17=109	109(36)	4n-74	C <sup>38</sup> C[M-2]	14(36)-74=430	36[11]+34=430
Au <sub>38</sub> L <sub>18</sub> Cl <sub>2</sub> <sup>4+</sup>	38	38[3.5]-18-1+2=116	116(38)	4n-80	C <sup>41</sup> C[M-3]	14(38)-80=452	38[11]+36+2-4=452
Au <sub>39</sub> L <sub>14</sub> Cl <sub>6</sub> <sup>3+</sup>	39	39[3.5]-14-3+1.5=121	121(39)	4n-86	C <sup>44</sup> C[M-5]	14(39)-86=460	39[11]+28+6-3=460
Au <sub>39</sub> L <sub>14</sub> Cl <sub>6</sub> <sup>+1</sup>	39	39[3.5]-14-3+0.5=120	120(39)	4n-84	C <sup>43</sup> C[M-4]	14(39)-84=462	39[11]+28+6-1=462
Au <sub>40</sub> R <sub>24</sub>	40	40[3.5]-12=128	128(40)	4n-96	C <sup>49</sup> C[M-9]	14(40)-96=464	40[11]+24=464
Au <sub>102</sub> R <sub>44</sub>	102	102[3.5]-22=335	335(102)	4n-262	C <sup>132</sup> C[M-30]	14(102)-262=1166	102[11]+44=1166

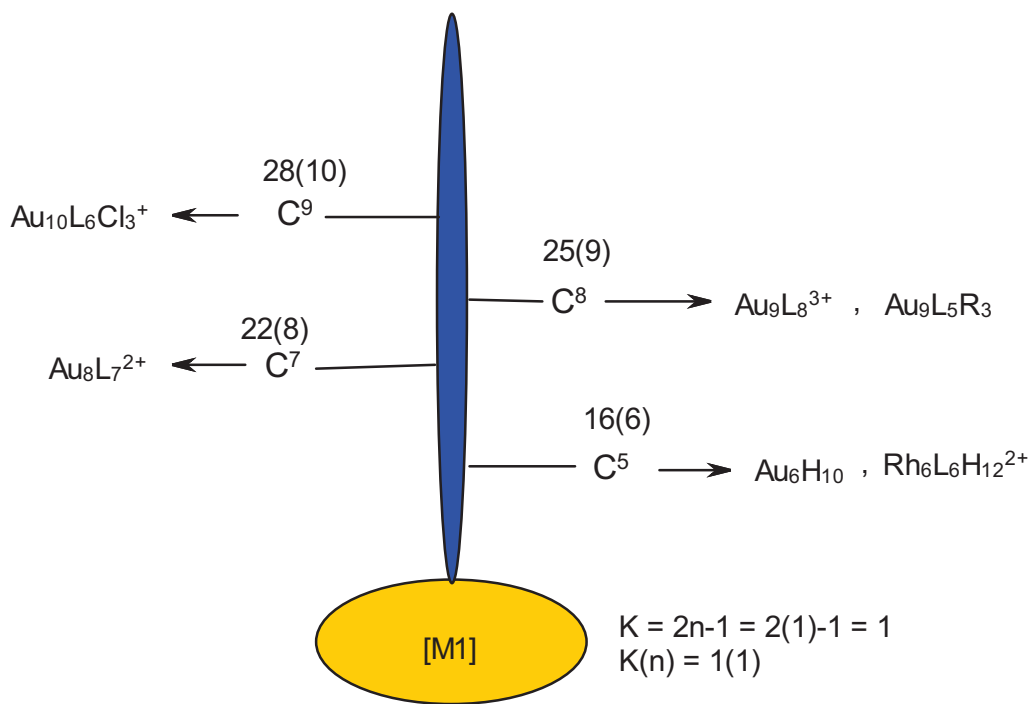
Table 2. Grouping of Golden Clusters

CLUSTER	K(n)	Kp = C <sup>y</sup> C[Mx]	CLOSO SERIES, [Mx]	CLAN	GROUP	BLACK HOLES
		y	X value			
Au <sub>144</sub> R <sub>60</sub>	474(144)	187	-43		[M-43]	BLACKHOLE NUCLEUS
Au <sub>102</sub> R <sub>44</sub>	335(102)	132	-30		[M-30]	BLACKHOLE NUCLEUS
Au <sub>40</sub> R <sub>24</sub>	128(40)	49	-9		[M-9]	BLACKHOLE NUCLEUS
Au <sub>39</sub> L <sub>14</sub> Cl <sub>6</sub> <sup>3+</sup>	121(39)	44	-5		[M-5]	BLACKHOLE NUCLEUS
Au <sub>39</sub> L <sub>14</sub> Cl <sub>6</sub> <sup>+1</sup>	120(39)	43	-4		[M-4]	BLACKHOLE NUCLEUS
Au <sub>38</sub> L <sub>18</sub> Cl <sub>2</sub> <sup>4+</sup>	116(38)	41	-3		[M--3]	BLACKHOLE NUCLEUS
Au <sub>36</sub> R <sub>34</sub>	109(36)	38	-2		[M-2]	BLACKHOLE NUCLEUS
Au <sub>25</sub> L <sub>10</sub> (SR) <sub>5</sub> <sup>2+</sup>	76(25)	27	-2		[M-2]	BLACKHOLE NUCLEUS
Au <sub>10</sub> L <sub>3</sub> R <sub>4</sub>	30(10)	11	-1		[M-1]	BLACKHOLE NUCLEUS
Au <sub>20</sub> L <sub>10</sub> Cl <sub>4</sub> <sup>2+</sup>	59(10)	20	0		[M0]	BLACKHOLE NUCLEUS
Au <sub>22</sub> L <sub>12</sub>	65(22)	22	0		[M0]	BLACKHOLE NUCLEUS
Au <sub>6</sub> H <sub>10</sub>	16(6)	5	1		[M1]	
Rh <sub>6</sub> L <sub>6</sub> H <sub>12</sub> <sup>2+</sup>	16(6)	5	1		[M1]	
Au <sub>8</sub> L <sub>7</sub> <sup>+2</sup>	22(8)	7	1		[M1]	
Au <sub>9</sub> L <sub>8</sub> <sup>+3</sup>	25(9)	8	1		[M1]	
Au <sub>10</sub> L <sub>6</sub> Cl <sub>3</sub> <sup>+1</sup>	28(10)	9	1		[M1]	
Au <sub>4</sub> L <sub>4</sub> L <sub>2</sub>	9(4)	2	2		[M2]	
Au <sub>8</sub> L <sub>8</sub> <sup>+2</sup>	21(8)	6	2		[M2]	
Au <sub>10</sub> L <sub>8</sub> Cl <sub>1</sub> <sup>+1</sup>	27(10)	8	2		[M2]	
Au <sub>11</sub> L <sub>10</sub> <sup>3+</sup>	30(11)	9	2		[M2]	
Au <sub>11</sub> L <sub>7</sub> X <sub>3</sub>	30(11)	9	2		[M2]	
Au <sub>12</sub> L <sub>10</sub> Cl <sub>1</sub> <sup>+3</sup>	33(12)	10	2		[M2]	
Au <sub>13</sub> L <sub>10</sub> Cl <sub>3</sub> <sup>3+</sup>	36(13)	11	2		[M2]	
Au <sub>14</sub> L <sub>8</sub> R <sub>4</sub>	39(14)	12	2		[M2]	
Au <sub>6</sub> L <sub>8</sub> <sup>+2</sup>	14(6)	3	3		[M3]	
Au <sub>6</sub> L <sub>8</sub> <sup>+2</sup>	14(6)	3	3		[M3]	
Au <sub>8</sub> L <sub>8</sub> Cl <sub>2</sub> <sup>+2</sup>	20(8)	5	3		[M3]	
Au <sub>15</sub> L <sub>12</sub> (Cl)(H) <sup>3+</sup>	41(15)	12	3		[M3]	
Zn <sub>6</sub> H <sub>10</sub>	13(6)	2	4		[M4]	
B <sub>5</sub> H <sub>9</sub>	8(5)	-1	6		[M6]	
B <sub>4</sub> H <sub>10</sub>	5(4)	-2	6		[M6]	
B <sub>6</sub> H <sub>10</sub>	10(6)	-1	7		[M7]	
C <sub>6</sub> H <sub>10</sub>	7(6)	-4	10		[M10]	

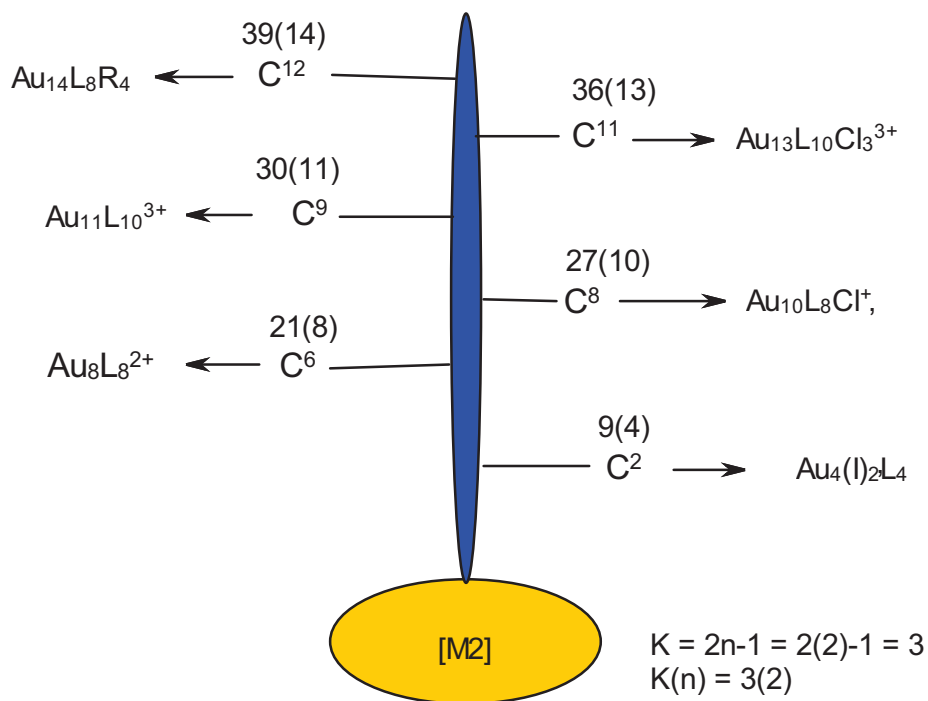


GR-1

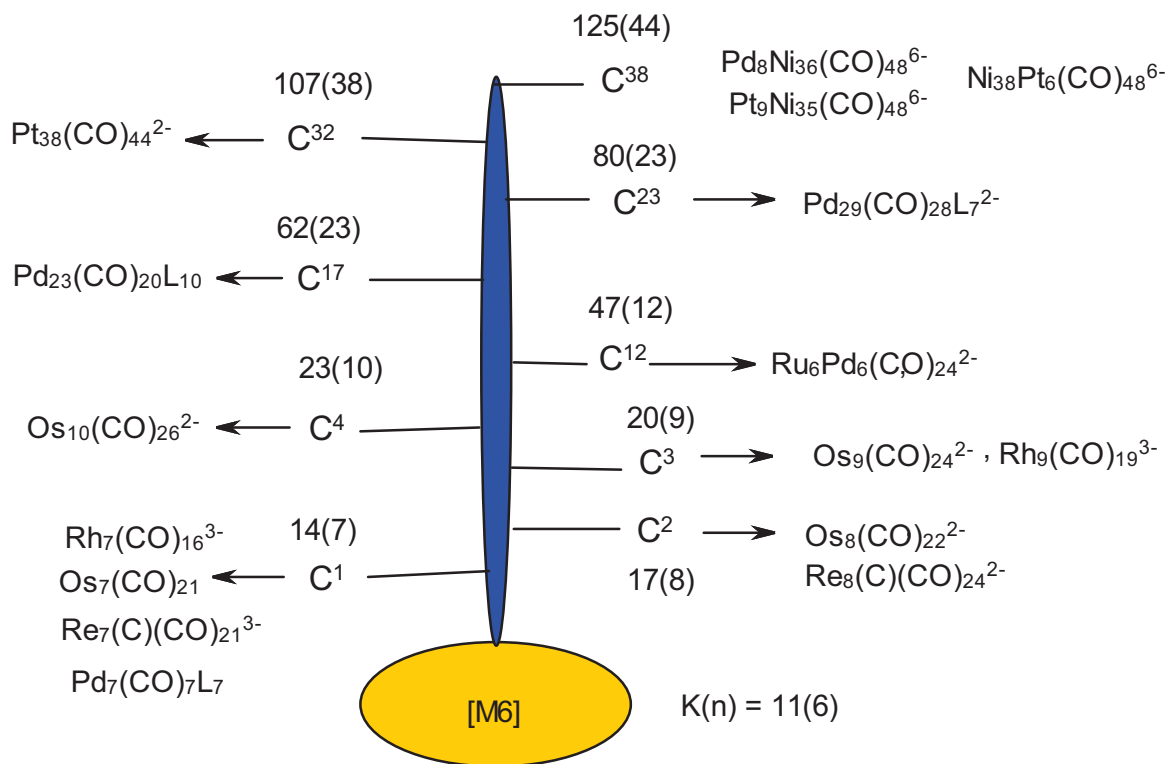
Clan (Group) Cluster Trees



CLUSTER GROUP(CLAN) TREE



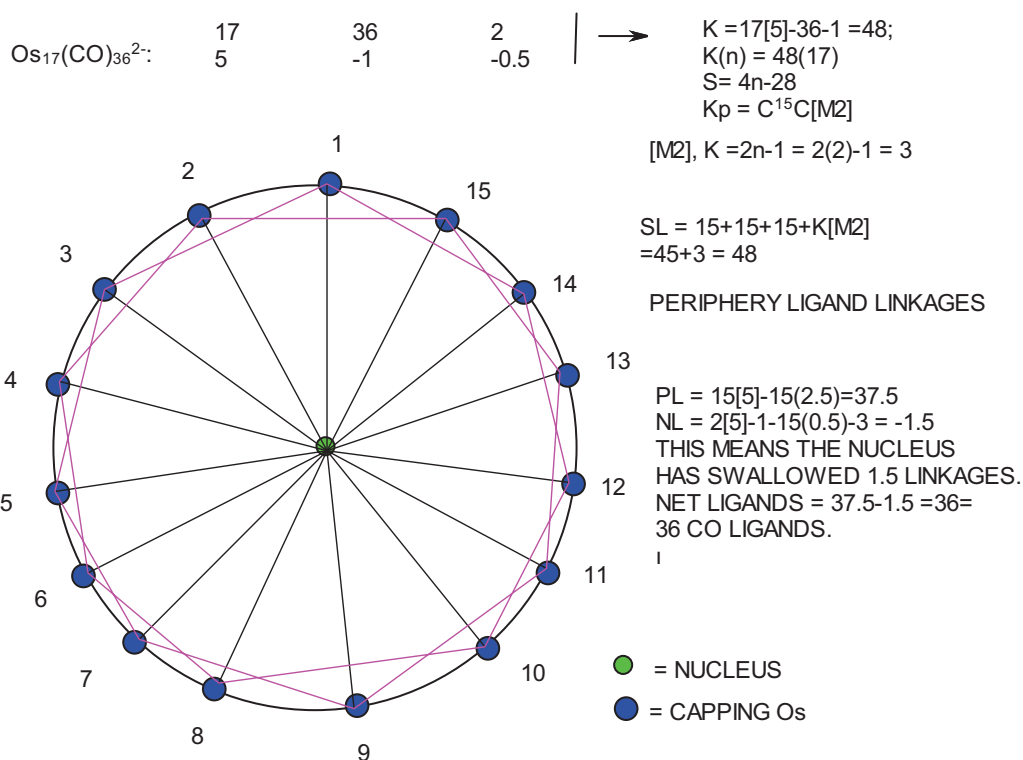
CLUSTER GROUP(CLAN) TREE

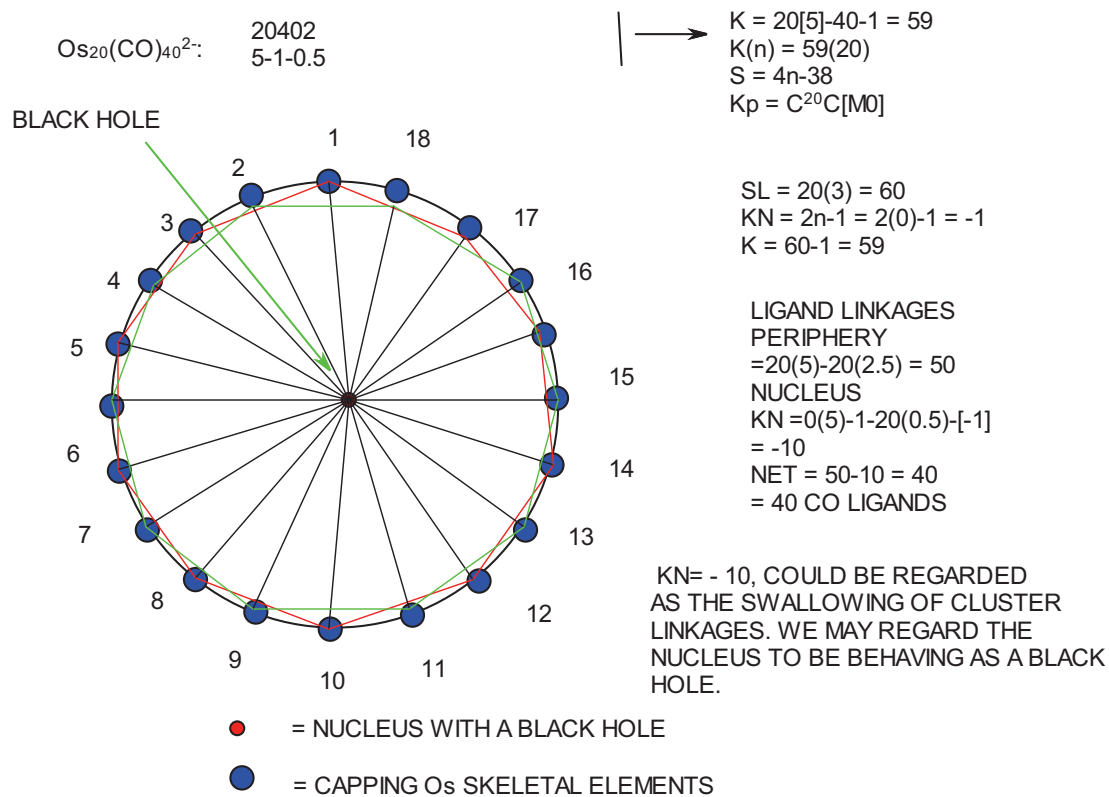


CLUSTER GROUP(CLAN) TREE

### The Existence of Blackholes in the Nuclei of Some Golden Clusters

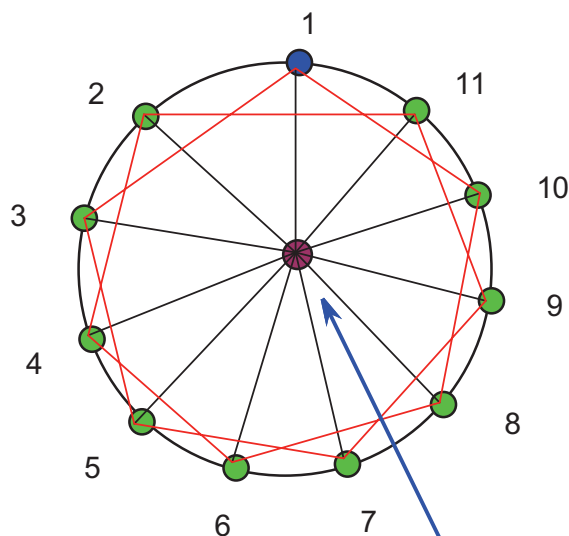
In the previous work, it was discovered that the series method could be applied to the analysis and categorization of golden clusters (Kiremire, 2016a 2017a). It was also found that the majority of the simple clusters of nuclearity index 4-13 had either ONE or TWO golden skeletal elements in the cluster nucleus (Kiremire, 2016a, 2017a). This information was in agreement with earlier observation by the series method that indeed some clusters had octahedral cluster nuclei in them (Kiremire, 2016b). The subsequent work also revealed that, clusters could be explained more clearly in terms of their structures and ligand distribution onto skeletal elements by using skeletal numbers and valences (Kiremire, 2017c). Using skeletal numbers and the ligand distribution concept, it has been discovered that some golden cluster nuclei with  $[Mx]$ , where  $x \leq 0$  do “swallow” skeletal and/or ligand linkages. As a consequence, the numbers of linkages left for binding to ligands are considerably diminished giving rise to some golden clusters being left naked, that is, having no ligands at all. It is proposed that clusters with nuclei which appear to “swallow” cluster linkages be regarded as NUCLEI WITH BLACKHOLES. Examples of golden clusters having nuclei with black-holes are given F-38 to F-41.





Au<sub>10</sub>L<sub>3</sub>R<sub>4</sub>:      10      3      4  
                          3.5      -1      -0.5

- = CAPPING Au
- = [M-1] NUCLEUS
- = FICTITIOUS ELEMENT



$$SL = 11 + 11 + 11 + K[M-1]$$

$$= 33 - 3 = 30$$

BLACKHOLE IN THE NUCLEUS

→  $K = 10[3.5] - 3 - 2 = 30$   
 $K(n) = 30(10)$   
 $S = 4n - 20$   
 $K_p = C^{11}C[M-1]$   
 THUS, 11 SKELETAL ELEMENTS  
 CAPPING ONE OF WHICH IS  
 FICTITIOUS (EMPTY HOLE) SINCE  
 WE HAVE ONLY 10 AVAILABLE  
 SKELETAL ELEMENTS.

$$[M-1], K = 2n - 1 = 2(-1) - 1 = -3$$

THIS MEANS THREE SKELETAL LINKAGES  
 HAVE BEEN SWALLOWED.

PERIPHERY LIGAND LINKAGES  
 $PL = 11[3.5] - 11(2.5) = 11$   
 NUCLEAR LIGAND LINKAGES  
 $= -1[3.5] - 11(0.5) - [-3] = -6$   
 THUS, SIX LIGAND LINKAGES HAVE BEEN  
 SWALLOWED BY THE NUCLEUS.  
 $NET = 11 - 6 = 5 = 3L + 4R$

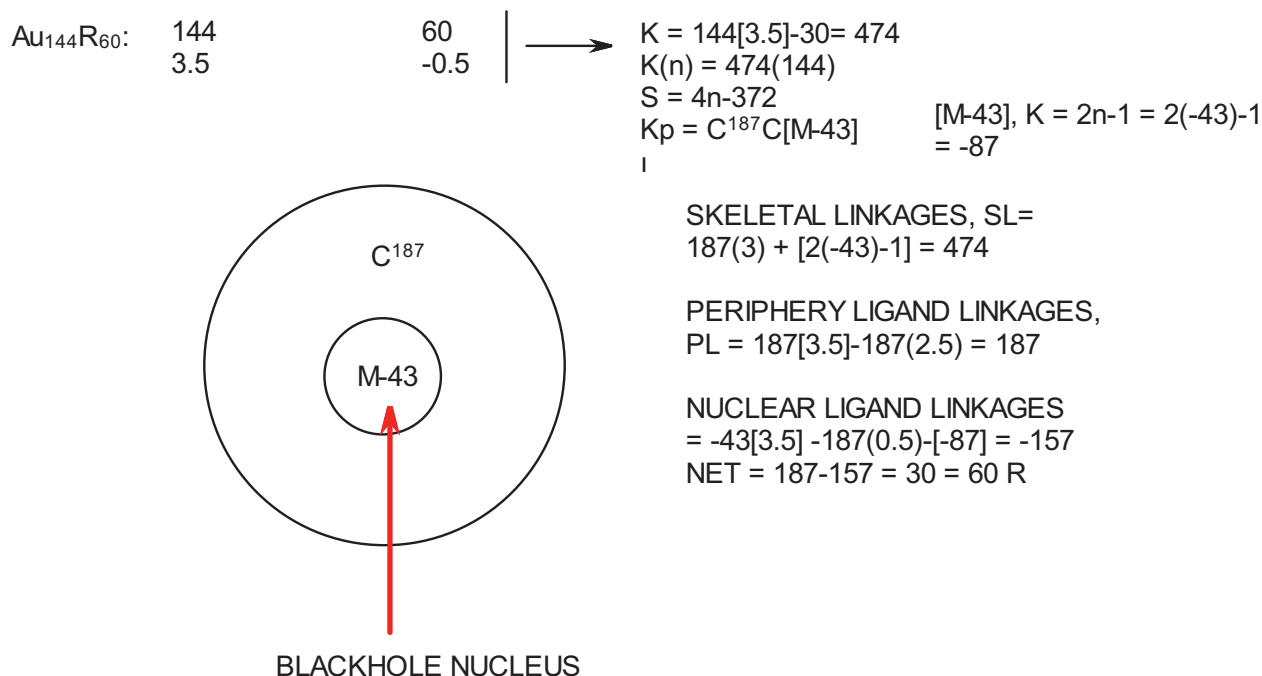


Table 3. Data Interpretation

		K	K(n)	SERIES	Kp	Ve	VF	RESULT
1	$Au_6L_8^{2+}$	$6[3.5]-8+1 = 14$	14(6)	4n-4	$C^3C[M3]$	$14(6)-4=80$	$6[11]+16-2=80$	Different
2	$Au_7L_8^{3+}$	$7[3.5]-8+1.5 = 18$	18(7)	4n-8	$C^5C[M2]$	$14(7)-8 = 90$	$7[11]+16-3=90$	Different
3	$Au_6L_8^{2+}$	$6[3.5]-8+1 = 14$	14(6)	4n-4	$C^3C[M3]$	$14(6)-4=80$	$6[11]+16-2=80$	Different
4	$Au_8L_8Cl_2^{2+}$	$8[3.5]-8-1+1 = 20$	20(8)	4n-8	$C^5C[M3]$	$14(8)-8=104$	$8[11]+16+2-2=104$	Different
5	$Au_{11}L_{12}^{3+}$	$11[3.5]-12+1.5 = 28$	28(11)	4n-12	$C^7C[M4]$	$14(11)-12=142$	$11[11]+24-3 = 142$	Different
6	$Au_{11}L_7Cl_3$	$11[3.5]-7-1.5 = 30$	30(11)	4n-16	$C^9C[M2]$	$14(11)-16=138$	$11[11]+14+3 = 138$	Similar
7	$Au_{11}L_8Cl_2^{+}$	$11[3.5]-8-1+0.5 = 30$	30(11)	4n-16	$C^9C[M2]$	138	$11[11]+16+2-1=138$	Similar
8	$Au_{20}L_8^{4+}$	$20[3.5]-8+2 = 64$	64(20)	4n-48	$C^{25}C[M-5]$	$14(20)-48=232$	$20[11]+16-4=232$	Similar?
9	$Au_{13}L_{10}Cl_2^{3+}$	$13[3.5]-10-1+1.5 = 36$	36(13)	4n-20	$C^{11}C[M2]$	$14(13)-20=162$	$13[11]+20+2-3=162$	Similar?
10	$Au_{22}L_{12}$	$22[3.5]-12 = 65$	65(22)	4n-42	$C^{22}C[M0]$	$14(22)-42 = 266$	$22[11]+24=266$	Different
11	$Au_{22}L_{14}$	$22[3.5]-14 = 63$	63(22)	4n-38	$C^{20}C[M2]$	$14(22)-38 = 270$	$22[11]+28=270$	Different

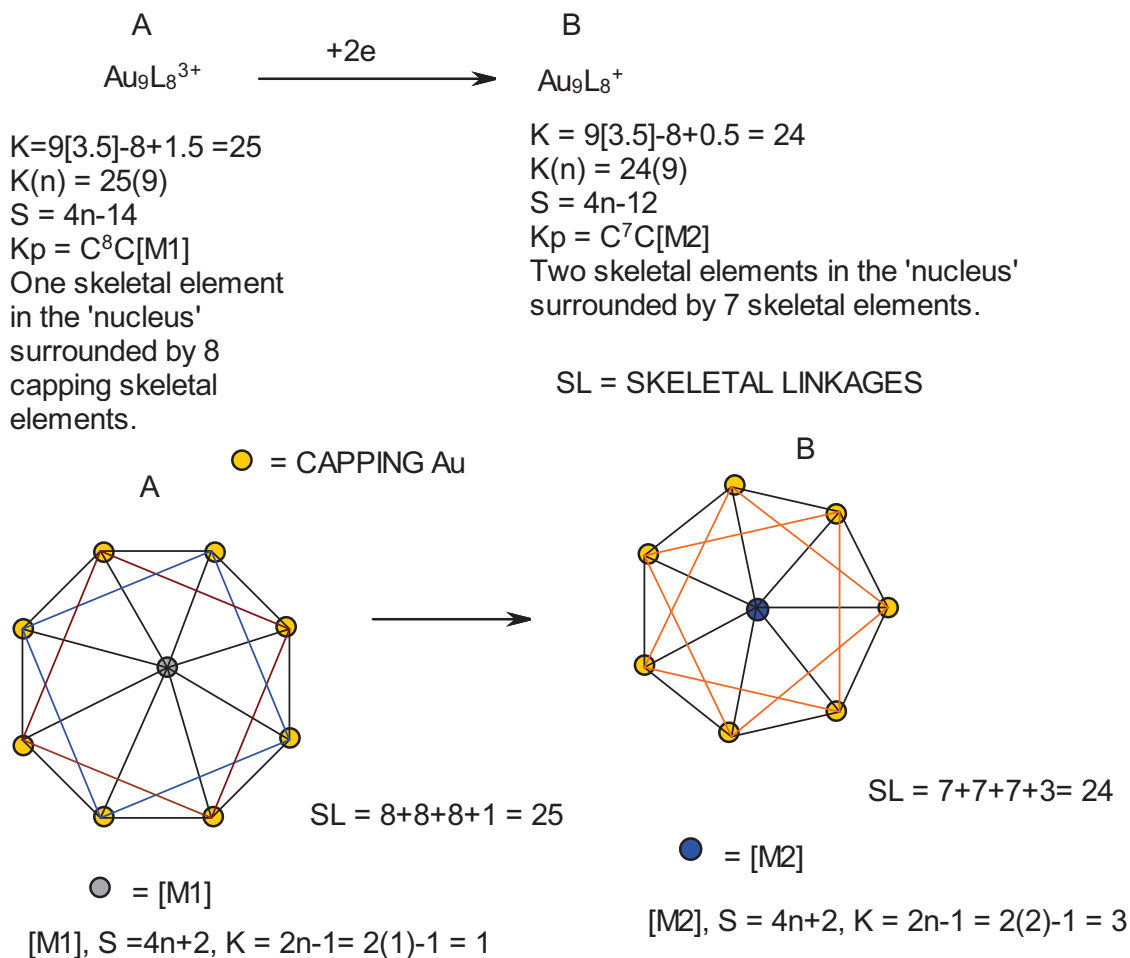
### 3. Data Interpretation

A number of golden clusters have been studied by UV-Vis-NID method (Wang, et al, 2016). For the purposes of illustrating how the series method analysis of clusters could be utilized, these findings are given in Table 3. For ease of differentiation of the clusters and grouping them, let us refer to the clusters with the same closo nucleus [Mx] as being in the same CLUSTER GROUP but different series  $S = 4n+q$  (q varies), while those which belong to the same series  $S = 4n+q$  (q is the same) as being in the same CLUSTER PERIOD. This approach is similar to what we have in the ordinary periodic table of elements. Let us look at the following clusters:  $Pd_{10}(CO)_{12}L_6$ ;  $K(n) = 22(10)$ ,  $S = 4n-4$ ,  $Kp = C^3C[M7]$ ;  $Pd_{23}(CO)_{21}L_{10}$ ;  $K = 61(23)$ ,  $S = 4n-30$ ,  $Kp = C^{16}CM7$  and  $Au_4Pd_{28}(CO)_{22}L_{16}$ ;  $K=88(32)$ ,  $S=4n-48$ ,  $Kp = C^{25}C[M7]$ . All these three clusters possess the similar cluster nucleus [M7] but different number of capping elements. These clusters are regarded as being in the same CLUSTER GROUP but different cluster capping periods-one has 3 capping skeletal elements, the other 16 capping elements and lastly the other has 25 capping elements. Let us take another example:  $Pd_{29}(CO)_{28}L_7^{2-}$ ;  $Pd_{30}(CO)_{26}L_{10}$ ;  $K = 84$ ,  $K(n) = 84(30)$ ,  $S = 4n-48$ ,  $Kp = C^{25}C[M5]$  and  $Au_4Pd_{28}(CO)_{22}L_{16}$ ;  $K=88(32)$ ,  $S=4n-48$ ,  $Kp = C^{25}C[M7]$ . These two clusters belong to the same CLUSTER PERIOD,  $S = 4n-48$ . They have the same number of capping elements but different nuclear sizes, one with 5 skeletal elements in the nucleus and the other 7. With this proposed definition of CLUSTER GROUP and CLUSTER PERIOD introduced, we

can now have some idea or understanding of the results indicated in the table. According to the series method, clusters 1 {[M3], C<sup>3</sup>} and 2 {[M2], C<sup>5</sup>}: these two belong to different cluster groups and cluster periods; clusters 3 {[M3], C<sup>3</sup>}, 4 {[M3], C<sup>5</sup>}, and 5 {[M4], C<sup>7</sup>}: cluster 3 and 4 belong to the same group but different periods while cluster 5 has nothing in common with clusters 3 and 4; 6 {[M2], C<sup>9</sup>} and 7 {[M2], C<sup>9</sup>}: clusters 6 and 7 belong to the same group and period; 8 {[M-5], C<sup>25</sup>}, 9 {[M2], C<sup>11</sup>}: clusters 8 and 9 have nothing in common; 10 {[M0], C<sup>22</sup>} and 11 {[M2], C<sup>20</sup>}: clusters 10 and 11 are also different as they have nothing in common.

CONVERSION OF A<sub>9</sub>L<sub>8</sub><sup>3+</sup> CLUSTER TO Au<sub>9</sub>L<sub>8</sub><sup>+</sup> CLUSTER

The change of skeletal structure of A<sub>9</sub>L<sub>8</sub><sup>3+</sup> to a different one of Au<sub>9</sub>L<sub>8</sub><sup>+</sup> was reported by Mingos (Mingos, 1984). This transformation can also be explained by the series approach. The K(n) value of A<sub>9</sub>L<sub>8</sub><sup>3+</sup> is 25(9) while that of Au<sub>9</sub>L<sub>8</sub><sup>+</sup> is 24(9). The decrease in K value by 1 results in a decrease of skeletal capping by 1 with a parallel increase in the nuclear index by 1. That is, instead of the geometry having 8 capping elements and 1 in the nucleus it changes into another on having 7 capping skeletal elements and 2 nuclear elements. In terms of cluster grouping proposed, the cluster has moved from CLUSTER GROUP 1[M1] to CLUSTER GROUP 2[M2]. This is illustrated in F-42.



Cluster Isomerism

Skeletal elements with the same nuclearity index (n) and same skeletal number K have been found to portray different geometrical shapes. We can refer to this as K ISOMERISM. This has been observed (Hughes& Wade,2000) for Os<sub>6</sub>(CO)<sub>18</sub><sup>2-</sup> [K = 11] and Os<sub>6</sub>(H)<sub>2</sub>(CO)<sub>18</sub> [K = 11] in F-43. The encounter with K isomerism in golden cluster A<sub>9</sub>L<sub>8</sub><sup>3+</sup> (Mingos, 1984) is not a surprise. The rough sketches of the isomerism are illustrated in F-43 to F-48.



K- ISOMERISM

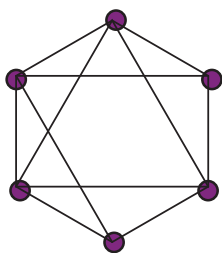


$K = 6[5] - 18 - 1 = 11$

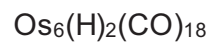
$K(n) = 11(6)$

$S = 4n + 2$

CLOSO; [M6]



$K = 11$

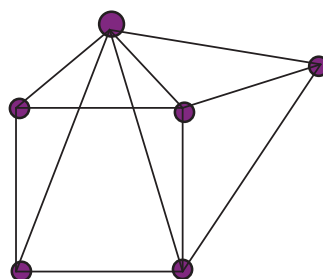


$K = 6[5] - 1 - 18 = 11$

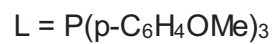
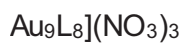
$K(n) = 11(6)$

$S = 4n + 2$

CLOSO, [M6]



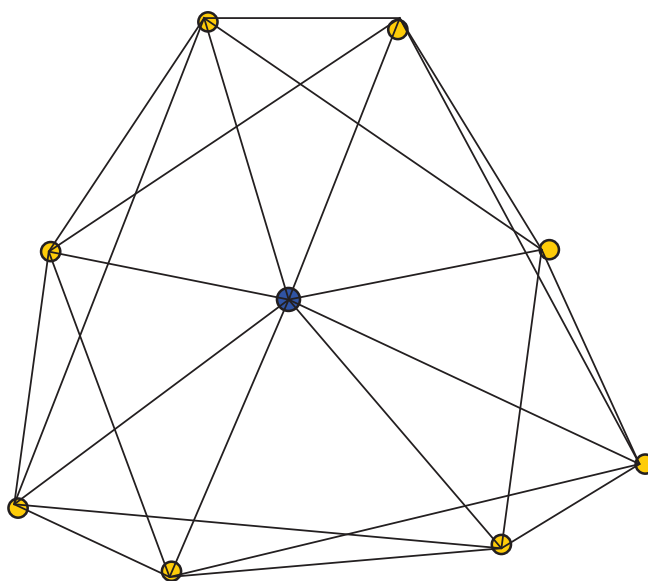
$K = 8 + 3 = 11$

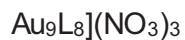


ISOMERISM

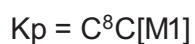
$K_p = C^8C[M1]$

$K(n) = 25(9)$

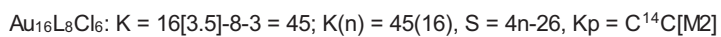
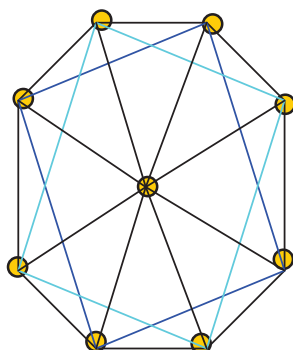




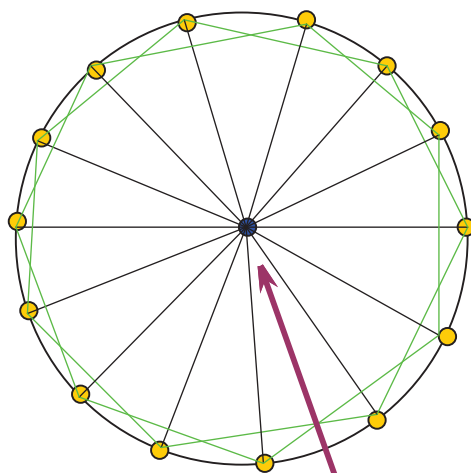
ISOMERISM



$K(n) = 25(9)$



K ISOMERISM PRESENT AS WELL AS A BLACKHOLE NUCLEUS



SKELETAL LINKAGES =  $14+14+14+3 = 45$   
 3 ARE FROM [M2],  $S = 4n+2$ ,  $K = 2n-1$   
 $= 2(2)-1 = 3$

Ligand linkage distribution

Periphery =  $14[3.5]-14(2.5) = 14$

Nucleus =  $2[3.5]-14(0.5)-3 = -3$

This means that the nucleus has negative nuclear linkages for ligands-BLACKHOLE.

The NET linkages available for ligands =

$14+(-3) = 8$ . This is the same as  $8I + 6Cl$ .

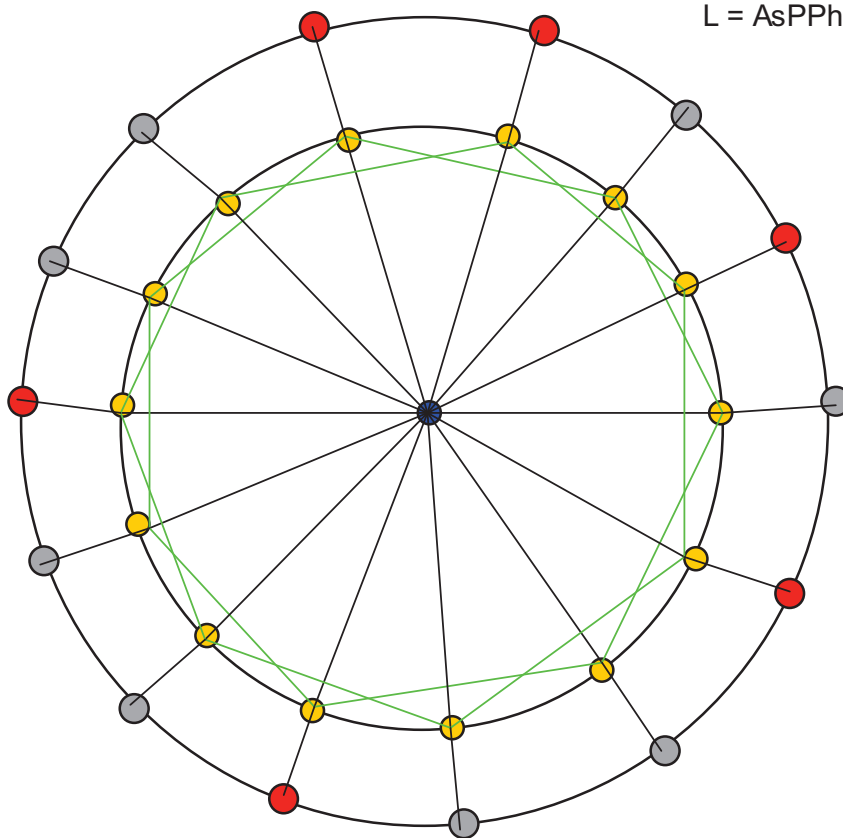
● = [M2] BLACKHOLE NUCLEUS

● = CAPPING Au

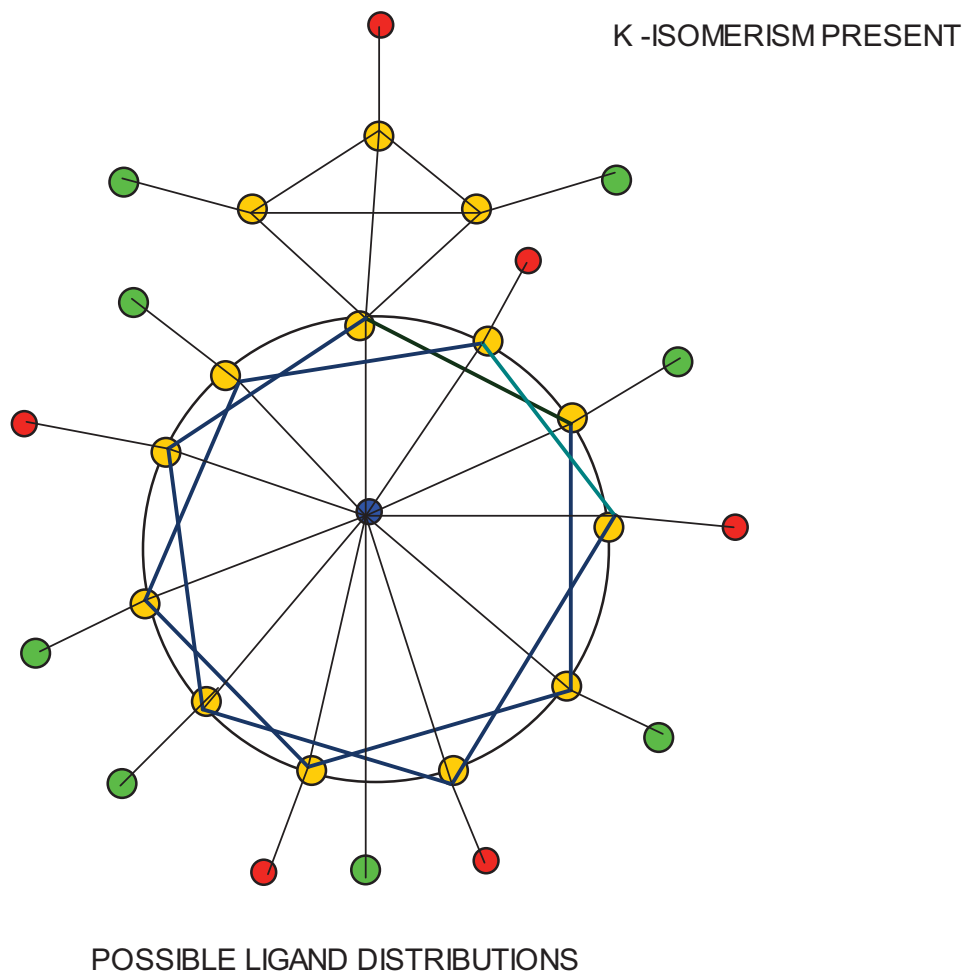
BLACKHOLE

$$\text{Au}_{16}\text{L}_8\text{Cl}_6: K = 16[3.5]-8-3 = 45; K(n) = 45(16), S = 4n-26, Kp = C^{14}C[M2]$$

L = AsPPh<sub>3</sub>



$$\text{Au}_{16}\text{L}_8\text{Cl}_6: K = 16[3.5]-8-3 = 45; K(n) = 45(16), S = 4n-26, K_p = C^{14}C[M_2]$$



DECAPPING CLUSTER SERIES:  $-K_p = C^yC[M_x]$ capping

During the course of developing the  $14n/4n$  series method for categorizing clusters, a capping symbol  $K_p = C^yC[M_x]$  was introduced. This is easily illustrated by the scheme SC-7.

SC-7

$S = 4n+q$	$4n+10$	$4n+8$	$4n+6$	$4n+4$	$4n+2$	$4n+0$	$4n-2$	$4n-4$
	KLADO	HYPHO	ARACHNO	NIDO	CLOSO	MONOCP	BICAP	TRICAP
$K_p = C^yC[M_x]$	$C^4C$	$C^3C$	$C^2C$	$C^1C$	$C^0C$	$C^1C$	$C^2C$	$C^3C$
	$4n-6$	$4n-8$	$4n-10$	$4n-12$	$4n-14$	$4n-16$	$4n-18$	$4n-20$
	TETRACP	PENTACP	HEXACP					
$K_p = C^yC[M_x]$	$C^4C$	$C^5C$	$C^6C$	$C^7C$	$C^8C$	$C^9C$	$C^{10}C$	$C^{11}C$

Previously, the series were capturing clusters which were mono-capped, bi-capped, tri-capped, and so on (Kiremir, 2015, 2016b). The symbol was not extended to the lower series such as CLOSO, NIDO, ARACHNO, and KLAPO. According to the series, the capping or de-capping step involves one skeletal element ( $\Delta n = 1$ ) and three skeletal linkages ( $\Delta K = 3$ ). Looking at the symbol,  $K_p = C^yC[M_x], y = 1$  when  $S = 4n+0$ , then  $S = 4n-2, y = 2, 4n-4, y = 3$ , etc. Moving backwards, from  $S = 4n+0, y = 1$ , then for  $S = 4n+2$ , we can set the value of  $y = 0$  and so the capping symbol will be  $K_p = C^0C[M_x]$ . Further movement backwards to  $S = 4n+4, y = -1$ , hence,  $K_p = C^{-1}C[M_x]$ . More backward movement, the capping symbol will be as indicated in the Table 4 and SC-7. The table numerically represents the concept (Rudolph, 1976) of correlating borane polyhedral geometrical structures.

Table 4. Decapping Series

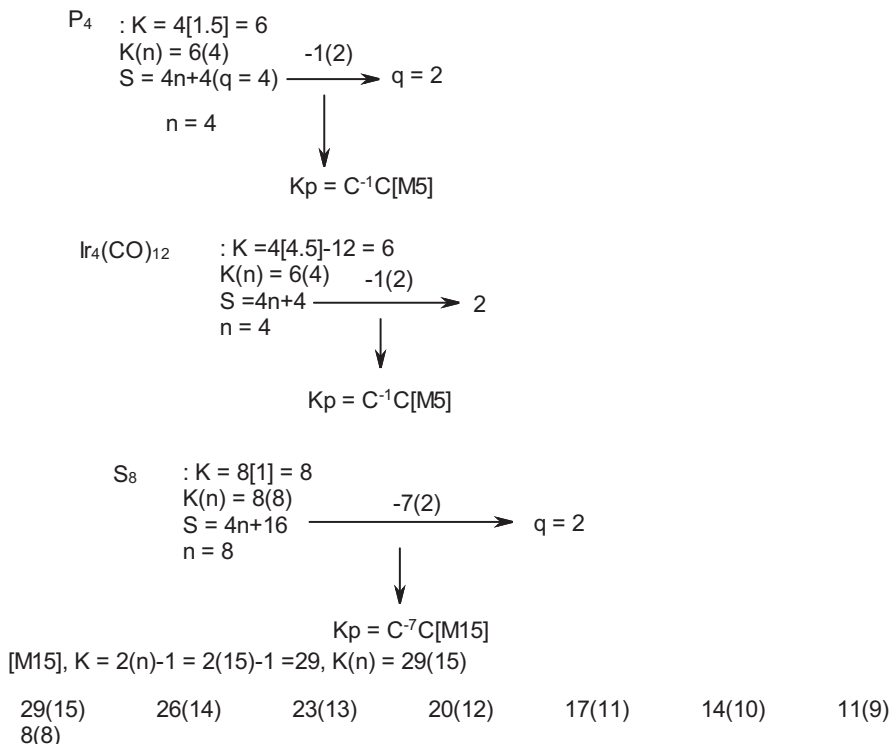
	[M12]	K(n)	[M11]	K(n)	[M10]	K(n)	[M9]	K(n)
C <sup>0</sup>	C <sup>0</sup> C[M12]	23(12)	C <sup>0</sup> C[M11]	21(11)	C <sup>0</sup> C[M10]	19(10)	C <sup>0</sup> C[M9]	17(9)
C <sup>-1</sup>	C <sup>-1</sup> C[M12]	20(11)	C <sup>-1</sup> C[M11]	18(10)	C <sup>-1</sup> C[M10]	16(9)	C <sup>-1</sup> C[M9]	14(8)
C <sup>-2</sup>	C <sup>-2</sup> C[M12]	17(10)	C <sup>-2</sup> C[M11]	15(9)	C <sup>-2</sup> C[M10]	13(8)	C <sup>-2</sup> C[M9]	11(7)
C <sup>-3</sup>	C <sup>-3</sup> C[M12]	14(9)	C <sup>-3</sup> C[M11]	12(8)	C <sup>-3</sup> C[M10]	10(7)	C <sup>-3</sup> C[M9]	8(6)
C <sup>-4</sup>	C <sup>-4</sup> C[M12]	11(8)	C <sup>-4</sup> C[M11]	9(7)	C <sup>-4</sup> C[M10]	7(6)	<b>C<sup>-4</sup>C[M9]</b>	<b>5(5)</b>
C <sup>-5</sup>	C <sup>-5</sup> C[M12]	8(7)	<b>C<sup>-5</sup>C[M11]</b>	<b>6(6)</b>	<b>C<sup>-5</sup>C[M10]</b>	<b>4(5)</b>	C <sup>-5</sup> C[M9]	2(4)
C <sup>-6</sup>	<b>C<sup>-6</sup>C[M12]</b>	<b>5(6)</b>	C <sup>-6</sup> C[M11]	3(5)				
C <sup>-7</sup>	C <sup>-7</sup> C[M12]	2(5)	C <sup>-7</sup> C[M11]	0(4)				

	[M8]	K(n)	[M7]	K(n)	[M7]	K(n)
C <sup>0</sup>	<b>C<sup>0</sup>[M8]</b>	<b>15(8)</b>	<b>C<sup>0</sup>[M7]</b>	<b>13(7)</b>	<b>C<sup>0</sup>[M7]</b>	<b>13(7)</b>
C <sup>-1</sup>	C <sup>-1</sup> [M8]	12(7)	C <sup>-1</sup> [M7]	10(6)	C <sup>-1</sup> [M7]	10(6)
C <sup>-2</sup>	C <sup>-2</sup> [M8]	9(6)	C <sup>-2</sup> [M7]	7(5)	C <sup>-2</sup> [M7]	7(5)
C <sup>-3</sup>	C <sup>-3</sup> [M8]	6(5)	<b>C<sup>-3</sup>[M7]</b>	<b>4(4)</b>	<b>C<sup>-3</sup>[M7]</b>	<b>4(4)</b>
C <sup>-4</sup>	<b>C<sup>-4</sup>[M8]</b>	<b>3(4)</b>	C <sup>-4</sup> [M7]	1(3)	C <sup>-4</sup> [M7]	1(3)

	[M6]	K(n)	[M5]	K(n)	[M4]	K(n)	[M3]	K(n)	[M2]	K(n)
C <sup>0</sup>	<b>C<sup>0</sup>[M6]</b>	<b>11(6)</b>	<b>C<sup>0</sup>[M5]</b>	<b>9(5)</b>	<b>C<sup>0</sup>[M4]</b>	<b>7(4)</b>	<b>C<sup>0</sup>[M3]</b>	<b>5(3)</b>	<b>C<sup>0</sup>[M2]</b>	<b>3(2)</b>
C <sup>-1</sup>	C <sup>-1</sup> [M6]	8(5)	C <sup>-1</sup> [M5]	6(4)	C <sup>-1</sup> [M4]	4(3)	C <sup>-1</sup> [M3]	2(2)	C <sup>-1</sup> [M2]	0(1)
C <sup>-2</sup>	C <sup>-2</sup> [M6]	5(4)	<b>C<sup>-2</sup>[M5]</b>	<b>3(3)</b>	<b>C<sup>-2</sup>[M4]</b>	<b>1(2)</b>				
C <sup>-3</sup>	<b>C<sup>-3</sup>[M6]</b>	<b>2(3)</b>	C <sup>-3</sup> [M5]	0(2)						

Table 5. Some of Rudolph Type of Series and Corresponding Boran

[M12]	K(n)	S	F <sub>B</sub>	[M6]	K(n)	S	F <sub>B</sub>
C <sup>0</sup> C[M12]	23(12)	4n+2	[BH](12)+2e = B <sub>12</sub> H <sub>12</sub> <sup>2-</sup>	C <sup>0</sup> [M6]	11(6)	4n+2	[BH](6)+2e = B <sub>6</sub> H <sub>6</sub> <sup>2-</sup>
C <sup>-1</sup> C[M12]	20(11)	4n+4	[BH](11)+4H = B <sub>11</sub> H <sub>15</sub>	C <sup>-1</sup> [M6]	8(5)	4n+4	[BH](5)+4H = B <sub>5</sub> H <sub>9</sub>
C <sup>-2</sup> C[M12]	17(10)	4n+6	[BH](10)+6H = B <sub>10</sub> H <sub>16</sub>	C <sup>-2</sup> [M6]	5(4)	4n+6	[BH](4)+6H = B <sub>4</sub> H <sub>10</sub>
C <sup>-3</sup> C[M12]	14(9)	4n+8	[BH](9)+8H = B <sub>9</sub> H <sub>17</sub>	<b>C<sup>-3</sup>[M6]</b>	<b>2(3)</b>	4n+8	[BH](3)+8H = B <sub>3</sub> H <sub>11</sub>
C <sup>-4</sup> C[M12]	11(8)	4n+10	[BH](8)+10H = B <sub>8</sub> H <sub>18</sub>				
C <sup>-5</sup> C[M12]	8(7)	4n+12	[BH](7)+12H = B <sub>7</sub> H <sub>19</sub>				
<b>C<sup>-6</sup>C[M12]</b>	<b>5(6)</b>	<b>4n+14</b>	<b>[BH](6)+14H = B<sub>6</sub>H<sub>20</sub></b>				



SC-8

Appendix-1

Skeletal k Values of Main Group Elements								
Group	Series, S=4n+q	k = 2n-q/2						
1	4n-3	3.5	Li	Na	K	Rb	Cs	
2	4n-2	3	Be	Mg	Ca	Sr	Ba	
3	4n-1	2.5	B	Al	Ga	In	Tl	
4	4n+0	2	C	Si	Ge	Sn	Pb	
5	4n+1	1.5	N	P	As	Sb	Bi	
6	4n+2	1	O	S	Se	Te	Po	
7	4n+3	0.5	F	Cl	Br	I	At	
8	4n+4	0	Ne	Ar	Kr	Xe	Rn	

Appendix-2

Skeletal k Values of Transition Metals				
3d-TM	4d –	5d-TM	Series, S =	k = 2n-q/2
*	TM*	*	4n+q	
Sc	Y	La	4n-11	7.5
Ti	Zr	Hf	4n-10	7
V	Nb	Ta	4n-9	6.5
Cr	Mo	W	4n-8	6
Mn	Tc	Re	4n-7	5.5
Fe	Ru	Os	4n-6	5
Co	Rh	Ir	4n-5	4.5
Ni	Pd	Pt	4n-4	4
Cu	Ag	Au	4n-3	3.5
Zn	Cd	Hg	4n-2	3

4. Conclusion

A collection of known golden clusters have been analyzed and categorized using skeletal numbers. A large percentage of them are centered around [M0], [M1] and [M2] closo-based axes. The [Mx] may be regarded as similar to groups of elements in the periodic table. The clusters which lie on the closo lines [Mx], x ≤ 0, have a tendency of possessing metallic character. In this connection, the golden clusters are closer to the metallic region of metallic clusters than that of non-metallic. A concept of a black-hole nucleus has been introduced as well as that of numerical categorization of clusters which lie lower than the closo base line. The two dimensional ideal shapes of clusters have been sketched using graph theory derived from the 4n series method.

## Acknowledgement

My gratitude is extended to Dr. P.E.T. Kiremire for editing the draft and Mrs. Merab Kambamu Kiremire for the continued encouragement to write these articles.

## References

- Corti, C. W., Holliday, R. J., & Thompson, D. J. (2005). Commercial Aspects of Gold Catalysis A. General, 291, 253-261. <https://doi.org/10.1016/j.apcata.2005.01.051>
- Cotton, F. A., & Wilkinson, G. (1980). *Advanced Inorganic Chemistry, 4<sup>th</sup> Ed.*, John Wiley and Sons, New York, 1980.
- Gimeno, M. C. (2008). Modern Supramolecular Gold-Metal Interactive and Applications. Edited A. Laguna, 2008. Wiley-VCH, Weinheim.
- Greenwood, N. N., & Earnshaw, A. (1998). *Chemistry of the Elements, 2<sup>nd</sup> Ed.* Butterworth, Oxford.
- Hughes, A. K., & Wade, K. (2000). Metal-metal and metal-ligand strengths in metal carbonyl clusters. *Coord. Chem. Rev.*, 197, 191-229. [https://doi.org/10.1016/S0010-8545\(99\)00208-8](https://doi.org/10.1016/S0010-8545(99)00208-8)
- Kilmartin, J. (2010). Molecular Gold Clusters as Precursors to Heterogeneous Catalysis. PhD Thesis.
- Kiremire, E. M. R. (2015). Capping and Decapping Series of Boranes. *Int. J. Chem.*, 7(2), 186-197. <https://doi.org/10.5539/ijc.v7n2p186>
- Kiremire, E. M. R. (2016a). Clusters of Gold Containing P-Block Elements. *Am. J. Chem.*, 6(5), 126-144.
- Kiremire, E. M. R. (2016b). Unusual underground capping Carbonyl Clusters of Palladium. *Int. J. Chem.*, 8(1), 145-158 <https://doi.org/10.5539/ijc.v8n1p145>
- Kiremire, E. M. R. (2017a). The Golden Series and Clusters of Gold-unique Shapes and Bonding. *Int. J. Chem.*, 9(1), 38-57. <https://doi.org/10.5539/ijc.v9n1p38>
- Kiremire, E. M. R. (2017b). The Six Silent Laws of Chemical Clusters. *Am. J. Chem.*, 7(2), 21-41.
- Kiremire, E. M. R. (2017c). Boranes, Metalloboranes, Transition Metal Carbonyls and Other Cluster Formulas Obey the Law of Skeletal Numbers and Their Valences. *Am. J. Chem.*, 7(4), 113-144.
- Kiremire, E. M. R. (2017d). Numerical Characterization of Fragments, Molecules, and Clusters Using Skeletal Numbers and Nuclearity Trees. *Am. J. Chem.*, 7(3), 73-96.
- Konishi, K. (2014). Phosphine-Coordinated Pure-Gold Clusters and Unique Optical Properties /Responses. *Structure and Bonding*, 161, 49-86. [https://doi.org/10.1007/430\\_2014\\_143](https://doi.org/10.1007/430_2014_143)
- Kwok-Ming, L. (2011). Synthesis, characterization and photophysical properties of Chalcogenido, phosphinidene and alkyl Complexes of Gold(I) and its Congener and their Supramolecular assembly arising from metal-metal interactions. PhD Thesis.
- Mingos, D. M. P. (1984). Gold Cluster Compounds: Are they materials in miniature? *Gold Bull.*, 17(1), 5-12. <https://doi.org/10.1007/BF03214670>
- Rudolph, R. W. (1976). Boranes and heteroboranes: a paradigm for the electron requirements of clusters? *Acc. Chem. Res.*, 9(12), 446-452. <https://doi.org/10.1021/ar50108a004>
- Zhang, Q. F., Williard, P. G., & Wang, L. S. (2016). Polymorphism of Phosphine-Protected Gold nano-clusters: Synthesis A, Weinheim.
- Zhang, Y., Chu, W., Foroushani, A. D., Wang, H., Li, D., Liu, J., Barrow, C. J., Wang, X., & Yang, W. (2014). New Gold Nanostructures for Sensor Applications. A Review. *Materials*, 7, 5169-5201. <https://doi.org/10.3390/ma7075169>

## Copyrights

Copyright for this article is retained by the author(s), with first publication rights granted to the journal.

This is an open-access article distributed under the terms and conditions of the Creative Commons Attribution license (<http://creativecommons.org/licenses/by/4.0/>).

# Using Solar-TiO<sub>2</sub> and Biocarbon to Decompose and Adsorb Amoxicillin from Polluted Waters

Nilce Ortiz<sup>1</sup>, Andre Silva<sup>2</sup>, Giselle Natalia Silva Lima<sup>1</sup>, Fernanda Pagano Hyppolito<sup>1</sup>

<sup>1</sup>Institute for Nuclear and Energy Research – IPEN, Brazil

<sup>2</sup>Carbosolo Desenvolvimento Agrícola Ltda, Brazil

Correspondence: Nilce Ortiz, PhD, Center for Environmental Chemistry, Institute for Nuclear and Energy Research – IPEN, São Paulo, Brazil. E-mail: nortizbr@gmail.com

Received: December 28, 2017 Accepted: January 28, 2018 Online Published: January 28, 2018

doi:10.5539/ijc.v10n1p131

URL: <https://doi.org/10.5539/ijc.v10n1p131>

## Abstract

Surface water discharge of domestic sewage poses a treat mostly due to antibiotics content as amoxicillin. Its environmental presence provides the bacterial resistance enhancement and disturbance in aquatic life. The biocarbon is an organic carbon compound obtained by biomass pyrolysis at 300°C to 750°C under low oxygen environment. It is an effective adsorbent derived from agricultural and industrial solid biomass also frequently used to remove various pollutants, including dyes, pesticides, organic compounds and heavy metals from aqueous solutions. The importance of this natural material rises as low cost abundant and renewable alternative to activated carbon used on wastewater treatment application. Several technologies are employed to modify crude precursors on biocarbon preparation including chemical, physical and biological treatments with the addition of functional groups. The raw biomass material also provides some radicals and humic acids with promising water adsorbent results. The integrated process of the efficient Solar-TiO<sub>2</sub> photodecomposition followed by biocarbon adsorption resulted on 94% of amoxicillin removal percentage and avoids the toxic treatment sludge production.

**Keywords:** amoxicillin, adsorption, biocarbon, antibiotic, photodecomposition, solar

## 1. Introduction

In Brazil as in many countries the worthless biocarbon fine material is seeing as a work related disease and environmental problem. Its relation with suspended particle pollution and lungs disease is direct, usually is also related with infant work and slavery condition. The development of better technological use for the biocarbon can provide investments for its fine particle collection and use of this valuable high surface area renewable source on environmental conservation. Nowadays the Brazil economical condition can promote new ways for its better use and the research projects are providing a possible and feasible target for better future.

The pharmaceuticals production is essential and responsible for life quality and public health improvement, increasing the life expand and perform a significant role in prevention, diagnostic and treatment in human and veterinary medicine. Published environmental studies indicated the raw sewage discharge and urban drainage wastewater as the main routes and sources of pharmaceuticals input in the aquatic environment (Sun, Chen, Wan, & Yu, 2015).

The antibiotics presence in the environment shows direct association with chronic toxicity and the prevalence of bacterial resistance gene. Published studies confirm the presence of the amoxicillin in domestic wastewater in the range form ng L<sup>-1</sup> to mg L<sup>-1</sup>. Its presence, persistence and bioaccumulation in the environment may induce resistant gene contamination, toxic effects and change the natural balance of the aquatic ecosystems.

The amoxicillin has a complex chemical structure with C<sub>16</sub>H<sub>19</sub>N<sub>3</sub>O<sub>5</sub>S with the molecular weight of 365.4 g mol<sup>-1</sup> and three acids dissociation on pH 2.4 (for carboxyl), pH 7.4 (amine ) and pH 9.6 (phenol) the solubility in water is 3430 mg L<sup>-1</sup> at 20°C and log Kow 0.87.



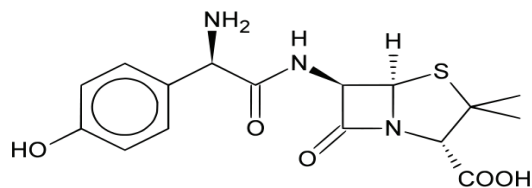


Figure 1. Amoxicillin chemical structure

There are many environmental causes of the amoxicillin presence in surface waters in small proportions. Such behavior provides excellent conditions for microorganism's changes and adapts their genetic material, to create resistance to the antibiotic and produce enzymes called beta-lactamases, which destroy penicillin base antibiotics. The resistant bacteria reproduce and multiplied, which the elimination of the weak ones, and those that have become resistant remain, posing a public health risk. Some of these threats involve the development of abnormalities and deterioration of animal reproduction. Recently published works indicate the traditional disinfection process of chlorination is not enough to deactivate such adaptation process (Lisle, 1995).

Brazil has the world largest protein production and the antibiotics use in veterinary medicine is excessive. Their application in sick animals is usually too much and also it is commonly served to healthy animals, as a ration supplement. The presence of amoxicillin contamination decrease the water quality of springs, dams and rivers, such as the Atibaia River, which supplies 90% of the drinkable water to a population of Campinas located in São Paulo state.

The photodecomposition usually involves the production of the HO\* and O<sub>2</sub> radicals in most heterogeneous photocatalytic cases the HO\* is widely regarded as the main active oxidant. The HO\* production dominate the amoxicillin decomposition mechanism (Benacherine, Debbache, Ghoul, & Mameri, 2017). The photodecomposition process uses the TiO<sub>2</sub> as a catalyzer, generating the hydroxyl radical by many equations. However, the most commonly found in the literature are the Equation 1 and 2 summarized above:



Published results indicate the stirring time for complete degradation of amoxicillin was 120 min of solar irradiation with 89% of initial amoxicillin removed. The use of solar radiation indicates does not only higher degradation efficiency but also accelerate the photocatalytic process in comparison with UV lamps (Alalm, Tawfik, & Ookawara, 2016).

There are many methods for amoxicillin and amoxicillin decomposition by products to removal from contaminated water such as nano filtration membrane, electro coagulation, electrochemical oxidation, biodegradation, reverse osmosis, ozonation, Fenton oxidation, catalytic degradation, and adsorption. Adsorption is known as an efficient process to remove various antibiotic pollutants from aqueous solutions due to simple design, flexibility, easy operation, suitability for batch and continuous processes. Additionally, all traditional water treatment processes with low pollutants concentration still result in an environmental problem as the correct disposal of the contaminated sludge. The solar energy with TiO<sub>2</sub> promote the formation of hydroxyl radicals and increase the amoxicillin decomposition velocity possibly leading to the mineralization. The photodecomposition integrated with the fine waste biocarbon adsorption promotes the water treatment efficiency and quality polishment removing the antibiotics decomposition by-products in an efficient low cost integrated process with renewable materials.

## 2. Material and Methods

The eucalyptus urophilia biochar samples were a solid waste from carboniferous plant. Usually considered as an environmental problem and work related disease the low particle size material provides higher surface area for adsorption. Its natural humidity is about 5% to 7% and the total carbon is in the range of 75% to 78%. Its particle size analysis shows mostly particles from 1 to 50µm and after micronization they reaches the average diameter lower than 37 µm (0.04 nm).

The experimental procedures used the dissolution of the amoxicillin powder brought as active medicine compound and, the preparation of the calibration curve applied the amoxicillin standard in different concentrations in the interval of 0.1 and 0.9 of adsorbance. The spectrophotometer Carry 1E allows the adsorbance measurements in  $\lambda = 237$  nm (Standard Methods). The experiments design began before some exploration trials, using solar chamber and a luximeter with lux equal to one lumen per square meter.

The photodecomposition experiments used the commercial grade TiO<sub>2</sub> anatase and the preparation of the initial amoxicillin solutions were by the dilution of the stock solution (Ramasundaram, et al 2017). The addition of 30 mg of TiO<sub>2</sub> was in a 400 mL of distilled water and amoxicillin initial concentrations were in the range of 20 to 80 mg L<sup>-1</sup>

accordingly with the environmental monitoring results cited in literature. The control of the temperature on  $40^{\circ}\text{C} \pm 0.5^{\circ}\text{C}$ , and the pH 5.5 were during the all processes, the agitation of the solid suspension was until 120 minutes inside the solar chamber. The luximeter measurement in the solar beam allowed to measure and control the radiation incidence experimentally fixed in 1000 lumen. The collection of the solid suspensions aliquots were after 30 min each, added at Falcon flasks with 3 mg of micronized biocarbon. After the homogenization, the flasks suspensions were centrifuged at 15000 rpm for 15 min. The measurement of the clean supernatant in the spectrophotometry UV-Vis allowed quantifying the amoxicillin adsorbance and converting their values to concentration with a previously prepared calibration curve.

### 3. Results and Discussion

The results of the kinetics studies of photodecomposition and biocarbon sorption provide valuable insights about the kinetics models: pseudo-first-order, pseudo-second-order, and intraparticle with the determination of photodecomposition and adsorption rates.

pseudo-first-order equation:

$$\log(q_e - q_t) = \log(q_e) - \frac{K_1}{2.303}t \quad (3)$$

Where:  $K_1$  is the pseudo-first-order rate ( $\text{min}^{-1}$ ), and  $q_e$  ( $\text{mg g}^{-1}$ ) refers to the experimental adsorbed mass at equilibrium. The plotting of the calculated values of  $\ln(q_e - q_t)$  for  $t$  (time), and the calculation of  $K_1$  used the slope values of the line equation.

Pseudo-second order equation:

$$\frac{t}{q_t} = \frac{1}{K_2} + \frac{1}{q_e}t \quad (4)$$

Where:  $K_2$  ( $\text{g.mg}^{-1}.\text{min}^{-1}$ ) is the kinetics adsorption rate, the values of  $t/q_t$  are plotted for  $t$  (min), and the calculation predicted the adsorption capacity  $q_e$  ( $\text{mg g}^{-1}$ ) and the integrated adsorption rate  $K_2$  with the slope and the intercept of the line equation, respectively.

Intraparticle equation:

$$\log(q_t) = \log(K_{id}) + \text{alog}(t) \quad (5)$$

The use of the experimental results allows perform the kinetics calculations. Table 1 presents the kinetics rates calculated using the equations 3 to 5. The pseudo-first-order equation represents a logarithm of the reactant species and the reaction time, larger  $K_1$  indicate fast reactant consumption and small time to complete the reaction, the  $R^2$  values obtained for the pseudo-first equation indicate lower correspondence between the results and the theory. Some published results indicate the solar photodecomposition processes with goethite as pseudo-first-order kinetics with  $K=0.26 \times 10^{-2} \text{min}^{-1}$  (Benacherine, Debbache, Ghoul, & Mameri, 2017).

The experimental results indicated lower correlation with pseudo-first-order, just one  $K_1$  value was  $1.6 \times 10^{-2} (\text{min}^{-1})$  with  $R^2 = 0.977$ , all results indicated better correlation with the pseudo-second-order.

Considering the pseudo-second-order reaction the sum of the exponents in the equation rate is equal to two. The reactant concentrations are plotted with time. The pseudo-second-order reaction depends on the initial concentration, of the two different reactants A and B combine in a single elementary step. Before the rate which A decreases they can be expressed using differential equation, rearranged, integrated and followed the linear equation which the slope value is  $K_2$ . The pseudo-second order showed better correspondence with the experimental results corroborating with published results for biocarbon adsorption and amoxicillin removal treatments, Table 2. The interparticle reaction usually point out the slow step of the adsorption reaction.

Table 1. Kinetics results of the integrated processes (solar photodecomposition and biocarbon adsorption)

<i>Concentration</i> ( <i>mg.L<sup>-1</sup></i> )	<i>Pseudo-first</i> <i>K<sub>1</sub> 10<sup>-2</sup> (min<sup>-1</sup>)</i>	<i>R<sup>2</sup></i>	<i>Pseud-second</i> <i>K<sub>2</sub>(g mg<sup>-1</sup>.min<sup>-1</sup>)</i>	<i>R<sup>2</sup></i>	<i>Interparticle</i> <i>K<sub>id</sub></i>	<i>R<sup>2</sup></i>
21.9	1.1	0.523	17.715	0.964	1530.81	0.005
34.3	1.3	0.053	302.11	0.926	882.65	0.006
42.5	1.7	0.364	350.88	0.951	743.21	0.003
45.5	1.6	0.977	46.447	0.926	797.11	0.007
65.2	1.4	0.236	21.566	0.701	249.51	0.020
81.7	1.8	0.143	161.81	0.950	566.63	0.004

Table 2. Published results of biocarbon, methylene blue, and amoxicillin adsorption kinetics

<i>Biocarbon</i>	<i>Toxic compound</i>	<i>Adsorption capacity (mg g<sup>-1</sup>)</i>	<i>Kinetics model</i>	<i>Reference</i>
Eucalyptus with citric acid	Methylene Blue	178.57	Pseudo-first-order, Elovich, and intraparticle	(Sun,Chen,Wan,& Yu, 2015)
Eucalyptus activated at 400°C for 30 min.	Methylene Blue	9.50	Pseudo-second-order	(Sun,Wan,&Luo,2013)
Granular activated carbon PA	Amoxicillin	0.63	Pseudo-second-order	(Franco et al, 2017)
Biomass Arundo donax Linn - Microwave	Amoxicillin	196.9	Pseudo-second-order	(Chayid,&Ahmed,2015)
TiO <sub>2</sub> / zeolite	Amoxicillin	-	-	(Fan et al, 2016)

The concentrations of the initial amoxicillin were in the range of 28 to 83 mg L<sup>-1</sup> similar with those related in literature in hospital discharge (Kanakaraju; Kockler; Motti, Glass,& Oelgemoller, 2015) (Githinji; Musey; & Ankumah, 2010) (Kavitha,& Namasivayam, 2007). The higher removal percentage was 94% for integrated process with initial amoxicillin concentration of 81.7 mg L<sup>-1</sup> resulting in 825.71 mg g<sup>-1</sup> higher of those systems found for eucalyptus/ citric acid (Sun, Chen, Wan,& Yu, 2015).

The use of integrated processes as solar/TiO<sub>2</sub> photodecomposition followed by adsorption has many advantages as a great potential for a photocatalysis with the application of solar treatment chambers and possible self-cleaning surfaces (Ramasendaram et al, 2017). However, the practical applications and continuous use demand solutions to kinetics problems, and they may rise as the adsorbent reduced surface area, TiO<sub>2</sub> oxidation surface and solid low stability due long term use and the potential oxide mass production.

The amoxicillin degradation with solar/TiO<sub>2</sub> anatase proceeds about three times faster than with ultraviolet (UV) lamp. The disproportional improvement oxidation rates may be explained by the difference between the small spectrum irradiance of UV band and the broad spectrum of solar visible light (Klauson; Babkina; Stepanova; Krichevskaya; & Preis, 2010). The intensity of radiation spectrum grows with increasing wavelength from 300 to 500 nm. The combination of solar photodecomposition and the adsorption process is actually efficient and low cost in spite some application difficulties to be overcome in near future.

The integrated process study include the adsorption isotherms, performing the calculations of Langmuir, Freundlich and Redlich-Peterson isotherms, equations 6, 7 and 8 respectively (Sampranpiboon, Charnkeitkong,& Feng,2014) (Ho, Chiu, &Wang, 2005). The Langmuir isotherm adsorption assumes an ideal solid surface composed by series of distinct sites capable of binding the adsorbate in a molecular coverage, the reaction is treated as a chemical reaction between the adsorbate molecule and the surface as a pseudo-second-order reaction. The Freundlich isotherm is empirical but widely used and the value of n is considered a measure of the adsorption intensity higher the 1 the n more favorable is the adsorption processes. The Redlich-Peterson (R-P) is more accurate than the Langmuir and Freundlich due the “g” value equals to 1 (Wu, &Tseng, 2010). Usually the R-P is in accordance with Langmuir and Freundlich isotherm equations, such behaviors could also be observed in this study

$$C_e/q_e = 1/Q_0b + C_e/Q_0, \quad (6)$$

$$\log q_e = \log K_f + 1/n \log C_e \quad (7)$$

$$\ln (C_e/q_e) = g \ln C_e - \ln K_r \quad (8)$$

Where:  $C_e$  = equilibrium concentration ( $\text{mgL}^{-1}$ );  $q_e$  = the amount adsorbed at equilibrium ( $\text{mg.g}^{-1}$ );  $Q_0$  and  $b$  are Langmuir constants;  $Q_0$  indicates the adsorption capacity of the material and  $b$  indicates the energy of adsorption.  $K_f$  and  $n$  are Freundlich constants.  $K_f$  indicates the adsorption capacity of the material and  $n$  indicates efficiency of adsorption.  $K_r$  and  $g$  are Redlich-Peterson constants;  $K_r$  indicates the adsorption capacity and “ $g$ ” is the exponent between 0 and 1.

Table 3. Langmuir, Freundlich, and R-P isotherms for integrated processes with solar/ $\text{TiO}_2$  and biocarbon

<b>Langmuir</b>	<b><math>R^2</math></b>	<b><math>K_0</math></b>	<b><math>b</math></b>
$y = 0.004 + 0.001x$	0.864	970.9	0.23
<b>Freundlich</b>	<b><math>R^2</math></b>	<b><math>K_f</math></b>	<b><math>n</math></b>
$y = 2.334 + 0.377x$	0.956	215.7	2.66
<b>Radlich-Peterson</b>	<b><math>R^2</math></b>	<b><math>K_f</math></b>	<b><math>g</math></b>
$y = -6.651 + 1.002x$	0.955	773.6	1.00

The RL values were in the interval from 0 to 1, with favorable adsorption accordingly with Langmuir isotherm. The Freundlich isotherm constant  $n$  was also in the interval of  $2 < n < 10$ , the indication of the agreement with Freundlich model with equal adsorption heating and Redlich – Peterson parameters were also promising.

#### 4. Conclusions

The biocarbon was efficient, low cost and renewable adsorbent material showing high efficiency (more than 95%) to remove amoxicillin and its photodecomposition by-products. The integrated process of solar/ $\text{TiO}_2$  photodecomposition and biocarbon adsorption presented promising results and led to the better antibiotic removal process allowing the processes parameters optimization as antibiotics initial concentration, agitation time, solar radiation incidence time,  $\text{TiO}_2$  mass, pH and temperature. The optimization of these parameters is feasible to improve the results. The combined adsorption and  $\text{TiO}_2$  solar photodecomposition of antibiotics are so far the best-integrated processes with low toxic sludge production, using the low particle biocarbon well known as worthless, an environmental risk and work related disease as high surface area solid waste, such natural renewable material showed removal capacity effectiveness and the better compromise solution for environment conservation X price.

#### Acknowledgment

The National Council for Scientific and Technological Development (CNPq) by PIBIC program and São Paulo Research Foundation (Fapesp).

#### References

- Alalm, M. G., Tawfik, A., & Ookawara, S. (2016). Enhancement of photo catalytic f  $\text{TiO}_2$  by immobilization on activated carbon for degradation of pharmaceuticals. *Journal of Environmental Chemical Engineering*, 4, 929-1937. <http://dx.doi.org/10.1016/j.jece.2016.03.023>
- Benacherine, M. M., Debbache, N., Ghoul, I., & Mameri, Y. (2017). Heterogeneous photo induced degradation of amoxicillin by goethite under artificial and natural irradiation. *Journal of photochemistry and photobiology A: Chemistry*, 335, 70-77. <http://d.o.i.org/10.1016/j.photochem.2016.11.008>
- Chayid, M. A., & Ahmed, M. J. (2015). Amoxicillin adsorption on microwave prepared activated carbon from arundo donax Linn: Isotherms, Kinetics and thermodynamics studies. *Journal of Environmental Chemical Engineering*, 3, 1592-1601. <http://dx.doi.org/10.1016/j.jece.2015.05.021>
- Fan, S., Tang, J., Wang, Y., Li, H., Zhang, H., Tang, J., Wang, Z., & Li, X. (2016). Biochar prepared from co-pyrolysis of municipal sewage sludge and tea waste for the adsorption of methylene blue from aqueous solutions: kinetics, isotherm, thermodynamic and mechanism. *Journal of Molecular Liquids*, 220, 432-441. <https://doi.org/10.1016/j.molliq.2016.04.107>
- Franco, M. A. E., Carvalho, C. B., Bonetto, M. M., Soares, R. P., & Féris, L. A. (2017). Removal of amoxicillin from water by adsorption onto activated carbon n batch process and fixed bed column: kinetics, isotherms, experimental design and breakthrough curves modeling. *Journal of Cleaner Production*, 161, 947-956. <http://dx.doi.org/10.1016/j.jclepro.2017.05.197>
- Githinji, L. J. M., Musey, M. K., & Ankumah, R. O. (2010). Evaluation of the fate of the ciprofloxacin and amoxicillin n domestic wastewater, *Water Air Soil Pollut*. <https://doi.org/10.1007/s.11270.010.0697.1>

- Ho, Y., Chiu, W., & Wang, C. (2005). Regression analysis for the sorption isotherms of basic dyes on sugarcane dust-Bioresource tech, *96*, 1285-1291.
- Kanakaraju, D., Kockler, J., Motti, C. A., Glass, B. D., & Oelgemoller, M. (2015). Titanium dioxide/zeolite integrated photo catalytic adsorbents fro the degradation of amoxicillin, *Applied Catalysis B: Environmental*, *166-167*, 45-55. <https://doi.org/10.1016/j.apcatb.2014.11.001>
- Kavitha, D., & Namasivayam, C. (2007). Experimental and kinetic studies on methylene blue adsorption by coir pith carbon, *Bioresource Technology*, *98*(1), 14-21.
- Klauson, D., Babkina, J., Stepanova, K., Krichevskaya, M., & Preis, S. (2010). Aqueous photo catalitic oxidation of amoxicillin, *Catalysis Today*, *151*, 39-45. <https://doi:10.1016/j.cattd.2010.01.015>
- Ramasundaram, S., Seid, M., Lee, W., Kim, C. U., Kim, S. W., Hong, S. W., & Choi, K. J. (2017). Preparation, characterization, and application of TiO<sub>2</sub>-patterned polyimide film as a photo catalyst for oxidation of organic contaminants. *Journal of Hazardous Materials*, *340*, 300-308. <https://dxdoi.org/10.1016/j.jhazmat.2017.06.069>
- Sampranpiboon, P., Charnkeitkong, P., & Feng, X. (2014). Equilibrium isotherm models for adsorption of Zinc (II) ion from Aqueous Solution on Pulp Waste. WSEAS Transactions on Environment and Development
- Sun, L., Chen D., Wan, S., & Yu, Z. (2015). Performance, kinetics, and equilibrium of methylene blue adsorption on biochar derived from eucalyptus saw dust modified with citric, tartaric, and acetic acids, *Bioresource Technology*, *198*, 300-308. <https://doi.org/10.1016/j.biortech.2015.09.026>
- Sun, L., Wan, S., & Luo, W. (2013). Biochars prepared from anaerobic digestion residue, palm bark, and eucalyptus for adsorption of cationic methylene blue dye: Characterization, equilibrium, and kinetic studies, *Bioresource Technology*, *140*, 406-413. <http://dx.doi.org/10.1016/j.biortech2013.04.116>
- Wu, F., & Tseng, R. (2010). A new linear form analysis of Redlich-Peterson isotherm equation for the adsorptions of dyes, *Chemical Engineering Journal*, *162*, 21-27. <https://doi.org/10.1016/j.cej.2010.03.006>

## Copyrights

Copyright for this article is retained by the author(s), with first publication rights granted to the journal.

This is an open-access article distributed under the terms and conditions of the Creative Commons Attribution license (<http://creativecommons.org/licenses/by/4.0/>).

# Modeling the Transition State Structures of the Reductive-Half Reaction Active Site of Xanthine Oxidase Bound to Guanine Analogues: A Density Functional Theory Approach

Mamaru Bitew Alem<sup>1</sup>, Yilkal Bezie Ayele<sup>2</sup>

<sup>1</sup>Department of Chemistry, Debre Markos University, Ethiopia

<sup>2</sup>Department of Biotechnology, Debre Markos University, Ethiopia

Correspondence: Mamaru Bitew Alem, Department of Chemistry, Debre Markos University, Ethiopia.  
E-mail: mamaru2005@gmail.com

Received: November 28, 2017 Accepted: January 16, 2018 Online Published: January 28, 2018

doi:10.5539/ijc.v10n1p137

URL: <https://doi.org/10.5539/ijc.v10n1p137>

## Abstract

Modeling and characterization the transition state structure of enzyme catalyzed reactions is essential. A DFT method employing B3LYP level of theory with 6-31G (d',p') basis set for non-metals and LanL2DZ basis set for molybdenum have been used. The bond orders of chemical fragments were calculated using AOMix software. The effect of chalcogen replacement, amine group and methyl group in the parent structure of xanthine bound to xanthine oxidase active site were compared. The transition state structure of model substrates (2AX, 2A6TP, 2A6SP and 2A6MP) bound to the truncated form of XO active site has been confirmed by the presence of one negative imaginary frequencies ( $s^{-1}$ ) (-60), (-140), (-230) and (-270), respectively. The corresponding normalized energy barriers (kcal/mol) from pre-transition state to the transition state, respectively, are (13.869), (21.753), (23.109) and (0.212). In this work, 2A6SP and 2A6TP substrates were found to be potential xanthine oxidase inhibitors. The large bond distances and minimum bond order for  $C_{RH}-H_{RH}$  bond, and small bond distances and maximum bond order for  $S_{M0}-H_{RH}$  bond at the transition state for chalcogen replaced 2AX confirms early transition state structure. Methyl substituted 2AX analog found to have post transition state structure. A potential xanthine oxidase inhibitor can be designed from purine family enzymes using DFT approach.

**Keywords/Phrases:** DFT, xanthine oxidase, modeling, stepwise mechanism, transition state

## 1. Introduction

Xanthine oxidoreductase (XOR) is a molybdenum-containing enzyme encoded by the human genome and catalyzes the sequential hydroxylation of hypoxanthine to xanthine and xanthine to uric acid [Enroth et al. (2000), Okamoto et al. (2004) and Nishino, Okamoto, Eger and Pai (2008)]. The enzyme was first discovered, in 1902 from bovine milk by F. Schardinger [Berry and Hare (2004), and Enroth et al. (2000)] as aldehyde reductase. But, Dixon *et al.* (1926) isolated the enzyme from cow's milk and showed that the enzyme was identical to the xanthine-oxidizing enzyme [Nishino et al. (2008)]. Since then, the enzyme has been routinely isolated from various sources [Enroth et al. (2000) and Okamoto et al. (2004)]. The X-ray crystal structure for XO (xanthine oxidase) enzymes has been resolved from various sources such as bovine milk xanthine oxidase (*bmXOR*) [Enroth et al., (2000)] (Figure 1.1).

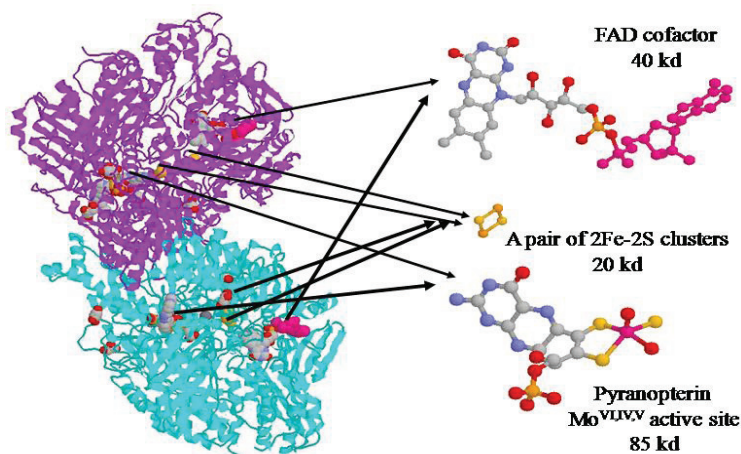


Figure 1.1. The crystal structure of bovine milk xanthine oxidase (left) and arrangement of the redox active centers: Mo MPT, [2Fe-2S] cluster and FAD (PDB accession code of 1V97) [Okamoto et al. (2004)]

The illustration was prepared using protein explorer [Martz (2002)]

The *bmXOR* enzyme is a homodimer with a molecular mass of about ~300 kDa [Enroth et al. (2000) and Okamoto et al. (2004)]. Each monomer consists of four redox active centers: Molybdopterin cofactor, a pair of non-identical 2Fe-2S centers, and one FAD (Flavin adenine dinucleotide) cofactor [Cao, Pauff, and Hille, (2011), Leimkühler, Stockert, Igarashi, Nishino, and Hille, (2004) and Pauff, Cao and Hille, (2008)]. The smallest (S) subunits (20-kDa each, consisting two pairs of [Fe<sub>2</sub>S<sub>2</sub>] (S<sub>Cys</sub>)<sub>4</sub> clusters) are connected by a long segment to the medium (M) subunits (40-kDa each, consisting two FAD cofactors). Similarly, the medium subunits are connected to the large (L) subunits (85-kDa each, consisting two molybdopterin cofactors) [Mohamed, Al-Omar, El-Subbagh, Beedham, and Smith, (2005) and Schwarz and Mendel, (2006)]. The enzyme, XOR has two interconvertible forms, Xanthine Dehydrogenase (XDH) and XO [and Berry and Hare, (2004) and Enroth et al. (2000)]. The enzyme, *bmXOR* from mammalian sources including human, is synthesized as the dehydrogenase form, but it can be readily converted to the oxidase (XO) form upon oxidation of sulfhydryl residue [Leimkühler et al. (2004), Pauff, Zhang, Bell, and Hille, (2008) and Pauff, Cao, and Hille, (2009)]. The main differences in the catalytic properties of XDH and XO are the reactivity of the FAD cofactor towards the competing electron acceptors, NAD<sup>+</sup> and molecular oxygen, which are electron acceptors for XDH and XO, respectively [Pauff, Zhang, Bell, and Hille, (2007), Pauff et al., (2008) and Pauff et al. (2009)].

The enzyme is widely distributed throughout various mammalian organs and microorganism cells. In mammals, including human, the enzyme is known to be found in various organs of our body including kidney, liver, small intestine, and lactating mammary gland [Pauff et al., (2007)]. In addition to its role in hydroxylation of various N-heterocyclic compounds, it is suggested to be involved in drug oxidation, activation, and detoxification of xenobiotics [Mohamed et al., (2005)]. However, the most noticeable disease in humans is the deposition of uric acid, known to be responsible for gouty conditions [Romao, (2009)]. This condition is more pronounced in the joints, through the deposition crystals of sodium urate [Kalra, Jena, Tikoo, and Mukhopadhyay, (2007)]. The hydroxylation products are the main reason for gouty condition or hyperuricemia which is a painful disease occurred in joints [Bjelakovic et al., (2002), Kalra et al., (2007) and Romao, (2009)]. In the course of the reaction, reactive oxygen species (ROS), O<sub>2</sub><sup>-</sup> and H<sub>2</sub>O<sub>2</sub> are generated at FAD as end product of the reaction [Berry and Hare, (2004)]. These reactive oxygen species together with the hydroxylated product of the reaction, uric acid, are suggested in different pathological states, in the area of human health. It is also involved in different pathological states such as endothelia dysfunction, hypertension, carcinogenesis, hepatitis, oxidative damage, and heart failure [Berry and Hare, (2004)]. Hence, health organizations show interest in the enzyme as the enzyme is more frequently linked to major metabolic pathways of drugs and due to its adverse effect in the area of human health [Mohamed et al., (2005), and Alfaro and Jones, (2008)]. Thus, understanding the catalytic cycle of the reaction mechanism would be beneficial from human health perspective [Leimkühler et al., (2004), Pauff et al. (2007), Pauff et al. (2008), Zhang, and Wu, (2005)].

As shown in Figure 1.1, the redox sites of the *bmXOR* enzymes are organized in a linear fashion, ideal for electron transfer. As with many oxidoreductase enzymes, the redox sites are characterized for their suitability to undergo simultaneous interaction with both the reducing and oxidizing substrates. The reducing substrates react at the reductive and the oxidizing substrates at the oxidative half-reaction active sites [Voityuk, Albert, Romao, Huber, and Roesch, (1998)]. They also need additional components (such as pairs of [Fe<sub>2</sub>S<sub>2</sub>](S<sub>Cys</sub>)<sub>4</sub> clusters) to facilitate the flow of electrons between the

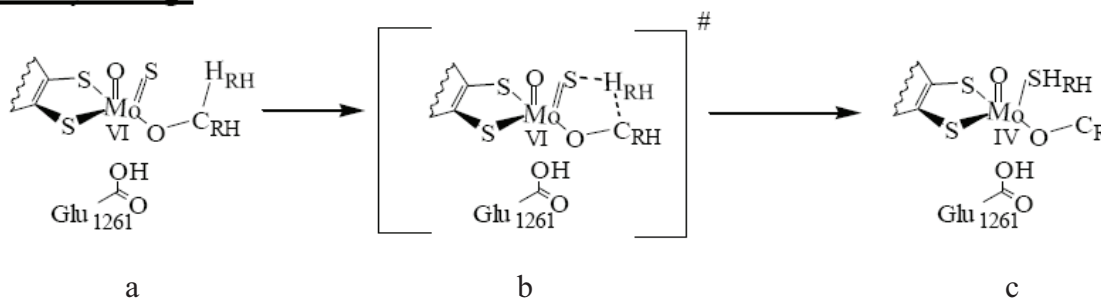
reduction and oxidation half-reaction sites [Pauff et al. (2009), and Xia, Dempski, and Hille, (1999)]. The reaction stoichiometries of these enzymes are unique among other hydroxylation reactions catalyzed by mono-oxygenase enzymes. Monooxygenase enzymes hydroxylate their substrates using the oxygen, derived from molecular oxygen (equation 1). Unlike the mono-oxygenase enzymes, the XOR enzymes use oxygen derived from water and generates a pair of reducing equivalents (equation 2) [Choi, Stockert, Leimkuhler, Hille, (2004), Hille, Kim, and Hemann, (1993) and Hille, (2006)].



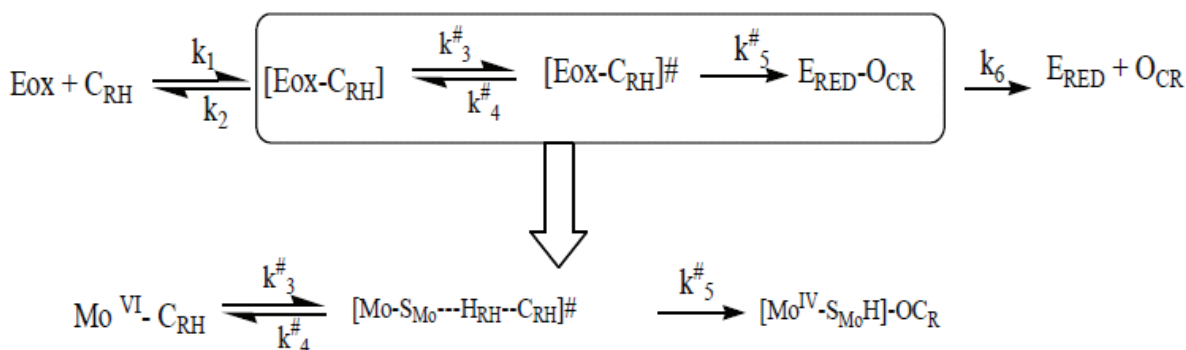
1.1 Overview of the Catalysis Stage and the Nature of the Transition State

The catalysis stage of the reaction mechanism is the main concern of theoretical research since the transition state structure is part of this stage. The geometry of the transition state structure is central in understanding the catalytic reaction mechanism [Ayala and Schlegel, (1997)] although the smallest fraction of the catalytic cycle is spent in the transition state [Schramm, (1998)]. As shown by the mechanistic transformation (Scheme 1.2), the transformation of the tetrahedral Michaelis-Menten complex [(Enzyme)-(MoVI=O(=S)(-O-C<sub>RH</sub>))] to the product bound intermediate [(Enzyme)-(MoIV=O(-SH)(-O-C<sub>R</sub>))] is proposed to pass through the tetrahedral transition state (Schemes 1.1, Structure b). The generalized reaction equation for reactions to form their product is shown in Scheme 1.2. The tetrahedral transition state complex ((Enzyme)-[MoVI=S---H<sub>RH</sub>---C<sub>RH</sub>]#), shown in Scheme 1.2, is described by placing the substrate bound hydrogen (H<sub>RH</sub>) between the Mo bound sulfido (S<sub>Mo</sub>) terminal and the substrate (C<sub>RH</sub>) bound carbon. Depending on the type of the substrates (C<sub>RH</sub>), the (Enzyme)-[MoVI=S---H<sub>RH</sub>---C<sub>RH</sub>]# transition state structure was proposed to dissociate into O-C<sub>R</sub> and (Enzyme) [MoVI=O(=S)(-OH)] without forming a stable intermediate or by forming an (Enzyme)-[MoIV-O-C<sub>R</sub>] intermediate.

**Catalysis stage**



Scheme 1.1. A hypothetical schematic model, representing the catalytically crucial elements of the reductive-half reaction, for the hydroxylation of substrates (CR<sub>H</sub>), by *bmXOR* enzymes



Scheme 1.2. A hypothetical description for the transition state structure that involved the transfer of substrate proton (H<sub>RH</sub>) from C<sub>RH</sub> to S<sub>MO</sub>

A transition state structure is the molecular species that is represented by the top of the potential energy curve in a simple one-dimensional reaction coordinate diagram [Senthilkumar and Kolandaivel, (2003)]. The energy of this species is needed in order to determine the activation energy of the reaction and thus the reaction rate. It is a distinct species in the reaction coordinate that determine the absolute reaction rate.



From spectroscopic studies, it is suggested that the molybdenum center cycles through three oxidation states (VI, V, IV) [Senthilkumar and Kolandaivel, (2003) and Ilich and Hille, (1999)]. Even though the transition state structure is central to understanding catalysis, no transition state structures have been established to date [Senthilkumar and Kolandaivel, (2003)]. Understanding how enzymes work and modeling enzymatic transition state provide an understanding of catalysis, and permit the design of inhibitors [Schramm, (1998)]. But, modeling the transition state structure can't be achieved by any modern practical method due to its very small half-life [Schramm, (1998)]. The transition state for chemical reactions is proposed to have lifetimes near 10-13 sec, the time required for a single bond vibration [Schramm, (1998)]. No physical or spectroscopic method is available to directly observe the structure of the transition state for enzymatic reactions [Schramm, (1998)]. However, modeling and understanding the nature of the transition state is a key in probing the reaction mechanism for different chemical and biochemical transformations [Ayala and Schlegel, (1997)]. Understanding if catalysis is substrate dependent is a key factor in catalysis. Also identifying whether the transition state structure occurs at a late or an early transition state is a key factor in understanding whether the transition state structure resembles the substrate or the product [Alfaro and Jones, (2008), and Ayala and Schlegel, (1997)]. Therefore, computation chemistry is expected to play a role in providing insight on the nature of the transition state by providing parameters like bond order and bond distance. It also shows the transition state structure with its full geometry which can't be achieved by any other chemical or biochemical techniques.

### 1.2 Effect of Substituent Groups on the Transition State Structure

The nucleic acid bases are interesting compounds due to their biochemical, pharmacological, chemical and physicochemical importance. Substitution of *thio* and *seleno* groups to the nucleic acid bases makes it more interesting compound due to its mutation properties of biological importance and pharmacological point of view [Dinesh, Shikha, Bhavana, Nidhi, Dileep, (2010) and Kim, Jang, Cho and Hwang, (2010)]. The *thio* derivatives also belong to a family of t-RNA with a potential application in the drug industry [Senthilkumar and Kolandaivel, (2003)]. Thus, a number of analogues of nucleic acid bases have been the target of extensive studies because of their importance in many biological studies. But, relative to *oxo* substituted, the *thio* and *seleno* substituted purine derivatives are less studied [Civcir, (2001)]. The oxygen of both purine and pyrimidine bases is substituted with sulfur, selenium, or methyl to produce an important class of analogues [Kim, Jang, Cho and Hwang, (2010)]. For example, *thio* substituted guanine derivative 2-amino-6-thiopurine (2A6TP) has interesting chemotherapy effects, including powerful antitumoral activity [Civcir, (2001)]. The nature of the transition state for XO is expected to be substrate dependent and anticipates the Hammond principle [Alfaro and Jones, (2008)]. The Hammond postulate predicts that transition state structure resembles more like reactant with faster reaction rates [Alfaro and Jones, (2008)]. In addition, the affinity of the enzyme towards different reducing substrate differs from substrate to substrate. The electronic nature of substituent found in the geometry of the substrate to be hydroxylated plays a role for the enzyme to show different affinity towards different reducing substrates [Alfaro and Jones, (2008)].

In general, the parametric changes are shown to dictate the position of HRH at the transition state. Along the reaction pathway, depending on the nature and type of substrates, the transition states are proposed to occur either during the late transition state (that resembled the products) or early transition state (that resembled the reactants). The Hammond postulate can be greatly influenced by the nature of the substrate which is suggested to influence the bond distances ( $C_{RH}-H_{RH}$ ,  $C_{RH}-O_{eq}$  and  $S_{Mo}-H_{RH}$ ) and hence, the nature of the transition state structure [Alfaro and Jones, (2008)].

The enzyme can oxidize a wide range of substrates, so the use of chalcogen and methyl substituted purine derivatives might give an insight in probing reaction mechanism of XO. The chalcogen replacement on the pyrimidine ring is expected to affect the ability of the molecule to delocalize emerging charge during nucleophilic reaction. Therefore, the ring substitution with different electronic nature gives different insight about the nature of the interaction between the active site and reducing substrates.

Understanding the effect of chalcogen replacement, at the transition state and the behavior of purine derivatives towards xanthine oxidase, is important to alleviate the problems related to the enzyme. It also helps to understand the electronic nature of different purine derivatives. The presence of chalcogens and methyl in the geometry of the substrate, xanthine, may have a role to influence the overall electron transfer process as they exhibit different ways to distribute electron density in a molecule. The different electronic nature of oxygen, sulfur, selenium, amine group and methyl group in the structure of xanthine are also expected to affect the nature of the carbon atom to be hydroxylated and the Mo center of the active site through electron transfer process.

The chalcogens (O, S and Se) are expected to have different electron negativity and polarizability. This difference is expected to affect the reactivity of the geometries (Figure 2.2). However, when *oxo* group is substituted with *methyl* ( $CH_3$ ) group, the nature of aromaticity is expected to be altered. The aromaticity of the parent molecule involves free electrons of two nitrogen atoms from pyrimidine and imidazole rings. Up on substitution of *methyl* group only a pair of free electron

involved for aromaticity. Thus, the ability of the charge delocalization on the geometries could show variation during nucleophilic reaction. It is also expected to influence the nature of the transition state and the allocation of two electrons on the active site. In this work, the effect of chalcogen replacement and methyl group at the transition is expected to be addressed. Although the transition state structure is characterized by one imaginary negative frequency [Ayala, and Schlegel, (1997) and Contreras, Lorena and Gerli, (2008)], the imaginary negative frequencies and linear motions of the  $H_{RH}$ , at the transition state, is also proposed to vary depending on the affinity of the substrates (orientation of substrates and substrate-binding sites) [Bayse, (2009)]. The frequencies and intensities are expected to depend on the conformation and binding-sites of the substrates. The variations in the activation energy for all complexes are presumed to be due to the absence of the factors that are supposed to stabilize the charge accumulation [Bayse, (2009)].

In this work, sulfur, selenium, and methyl substituted guanine analogs are used to model the transition state structure of the active site and develop a more unified mechanism. The purpose is to identify the role of chalcogen groups at the transition state. In this work, the behaviors of structurally similar structures at the transition state are characterized to support the hypothesis that if catalysis is substrate dependent is a key factor in catalysis. Identifying whether, the transition state structure occurs at a late or an early transition state is a key factor in understanding whether the transition state structure resembles the substrate or the product [Pauff, (2008)]. This is significant to connect the rate of reaction process with structural difference. It is also applicable to understand the relationship between the rate of reaction and the stability of products.

## 2. Materials and Methods

### 2.1 Materials

Several software packages were used in order to model the transition state structures and probe a plausible reaction mechanistic route for the oxidation of guanine by xanthine oxidase. One of the two software programs that were used to sketch various structures was ChemDraw ultra 2003 version 8 (Cambridge soft corp., Cambridge, MA, U.S.A.). In addition to ChemDraw, GaussView 3.0 version 6.0 (Gaussian, inc., Pittsburgh, PA, USA) was used to build molecules, set up input files, compute bond distances, and visualize frontier orbitals. The geometries constructed using GaussView were used as input files for Gaussian<sup>®</sup> 03W software version 6.0 (Gaussian, inc., Pittsburgh, PA, USA). This program was used to perform geometry optimization, frequency, linear transit optimization scan, and single point energy calculations. The output geometries, from this program, were computed using AOMix 2011/2012 revision 6.6 (center for catalysis research and innovation, University of Ottawa, Ottawa, ON, Canada) in order to perform molecular orbital analysis and constituent of chemical fragments. Finally, Microsoft word 2007, Microsoft powerpoint 2007, and Microsoft excel 2003 and 2007 (Microsoft, inc., Redmond, Washington, USA) were used for data treatment and thesis write-up. All electronic structure calculations and data handling were performed on Dell computer Optiplex780 model, 2011 (Dell, Inc., Wilkie Sdh Bhd., Penang, Malaysia).

### 2.2 Methods

#### 2.2.1 Computation Details

Electronic structure calculations were performed by applying Density Functional Theory (DFT) employing B3LYP [Chowdhry, Robert, Stephen, and Dines, (2007)] (Beeke 3 parameter method for calculating the molecular energy due to overlapping orbital plus Lee-Yang Parr method of accounting electron correlation) level of theory. The calculations were performed on the truncated form of the active site (Fig. 2. 1, *upper left panel*) bound to guanine (Fig. 2. 1, *upper right panel*), as shown in Figure (2.1, *lower panel*).

1. The 6-31G (d', p') basis set with polarization and diffuse functions was applied for non-metal atoms (C, H, O, N, S, and Se). Similarly, the LANL2DZ (Los Alamos National Laboratory 2-Double-zeta) basis set and LANL2 effective core potential were applied for Mo atom [Chowdhry et al., 2007]. The geometries developed using GaussView were used as input files for the geometry optimization. The optimized geometries were also used as input files for single point energy calculation. In all calculations (linear transit scans, geometry optimization, frequency, transition states search, and single point energy) the "# b3lyp gen pseudo=read #p ginput pop=full gfpri" key words and general job type [Foresman, J.B., (1993)] were used. In all calculations, the general job type and key words were used by applying other key words relevant to the respective calculations. During the electronic structure calculation, the runs were aborted many times due to electric power outage and other errors. In such events, calculations were resumed using the keyword "Opt=restart". This keyword was used to restart the calculation when the electronic structure calculations were interrupted. The calculations that required constraints on the coordinates, the "Opt=modredundant" keyword was used [According to Gaussian 03 versions 6.0 manual F1 option]. For similar interruption the "# opt=(restart, modredundant)" keyword was used.

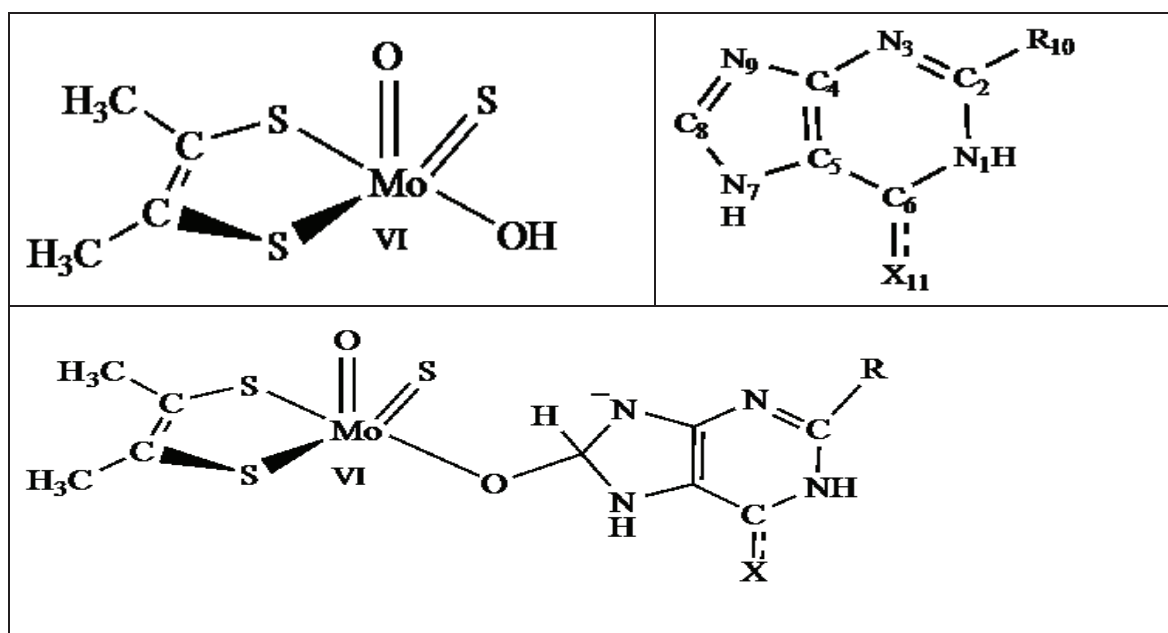


Figure 2.1. The truncated analogue for the reductive half-reaction active site structure of xanthine oxidase (upper left panel) bound to guanine derivatives (upper right panel), as shown in the (lower panel)

The structure shown in *upper right panel* represents guanine derivatives depending on the substituent group (X) and (R). Thus, if (X) is substituted with oxygen and (R) is the amino group, the structure was guanine (2AX). The derivatives for guanine were generated by maintaining (R) to be  $\text{NH}_2$  and varying (X) with 'S' (2-amino-6-thiopurine, 2A6TP), 'Se' (2-amino-6-selenopurine, 2A6SP) and 'CH<sub>3</sub>' (2-amino-6methylpurine, 2A6MP).

### 2.3 Modeling and Characterizing the Transition State Structures

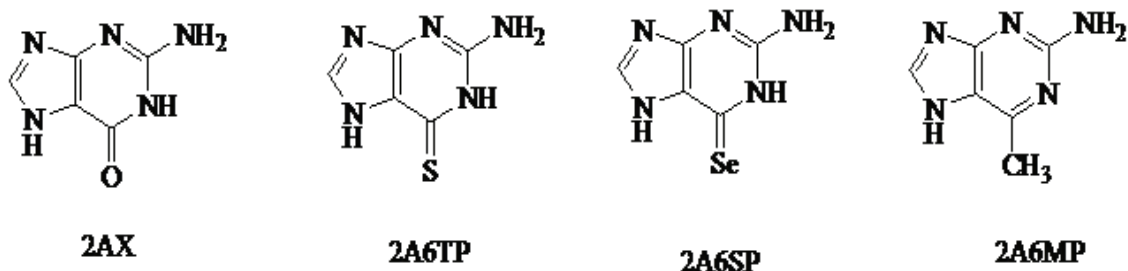


Figure 2.2. The structures used to model and characterize the transition state structures for guanine analogues

The abbreviations are 2AX (2-amino xanthine), 2A6TP (2-amino-6-thiopurine), 2A6SP (2-amino-6-selenopurine) and 2A6MP (2-amino-6methylpurine).

The transition state structure (TS) was located using a direct frequency calculation by binding the equatorial oxygen of the active site ( $\text{O}_{\text{eq}}$ ) with  $\text{C}_8$  of the structures shown in Figure (2.2). The substrate bound active site (Fig. 2.1, *lower panel*) was constructed by placing the substrate "H or  $\text{H}_{\text{RH}}$ " in the middle between active site sulfido terminal ("S or  $\text{S}_{\text{Mo}}$ ") and the interaction site of the substrate or substrate carbon (" $\text{C}_{\text{RH}}$ "), as shown in Figure 2.3. The  $\text{C}_{\text{RH}}$  in Figure 2.3 was substituted with the derivatives shown in Figure 2.2

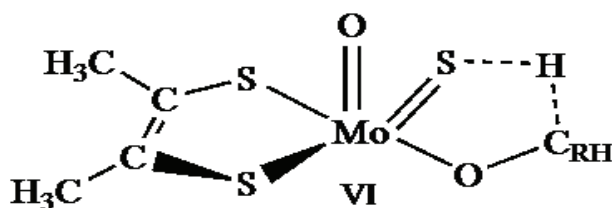


Figure 2.3. The general model structure used for the transition state structure search

The tetrahedral transition state structures were modeled by placing the substrate bound hydrogen ( $\text{H}_{\text{RH}}$ ) between the

sulfido ( $S_{Mo}$ ) terminal and the substrate carbon ( $C_{RH}$ ) center. The  $C_{RH}$  was substituted with the structures shown in Figure 2.2.

In the direct frequency calculation approach, the vibration frequency of a given structure was calculated without applying any constraint. The structures were optimized by applying “*opt freq*” key words to the general key words and job type mentioned in sub-section 2. 2. 1. In addition to the transition state structure the two structures (pre- and post-transition state structure) were optimized. The pre-transition state structure resembles the substrate bound (close to substrate bound (Fig. 2.4, *upper right panel*). The post-transition state structure resembles the product bound (close to product bound) (Fig. 2.4, *upper left panel*). These structures were developed from the output geometry of transition state structure by adding constraint.

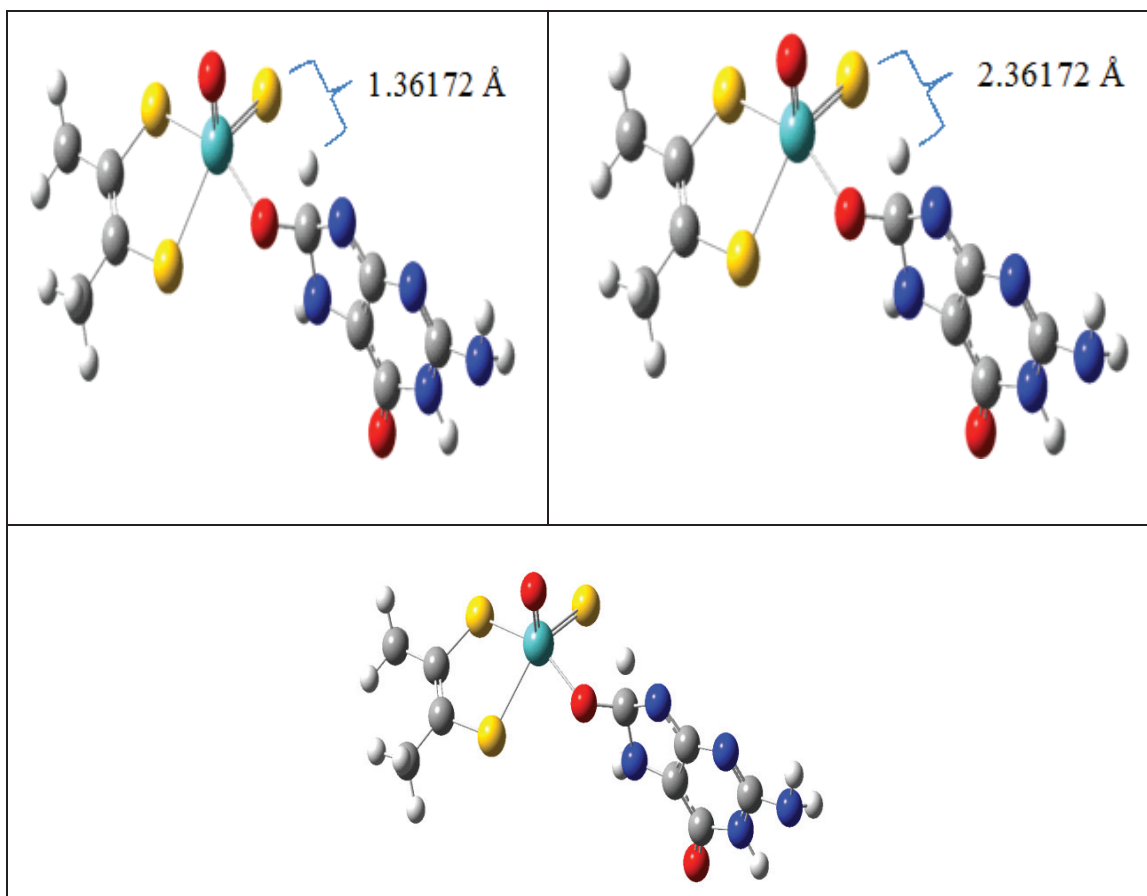


Figure 2.4. A sample input geometry for 2AX bound to the reductive half -reaction active site of xanthine oxidase enzyme, used for transition state structure characterization

The upper panels (left) and (right) were pre-transition state and post-transition state structures developed from output geometry of transition state structure (bottom panel). The input geometries for structures shown in Figure (2.2) bound the reductive half reaction of XO active site, shown in Figure (2.1), upper left panel were prepared in similar manner to this figure (Figure 2.4), as described in Figure 2.3.

The pre-transition state structure resembled substrate bound (structure close to substrate bound, but not substrate bound) where substrate hydrogen (“ $H_{RH}$ ”) was bound to the interaction site of the substrate ( $C_8$ -imidazole or “ $C_{RH}$ ”) (Fig. 2.4, *upper right panel*). The post-transition state structure resembled product bound where substrate hydrogen (“ $H_{RH}$ ”) was bound to the sulfido terminal (“ $S_{Mo}$ ”) of the active site (Fig. 2.4, *upper left panel*). The two structures were optimized by adding constraint and applying “*opt=moderedundant*” key words to the general job type mentioned in Sub-section 2.2.1. The  $S_{Mo}$ - $H_{RH}$  bond distance coordinates were frozen to 2.26172 Å and 1.36172 Å, respectively, for the pre- and post-transition state structures. These assumptions were made based on the typical C-H (in methane) and S-H (in thiol or sulfhydryl group) bond distances, respectively, 1.09 Å and 1.35 Å. The structures represented by CH (pre-transition state) and SH (post-transition state), respectively, were found between the normal carbon-hydrogen and sulfur-hydrogen bond distances (1.09 Å) and (1.35 Å). The geometry optimization of three structures (CH, TS and SH) were used to locate the transition state structures. All calculations were carried out at (VI) oxidation state for Mo ( $Mo^{VI}$ ) and constant charge and multiplicity, respectively, whole numbers (-2) and (1). The values were calculated from the negative charge around Mo

and its oxidation state or number of unpaired electrons. Several qualitative and quantitative data were generated from the optimized structures such as total electronic energy, Mulliken atomic charge, bond distance, and frontier orbitals. The output geometry from optimized structures was used as input geometry for single point energy calculations, with the same charge and multiplicity. The outputs from the single point energy calculations were used as input files for AOMix calculation in order to generate percent contribution of chemical fragments, bond orders, and band gap energies.

### 3. Result and Discussion

#### 3.1 Transition State Modeling and Characterization

In order to model the transition state structures, a series of geometry optimizations were performed at DFT/B3LYP level. From the optimized geometries, several parameters such as the total electronic energies, frequencies, bond order indices, bond distances, percent contributions of chemical fragments, and wave function descriptions were assembled, to characterize the transition state structures for the chalcogen and methyl substituted geometries.

#### 3.2 Predicting the Transition State Structure Based on the Total Energy and Frequency

The structures shown in Figures (2.1, right upper panel and 2.2) were bound to the truncated form of the active site structure (Fig. 2.1, upper left panel) as shown in Figure (2.1, lower panel and 2.3) and optimized at DFT/B3LYP level. The total electronic energies on pre- (CH), post- (SH) and transition state (TS) structures were collected and plotted against the reaction coordinates as shown in Figure (3.1).

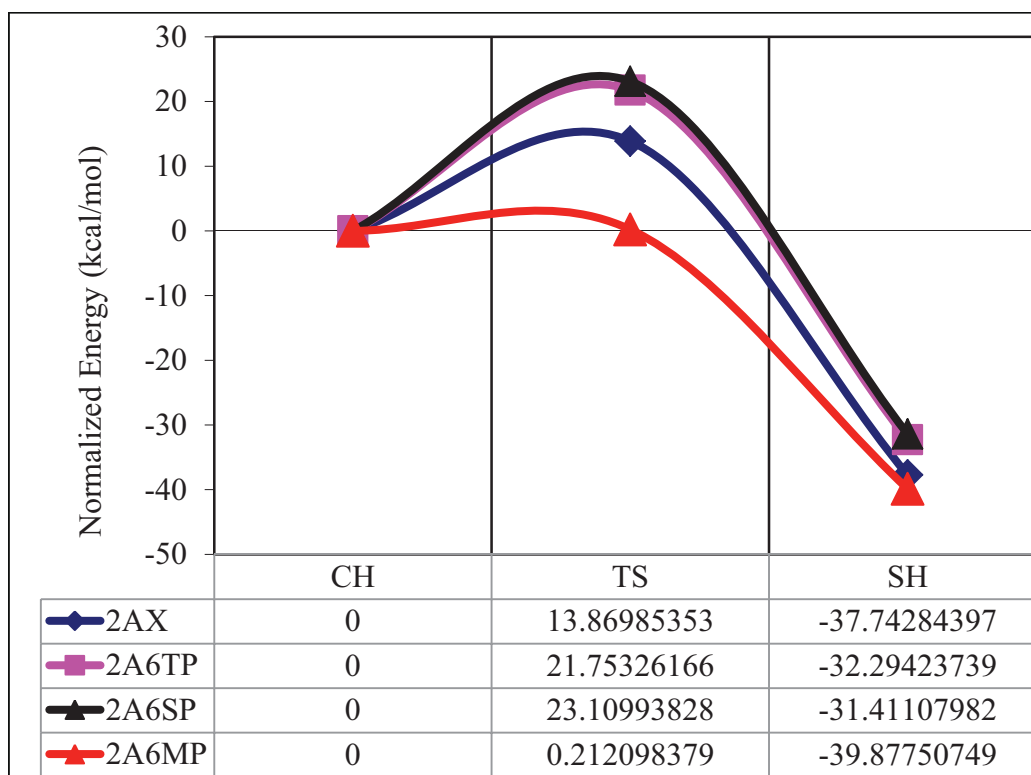


Figure 3.1. The normalized energy plot for guanine (2AX) and its substituted analogs

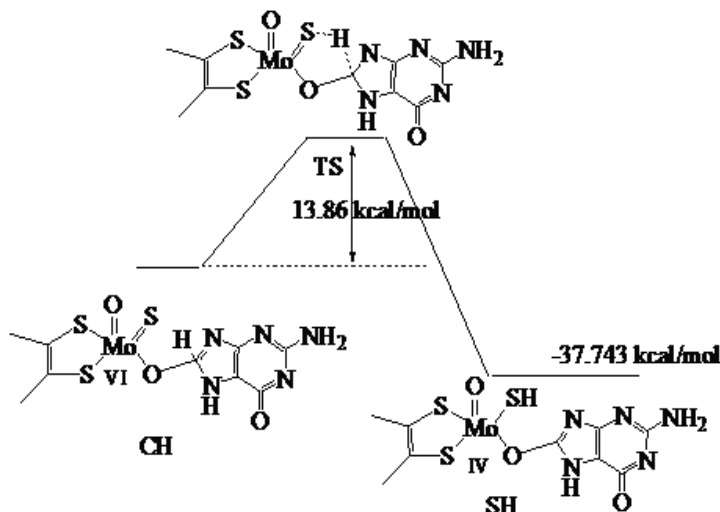


Figure 3.2. A sample reaction coordinates, for the reductive half reaction of guanine bound to xanthine oxidase enzyme. The energy profile for guanine analogs bound to XO enzyme were examined as shown in Figure 3.2. Thus, the highest energy gap [ $\Delta H^\ddagger (E_{TS}-E_{CH})$ ] between the energies of pre-transition state (CH) and transition state structures (TS) was observed for the reaction coordinate of Eox-2A6SP (23.109 kcal/mol). Whereas, the lowest energy at the transition state (TS) was observed for the reaction coordinates of 2A6MP (0.212 kcal/mol) bound to the reductive half reaction active site of xanthine oxidase (Eox-2A6MP), as shown in Figure 3.1. The minimum energy was due to the charge delocalization at the transition state. The reason for the charge delocalization was the highest partial negative charge developed at N<sub>7</sub> imidazole ring and C<sub>8</sub> of the molecule. The accumulation of the highest partial negative charge at N<sub>7</sub> and C<sub>8</sub> of imidazole was due to the shifting of bond pair electrons from adjacent C<sub>8</sub> carbon and the flow of electrons due to the inductive effect created by methyl group, respectively. Generally, the energy at the TS for the 2AX analogs were 0.212 kcal/mol (Eox-2A6MP), 13.869 kcal/mol (Eox-2AX), 21.753 kcal/mol (Eox-2A6TP), and 23.109 kcal/mol (Eox-2A6SP). The lowest energy at transition state for Eox-2A6MP indicated the ease for 2A6MP to enter the transition state and create a thermodynamically favorable reaction. The difference in energy ( $\Delta H^\ddagger$ ) at TS indicated that the effect of chalcogen and methyl replacement was due to the ability of the inductive effect (CH<sub>3</sub>) on charge delocalization. The replacement of chalcogen and methyl group at C<sub>6</sub>-pyrimidine of guanine was shown to affect the interaction site. In this work, the ability of the substrate to stabilize the emerging charge was determined by the nature of the substituent groups. The capacity of the charge stabilization of different molecules was also the reason for geometries to have different reaction rates and activation barriers.

In this work we have derived a formula which can relate turnover rate with enthalpy as:

$$k_{cat} = e^{-\Delta H^\ddagger} \dots\dots\dots(3)$$

The catalytic turnover rate ( $k_{cat}$ ) was shown to have the inverse relation with the change in enthalpy ( $\Delta H^\ddagger$ ). If  $k_{cat}$  was calculated from  $\Delta H^\ddagger$ , the complex (Eox-2A6MP) with the smallest energy barrier at the transition state was expected to be converted in a very high concentration compared to the complexes with high enthalpy change. The energy obtained at the transition state was shown to clearly support the hypothesis that there would be a variation on the behavior of the transition state and reactivity upon the replacement of the chalcogen and methyl groups on the carbon (C<sub>6</sub>) of pyrimidine ring. Thus, the highest energy shown by 2A6SP substrate indicated that the substrate had the least ability to delocalize the emerging charge at the transition state (TS). This is due to the highest polarizability of selenium compared to other substituent groups (CH<sub>3</sub>, O and S). The mobility of the electron cloud (polarizability) was due to the ability of the electron distribution to change temporarily and increase down the group of the periodic table. This was due to an increase in atomic size. The  $\pi$ -electrons were more polarizable than the  $\sigma$ -electrons. Thus the maximum mobility of the electron cloud in Eox-2A6SP was due to the presence of  $\pi$ -electrons, in addition to high atomic size of selenium. Whereas, the mobility of electron cloud in methyl substituted guanine analog, Eox-2A6MP was minimum rather high charge accumulation was preferred through inductive effect. According to the data, the polarizable substituents were expected to slow down the reaction. On the other hand, the electron donating substituents (such as methyl group) were expected to speed up the reaction of XO by stabilizing the transition state structure. The highest activation barrier for Eox-2A6SP also revealed the lowest reduction potential of the metal.

In addition to the energies at the transition state, the energies for the post-transition state structure (the structure near to the product bound, SH) were collected. The energies at SH for the structures bound to the active site were -39.87 kcal/mol, -37.74 kcal/mol, -32.29 kcal/mol and -31.41 kcal/mol for (Eox-2A6MP), (Eox-2AX), (Eox-2A6TP), (Eox-2A6SP), respectively. The release of such energy in an exothermic manner revealed that the structures were thermodynamically more stable compared to the substrate bound structures (CH). Even though all substrates were converted in to their post-transition state exothermically, the highest exothermicity was observed in the presence of substrates with methyl group substitution (-39.87 kcal/mol). The highest exothermicity was due to the high interaction between the active site and substrate (2A6MP). Therefore, Eox-2A6MP could be easily converted in to product with minimum activation barrier and considerably large exothermicity. The product obtained from the reaction involving Eox-2A6SP (2-amino-6-selenouric acid) was destabilized by 8.46 kcal/mol relative the most stable product, 2A6MP bound (2-amino-6-methyluric acid). The experimental work by Kalra *et al*, 2007 showed that the presence of 2A6SP (2-amino-6-selenopurine) as a substrate was claimed to a preferential inhibitor for XO. Even though, there is no experimental data reported in the presence of 2A6TP, the theoretical work was shown to reveal a small energy difference (2 kcal/mol). As a result, 2A6TP could be a potential inhibitor. Thus, the highest activation energies reported in the presence of the two substrates (2A6TP and 2A6SP) at the transition state (Figure 3.1) were expected to be due to their inhibition activity when reacted with the enzyme.

The potential energy surface diagram, shown in Figure 3.1, revealed that the total energies obtained in the presence of all substrates, at the transition state, was closer to the energy of the structure near to substrate bound structure (CH). According to the Hammond's principle, the position of all transition state structures was found to be early transition state. According to the Hammond postulate, the transition state structure was expected to be more reactant like with faster reaction rate [Alfaro, and Jones, (2008)]. However, the position of the transition state structure for Eox-2A6MP was found to be product like relative to the transition structures located in the presence of chalcogen substituted guanine analogs. This is inconsistent with Hammond principle, and the anti-Hammond effect is consistent with inductive effect enhancing the rate of tetrahedral transition state formation. Potentially this might show an effect on the allocation of two electrons. The finding clearly point out the effect of electron donating groups through resonance (O, S and Se) and through inductive effect (CH<sub>3</sub>). Methyl and amine group substituted purines were shown to be more reactive than the chalcogen and amino group substituted purines. This was due to the charge stabilization at transition state that was favored by inductive effect and localization of the electron cloud around a single atom. In summary, the results obtained from the total electronic energy was shown to confirm the highest reactivity and product stability for the methyl substituted analog, early transition state structure for *oxo*, *thio* and *seleno* substituted guanine analogs, product like transition state structure for *methyl* substituted analog, different reduction potential of the metal, and potential inhibition of XO by 2A6TP and 2A6SP.

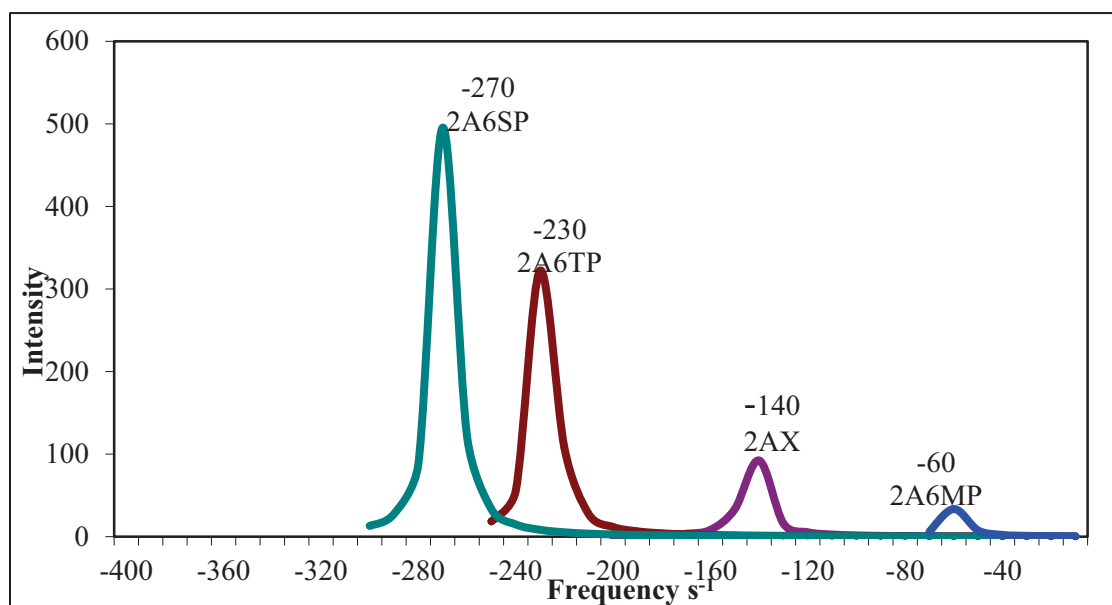


Figure.3.3. The frequency values used to characterize the transition state geometries through the presence of one negative imaginary frequency

The imaginary negative frequencies obtained from the substrates bound to the truncated reductive-half reaction active site were shown in Figure (3.3) and Table (3.1). From 2AX derivatives, the highest vibrational frequencies were observed on

methyl (CH<sub>3</sub>) substituted analogs. This indicated that the time required to cross the transition state for methyl substituted analog were short as compared to silico, thio and oxo-counter parts.

Table 3.1. The data used to characterize the transition state structure obtained from linear transit scan calculation in the presence of 2AX derivatives

Structure	Bond distance (Å)		Frequency (s <sup>-1</sup> )	% Mod <sub>xy</sub>	Bond order	
	S <sub>Mo</sub> -H <sub>RH</sub> distance	C <sub>RH</sub> -H <sub>RH</sub> distance			S <sub>Mo</sub> -H <sub>RH</sub>	C <sub>RH</sub> -H <sub>RH</sub>
2AX	1.86172	1.22676	-142.309	24.14	0.301	0.657
2A6TP	1.83274	1.24180	-227.924	21.18	0.324	0.634
2A6SP	1.81862	1.24824	-269.000	20.24	0.336	0.623
2A6MP	1.96592	1.19766	-59.386	19.05	0.238	0.701

Since frequency and time were inversely related, an imaginary negative frequency could tell us the time required to cross the transition state. The highest vibrational frequency value of Eox-2A6MP revealed that the time required to cross the energy barrier was minimal. Based on the vibrational frequency values, the 2AX derivatives were shown to assume the following trend: 2A6SP < 2A6TP < 2AX < 2A6MP. This indicated that the Eox-2A6MP was kinetically more favorable than other chalcogen substituted structures. The frequency data revealed that the Eox-2A6SP required more time to cross the energy barrier. This was consistent with the ability of the substrate to inhibit XO. In prior study [Kalra *et al.*, 2007] performed a toxicity experiment and suggested that the inhibitor was nontoxic. They also suggested that the inhibitors anti-cancer activity in combination with 6-Mercaptopurine [Kalra *et al.*, 2007]. Hence, this work gives the electronic structure description of preferential inhibitor and anti-cancer drug, 2A6SP.

As shown in Table 3.1, a difference in reactivity was observed in the presence of chalcogen replaced substrates. The reactivity between *oxo* substituted and *thio* substituted structures was faster by two orders of magnitude compared to the reactivity observed in the presence of *thio* and *seleno* substituted substrates. The total electronic energy data also revealed small difference between *thio* and *seleno* substituted substrates. This indicated the periodic trend shared by the two atoms or the small difference experienced by the atoms. Based on the data, the frequency value was in line with the energy barrier obtained from linear transit scan Figure 3.1. In addition to frequency data, bond distances (S<sub>Mo</sub>-H<sub>RH</sub> and C<sub>RH</sub>-H<sub>RH</sub>) were also computed at the transition state using Gauss View software package. As the observed bond distances reported in Table 3.1 revealed, at the transition state, the substrates with *oxo*, *thio* and *seleno* substitution revealed a decrease in S<sub>Mo</sub>-H<sub>RH</sub> bond distance and an increase in C<sub>RH</sub>-H<sub>RH</sub> bond distance. Whereas, the maximum S<sub>Mo</sub>-H<sub>RH</sub> bond distance (1.96592 Å) and minimum C<sub>RH</sub>-H<sub>RH</sub> bond distance (1.19766 Å) were reported for Eox-2A6MP at the transition state structure. The data revealed the direct relation between S<sub>Mo</sub>-H<sub>RH</sub> bond distance and vibrational frequency value. In addition, the data supported the inverse relation between peak intensities (Figure 3.3) and S<sub>Mo</sub>-H<sub>RH</sub> bond distance. As a result, the intensity of the peak had a direct relation with the speed of vibration observed for hydrogen atom at the transition state. The computation data revealed the preferential non-toxic inhibitor for XO enzyme. In addition, the relative kinetic and thermodynamic stabilities of selected purine derivatives (2AX analogs) were reported based on the total electronic energy and vibrational frequency data. Therefore, the highest thermodynamic stability was the highest kinetically favorable the reaction.

### 3.4 Characterization of Transition State Structure Using Bond Order, Bond Distance, Mulliken Atomic Charge and Wave Function

The bond order for C<sub>RH</sub>-H<sub>RH</sub> bond decreased as H<sub>RH</sub> migrated from C<sub>RH</sub> to S<sub>Mo</sub> at the transition state, Table 3.2. Whereas, the bond order for S<sub>Mo</sub>-H<sub>RH</sub> increased as H<sub>RH</sub> migrated from C<sub>RH</sub> to S<sub>Mo</sub>. This indicated that the breaking and formation of C<sub>RH</sub>-H<sub>RH</sub> and S<sub>Mo</sub>-H<sub>RH</sub> bonds, respectively, at the transition state.

Table 3.2. The bond order for C<sub>RH</sub>-H<sub>RH</sub> and S<sub>Mo</sub>-H<sub>RH</sub> of 2AX analogs at the transition state (TS)

structure	C <sub>RH</sub> -H <sub>RH</sub>	S <sub>Mo</sub> -H <sub>RH</sub>
2 AX	0.657	0.301
2A6TP	0.634	0.324
2A6SP	0.623	0.336
2A6MP	0.701	0.238

The C<sub>RH</sub>-H<sub>RH</sub> bond order was shown to decrease as we go from *oxo* to *seleno* substituted geometry at the transition state



and the converse was true for  $S_{M_0}$ - $H_{RH}$  bond order as shown in Table 3.2.

The bond order for  $C_{RH}$ - $H_{RH}$  are 0.657 (43.6 %), 0.634 (42.7%) and 0.623 (42.38 %), respectively, at the transition state, for *oxo*, *thio* and *seleno* substituted geometries, as shown in Table 3.3. The bond order difference for  $C_{RH}$ - $H_{RH}$  bond order between pre- transition state and transition state were 12%, 14%, 15%, respectively, for *oxo*, *thio* and *seleno* substituted geometries. Whereas, the bond order differences between the transition state and post-transition state were 44 %, 42 % and 42 %, respectively, for *oxo*, *thio* and *seleno* substituted geometries. This indicates that the nature of  $C_{RH}$ - $H_{RH}$  bond order was closer to pre transition state structure for all three geometries.

Table 3.3. The bond order profile for 2AX analogs along the reaction coordinates

Bond Order	2AX			2A6TP			2A6SP			2A6MP		
	CH	TS	SH	CH	TS	SH	CH	TS	SH	CH	TS	SH
Mo-Oeq	1.234	1.054	0.655	1.176	1.022	0.634	1.167	1.014	0.634	1.19	1.085	0.652
Oeq- $C_{RH}$	1.028	1.25	1.814	1.176	1.314	1.864	1.126	1.329	1.874	1.122	1.249	1.824
$C_{RH}$ - $H_{RH}$	0.844	0.657	0.003	0.845	0.634	0.003	0.845	0.623	0.002	0.827	0.701	0.002
$S_{M_0}$ - $H_{RH}$	0.083	0.301	1.049	0.077	0.324	1.048	0.077	0.336	1.046	0.088	0.238	1.05

Methyl substituted geometry (Eox-2A6MP) was shown to exhibit maximum ( $C_{RH}$ - $H_{RH}$ , 0.701) and minimum ( $S_{M_0}$ - $H_{RH}$ , 0.238) bond orders at the transition state. The % difference in bond order for  $C_{RH}$ - $H_{RH}$  bond at the pre- and post-transition state structure with respect to the transition state structure, respectively, were 8 % and 46 %. On the other hand, for  $S_{M_0}$ - $H_{RH}$  bond at the pre- and post-transition state structure from transition state structure were observed as 10% and 59 %, respectively. Relative to the chalcogen substituted geometries, the nature of  $C_{RH}$ - $H_{RH}$  and  $S_{M_0}$ - $H_{RH}$  bond orders at the transition state were maximum (46 %) and minimum (17%), respectively. This indicated that the  $C_{RH}$ - $H_{RH}$  bond breaking and  $S_{M_0}$ - $H_{RH}$  bond formation for 2A6MP were expected to take place after the transition state. Similar to the energy barrier, the bond order also revealed that the nature of the transition state structure for 2A6MP was product like compared to the other geometries that showed early transition state structure.

The bond order for Mo-Oeq and Oeq- $C_{RH}$  were decreased and increased, respectively, by 20 % and 19 %, as the  $H_{RH}$  migrated from the substrate ( $C_8$ ) to the active site terminal sulfido ( $S_{M_0}$ ). On the other hand, the bond order for Mo- $S_{M_0}$  and  $S_{M_0}$ - $H_{RH}$  were decreased and increased, respectively, by 18 % and 66 %, up on the migration of hydrogen. The percent bond order data for Mo-Oeq and Oeq- $C_{RH}$  bonds clearly confirmed that the breaking and formation of Mo-Oeq and Oeq- $C_{RH}$  bonds. This bond breaking and formation for Mo-Oeq and Oeq- $C_{RH}$  bonds, at the transition state was quantitatively similar. Unlike to these, the bond order change for Mo- $S_{M_0}$  and  $S_{M_0}$ - $H_{RH}$  as  $H_{RH}$  migrates from  $C_{RH}$  to  $S_{M_0}$  was found not to be similar (18 % and 66 %). This was because the bond order for Mo- $S_{M_0}$  was not bond breaking rather it corresponds to a partial loss of the double-bond character (bond lengthening).

In addition to the bond order, various bond distances which were expected to be involved in the bond formation and bond breaking while  $H_{RH}$  linearly migrates from  $C_{RH}$  ( $C_8$ ) of guanine to terminal sulfido ( $S_{M_0}$ ). The bond distances of  $C_{RH}$ - $H_{RH}$ , Oeq- $C_{RH}$ ,  $S_{M_0}$ - $H_{RH}$  and Mo-Oeq bonds for 2AX analogs at transition state were shown in Table 3.4. The substituent R (at  $C_6$ ) stands for O, S, Se and  $CH_3$  groups keeping the amine (at  $C_2$ ) constant for 2AX analog, as described in Figure 2.1.

Table 3.4. Transition state bond lengths and activation enthalpies for substituted 2AX analogs. The bond distances are expressed in angstrom (Å)

R	$C_{RH}$ - $H_{RH}$	Oeq- $C_{RH}$	$S_{M_0}$ - $H_{RH}$	Mo-Oeq	$\Delta H^\ddagger$ (kcal/mol)
O	1.22636	1.40185	1.86172	1.98429	13.869
S	1.24074	1.37523	1.83274	1.98945	21.753
Se	1.24836	1.37046	1.81862	1.99332	23.109
$CH_3$	1.19766	1.39728	1.96592	1.97015	0.212

As described in Table (3.4), the bond distance for  $C_{RH}$ - $H_{RH}$  at the transition state increased from *oxo* to *seleno*. The minimum  $C_{RH}$ - $H_{RH}$  bond distance (1.19766 Å) was observed for *methyl* substituted geometry at transition state. Maximum  $C_{RH}$ - $H_{RH}$  bond distance (1.24836 Å) with high activation enthalpy (23.109 kcal/mol) was observed for *seleno* substituted geometry. Whereas, minimum  $C_{RH}$ - $H_{RH}$  bond distance (1.19766 Å) with minimum activation enthalpy (0.212 kcal/mol) was shown for the methyl substituted geometry. The minimum  $C_{RH}$ - $H_{RH}$  bond distance at the transition state revealed that the hydrogen atom to be transferred from substrate carbon ( $C_{RH}$ ) to  $S_{M_0}$  was not far from its origin. This was due to the high negative charge development on the imidazole ring ( $C_8$ ) contributed from the methyl group through inductive effect, and this can induce strong carbon-hydrogen bond. The change in  $C_{RH}$ - $H_{RH}$  bond distances between the transition and

pre-transition state was computed as 1.99 %, 2.52 %, 2.35, and 1.24 %, respectively, for *oxo*, *thio*, *seleno* and *methyl* substituted geometries. These bond distance change suggested that the nature of  $C_{RH}-H_{RH}$  bond distances were reactant like for the first three geometries. Whereas, the later transition state structure was relatively product like. The variation in bond distances, bond orders, and energies observed at the transition state, in the presence of various substrates, indicated that the enzyme and reduction potential on the metal center was substrate dependent. The bond distances of Mo-O<sub>eq</sub> at CH, TS and SH were, respectively, 1.92289 Å, 1.98429 Å and 2.19682 Å. The bond distance was shown to lengthen by 0.27393 Å as H<sub>RH</sub> migrates from C<sub>RH</sub> to S<sub>Mo</sub>. On the contrary, the bond distance of Oeq-C<sub>RH</sub> at CH, TS and SH were, respectively, 1.49475 Å, 1.40185 Å and 1.26121 Å as hydrogen (H<sub>RH</sub>) migrated from C<sub>8</sub> of 2AX to the sulfido terminal (S<sub>Mo</sub>). The bond distance was shown to shorten by 0.23354 Å. The bond lengthening and shortening clearly confirmed that the breaking and formation of Mo-Oeq and Oeq-C<sub>RH</sub> bonds, respectively, as hydrogen migrated from the pre- transition state to post transition state. At the transition state, the Mo-Oeq bond distance considerably lengthens to 1.98429 Å by 0.05614 Å and the Oeq-C<sub>RH</sub> distance was longer than that of the post transition state, SH, by 0.2125 Å. Also the C<sub>RH</sub>-H<sub>RH</sub> bond distance lengthens to 1.22636 Å by 0.10579 Å, while the S<sub>Mo</sub>-H<sub>RH</sub> distance was much longer than that of post transition state by 0.5 Å. Relative to S<sub>Mo</sub>-H<sub>RH</sub> bond difference (0.5 Å) from post transition state, the bond distance for Oeq-C<sub>RH</sub> (0.2125 Å) from post transition state was found to be minimum. This geometrical feature suggests that it was the oxygen atom transfer that induced the hydrogen atom transfer from substrate carbon (C<sub>8</sub> of 2AX) to the sulfido terminal (S<sub>Mo</sub>). The shorter bond distance shown for Oeq-C<sub>RH</sub> bond might play a role for the transfer of two electrons from substrate to the active site. The C<sub>RH</sub>-H<sub>RH</sub> bond distance was elongated from 1.12057 Å to 2.94377 Å unlike that of the S<sub>Mo</sub>-H<sub>RH</sub> bond which was decreased from 2.36172 Å to 1.36172 Å as H<sub>RH</sub> migrated from C<sub>8</sub> of guanine to S<sub>Mo</sub>. At the transition state, the C<sub>RH</sub>-H<sub>RH</sub> bond distance (1.22636 Å) was lower than S<sub>Mo</sub>-H<sub>RH</sub> bond distance (1.86172 Å). This clearly revealed that the transition state structure was reactant like. In summary, the results obtained from bond order and bond distance revealed the presence of an early transition state for *oxo*, *thio* and *seleno* substituted geometries, a product like transition state for the methyl substituted geometry, a substrate dependence of xanthine oxidase activity, and an oxo transfer that induced a hydrogen transfer.

In addition to the bond distances, the wave functions of the geometries at CH, TS and SH were shown in The distribution of the electron densities around chalcogen were found to increase from *oxo* to *seleno* replacement and decrease at C<sub>8</sub>, as shown in Figure 3.4. This was due to the polarization power of the electron cloud by chalcogens. In addition, the percent molybdenum contribution for *oxo*, *thio* and *seleno* substituted geometries, respectively, were 24.14 %, 21.18% and 20.24%. This confirmed that the reduction potential of the metal was substrate dependant.

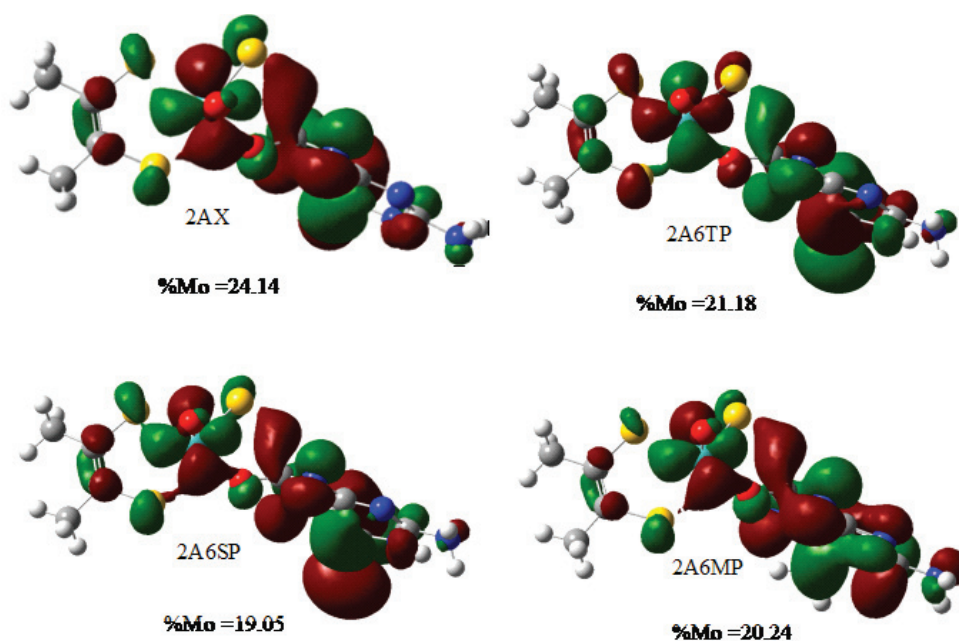


Figure 3.4. The wave function of the HOMO's obtained from the transition state structure for the *oxo*-2AX (*upper left*), *thio*-2A6TP (*upper right*), *seleno*-2A6SP (*lower left*), and *methyl*-2A6MP (*lower right*) substituted geometries

On the other hand, the methyl substituted geometry was found to have no electron density around the substituent (CH<sub>3</sub>), rather the electron densities were found more concentrated on the interaction site (C<sub>8</sub>) carbon. The transfer of (electron donation) from methyl through inductive effect was the main reason for the maximum electron density on the interaction

carbon. This was found to be the reason for the reaction of 2A6MP to be fast and thermodynamically more stable.

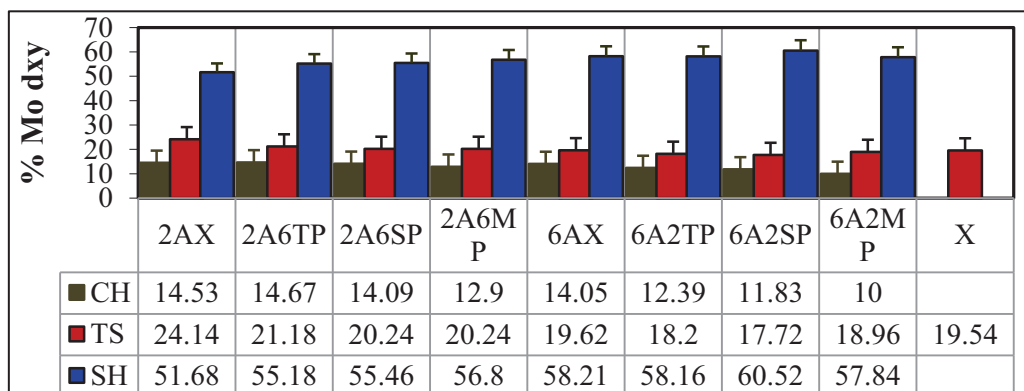


Figure 3.5 A plot for percent molybdenum contribution difference at homo relative to the transition state

The abbreviation X stands for the physiological substrate, xanthine. The percent molybdenum contribution for xanthine was obtained from reference [Haftom, 2011].

The percent  $\text{Mod}_{xy}$  contribution of selected model substrates at the transition state was similar to that of physiological substrate, xanthine (X), as shown in Figure (3.5). Therefore, the spin density distribution at the transition state was almost similar. However, the rate of electron transfer was completely dependent on the nature of the substituents on the aromatic ring.

#### 4. Conclusion

In the present work a DFT method and B3LYP level of theory has been employed for electronic structure calculation and quantum mechanical description of the transition state structure of guanine derivatives bound to xanthine oxidase enzyme.

The geometry optimization and frequency calculation has been performed on 2AX analogs bound to the truncated form of the reductive half-reaction active site of xanthine oxidase in order to model and characterize the transition state. The polarizability and inductive effect of the substituent, respectively, was shown to decrease and increase the reactivity of the substrate to be hydroxylated. The purine derivatives with substituents that created inductive effect was shown to stabilize the transition state structure and allowed the ease of conversion to respective products better than the remaining purine derivatives. Such types of substrates were expected to increase the rate of formation of urate crystals in the kidney. Therefore, they couldn't serve as enzyme inhibitor. On the other hand, polarizable substituent like *seleno* destabilizes the transition state since they were proposed to create inductive effect and resonance stabilization. Among eight model substrates used in this work, the 2A6SP and 2A6TP was found as a potential xanthine oxidase inhibitor. Following this, we concluded that purine derivatives that are substituted with polarizable substituent could serve as XO inhibitor. The reactivity of chalcogen substituted geometries decreased down a group. Therefore, it was concluded that the *oxo* substituted geometries were twofold more reactive than the *thio* and *seleno* substituted geometries. Relative to chalcogen substituted geometries; the methyl substituted geometry was more reactive and fast. Hence, the inductive effect was shown to play large effect in charge stabilization by creating resonance stabilization.

The total electronic energy and vibrational frequency analysis revealed that the reactions catalyzed by xanthine oxidase enzyme were kinetically and thermodynamically favorable. The natures of the transition state structure were characterized using bond order, bond distance, frequency value and total electronic energy. The natures of the transition state structures for chalcogen replaced geometries were found to be early transition state. On the other hand, the transition state structure for methyl substituted geometry was found to be product like. During the progress of the reaction, the reduction potential of the metal was shown to vary from substrate to substrate. As a result, it was concluded that the catalysis of xanthine oxidase was entirely substrate dependent.

#### 5. Competing Interests

The authors declare that they have no competing interests.

#### 6. Authors' Contributions

All authors had significant intellectual contribution towards the design of the study, data collection and analysis and write-up of the manuscript. Mamaru Betew conducted the experiment, analyzed the data, wrote the draft manuscript followed it up through revisions and Yilkal Bezie took part actively reviewed and edited the draft manuscript, provided comments and suggestions and prepared it for publication as per the guide line.

## References

- Alfaro, F. J., & Jones, P. J. (2008). studies on the mechanism of aldehyde oxidase and xanthine oxidase. *J. Org. Chem.*, *73*, 9469–9472. <https://doi.org/10.1021/jo801053u>
- Ayala, P. Y., & Schlegel, H. B. (1997). A combined method for determining reaction paths, minima, and transition state geometries. *J. Chem. Phys.*, *107*, 375-384. <https://doi.org/10.1063/1.474398>
- Bayse, A. C. (2009). Density-functional theory models of xanthine oxidoreductase activity: comparison of substrate tautomerization and protonation. *Dalton Trans.*, 2306–2314. <https://doi.org/10.1039/b821878a>
- Berry, E. C., & Hare, M. J. (2004). Xanthine oxidoreductase and cardiovascular disease: molecular mechanism and pathophysiological implications. *J. physio.*, *555*, 589-606. <https://doi.org/10.1113/jphysiol.2003.055913>
- Bjelaković, G., Stojanović, I., Bjelaković, G. B., Pavlović, D., Kocić, G., & Milić, D., A. (2002). Competitive inhibitors of enzymes and their therapeutic application. *Med. Bio.*, *9*, 201–206.
- Cao, H., Pauff, J., & Hille, R. (2011). Substrate orientation and the origin of catalytic power in xanthine oxidase. *Indian. J. chem.*, *50*, 355-362.
- Choi, Y. E., Stockert, A. L., Leimkuhler, S., & Hille, R. (2004). Studies on the mechanism of action of xanthine oxidase. *J. Inor. Biochem.*, *98*, 841–848. <https://doi.org/10.1016/j.jinorgbio.2003.11.010>
- Chowdhry, B. Z., Robert, R., Stephen, S., & Dines, T. J. (2007). Computational chemistry using modern electronic structure methods. *J. Chem.Edu.*, *84*, 1364-1370. <https://doi.org/10.1021/ed084p1364>
- Civcir, U. P. (2001). A theoretical study of tautomerism of 6-thiopurine in the gas and aqueous phases using AM1 and PM3. *J. Mol. Stru.*, *535*, 121-129. [https://doi.org/10.1016/S0166-1280\(00\)00586-8](https://doi.org/10.1016/S0166-1280(00)00586-8)
- Contreras, J. G., Lorena, A., & Gerli, L. A. (2008). Conformational preference in 4,6-dimethyl-1,3-thioxanej. *Chil. Chem. Soc.*, *53*, 1400-1403.
- Dinesh, S., Shikha, G., Bhavana, G., Nidhi, S., & Dileep, S. (2010). Biological activities of purine analogs. *J. Pharm. Scient. Innovation.*, *1*, 29-34.
- Enroth, C., Bryan, T. B., Okamoto, K., Nishinoi, T., Nishino, T., & Pai, F. E. (2000). Crystal structures of bovine milk xanthine dehydrogenase and xanthine oxidase: structure-based mechanism of conversion. *Proc. Nat. Acad. Sci.*, *97*, 10723–10728. <https://doi.org/10.1073/pnas.97.20.10723>
- Foresman, J. B. (1993). Exploring chemistry with electronic structure methods. 2<sup>nd</sup> edition. *Gaussian, Inc. Pittsburgh, Pennsylvania*. 5-20.
- Gaussian 03 versions 6.0 (Gaussian, Inc., Pittsburgh, PA) manual in the help menu F1 option. Haftom G., (2011). Theoretical studies on reaction mechanism of xanthine oxidoreductase enzyme bound to hetrocyclic substrates xanthine, hypoxanthine and allopurinol. *MSc. Thesis*. Arba Minch University, Ethiopia.
- Hille, R. (2006). Structure and function of xanthine oxidoreductase. *Eur. J. Inorg. Chem.* *10*, 1913–1926. <https://doi.org/10.1002/ejic.200600087>
- Hille, R., Kim, H. J., & Hemann, C. (1993). Reductive half-reaction of xanthine oxidase: mechanistic role of the species giving rise to the “rapid type 1 molybdenum (v) electron paramagnetic resonance signal. *Biochem.*, *32*, 3973-3980. <https://doi.org/10.1021/bi00066a018>
- Ilich, P., & Hille, R. (1999). Mechanism of formamide hydroxylation catalyzed by a molybdenum dithiolene complex: a model for xanthine oxidase reactivity. *J. Phys. Chem. B*, *103*, 5406-5412. <https://doi.org/10.1021/jp9904825>
- Kalra, S., Jena, G., Tikoo, K., & Mukhopadhyay, K. A. (2007). Preferential inhibition of xanthine oxidase by 2-amino-6-hydroxy-8-mercaptapurine and 2-amino-6-purinethiol. *Bio.Medic. Chem.*, *8*, 1471-2091.
- Kim, Y., Jang, H., Y., Cho, H., & Hwang, S. (2010). Tautomers and acid dissociation constants of 6-selenoguanine from density functional theoretical calculations. *Bull. Korean Chem. Soc.*, *31*, 3013-3016. <https://doi.org/10.5012/bkcs.2010.31.10.3013>
- Leimkuhler, S., Stockert, A. L., Igarashi, K., Nishino, T., & Hille, R. (2004). The role of active site glutamate residues in catalysis of rhodobacter capsulatus xanthine dehydrogenase. *J. Biol. Chem.*, *279*, 40437-40444. <https://doi.org/10.1074/jbc.M405778200>
- Martz, E. (2002). Protein explorer: easy yet powerful macromolecular visualization, *Trends in Biochem. Sci.*, *27*, 107-109. [https://doi.org/10.1016/S0968-0004\(01\)02008-4](https://doi.org/10.1016/S0968-0004(01)02008-4)
- Mohamed, A., Al-Omar, M. A., El-Subbagh, H. I., Beedham, C., & Smith, J. (2005). Role of molybdenum hydroxylases

- in diseases. *Saudi Pharm. J.*, *13*, 1 - 13.
- Nishino, T., Okamoto, K., Eger, T. B., Pai, F. E., & Nishino, T. (2008). Mammalian xanthine oxidoreductase mechanism of transition from xanthine dehydrogenase to xanthine oxidase. *Fed. Euro. Bio. Sci. Journal.*, *275*, 3278–3289. <https://doi.org/10.1111/j.1742-4658.2008.06489.x>
- Okamoto, K., Matsumoto, K., Hille, R., Eger, B. T., Pai, E. F., & Nishino, T. (2004). The crystal structure of xanthine oxidoreductase during catalysis: implications for reaction mechanism and enzyme inhibition. *Proc. Nat. Acad. Sci.*, *101*, 7931–7936. <https://doi.org/10.1073/pnas.0400973101>
- Pauff, J. M., Cao, H., & Hille, R. (2008). Substrate orientation and catalysis at the molybdenum site in xanthine oxidase: crystal structures in complex with xanthine and lumazine. *J. Biol. Chem.*, *284*, 1–17.
- Pauff, J. M., Cao, H., & Hille, R. (2009). Substrate orientation and catalysis at the molybdenum site in xanthine oxidase: crystal structures pictures in complex with xanthine and lumazine. *J. Biol. Chem.*, *284*, 8760–8767. <https://doi.org/10.1074/jbc.M804517200>
- Pauff, J. M., Zhang, J., Bell, C. E., & Hille, R. (2007). Substrate orientation in xanthine oxidase, crystal structure with 2-hydroxy-6-methylpurine. *J. Biol. Chem.*, *282*, 1–16.
- Romao, J. M. (2009). Molybdenum and tungsten enzymes: a crystallographic and mechanistic overview. *Dalton Trans.*, *21*, 4053–4068. <https://doi.org/10.1039/b821108f>
- Schramm, V. L. (1998). Enzymatic transition states and transition state analog design. *Annu. Rev. Biochem.*, *67*, 693–720. <https://doi.org/10.1146/annurev.biochem.67.1.693>
- Schwarz, G., & Mendel, R. R. (2006). Molybdenum cofactor biosynthesis and molybdenum enzymes. *Annu. Rev. Plant Biol.*, *57*, 623–647. <https://doi.org/10.1146/annurev.arplant.57.032905.105437>
- Senthilkumar, L., & Kolandaivel, P. (2003). Post hartree–fock and density functional theory studies on tautomerism of 6-thioxanthine in gas phase and in solution. *J. Mol. Stru.*, *638*, 69–78. [https://doi.org/10.1016/S0166-1280\(03\)00546-3](https://doi.org/10.1016/S0166-1280(03)00546-3)
- Voityuk, A. A., Albert, K., Romao, M. J., Huber, R., & Roesch, N. (1998). Substrate oxidation in the active site of xanthine oxidase and related enzymes. a model density functional study. *Inorg. Chem.*, *37*, 176–180. <https://doi.org/10.1021/ic9707570>
- Xia, M., Dempski, R., & Hille, R. (1999). The reductive half-reaction of xanthine oxidase. Reaction with aldehyde substrates and identification of the catalytically labile oxygen. *J. Biol. Chem.*, *274*, 3323–3330. <https://doi.org/10.1074/jbc.274.6.3323>
- Zhang, X. H., & Wu, Y. D. (2005). A theoretical study on the mechanism of the reductive half-Reaction of xanthine oxidase. *Inorg. Chem.*, *44*, 1466–147. <https://doi.org/10.1021/ic0487301>

## Copyrights

Copyright for this article is retained by the author(s), with first publication rights granted to the journal.

This is an open-access article distributed under the terms and conditions of the Creative Commons Attribution license (<http://creativecommons.org/licenses/by/4.0/>).

## Derivatives of 2-Aminopyridines as Inhibitors of Multidrug Resistant *Staphylococcus Aureus* Strains

Iniobong E. Ante<sup>1</sup>, Sherifat A Aboaba<sup>1</sup>, Hina Siddiqui<sup>2</sup>, Muhammad A Bashir<sup>2</sup>, Muhammad I Choudhary<sup>2</sup>

<sup>1</sup>Department of Chemistry, University of Ibadan, Ibadan, Nigeria

<sup>2</sup>H.E.J Research Institute of Chemistry, International Center for Chemical and Biological Sciences, University of Karachi, Karachi-75270, Pakistan

Correspondence: Sherifat A. Aboaba, Department of Chemistry, University of Ibadan, Ibadan, Nigeria.  
E-mail: saboaba@gmail.com

Received: December 27, 2017 Accepted: January 26, 2018 Online Published: January 28, 2018

doi:10.5539/ijc.v10n1p153

URL: <https://doi.org/10.5539/ijc.v10n1p153>

### Abstract

A new series of 2-aminopyridine derivatives were synthesised. N-acylation of 2-amino-3-chloro-5-(trifluoromethyl) pyridine and 2-amino-5-(trifluoromethyl) pyridine with series of acid chlorides afforded a total of fourteen (14) amide compounds. The structures of the new compounds have been established by their IR, NMR and mass spectra data. All the compounds were tested for their activity against four (4) multi-drug resistant (MDR) bacteria *Staphylococcus aureus* strains using microplate alamar blue assay. The MDR-*Staphylococcus aureus* strains employed for this study were Epidemic Methicilin Resistant *Staphylococcus aureus* (EMRSA-17), Methicilin Resistant *Staphylococcus aureus* (MRSA-252), Epidemic Methicilin Resistant *Staphylococcus aureus* (EMRSA-16) and Pakistani Drug resistant clinical isolate of *Staphylococcus aureus* (PRSA). Other bacteria strains also used include *Escherichia coli* (ATCC 2592), *Shigella flexneri* (ATCC 12022), *Staphylococcus aureus* (NCTC 6571) and *Pseudomonas aeruginosa* (NCTC 10662). The synthesised compounds exhibited very good activity against the four MDR-*Staphylococcus aureus* strains of which most of the compounds showed higher potencies for inhibiting the growth of the strains than vancomycin, the standard drug employed. The compounds reported here may serve as the starting point for the design and development of MDR-S.aureus inhibitors as antibacterial agents.

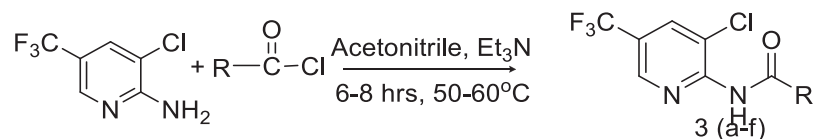
**Keywords:** N-acylation, Acid chlorides, 2, 4-difluoro-N-(5-(trifluoromethyl) pyridin-2-yl) benzamide, *Staphylococcus aureus*, Antibacterial

### 1. Introduction

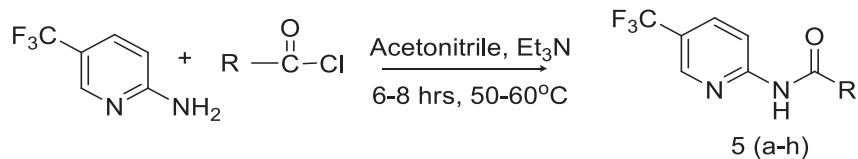
Methicilin Resistant *Staphylococcus aureus* (MRSA) infections are a major public health problem producing a large number of deaths every year worldwide (NNIS, 2004). These important nosocomial and community-acquired pathogen has developed resistance to various antibiotics (Chen et al., 2010).

Pyridine nucleus plays central role in the development of different medical agents such as antimicrobial (Remuzon et al., 1992), antiviral (Tabarini et al., 2006), anticancer (Cai et al., 2003), antifungal (Patrick & Kinsman, 1996), antioxidant (Feng & SSning, 2009), antidiabetic (Rajesh & Mukul, 2007), antitubercular and analgesic (Kasabe & Kasabe 2010). Aminopyridine and its derivatives are key intermediates for the synthesis of important pharmaceutical and agricultural products. Aminopyridine is used in the synthesis of antihistamines including methapyilene hydrochloride and pyrilamine maleate (Hettler, 1946), synthesis of aldipem an anxiolytic (Dimsdale, 1988), preparation of the urinary tract analgesic phenazopyridine hydrochloride (Shreve, 1943), nevirapine a drug for treatment of AIDS (Merluzzi, 1990) and an antibacterial medicine, cephapirin sodium (Craet, et al., 1973).

MRSA being resistant to many antibiotics and the pyridine ring system reported as promising potential antibacterial agents, we became interested in the synthesis of 2-aminopyridine derivatives by N-acylation which is scarce in literature giving rise to amide analogues. 2-amino-3-chloro-5-(trifluoromethyl) pyridine and 2-amino-5-(trifluoromethyl) pyridine with selected acid chlorides in water reflux with acetonitrile and triethylamine (scheme 1 and scheme 2) gave the profile of the aminopyridine derivatives studied (Table 1).



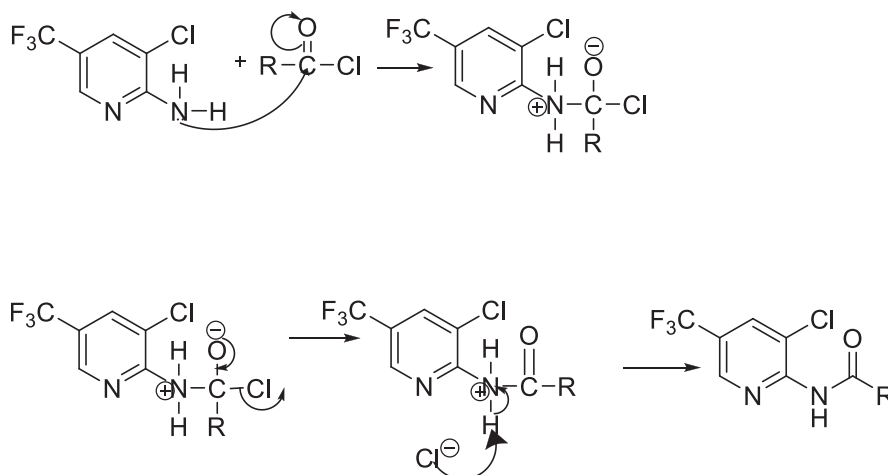
Scheme 1. Acylation of 2-amino-3-chloro-5-(trifluoromethyl) pyridine with acid chlorides



Scheme 2. Acylation of 2-amino-5-(trifluoromethyl) pyridine with acid chlorides

## 2. Results and Discussion

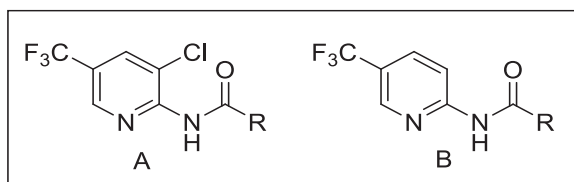
The *N*-acylation of the selected aminopyridines with series of acid chlorides to give the afore mentioned amides analogues followed the  $\text{S}_{\text{N}}2$  mechanism pathway (scheme 3) in which the nucleophile of the amino group attacks the carbonyl of the acid chloride to afford the expected amides using the polar aprotic solvent acetonitrile which prevents solvation and excess by-products, enhanced the yields of the amides.



Scheme 3. General Mechanism of the synthetic reaction

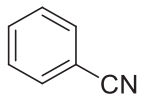
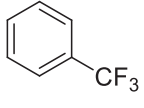
Scheme 1 and scheme 2 reactions gave six (6) and eight (8) analogues which were coded as **3a-f** and **5a-h** respectively resulting in a total of fourteen (14) compounds. All the amides were prepared under mild conditions and the obtained products were easily purified by column chromatography on silica gel.

Table 1. Structural profile of the aminopyridine derivatives studied



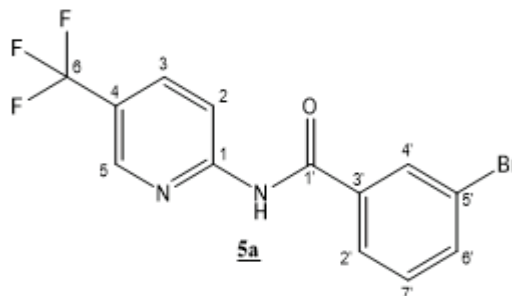
COMPOUNDS	TYPE	R
3a	A	
3b	A	
3c	A	
3d	A	
3e	A	
3f	A	
5a	B	
5b	B	
5c	B	
5d	B	
5e	B	
5f	B	



<b>5g</b>	B	
<b>5h</b>	B	

Structure elucidation of representative member (compound 5a)

The identity of the final synthesised products was determined by  $^1\text{H-NMR}$  and Infra Red (IR) spectroscopy and Mass Spectrometry (MS). Structure elucidation of a representative member (compound 5a) is presented below;



The  $^1\text{H-NMR}$  was performed in a 400 MHz spectrometer and deuterated methanol MeOD was used as solvent. H5 was observed as a broad singlet and resonated at  $\delta_{\text{H}}$  8.45 (1H, d,  $J_{2,5}=9.6$  Hz). The signal at  $\delta_{\text{H}}$  8.15 was due to H4' being coupled to H6' (1H, d,  $J_{4',6'}=2$  Hz). H6' resonated as a doublet of doublet at  $\delta_{\text{H}}$  8.12 ( $J_{6',4'}=2$  Hz,  $J_{6',7'}=8$  Hz). H2' resonated as a doublet at  $\delta_{\text{H}}$  7.97 being *ortho* coupled to H7' (1H, d,  $J_{2,7'}=7.6$  Hz). H3 resonated at  $\delta_{\text{H}}$  7.79 as a doublet coupled to H5 (1H, d,  $J_{3,5}=9.6$  Hz) and H7' was found coupled with both 2' and 6' and appeared as a doublet of a doublet at  $\delta_{\text{H}}$  7.48 ( $J_{7,2'}=7.6$  Hz,  $J_{7,6'}=8$  Hz);  $^{13}\text{C-NMR}$ :  $\delta$  165.72 (C=O), 156.03 (C-1), 146.3(C-5), 137.07 (C-3'), 136.5 (C-6'), 135.97 (C-3), 131.7 (C-4'), 131.4 (C-7'), 127.7 (C-2', C-6) 122.9 (C-5'), 114.6 (C-2); EI-MS  $m/z$  (rel. abund. %): 346.8 [ $\text{M}^++2$ ] (2), 343.8 [ $\text{M}^+$ ] (41), 314.8 (67), 235.9 (5), 184.7 (97), 182.8 (100), 154.8 (83), 103.9 (31), 82.8 (26), 75.9 (90), 57 (77);  $\nu_{\text{max}}$ : 3433.1, 3234.4, 31933.9, 3107.1, 2923.9, 2854.5, 1689.5, 1593.1, 1240.

The synthesised compounds were tested for their activity against four multi-Drug resistant (MDR) bacteria *S. aureus* strains and four other bacterial strains. The MDR- *S. aureus* strains employed for this study were Epidermic Methicilin Resistant *Staphylococcus aureus* (EMRSA)-17; methicilin resistant *Staphylococcus aureus* (MRSA)-252, Epidermic methicilin resistant *Staphylococcus aureus* (EMRSA)-16 and Pakistani drug resistant clinical isolate of *S. aureus* (PRSA) and the bacterial strains used were *E.coli* (ATCC 2592), *S. flexanari* (ATCC 12022), *S.aureus* (NCTC 6571) and *P. aeruginosa* (NCTC 10662) Table 2.

Table 2. Bioactivity of the compounds

BACTERIAL STRAINS	SYNTHESISED COMPOUNDS														CONTROL
	3a	3b	3c	3d	3e	3f	5a	5b	5c	5d	5e	5f	5g	5h	Vancomycin (20 $\mu\text{g}/\text{ml}$ )
EMRSA-17	35.9	36.6	26.8	28.4	38.9	39.4	24.5	13.0	12.1	-	36.1	41.4	27.4	43.1	20.7
MRSA-252	16.7	9.6	8.9	-	20.2	33.6	-	-	-	-	24.7	18.3	18.0	15.0	18.6
EMRSA-16	28.4	29.0	21.4	11.6	31.7	-	-	-	-	-	32.5	31.1	26.5	27.5	23.7
PRSA	28.0	29.5	22.7	28.0	38.0	28.2	21.8	21.8	-	-	29.6	37.4	20.1	33.4	40.4
															Oflaxacin (50 $\mu\text{g}/\text{ml}$ )
<i>E.coli</i>	-	5.7	5.2	-	-	3.8	1.3	1.9	-	4.3	1.8	3.6	6.5	4.5	87.7
<i>S. flexanari</i>	-	15.6	3.7	-	-	8.3	-	3.0	-	0.8	14.9	15.3	10.0	5.6	89.9
<i>S. aureus</i>	-	4.9	2.2	-	-	1.5	-	-	-	1.6	-	-	-	-	91.4
<i>P. aeruginosa</i>	12.1	-	-	-	15.0	-	-	-	-	1.5	-	-	-	-	84.4

The antibacterial (EMRSA-17) inhibitory activity invitro Fig.1 afforded a two fold increase in the activity of the compounds against EMRSA-17 was observed with respect to vancomycin (20.7  $\mu\text{g}/\text{mL}$ ) the standard, when a fluorine compound was at the *meta* position C5' as in **5f** (41.4  $\mu\text{g}/\text{mL}$ ), and **3e** (38.9  $\mu\text{g}/\text{mL}$ ).

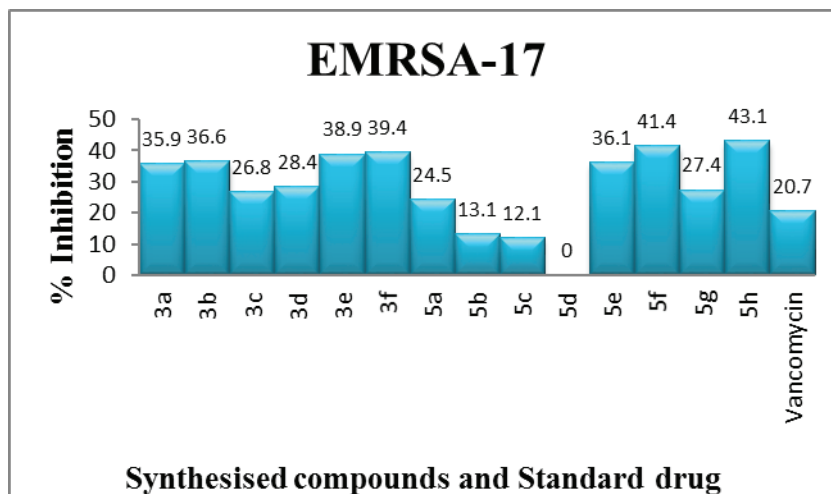


Figure 1. Inhibitory Activity against EMRSA-17

A slight decrease in activity was observed when in addition to the fluorine at the *meta* position another fluorine was at the *ortho* position C6' as observed in **3a** (35.9  $\mu\text{g}/\text{mL}$ ). An electron withdrawing substituent cyano (CN) at the *para* position C6' showed more increased activity when position C2 had chlorine as compared with **3b** (36.6  $\mu\text{g}/\text{mL}$ ) than when position C2 had no substituent as seen in **5g** (27.4  $\mu\text{g}/\text{mL}$ ). The absence of the benzylic ring system substituted with the presence of an electron donating alkyl chain was observed to increase the activity as seen in **3f** (39.4  $\mu\text{g}/\text{mL}$ ), when the end of the alkyl chain was replaced with benzene; an electron withdrawing group as against the methyl that was an electron donating group, a total loss of activity was observed as in **5d**.

The synthesised compounds were tested for their antibacterial (EMRSA-16) activity Fig.2. Significant level of activity was observed for the compounds with respect to the standard vancomycin (23.7  $\mu\text{g}/\text{mL}$ ) when the substituent at the *meta* position C5' was a halogen substituent fluorine as observed in **3a** (28.4  $\mu\text{g}/\text{mL}$ ), **3e** (31.7  $\mu\text{g}/\text{mL}$ ) and **5f** (31.1  $\mu\text{g}/\text{mL}$ ), though a total loss of activity was observed when the *meta* position C5' contained another halogen bromine and chlorine as in **5a** and **5b** respectively.

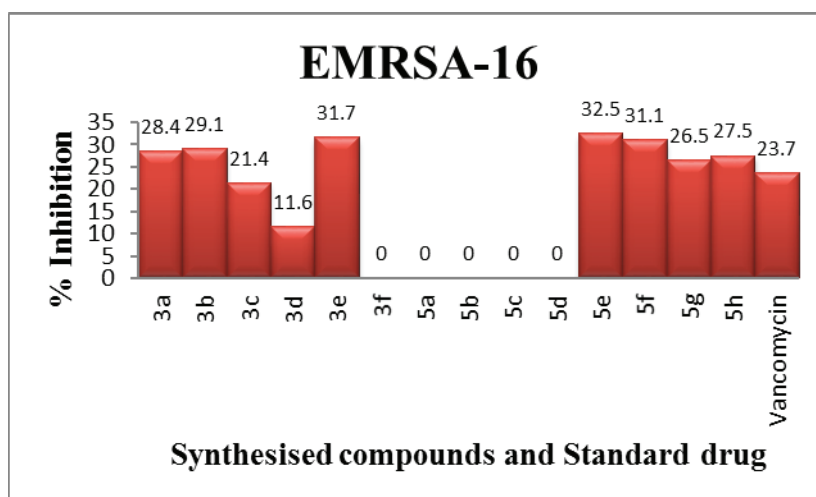


Figure 2. Inhibitory Activity against EMRSA-16

Moreso, with trifluoromethyl at position C6', significant activity was recorded similar to **3c** (21.4  $\mu\text{g}/\text{mL}$ ) and **5h** (27.5  $\mu\text{g}/\text{mL}$ ). This could have been due to the electron withdrawing ability of the halogen, fluorine present. When position C6' was substituted with yet another electron withdrawing group cyano (CN), same trend of significant activity was observed as in **3b** (29.1  $\mu\text{g}/\text{mL}$ ) and **5g** (26.5  $\mu\text{g}/\text{mL}$ ). The highest activity against EMRSA-16 was recorded for, when chlorine was the substituent at the *para* position C6' as reported in **5e** (32.5  $\mu\text{g}/\text{mL}$ ), the second chlorine atom at the *ortho* position C2' might have contributed to its activity because a halogen, iodine at the C6' position resulted to a total

loss in activity as in **5c**. When there was no substituent at both *meta* and *para* positions C5' and C6', a total loss of activity was observed compared to **3f** and **5d**.

Antibacterial (MRSA-252) inhibitory activity was performed Fig. 3. The highest activity against MRSA-252 was recorded when an alkyl chain was attached next to the carbonyl similar to **3f** (33.6  $\mu\text{g/mL}$ ) with respect to the standard, vancomycin (18.6  $\mu\text{g/mL}$ ).

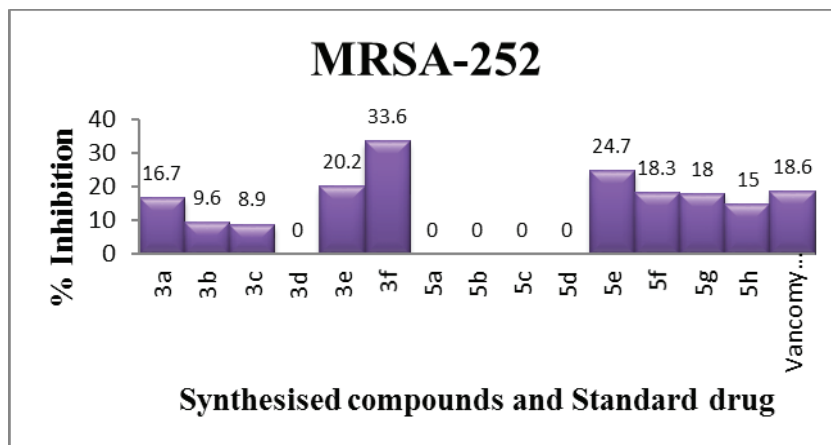


Figure 3. Inhibitory Activity against MRSA-252

The free rotation of the single bonds and the electron donating properties of the methyl and methine could have contributed. The next significant activity observed against MRSA-252 was when the *para* position C6' had chlorine and *meta* position C5' had fluorine substituents as in **5e** (24.7  $\mu\text{g/mL}$ ), **3e** (20.2  $\mu\text{g/mL}$ ), **5f** (18.3  $\mu\text{g/mL}$ ) and **3a** (16.7  $\mu\text{g/mL}$ ) respectively. Again, a total loss of activity was also observed for MRSA-252 strain when there was no substituent at the *para* position C6' as seen in **5a**, **5b**, **5c** and **5d** with exception of **5f** which had fluorine at the *meta* position. A new trend of total loss of activity was observed for this strain of MDR *S.aureus* when position C6' substituent was a nitro group ( $\text{NO}_2$ ) as in **3d**. This could be due to the electron donating effect of the lone pairs of electrons present in both nitrogen and oxygen; probably the mesomeric effect of both nitrogen and oxygen superseded its individual inductive effect for this particular strain. There was moderate activity observed when cyano and trifluoromethyl were at the *para* position C6' (18  $\mu\text{g/mL}$ ) and **5h** (15  $\mu\text{g/mL}$ ), a decrease in activity by half in addition to the *para* position still maintaining the cyano and trifluoromethyl was observed when chlorine was at position C2 similar to **3b** (9.6  $\mu\text{g/mL}$ ) and **3c** (8.9  $\mu\text{g/mL}$ ) respectively.

The antibacterial activity against PRSA Fig. 4 was observed to follow trend as the previous MDR-*S.aureus* strain afore mentioned.

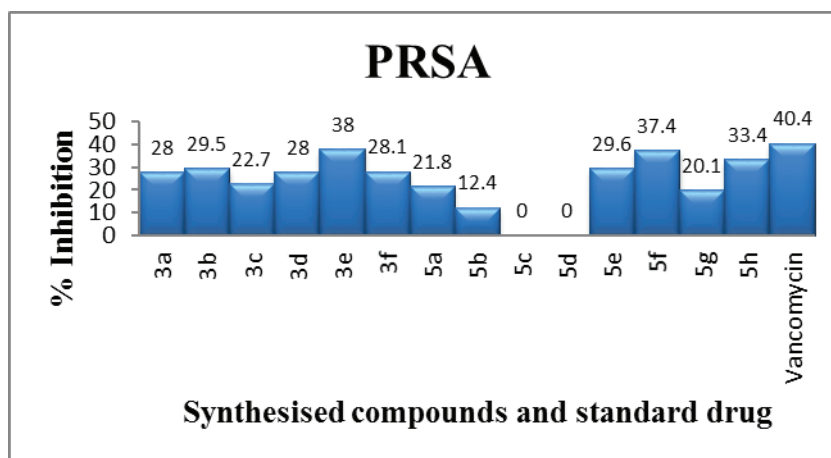


Figure 4. Inhibitory Activity against PRSA

The most significant activity with respect to the standard, vancomycin (40.4  $\mu\text{g/mL}$ ) was noticed when the *meta* position C5' had fluorine similar to **3e** (38.0  $\mu\text{g/mL}$ ) and **5f** (37.4  $\mu\text{g/mL}$ ) followed by when the substituent at the *para* position C6' was trifluoromethyl and chlorine as in **5h** (33.4  $\mu\text{g/mL}$ ) and **5e** (29.6  $\mu\text{g/mL}$ ) respectively.

### 3. Conclusion

It could be inferred that the electron withdrawing group at the *meta* position C5' with reference to fluorine especially and *para* position C6' with reference to the cyano and trifluoromethyl have a significant role and could be the key factor for the activities observed for the synthesised compounds against these MDR-*S.aureus* strains.

### 4. Experimental

#### 4.1 General

Chemicals were supplied by Aldrich and Sigma. NMR spectra were recorded on Avance Bruker 300, 400, 500, 600 and cryprobes FT-NMR spectrometers. Chemical shifts are reported in parts per million and were recorded in deuterated methanol, Acetone and dichloromethane accordingly with tetramethylsilane as the internal standard. NMR multiplicities are indicated by the symbols: s (singlet), d (doublet), t (triplet), q (quartet), and m (multiplet). IR spectra were recorded on a shimadzu 8900 FT-IR spectrometer using KBr discs and pellets. Mass fragmentations were recorded using MAT 312 mass spectrometer.

#### 4.2 N-Acylation

To Acetonitrile (10 ml), the respective aminopyridines (1mmol) and triethylamine (0.101 ml, 1mmol) were added. The mixture was placed on a hot plate magnetic stirrer and stirred for 20 min under water reflux before the corresponding acid chlorides (1mmol) were added. The mixture was inspected by TLC (Hexane-EtoAc). After being stirred for a further 4-6 hrs at 40-60 °C, it was concentrated to dryness. The residues were purified by silica gel gradient column chromatography (Hexane-EtoAc, 85:15) to afford the desired compounds (overall yield 65-85%). Their identity was confirmed by NMR and IR spectroscopy and MS spectrometry.

**N-(3-chloro-5-(trifluoromethyl) pyridin-2-yl)-3, 4-difluorobenzamide (3a).** Yield: ( 73%); m.p. 78-79 °C; IR: 3433 (N-H), 1670 (C=O); <sup>1</sup>H-NMR (MeOD): δ 8.72 (1H, brS, H5), 8.35 (1H, d, J=1.2Hz, H3), 7.95 (1H, d, J= 2Hz, H4'), 7.87 (1H, dd, J= 2, 8.8 Hz H2'), 7.45 (1H, d, J= 8.8Hz H7'); <sup>13</sup>C-NMR: δ 166.32 (C=O), 156.23 (C-1), 152.9 (C-6'), 152.7 (C-5'), 144.9 (C-5), 137.6 (C-3), 132.09 (C-3'), 126.6 (C-2'), 127.04 (C-2), 126.02 (C-4) 122.4 (C-6), 118.97 (C-4'), 118.74 (C-7'); MS: (m/z) 336 ([M+H]<sup>+</sup>), C<sub>13</sub>H<sub>6</sub>ClF<sub>5</sub>N<sub>2</sub>O (336.01)

**N-(3-chloro-5-(trifluoromethyl) pyridin-2-yl)-4-cyanobenzamide (3b).** Yield: (67%); m.p. 141-142 °C; IR: cm<sup>-1</sup> 3440.8 (N-H), 1676 (C=O). <sup>1</sup>H-NMR (MeOD): δ 8.73 (1H, brS, H5), 8.37 (1H, brS, H3), 8.13 (2H, d, J= 8Hz, H5', H7') 7.93 (2H, d, J= 8Hz, H2', H4'); MS: (m/z) 325 ([M+H]<sup>+</sup>), C<sub>14</sub>H<sub>7</sub>ClF<sub>3</sub>N<sub>3</sub>O (325.02)

**N-(3-chloro-5-(trifluoromethyl) pyridin-2-yl) 4(trifluoromethyl) benzamide (3c).** Yield: (71%); m.p. 80-81 °C; IR: cm<sup>-1</sup> 3433.1 (N-H), 1679.9 (C=O). <sup>1</sup>H-NMR (MeOD): δ 8.73 (1H, brS, H5), 8.37 (1H, d, J= 1.5Hz, H3), 8.17 (2H, d, J= 8.4 Hz, H2', H4'), 7.87 (2H, d, J= 8.4Hz, H5', H7'); <sup>13</sup>C-NMR: δ 165.26 (C=O), 153 (C-1), 144.66 (C-5), 138.17 (C-3'), 137 (C-3), 130.56 (C-6'), 129.84 (C-5', C-7'), 127.71 (C-2), 126.47 (C-2', C-4'); MS: (m/z) 368 ([M+H]<sup>+</sup>), C<sub>14</sub>H<sub>7</sub>ClF<sub>6</sub>N<sub>2</sub>O (368.02).

**N-(3-chloro-5-(trifluoromethyl) pyridin-2-yl) 4-nitrobenzamide (3d).** Yield: (67%); m.p. 108-109 °C; IR: cm<sup>-1</sup> 3435 (N-H), 1685.7 (C=O). <sup>1</sup>H-NMR (MeOD): δ 8.75 (1H, brS, H5), 8.42 (2H, d, J= 8.4 Hz, H2', H4'), 8.39 (1H, d, J= 1.8Hz, H3), 8.21 (2H, d, J= 8.4 Hz, H5', H7'). MS: (m/z) 345 ([M+H]<sup>+</sup>), C<sub>13</sub>H<sub>7</sub>ClF<sub>3</sub>N<sub>3</sub>O<sub>3</sub> (345.01).

**N-(3-chloro-5-(trifluoromethyl) pyridin-2-yl) 3-fluorobenzamide (3e).** Yield: (69%); m.p. 65-66 °C; IR: cm<sup>-1</sup> 3438.8 (N-H), 1678 (C=O). <sup>1</sup>H-NMR (MeOD): δ 8.73 (1H, brS, H5), 8.35 (1H, brS, H3), 7.83 (1H, dd, J= 1.2Hz, 7.6Hz, H2'), 7.73 (1H, dd, J= 2 Hz, 9.6Hz, H6'), 7.59 (1H, dd, J= 7.6Hz, 9.6Hz, H7'), 7.41 (1H, dd, J=1.2Hz, 2Hz H4'); <sup>13</sup>C-NMR: δ 165.65 (C-F, C-5'), 162.5 (C=O), 153.0 (C-1), 144.9 (C-5), 137.58 (C-3), 137.0 (C-3'), 131.90 (C-7'), 126.5 (C-2), 126.03 (C-6), 125.08 (C-2'), 122.4 (C-4), 120.7 (C-4'), 115.9 (C-6'); MS: ( m/z) 318 ([M+H]<sup>+</sup>), C<sub>13</sub>H<sub>7</sub>ClF<sub>4</sub>N<sub>2</sub>O (318.02).

**N-(3-chloro-5-(trifluoromethyl) pyridin-2-yl) butyramide (3f).** Yield: (74%); m.p. 128-129 °C; IR: cm<sup>-1</sup> 3433.1 (N-H), 1689.5 (C=O); <sup>1</sup>H-NMR (MeOD): δ 8.64 (1H, brS, H5), 8.27 (1H, d, J=1.5, H3), 2.53 (2H, t, J= 7.4, H2'), 1.81 (2H, m, H3'), 1.05 (3H, t, J=7.4, H4'); <sup>13</sup>C-NMR: δ 172.01 (C=O), 152.77 (C-1), 144.38 (C-5), 136.55 (C-3), 124.99 (C-2'), 123.09 (C-6), 38.0 (C-2'), 19.18 (C-3'), 13.95 (C-4'); MS: (m/z) 266 ([M+H]<sup>+</sup>), C<sub>10</sub>H<sub>10</sub>ClF<sub>3</sub>N<sub>2</sub>O (266.04).

**3-bromo-N-(5-(trifluoromethyl) pyridin-2-yl) benzamide (5a).** Yield: (80%); m.p. 82-83 °C; IR: cm<sup>-1</sup> 3433.1 (N-H), 1689.5 (C=O). <sup>1</sup>H-NMR (MeOD): δ8.66 (1H, brS, H5), 8.45 (1H, d, J= 8.8Hz, H2), 8.15 (1H, dd, J= 1.6, 2Hz, H4'), 8.12 (1H, dd, J=2, 8.8 Hz, H6'), 7.97 (1H, dd, J= 1.6, 7.6Hz, H2'), 7.79 (1H, d, J= 8.8 Hz, H3), 7.48 (1H, dd, J= 7.6, 8.8 Hz, H7'); <sup>13</sup>C-NMR: δ 165.72 (C=O), 156.03 (C-1), 146.3(C-5), 137.07 (C-3'), 136.5 (C-6'), 135.97 (C-3), 131.7 (C-4'), 131.4 (C-7'), 127.7 (C-2', C-6) 122.9 (C-5'), 114.6 (C-2); MS: (m/z) 344 ([M+H]<sup>+</sup>), C<sub>13</sub>H<sub>8</sub>BrF<sub>3</sub>N<sub>2</sub>O (343.98).

**3-Chloro-N-(5-(trifluoromethyl) pyridin-2-yl) benzamide (5b).** Yield: (65%); m.p. 132-133 °C; IR : cm<sup>-1</sup> 3434.1 (N-H), 1691.59 (C=O); <sup>1</sup>H-NMR (MeOD): δ 8.00 (1H, dd, J=1.6, 2Hz, H4'), 7.93 (1H, dd, J= 1.2, 7.8Hz, H3), 7.64 (1H,

dd, J=1.6, 8.4 Hz, H6'), 7.55 (1H, t, J=8.4, 8.8 Hz, H7'), 8.66 (1H, brs, H5), 8.45 (1H, d, J= 7.8, H2), 8.12 (1H, dd, J=2, 8.8Hz, H2'); <sup>13</sup>C-NMR: δ 165.82 (C=O), 156.0 (C-1), 146.3 (C-5), 136.8 (C-5'), 136.5 (C-3), 134.9 (C-3'), 133.02 (C-7'), 131.2 (C-6'), 128.8 (C-4'), 127.3 (C-2'), 114.5 (C-2); MS: (m/z) 299 ([M+H]<sup>+</sup>), C<sub>13</sub>H<sub>8</sub>ClF<sub>3</sub>N<sub>2</sub>O (300.03)

**4-iodo-N-(5-(trifluoromethyl) pyridin-2-yl) benzamide (5c).** Yield: (60%); m.p. 85-86 °C; IR: cm<sup>-1</sup> 3400(N-H), 1656.7(C=O); <sup>1</sup>H-NMR (MeOD): δ 8.65 (1H, brs, H5), 8.45 (1H, d, J=8.8Hz, H2), 8.12 (1H, dd, J=2, 8.8Hz, H3), 7.93 (2H, dd, J= 1.6, 8.4Hz, H5', H7'), 7.74 (2H, dd, J=1.6, 8.4Hz, H2', H4'); MS: ( m/z) 392 ([M+H]<sup>+</sup>), C<sub>13</sub>H<sub>8</sub>F<sub>3</sub>IN<sub>2</sub>O (391.96)

**3-phenyl-N-(5-(trifluoromethyl) pyridin-2-yl)propanamide (5d).** Yield: (62%); m.p. 130-131 °C; IR: cm<sup>-1</sup> 3433 (N-H), 1664.5 (N-H); <sup>1</sup>H-NMR (MeOD): δ 8.55 (1H, brs, H5), 8.31 (1H, d, J=8.8Hz, H2), 8.03 (1H, dd, J=2, 8.8Hz, H3), 7.23 (4H, q, H5', H6', H8', H9'), 7.18 (1H, m, H7), 3.02 (2H, t, J=7.6 Hz, H2'), 2.78 (2H, t, J=7.6 Hz, H3'); MS: (m/z) : 294 ([M+H]<sup>+</sup>), C<sub>15</sub>H<sub>13</sub>F<sub>3</sub>N<sub>2</sub>O (294.10)

**2, 4-dichloro-N-(5-(trifluoromethyl) pyridin-2-yl) benzamide (5e).** Yield: (85%); m.p. 94-95 °C; IR: cm<sup>-1</sup> 3429.2 (N-H), 1722.3(C=O); <sup>1</sup>H-NMR (MeOD): δ 8.72 (1H, brs, H5), 8.24 (1H, dd, J=2.4, 8.4Hz, H3), 7.82 (1H, dd, J=2, 8.4 Hz, H5') 7.64 (2H, d, J=8.4, H2, H4'), 7.49 (1H, d, J=2.4, H7'); <sup>13</sup>C-NMR: δ 168.67 (C=O), 155.49 (C-1), 147.07 (C-5), 137.79 (C-6'), 137.04 (C-4'), 134.42 (C-3), 133.3 (C-3'), 131.5 (C-2'), 130.75 (C-5'), 128.3 (C-7'), 124.4 (C-2); MS: (m/z) 334 ([M+H]<sup>+</sup>), C<sub>15</sub>H<sub>13</sub>F<sub>3</sub>N<sub>2</sub>O (333.99)

**3, 5-difluoro-N-(5-(trifluoromethyl) pyridin-2-yl) benzamide (5f).** Yield: (76%); m.p. 126-127 °C; IR: cm<sup>-1</sup> 3344.3 (N-H), 1670 (C=O); <sup>1</sup>H-NMR (MeOD): δ 8.66 (1H, brs, H5), 8.44 (1H, d, J= 8.8Hz, H2), 8.13 (1H, dd, J=2, 8.8Hz, H3), 7.63 (2H, d, J= 2.4Hz, H2', H4'), 7.26 (1H, d, J= 2.4Hz H6'); <sup>13</sup>C-NMR: δ 164.62 (C-5', C-7'), 162.98 (C=O), 155.79 (C-1), 146.30 (C-5), 138.43 (C-5'), 136.61 (C-3), 122.72 (C-6), 112.24 (C-4', C-2'), 108.4 (C-6'); MS: (m/z) 302 ([M+H]<sup>+</sup>), C<sub>13</sub>H<sub>7</sub>F<sub>5</sub>N<sub>2</sub>O (302.05).

**4-cyano-N-(5-(trifluoromethyl) pyridin-2-yl) benzamide (5g).** Yield: (67%); m.p. 98-99 °C; IR: cm<sup>-1</sup> 3367.5 (N-H), 1678.0 (C=O); <sup>1</sup>H-NMR (MeOD): δ 8.67 (1H, brs, H5), 8.47 (1H, d, J=8.8Hz, H2), 8.13 (3H, d, J=8.8Hz, H3, H5', H7'), 7.91 (2H, d, J= 8.8Hz, H2', H4'); <sup>13</sup>C-NMR: δ 165.91 (C=O), 155.8 (C-1), 146.3 (C-5), 138.8 (C-3'), 136.6 (C-3), 133.27 (C-5', C-7'), 129.69 (C-2', C-4'), 118.64 (C-8'), 116.32 (C-6'), 114.64 (C-2); MS: (m/z) 291 ([M+H]<sup>+</sup>), C<sub>14</sub>H<sub>3</sub>F<sub>3</sub>N<sub>3</sub>O (291.06).

**4-(trifluoromethyl)-N-(5-(trifluoromethyl) pyridin-2-yl) benzamide (5h).** Yield: (65%); m.p. 118-119 °C; IR: cm<sup>-1</sup> 3365.3 (N-H), 1708.8 (C=O); <sup>1</sup>H-NMR (MeOD): δ 8.67 (1H, brs, H5), 8.48 (1H, d, J=8.8Hz, H2), 8.16 (2H, d, J= 8Hz, H5', H7'), 7.98 (1H, d, J=8.8Hz, H3), 7.86 (2H, d, J=8Hz, H2', H4'); MS: (m/z) 334 ([M+H]<sup>+</sup>), C<sub>14</sub>H<sub>8</sub>F<sub>6</sub>N<sub>2</sub>O (334.05).

#### 4.3 Micro-Plate Alamar Blue Assay (MABA)

Antibacterial susceptibility testing was performed in a 96-well micro plate. Organisms were grown in Mueller-Hinton medium. Inoculums were adjusted to 0.5 McFarland turbidity index. The stock solutions of the compounds were prepared in DMSO in a 1:1 concentration, the stock solutions were serially diluted in Muller-Hinton broth to obtain the concentration of 20µg/ml and the volume of the 96 well plates were made up to 200µl. 5 × 10<sup>6</sup> bacterial cells were added in each of the 96-well plate. The plate was then sealed and incubated at 37°C for 18-20 hrs, Alamar blue dye (10%) was dispensed in each well and shaken at 80 RPM in a shaking incubator at 37°C for 3-4 hrs. Ofloxacin was used as the positive control for the bacteria isolates and Vancomycin for the MDR- *S. aureus* (DMSO showed no cidal effect on the growth of the bacterial cells). All experiment was done in triplicate. Change in colour of Alamar dye from blue to pink indicated the growth of bacteria strains. Absorbance was recorded at 570 and 600 nm by the ELISA reader (SpectraMax M2, Molecular Devices, CA, USA).

Percentage difference in reduction of Alamar Blue between treated and control cells were calculated using the formular:

$$\% = \frac{(\epsilon_{ox})\lambda_2 A\lambda_1 - (\epsilon_{ox})\lambda_1 A\lambda_2}{(\epsilon_{ox})\lambda_2 A'\lambda_1 - (\epsilon_{ox})\lambda_1 A'\lambda_2} \times 100$$

Where (ε<sub>ox</sub>) λ<sub>2</sub> = molar extinction coefficient of Alamar blue oxidized form at 600 nm

(ε<sub>ox</sub>) λ<sub>1</sub> = molar extinction coefficient of Alamar blue oxidized form at 570 nm

A λ<sub>1</sub> = Absorbance of test wells at 570 nm

A λ<sub>2</sub> = Absorbance of test wells at 600 nm

A' λ<sub>1</sub> = Absorbance of control well at 570 nm

A' λ<sub>2</sub> = Absorbance of control well at 600 nm

## Acknowledgements

We acknowledge The World Academy of Science (TWAS) for the Award of the 2013 ICCBS-TWAS Sandwich Postgraduate Fellowship awarded to Ms. Iniobong Ante with FR number: 3240275061 and H.E.J Research Institute of Chemistry, International Center for Chemical and Biological Sciences (ICCBS), University of Karachi, Pakistan where the fellowship was tenable.

## References

- Cai, S. X., Nguyen B., Jia, S., Herich, J., Guastella, J. Redd, S., Tseng, B., Drewe, J., & Kasibhatia, S. (2003). Discovery of substituted N-phenyl nicotinamides as potent inducers of apoptosis using a cell and caspase-based high throughput screening assay. *Journal of Medicinal Chemistry*, 46(12), 2474-2481. <https://doi.org/10.1021/jm0205200>
- Chen, S. Y., Wang, J. T., Chen, T. H., Lai, M. S., Chie, W. C., Chien, K. L., ... Chang, S. C. (2010). Impact of traditional hospital strain of Methicillin-Resistant *Staphylococcus aureus* (MRSA) and community strain of MRSA on mortality in patients with community-onset *S. aureus* bacteremia. *Medicine*, 89, 285-294. <https://doi.org/10.1097/MD.0b013e3181f1851e>
- Crast, L. B. Jr., Graham, R. G., & Chehey, L. C. (1973). Synthesis of Cephapirin and related cephalosporins from 7-(alpha-bromoacetomido) cephalosporanic acid. *Journal of Medicinal Chemistry*, 16(12), 1413-1415. <https://doi.org/10.1021/jm00270a025>
- Dimsdale, M. (1988). Alpidem. *Drugs of the future*, 13,106-109. <https://doi.org/10.1358/dof.1988.013.02.62368>
- Feng, S., & SSning, M. (2009). Green chemoselective synthesis of thiazolo [3, 2-a] pyridine derivatives and evaluation of their antioxidant and cytotoxic activities. *Bioorganic and Medicinal Chemistry Letters*, 19, 5565-5568. <https://doi.org/10.1016/j.bmcl.2009.08.046>
- Hettler, C. P. (1946). Heterocyclic Amines with Antihistaminic Activity. *Journal of the American Chemical Society*, 68(10), 1999-2002. <https://doi.org/10.1021/ja01214a037>
- Hishmat, O. H., Abdel Galil, F. M., & Farrag, D. S. (1990). [C] Synthesis and antimicrobial activity of new benzofuranylpyridine derivatives. *Pharmazie*, 45, 793-795.
- Kasabe, A. J., & Kasabe, P. J. (2010). Synthesis, antitubercular and analgesic activity evaluation of new 3-pyrazoline derivatives. *International Journal of Pharmacy and Pharmaceutical Sciences*, 2, 132-135.
- Merluzzi, V. J., Hargrave, K. D., Labadia, M., Grozinger, K., Skoog, M., Wu, J. C., ... Adams, J. (1990). Inhibition of HIV-1 replication by a nonnucleoside reverse transcriptase inhibition. *Science*, 250(2486), 1411-1413. <https://doi.org/10.1126/science.1701568>
- National Nosocomial Infections Surveillance National Nosocomial Infections Surveillance (NNIS) System Report, data summary from January 1992 through June 2004, issued October 2004. *Am J Infect Control*, 32, 470-485.
- Patrick, G. L., & Kinsman, O. S. (1996). Synthesis and antifungal activity of novel aza-D- homosteriods, hydroisoquinolines, pyridines and dihydrophyridines. *European Journal of Medicinal Chemistry*, 31(7-8), 607-613. [https://doi.org/10.1016/0223-5234\(96\)89557-2](https://doi.org/10.1016/0223-5234(96)89557-2)
- Rajesh, H. B., & Mukul, R. J. (2007). Synthesis and antidiabetic activity of 2, 5-di-substituted-3-imidazol-2-yl-pyrrolo [2, 3-b] pyridines and thieno [2, 3-b] pyridines. *Bioorg. and med. Chem.*, 15, 6782-6795. <https://doi.org/10.1016/j.bmc.2007.08.005>
- Remuzon, P., Bouzard, D., Cesare, P. D., Dussy, C., Jacquet, J., & Jaegly, A. (1992). Synthesis and antibacterial activity of new 5-substituted 1-cyclopropyl-6-fluoro-7-piperazinyl-1,4-dihydro-4-oxo-1,8-naphthyridine-3-carboxylic acids. *Journal of Heterocyclic Chemistry*, 29(4), 985-989. <https://doi.org/10.1002/jhet.5570290453>
- Shreve, R. N., Swaney, M. W., & Riechers, E. H. (1943). Studies in Azo dyes 1. Preparation and Bacteriostatic properties of Azo Derivatives of 2,6-Diamino pyridine. *Journal of the American Chemical Society*, 65(11), 2241-2243. <https://doi.org/10.1021/ja01251a066>
- Tabarini, O., Marufroni, G., Fravolini, A., Cecchetti, V., Sabatini, S., Clercq, E., ... Neyts, J. (2006). Synthesis and Anti-BVDN activity of Acridones as new potential; Antiviral Agents. *Journal of Medicinal Chemistry*, 49(8), 2621-2627. <https://doi.org/10.1021/jm051250z>

## Copyrights

Copyright for this article is retained by the author(s), with first publication rights granted to the journal.

This is an open-access article distributed under the terms and conditions of the Creative Commons Attribution license (<http://creativecommons.org/licenses/by/4.0/>).

## Reviewer Acknowledgements

*International Journal of Chemistry* wishes to acknowledge the following individuals for their assistance with peer review of manuscripts for this issue. Their help and contributions in maintaining the quality of the journal is greatly appreciated. Many authors, regardless of whether *International Journal of Chemistry* publishes their work, appreciate the helpful feedback provided by the reviewers.

### Reviewers for Volume 10, Number 1

Ahmet Ozan Gezerman, Yildiz Technical University, Turkey  
Amer A. Taqa, Mosul University, Iraq  
Chanchal Kumar Malik, Vanderbilt University, USA  
Greg Peters, University of Findlay, USA  
Hesham G. Ibrahim, Al-Mergheb University, Libya  
Mustafa Oguzhan Kaya, Siirt University, Turkey  
Priyanka Singh, University of Iowa, USA  
R. K. Dey, Birla Institute of Technology (BIT), India  
Severine Queyroy, Aix-Marseille Université, France  
Shyamal Kumar Chattopadhyay, Bengal Engineering and Science University, India  
Sitaram Acharya, Texas Christian University, USA  
Sitaram Bhavaraju, U.S.PHARMACOPEIA, USA  
Thirupathi Barla, Harvard University, USA

Albert John

On behalf of,

The Editorial Board of *International Journal of Chemistry*

Canadian Center of Science and Education

**➤ CALL FOR MANUSCRIPTS**

*International Journal of Chemistry (IJC)* is a peer-reviewed, open access journal, published by Canadian Center of Science and Education. It publishes original research and applied articles in all areas of chemistry. Authors are encouraged to submit complete unpublished and original works, which are not under review in any other journals. We are seeking submissions for forthcoming issues. All manuscripts should be written in English. Manuscripts from 3000–8000 words in length are preferred. All manuscripts should be prepared in MS-Word format, and submitted online, or sent to: [ijc@ccsenet.org](mailto:ijc@ccsenet.org)

**Paper Selection and Publishing Process**

- a) Submission acknowledgement. If you submit manuscript online, you will receive a submission acknowledgement letter sent by the online system automatically. For email submission, the editor or editorial assistant sends an e-mail of confirmation to the submission's author within one to three working days. If you fail to receive this confirmation, please check your bulk email box or contact the editorial assistant.
- b) Basic review. The editor or editorial assistant determines whether the manuscript fits the journal's focus and scope. And then check the similarity rate (CrossCheck, powered by iThenticate). Any manuscripts out of the journal's scope or containing plagiarism, including self-plagiarism are rejected.
- c) Peer Review. We use a double-blind system for peer review; both reviewers' and authors' identities remain anonymous. The submitted manuscript will be reviewed by at least two experts: one editorial staff member as well as one to three external reviewers. The review process may take two to four weeks.
- d) Make the decision. The decision to accept or reject an article is based on the suggestions of reviewers. If differences of opinion occur between reviewers, the editor-in-chief will weigh all comments and arrive at a balanced decision based on all comments, or a second round of peer review may be initiated.
- e) Notification of the result of review. The result of review will be sent to the corresponding author and forwarded to other authors and reviewers.
- f) Pay the publication fee. If the submission is accepted, the authors revise paper and pay the publication fee.
- g) Send printed journals by post. After publication, two hard copies of the journal will be sent to the corresponding author.
- h) Publication notice. The authors and readers will be notified and invited to visit our website for the newly published articles.

**More Information**

E-mail: [ijc@ccsenet.org](mailto:ijc@ccsenet.org)

Website: <http://ijc.ccsenet.org>

Paper Submission Guide: <http://submission.ccsenet.org>

Recruitment for Reviewers: <http://recruitment.ccsenet.org>

**➤ JOURNAL STORE**

To order back issues, please contact the editorial assistant and ask about the availability of journals. You may pay by credit card, PayPal, and bank transfer. If you have any questions regarding payment, please do not hesitate to contact the editorial assistant.

Price: \$40.00 USD/copy      Shipping fee: \$20.00 USD/copy

**ABOUT CCSE**

The Canadian Center of Science and Education (CCSE) is a private for-profit organization delivering support and services to educators and researchers in Canada and around the world.

The Canadian Center of Science and Education was established in 2006. In partnership with research institutions, community organizations, enterprises, and foundations, CCSE provides a variety of programs to support and promote education and research development, including educational programs for students, financial support for researchers, international education projects, and scientific publications.

CCSE publishes scholarly journals in a wide range of academic fields, including the social sciences, the humanities, the natural sciences, the biological and medical sciences, education, economics, and management. These journals deliver original, peer-reviewed research from international scholars to a worldwide audience. All our journals are available in electronic form in conjunction with their print editions. All journals are available for free download online.

**Mission**

To work for future generations

**Values**

Scientific integrity and excellence

Respect and equity in the workplace

**CONTACT US****General**

Tel: 1-416-642-2606

Fax: 1-416-642-2608

E-mail: [info@ccsenet.org](mailto:info@ccsenet.org)

Website: [www.ccsenet.org](http://www.ccsenet.org)

**Mailing Address**

1120 Finch Avenue West

Suite 701-309

Toronto, ON., M3J 3H7

Canada

**Visiting Address**

9140 Leslie St., Suite 110

Richmond Hill, Ontario, L4B 0A9

Canada



The journal is peer-reviewed  
The journal is open-access to the full text  
The journal is included in:

Academic Journals Database  
CABI  
CAS  
EBSCOhost  
Elektronische Zeitschriftenbibliothek EZB  
Google Scholar  
JournalTOCs  
LOCKSS  
NewJour

Open J-Gate  
PKP Open Archives Harvester  
Ulrich's  
Universe Digital Library  
WorldCat

## International Journal of Chemistry

Quarterly

Publisher Canadian Center of Science and Education  
Address 1120 Finch Avenue West, Suite 701-309, Toronto, ON., M3J 3H7, Canada  
Telephone 1-416-642-2606  
Fax 1-416-642-2608  
E-mail [ijc@ccsenet.org](mailto:ijc@ccsenet.org)  
Website <http://ijc.ccsenet.org>

ISSN 1916-9698

